Suspended Optical Graphene Modulators and Multiple-layer Terahertz Waveguides

By

Jiamin Liu

A thesis submitted in partial fulfilment of the requirements for the degree of
Master of Philosophy (MPhil)

Antennas & Electro-magnetic Research Group
School of Electronic Engineering and Computer Science
Queen Mary University of London
United Kingdom

June 2021

Declaration

I, Jiamin Liu, confirm that the research included within this thesis is my own or that where it has been carried out in collaboration with, or supported by others, that is duly acknowledged below and my contribution indicated. Previously published material is also acknowledged.

I attest that I have exercised reasonable care to ensure that the work is original, and does not to the best of my knowledge break any UK law, infringe any third party copyright or other intellectual property right, or contain any confidential material. I accept that the university has the right to use plagiarism software to check the electronic version of the thesis. I confirm that the thesis has not previously submitted for the award of a degree by this or any other university. The copy right of this thesis rests with the author and no quotation from it or information derived from it may be published without prior written consent of the author.

Signature:

Date:

Abstract

A development of suspended graphene modulators and layered THz waveguides is conducted by this research. The mainly purpose is to study suspended graphene modulators developed to approach the fundamental limits of graphene and layered THz waveguides for understanding the operating mechanism and possible applications.

A detailed review of graphene modulators and THz waveguides is presented. Problems and challenges in these fields are addressed and the proposed research is presented according to the review.

The suspended self-biasing graphene modulator reduce the compromise between modulation speed and modulation efficiency, and the proposed design is proven to be very close to the fundamental limits of graphene. A suspended triple-layer graphene modulator enhances the light-graphene interaction further. And the modulation speed is therefore increased further with higher modulation efficiency. Further, a comparison between the suspended graphene double-layer modulator and the sub-wavelength thickness modulator is conducted to show the benefit of suspending. A metal-clad suspended self-biasing graphene modulator shows how nearer fundamental limits design of graphene modulator happens.

Layered THz waveguides for the propagation of Surface Plasmon Polaritons (SPPs), filter and sensor applications are presented. The methodology and derivation for this research is shown.

The research work presented in this thesis provides a clear roadmap for next generation graphene modulators and THz waveguides.

Acknowledgments

I would like to express my thanks and sincere gratitude to Prof. Yang Hao for providing financial support and his final help during this PhD.

I would also express my thanks to Dr. Jing Tian and Dr. Yangjie Liu for their useful discussion and kind guidance in completing my first published paper. And to my second supervisor Dr. Khalid Rajab, independent assessor Dr. Akram Alomainy, for examining my Stage 0, Stage 1 and Stage 2, they kindly discussed the technical issues with me to help me pass the stage exams. Particularly, I should show my greatest gratitude to Dr. Khalid Rajab, without his help, I may have no chance to take my PhD final viva. Thank you Dr. Khalid Rajab, I will remember you for all of my life.

I should say thank you particularly to my colleague Mr. Benjamin Inigo Jones, Dr. Siamak Sarjoghian and Mr. Zia Ullah Khan for their help and discussion in my research. We have shared a lot with each other about life and research here. Many years later, I will still cherish my research with them at Queen Mary. I should also thank Dr. Jesus Requena Carrion, Dr, Yasir Alfadhl, Dr. Maged Elkashlan, Dr. Hassan Farooq, and Teacher Damon Owen for our work experience in Queen Mary University of London and helpful discussions during the work.

I also should thank Prof. Steve Uhlig, Teacher Melissa Yeo, Teacher Zi Parker, and Teacher Hayley Cork for their guidance and help for my PhD.

Particularly to Prof. Simon Dixon, for he saved my research and my future. I would also thank all the antennas and electromagnetics group members and all of my friends in Queen Mary University of London.

List of Publications

Journal Papers:

1. **Jiamin Liu**, Yangjie Liu, “Ultrafast suspended self-biasing graphene modulator with ultrahigh figure of merit,” ***Optics Communications,*** 2018, 427: 439-446. (**SCI** impact factor: **2.125**)
2. **Jiamin Liu**, Zia Ullah Khan, and Siamak Sarjoghian, “Suspended triple-layer graphene modulator with two modulation depths and ultra-high modulation speed,” ***OSA Continuum,*** 2019, 2(3): 827-838. (**SCI** impact factor: **3.000, Gold Open Access**)
3. **Jiamin Liu**, Zia Ullah Khan, and Siamak Sarjoghian, “Suspended graphene double-layer modulator with an ultrahigh figure of merit and a sub-wavelength thickness modulator with leaky mode,” ***Applied Optics,*** 2019, 58(14): 3729-3734. (**SCI** impact factor: **1.961**)
4. **Jiamin Liu**, Zia Ullah Khan, and Siamak Sarjoghian, “Metal-clad-suspended self-biasing graphene modulator with tunable figure of merit,” ***Journal of Optics,*** 2020, 49(3): 364-369. (**SCI** impact factor: **2.753, Open Access**)
5. **Jiamin Liu**, Zia Ullah Khan, and Siamak Sarjoghian, “Layered THz waveguides for SPPs, filter and sensor applications,” ***Journal of Optics,*** 2019, 48(4): 567-581. (**SCI** impact factor: **2.753, Open Access**)
6. **Jiamin Liu**, Zia Ullah Khan, Cong Wang, Han Zhang, and Siamak Sarjoghian, “Review of graphene modulators from the low to the high figure of merits,” ***Journal of Physics D: Applied Physics,*** 2020, 53: 233002. (**SCI** impact factor: **2.829, Gold Open Access**)
7. S. Sarjoghian, A. Rahimian, Y. Alfadhl, T. G. Sunders, **Jiamin Liu**, and Clive. G. Parini, “Hybrid Development of a Compact Antenna Based on a Novel Skin-Matched Ceramic Composite for Body Fat Measurement,” ***Electronics***, 2020, 9: 2139. (**SCI** impact factor: **2.412, Gold Open Access**)

Table of Contents

Chapter 1

Chapter 2

Chapter 3

Chapter 4

Chapter 5

Chapter 6

Chapter 7

Chapter 8

List of Figures

List of Tables

List of Abbreviations

2D	Two Dimensional
3D	Three Dimensional
AFM	Atomic Force Microscopy
AM	Amplitude Modulator
BP	Black Phosphorus
CMOS	Complementary Metal Oxide Semiconductor
DMPW	Double-dielectric-slab-coated Metal Plate Waveguide
DMW	Dielectric-slab-coated Metal-film Waveguide
DOS	Density of States
FM	Frequency Modulator
FOMs	Figure of Merits
GHPM	Graphene-based Hybrid Plasmonic Modulator
GHz	Gigahertz
GOG	Graphene-on-graphene
GoS	Graphene-on-silicon
GPM	Graphene Phase Modulator
GVD	Group Velocity Dispersion
h-BN	Hexagonal Boron Nitride
MHz	Megahertz
MNW	Metal Nanofilm-dielectric-plate Waveguide
MPA	Mode Power Attenuation
M-Z	Mach-Zehnder
MZI	Mach-Zehnder Interferometer
PEC	Perfect Electric Conductor
PM	Phase Modulator
PS	Polystyrene
PVD	Phase Velocity Dispersion
RI	Refractive Index

RIU	Refractive-index-unit
SDM	Suspended Double-layer Modulator
SEM	Scanning Electron Microscope
SGHPM	Symmetrical Graphene-based Hybrid Plasmonic Modulator
SPs	Surface Plasmons
SPW	Single-dielectric-slab-coated Parallel-plate Waveguide
SR	Short-range
STM	Sub-wavelength Thickness Modulator
TE	Transverse Electric
TEM	Transverse-electromagnetic
THz	Terahertz
THz SPPs	Terahertz Surface Plasmon Polaritons
TIR	Total Internal Reflecting
TM	Transverse Magnetic
TMDs	Transition Metal Dichalcogenide
TW	Three-layer-dielectric-slab Waveguide

Chapter 1

Introduction

1.1 General review of graphene

Graphene was first fabricated and demonstrated in 2004 [1], and since then there has been a plethora of research studies and potential applications on the topic. Numerous applications have been reported based on the absorption tunability and the ultrahigh mobility of graphene. The most focused and important are graphene-based modulators [2], transistors [3], antennas [4], absorbers [5], filters [6], and switches [7].

As reported, more than 3000 research papers on graphene had been published every year since 2004. Because of the path-breaking work in graphene, two of the authors (A. K. Geim and K. S. Novoselov) in reference [1] won the ***Nobel Prize in 2010***.

1.1.1 The structures of 2D materials

A selection of well-known 2D materials are shown in Fig. 1.1. Graphene consists of a monolayer arrangement of carbon atoms in a hexagonal lattice, forming a real 2D material. Initial theoretical treatments of graphene predicted that it would not be stable in free space, in part due to factors such as thermal fusing. The issues were overcome, and graphene was first fabricated by repeated peeling [1].

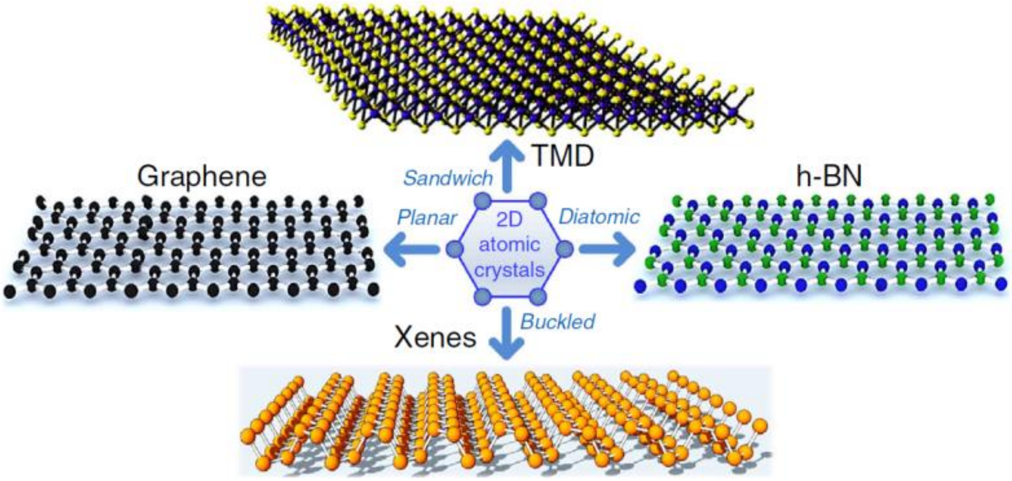

Fig. 1.1 Structures of 2D materials: graphene, TMD, h-BN, and Xenes. The figure is from reference [8].

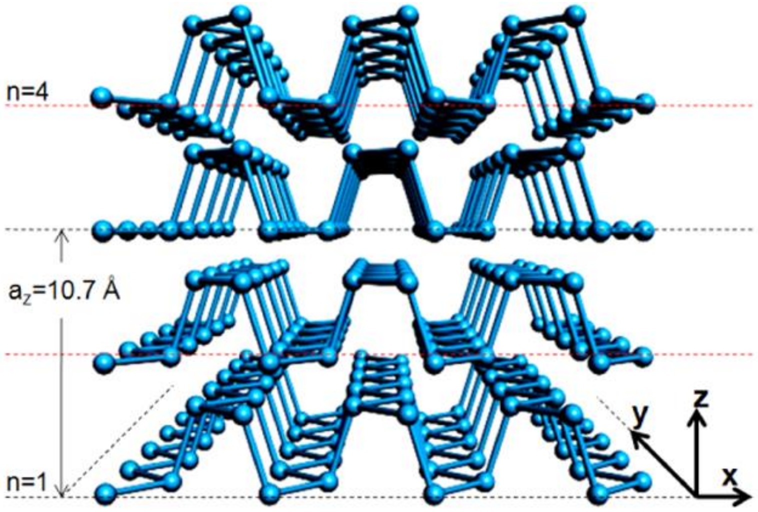

Fig. 1.2 Layer structure of Black Phosphorus: *n* is the number of layers, the lattice constant is a_z which is equal to 1.07 nm. From reference [9].

As the other 2D materials, Transition Metal Dichalcogenides (TMDs) [10-15] consist of one transition metal atom sandwiched by two dichalcogenide atoms. Hexagonal boron nitride (h-BN) [16-18] is very like graphene, and called "white graphene". Xenes [19-21], the most important is Black Phosphorus (BP) [9,21-22]. BP has a puckered layer structure, as seen in Fig. 1.2.

Even though the structures of these materials are very simple, they were not discovered earlier. This is mainly because: i). The monolayer is in a very great minority; ii). 2D material crystals are not clearly seen with an optical microscope on many substrates; iii). Like graphene, they were not obvious to survive without the parent crystals [23].

In this research, I will mainly focus on graphene. This mention of structures of other 2D materials [8-23] here is only for a comparison.

1.1.2 The basic physics of graphene

Graphene has a lot of merits, like high-temperature stability, ultrahigh Young's modulus of elasticity, and ultrahigh electron and hole mobilities. What we are interested in are its electro-optical properties.

Before graphene was firstly fabricated [1], the performances of traditional semiconductors, such as silicon, have been improved to near their developing limits. And the ability to control the electro-magnetic properties of a novel material by some exotic factors (like applied voltage) must be a necessary problem to be overcome and it is at the heart of research on electronic science. The emerging of graphene absolutely overcame this problem.

Conductivities of graphene can be tuned by the exotic doping from applied voltage, magnetic field, and impurity doping. It can be calculated by the Kubo formula [24], which includes the intraband contribution:

$$\sigma_{\mathrm{intra}}(\omega,\mu_{\mathrm{c}},\tau,T)=\frac{\mathrm{i}e^2k_{\mathrm{B}}T}{\pi\hbar^2(\omega+\mathrm{i}\tau^{-1})}\{\frac{\mu_{\mathrm{c}}}{k_{\mathrm{B}}T}+2\mathrm{In}[\mathrm{Exp}[-\frac{\mu_{\mathrm{c}}}{k_{\mathrm{B}}T}]+1]\} \qquad (1\text{-}1)$$

and the interband contribution:

$$\sigma_{\mathrm{inter}}(\omega,\mu_{\mathrm{c}},\tau,T)=\frac{\mathrm{i}e^2}{4\pi\hbar}\mathrm{In}[\frac{2\left|\mu_{\mathrm{c}}\right|-\hbar(\omega+\mathrm{i}\tau^{-1})}{2\left|\mu_{\mathrm{c}}\right|+\hbar(\omega+\mathrm{i}\tau^{-1})}] \qquad (1\text{-}2)$$

Then the conductivity is obtained as:

$$\sigma_{\mathrm{g}}(\omega,\mu_c,\tau,T)=\sigma_{\mathrm{intra}}(\omega,\mu_c,\tau,T)+\sigma_{\mathrm{inter}}(\omega,\mu_c,\tau,T) \qquad (1\text{-}3)$$

In Eqs. (1-1) ~ (1-3), ω is the angular frequency of the electro-magnetic waves; μ_c is the chemical potential of graphene which is also called as the Femi energy level; τ is the momentum relaxation time, which is highly related to the scattering mechanism. The scattering in graphene is mostly from the impurities. In the following research I take τ = 3.3 ps [25], and temperature $T = 300$ K; $e = 1.6\times10^{-19}$ C is the charge of an electron; the Boltzmann's constant is $k_B = 1.38\times10^{-23}$ J/K and the reduced Plank's constant is $\hbar = 1.055\times10^{-34}$ J*s.

In order to know the properties of graphene, Eqs. (1-1) ~ (1-3) are calculated. The conductivity of graphene is obtained as a function of chemical potential at different wavelength: $\lambda = 1.55$ μm (a), and $\lambda = 1$ mm (b), as shown in Fig. 1.3.

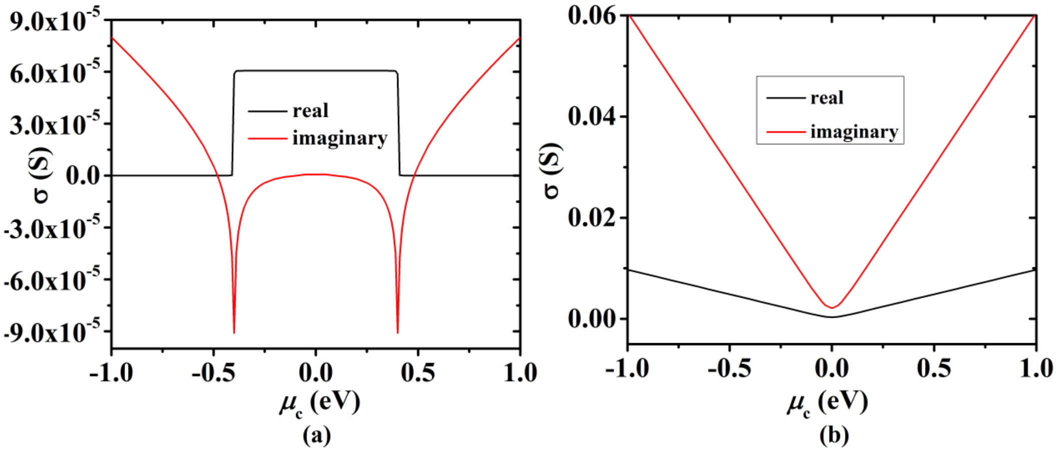

Fig. 1.3 Conductivity of graphene as a function of chemical potential: (a) at $\lambda = 1.55$ μm, and (b) at $\lambda = 1$ mm.

As clear from Fig. 1.3 (a), at the optical range of $\lambda = 1.55$ μm, the absolute values of both the real part and image part of the conductivity are in the scale of 0 ~ 0.06 mS and they are both highly tunable near the chemical potential of $|\mu_c| = 0.4$ eV, which tells us graphene acts like a semiconductor in this interested optical range. Fig. 1.3 (b) tells us that in the terahertz (THz) range (0.3 THz), both the real part and imaginary part of the conductivity are always positive, and the values are higher (in the scale of 0 ~ 0.06 S). Moreover, the highly tunable points disappear. Therefore, graphene acts as a metal film in the low-frequency range such as THz wave and microwave.

The band structure of graphene is used here to explain the quantum physics of graphene, as shown in Fig. 1.4.

Graphene is a zero-bandgap material. From the band structure of Fig.

1.4 (a), we can know how graphene absorbs photons. In the optical range, the energy of a photon is high. When the photon energy is higher than $2|\mu_c|$, the interband transition (Eq. (1-2)) of carrier electrons can take place, and graphene will be very absorptive for light.

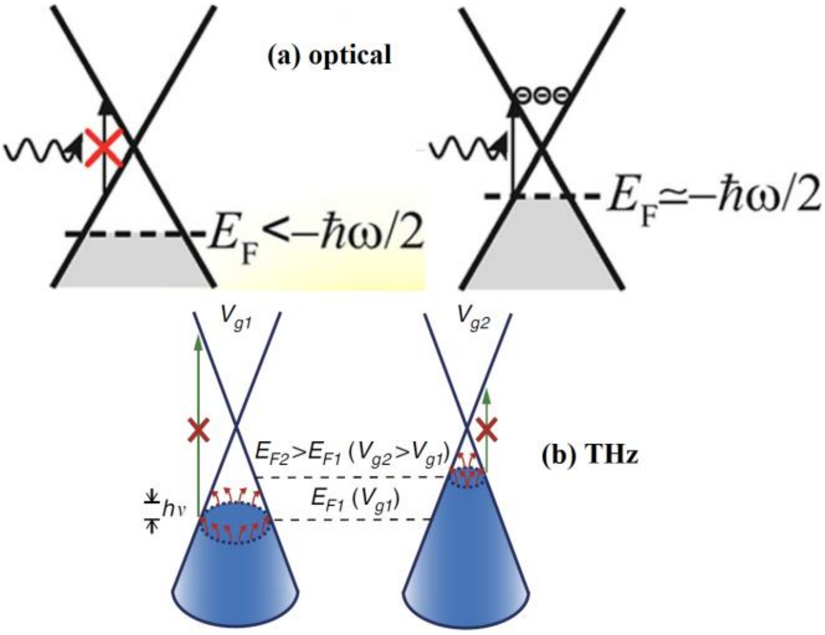

Fig. 1.4 Band structure of graphene: (a) the optical band shows the interband transition happens when the photon energy is double higher than the Femi level or the interband transition is forbidden, (b) the THz band shows the intraband transition dominates. Cut from reference [26,27].

Otherwise, if the photon energy is lower than $2|\mu_c|$, there will be no density of states (DOS) for the interband transition of carrier electrons. This happens in two cases: i). When graphene is p-doped (the Femi level is negative), there will be no carrier available for interband transition; ii). When graphene is n-doped (the Femi level is positive), all the possible states in the conducting band will have been occupied and the interband transition is forbidden, and graphene will be transparent for incident optical waves. Therefore, there is an absorptive threshold for optical waves, which happens at the points when $|\mu_c|$ is equal to half of the photon energy, for example, $|\mu_c| = 0.4$ eV for $\lambda = 1.55$ µm. This is why the conductivity of graphene is tunable and very sensitive to μ_c when $|\mu_c| =$

0.4 eV in Fig. 1.3 (a).

In the THz spectral domain, the photon energy is very low. So the interband transition will be very hard to take place. Even though it can take place, the DOS will be extreme low. In this case, the intraband transition (Eq. (1-1)) dominates, as seen Fig. 1.4 (b). This is why there is no tune point of conductivity in Fig. 1.3 (b).

The physics of graphene are very interesting in the optical range. In order to get a better knowledge of these physics, I calculate the conductivity at different optical wavelength: $\lambda = 0.758$ µm, 1.942 µm, and 10 µm, as shown in Fig. 1.5.

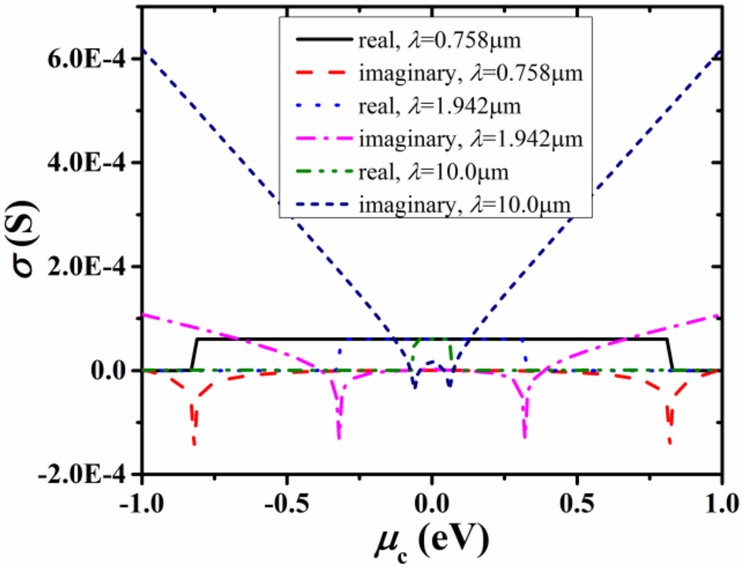

Fig. 1.5 Conductivity of graphene as a function of chemical potential μ_c of graphene: black solid line (real, $\lambda = 0.758$ µm), dashed red line (imaginary, $\lambda = 0.758$ µm), light blue dotted line (real, $\lambda = 1.942$ µm), pink dashed-dotted line (imaginary, $\lambda = 1.942$ µm), green dashed-dotted line (real, $\lambda = 10.0$ µm), dark blue dashed line (imaginary, $\lambda = 10.0$ µm).

We can see both the real part and imaginary part of the conductivity are very sensitive to the chemical potential near the half photon energy $\pi\hbar c/\lambda$ points (such as $|\mu_c| = 0.82$ eV, 0.32 eV, and 0.062 eV). When the wavelength is smaller, the tune points of the conductivity will move to the larger chemical potential, which makes graphene a constant absorber in the visible range. However, when the wavelength is much larger (such as in the THz range), the sensitive points disappear, and graphene behaves like a metal in the lower frequency range.

The physics of these materials [8-23] are different from graphene. For example, all the other 2D materials have a bandgap which is very good for transistor applications. The ratio between on-state current and off-state current for graphene devices is very low (only 3 to 7). The bandgap of monolayer MoS_2 [10-12] is 1.8 eV, and the ratio can be as high as 10^8, giving a great potential for transistor applications [11-13]. The bandgap for monolayer WSe_2 [13-15] has a very close value as MoS_2, which is 1.7 eV. The bandgap of h-BN [16-18] is 5.9 eV, which is almost as high as the bandgap of insulators, thus h-BN is used as a dielectric in electronic applications. Phosphorene [9,19-22] has a lower bandgap, in the scale of 0.3 ~ 2 eV. For bulk materials, the bandgaps are lower accordingly. Moreover, the bulk materials are indirect band type. The band parameters of these 2D materials can be seen Table 1:

Table 1 | Optical and electrical property of other 2D materials. From reference [8].

2D materials	Optical		Electrical		References
	Band gap (eV)	Band Type	Device Mobility (cm^2/Vs)	v_{sat} (cm/s)	
Graphene	0	D	10^3 - 5×10^4	1-5×10^7	[8]
1 Layer MoS_2	1.8	D	10 - 130	4×10^6	[8]
Bulk MoS_2	1.2	I	30 - 500	3×10^6	[8]
1 Layer WSe_2	1.7	D	140 - 250	4×10^6	[8]
Bulk WSe_2	1.2	I	500	\	[8]
h-BN	5.9	D	\	\	[8]
Phosphorene	0.3-2	D	50-1000	\	[8]

Graphene has the highest electronic mobility (as high as 200000 cm^2/Vs for material [28], and 50000 cm^2/Vs for devices). Therefore, graphene-based devices can achieve a very high speed. For other 2D materials, the mobility is very low: only 10 - 130 cm^2/Vs for monolayer MoS_2, 140 - 250 cm^2/Vs for monolayer WSe_2, which is not good for passive devices. For phosphorene [9,19-22], the mobility is much higher (in the scale of 50 - 1000 cm^2/Vs). Phosphorene is a very good candidate for transistor applications [22] and can achieve higher operation speed. For h-BN, the mobility is extremely low, which is almost zero. It is a dielectric. In order to get a better knowledge, the mobility scales of these monolayer 2D materials are shown in Fig. 1.6.

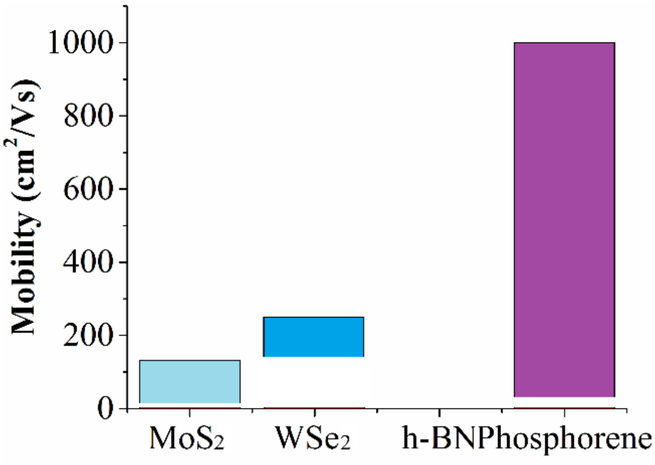

Fig. 1.6 Mobility scales of other 2D materials. Derived from reference [8].

From Fig. 1.6, we can see the difference of scales of mobility for these monolayer 2D materials clearly. For the bulk materials, the mobility should be higher than that of the monolayer materials. Such as the mobility can be 500 cm^2/Vs for bulk MoS_2 and WSe_2. This is because the 3D form of these materials makes the lattice scattering of the carrier electrons lower.

The mobility of a material is highly related to the mean free collision time τ, which has been talked in Eqs. (1-1) ~ (1-3). When an electric field E is added to these materials, the electrons will get a momentum $m_n v_n$. Therefore, we have a relation [29]:

$$-eE\tau = m_n v_n \qquad (1\text{-}4),$$

where e = 1.6×10^{-19} C is the charge of an electron, m_n is the mass of an electron, and v_n is the drift velocity of the electron. So we get a relation of $v_n = -e\tau E / m_n$, and the mobility of the electrons can be obtained as [29]:

$$\mu \equiv e\tau / m_n \qquad (1\text{-}5)$$

In the relation of Eq. (1-5), there are two main mechanisms which limit the mean free collision time: i). Lattice scattering (τ_L); And ii). Impurity scattering (τ_I). In addition, the total mean free collision time τ can be expressed as [29]:

$$\frac{1}{\tau}=\frac{1}{\tau_{\mathrm{L}}}+\frac{1}{\tau_{\mathrm{I}}} \tag{1-6}$$

The lattice scattering is attributed by the thermal oscillation of the atoms, which is much more important at higher temperature. What we are interested in is the impurity scattering, which is very important when the material is doped at room temperature. However, the impurity scattering is much less important at higher temperature. In my research, I will only consider the devices at room temperature, and the impurity scattering will be a key factor in the application of graphene.

1.1.3 The applications of graphene

Since the first realization of these 2D materials in free space, potential applications have served as motivation for research and have been frequently reported, especially for graphene. Significant interest in the graphene-based devices is emerged, and arguably the most important devices are the graphene-based passive wave components.

Passive devices, including modulators, filters, switches, splitters, and couplers, are often waveguide-based. Waveguides are used to achieve point-to-point electromagnetic wave transmission, and can be made of noble metals, semiconductors or dielectrics. Applications based on these materials have been stretched to their performance limits at microwave [30], THz [31] and optical wavelengths [32].

To deal with the issue of performance improvements for waveguide-based passive devices, researchers have begun to investigate how to exploit novel materials for the design of waveguides. Among these materials, the 2D materials are good candidates for fabricating waveguide-based passive devices, especially graphene.

Switches, splitters, and couplers are important passive devices for the developing of technology. Graphene can switch the transmission of light by tuning the chemical potential from low loss to high loss state at the absorbing threshold of interband transition. Fig. 1.7 illustrates a graphene switch enabled by the coupling of surface plasmons (SPs) from different graphene sheets [33], and the light can also be split. From Fig. 1.7 (a) and (b), we can see the intensity of the SP mode is coupling from one graphene sheet to another two graphene sheets. When the two arms of the later graphene sheets are both biased to have higher chemical potentials, the SP modes will be guided on the two sheets, and this device acts as a splitter. This is because only the intraband transition can take place in the two sheets of graphene. When one of the two arms is biased to have a lower chemical potential ($\mu_c < \hbar\omega/2$), the interband transition of this graphene sheet will take place, and the loss on this sheet will be very high, and it will stop the mode transmitting. Therefore, this device also acts as a 1 multiply 2 switch.

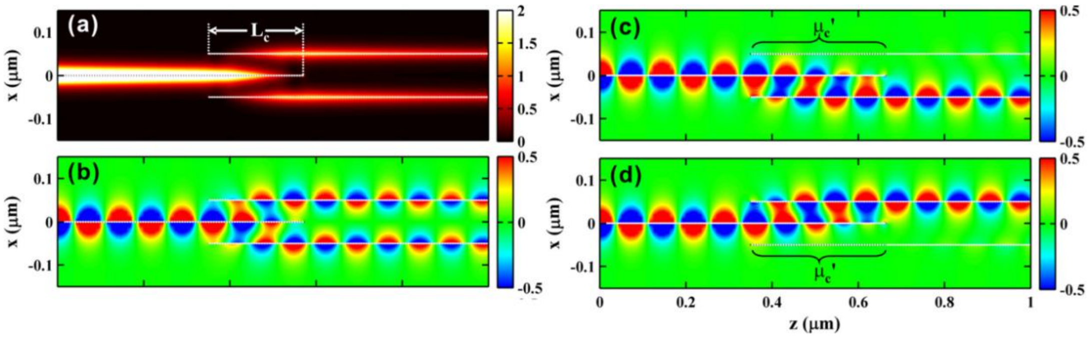

Fig. 1.7 Functions of graphene as a coupler, switch, and splitter. (a) is the intensity distribution of SP mode. The SP mode intensity is coupled from one graphene sheet to another two graphene sheets. (b) is the no biased splitter. (c) and (d) are the 1 multiply 2 switches. From reference [33].

Passive filters are also frequently used in computers, mobile phones, and many other applications. The graphene-based filter can be enabled by the resonance of a Fabry-Perot etalon, or the threshold of interband transition. From Fig. 1.8 (a), we can see two graphene waveguides are coupled by a graphene ring [6]. When the SP mode is coupled by the graphene ring, only those incident wavelengths which satisfy the resonance conditions of the graphene ring can be transmitted efficiently. Therefore, there will be some transmission peaks at the resonance wavelengths, as seen in Fig. 1.8 (d). In addition, this can be used as a frequency pass filter. From the mode field distribution in Fig. 1.8 (b) and (c), we can see when the resonance order is 2 or 3, there will be 2 or 3 field peaks accordingly.

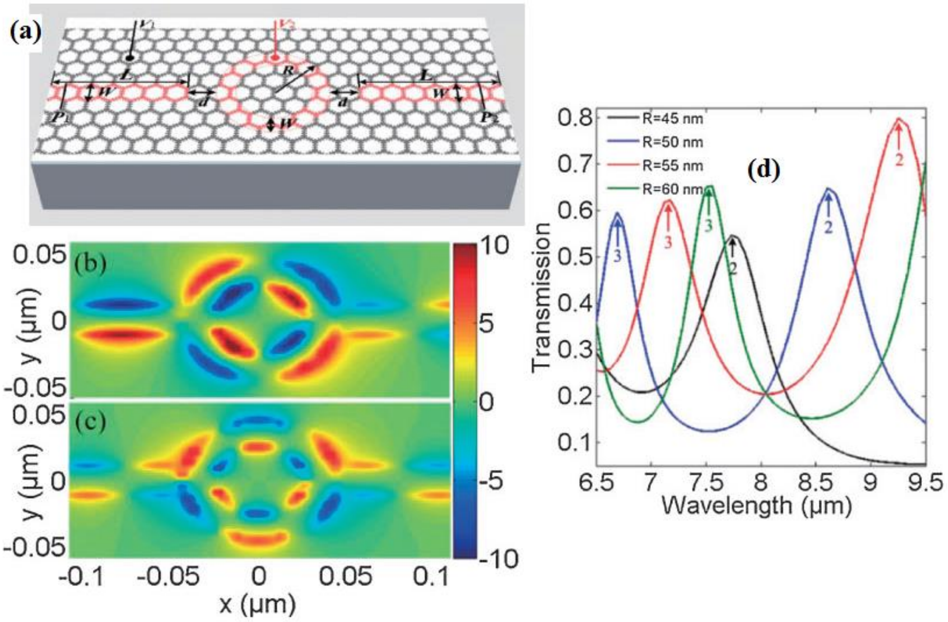

Fig. 1.8 Graphene-based tunable plasmonic filter. (a) is the structure of the filter: two side graphene waveguides are coupled by a graphene ring. (b) and (c) are the mode field distribution at the resonance wavelength of order number 2 and 3. (d) is the transmission of the filter as a function of wavelength. From reference [6].

Among all these passive devices, modulator is a device which benefits greatly from graphene. A graphene-based modulator has a much smaller footprint (as small as 0.18-0.3 μm^2 [34]), higher modulation speed (as high as 150 GHz [35]), larger modulation depth (can be more than 90% [35-37]), broader operation bandwidth (15 THz [34,37]), and lower energy consumption (0.482 fJ/bit [38]), than traditional silicon-based modulators.

The fundamental limits of graphene-based modulators have been discussed in [39], which should be a figure of merit (FOM) to measure the performance of a graphene modulator.

The review of graphene modulators will be presented separately below. It is divided into two parts. The first part is to address the research trend of graphene modulator, and the second part addresses the better figure of merits (FOMs). Firstly, I want to address the suspended graphene devices which are highly related to my research work on suspended graphene modulators.

1.1.4 The suspended graphene devices

Graphene has two important properties which have resulted in great interest and many potential applications: highly tunable absorption loss; and ultrahigh mobility. The value of the tunable absorption loss depends on the light-graphene interaction. The latter one is highly related to the impurity doping in graphene because of the impurity scattering (has been discussed in Eq. (1-6)).

How to achieve high mobility in graphene? The problem is to make the impurity scattering lower and it has two methods: i). Improving the quality of the substrate with much lower impurity residues; ii). Eliminating the substrate and totally suspending the graphene over a semiconductor wafer trench. Both of these two methods are aiming to make the impurity doping from the ambient to graphene lower. Here first I want to talk about the suspending graphene devices. There have been some papers [28,40-42] reported the suspending graphene devices. By suspending, we can achieve high-quality graphene devices.

The ultrahigh mobility of suspending graphene has been first reported by Bolotin et al. [28]. They firstly deposit a single layer graphene flake on the semiconductor wafer and then remove about 150 nm of the SiO_2 substrate by oxygen plasma etching. The schematic of this suspended graphene can be seen in Fig. 1.9.

As shown in Fig. 1.9 (a), there are six electrodes on the suspended graphene sheet, which are marked by number 1 - 6. The electrodes 1 and 4 are used to apply high voltage on the total sheet of graphene to realize current annealing. When the high voltage is applied, a very high current will be in the graphene sheet and will cause heat to erase the impurity which resides on the graphene. This current annealing will be very effective and the quality of the suspended graphene will be much better.

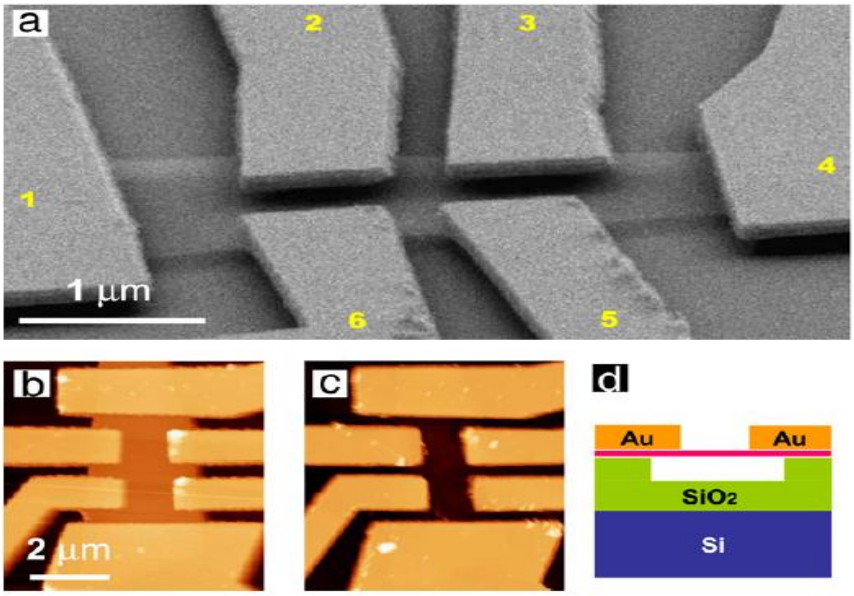

Fig. 1.9 (a) Scanning electron microscope (SEM) image of the suspended graphene with six electrodes. (b) Atomic force microscopy (AFM) image of the device with graphene, and without graphene (c). (d) is the schematic of the fabricated device. From reference [28].

When the voltage V_{xy} is applied on the electrodes 2 and 6, the current I will be measured, and the Hall resistance R_{xy} can be obtained as $R_{xy} = V_{xy}/I$. When the voltage V_{xx} is applied on the electrodes 2 and 3, the resistance R_{xx} can be obtained as $R_{xx} = V_{xx}/I$. Then the resistivity ρ_{xx} can be obtained as:

$$\rho_{xx} = R_{xx}(W/L) \qquad (1\text{-}7),$$

where W is the width of the suspended graphene, and L is the length of graphene between electrodes 2 and 3. The suspended graphene can be biased between graphene and the Si under SiO_2, the biasing method can be seen clearly in Fig. 1.10.

When the voltage is applied between graphene and the Si, there will be an electric field in the SiO_2, and the electrons or holes in the SiO_2 will move to the graphene sheet, and it will be n-doped (the Femi level is in the conducting band) or p-doped (the Femi level is in the valence band). The Dirac point happens at the zero doping.

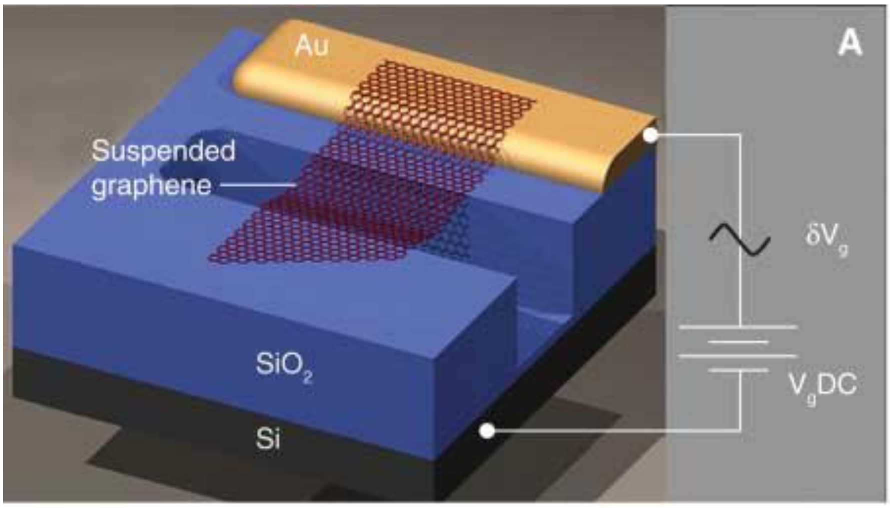

Fig. 1.10 Method of how to bias the suspended graphene. From reference [40].

The resistivity of the suspended graphene is measured as a function of applied voltage, as shown in Fig. 1.11 (a).

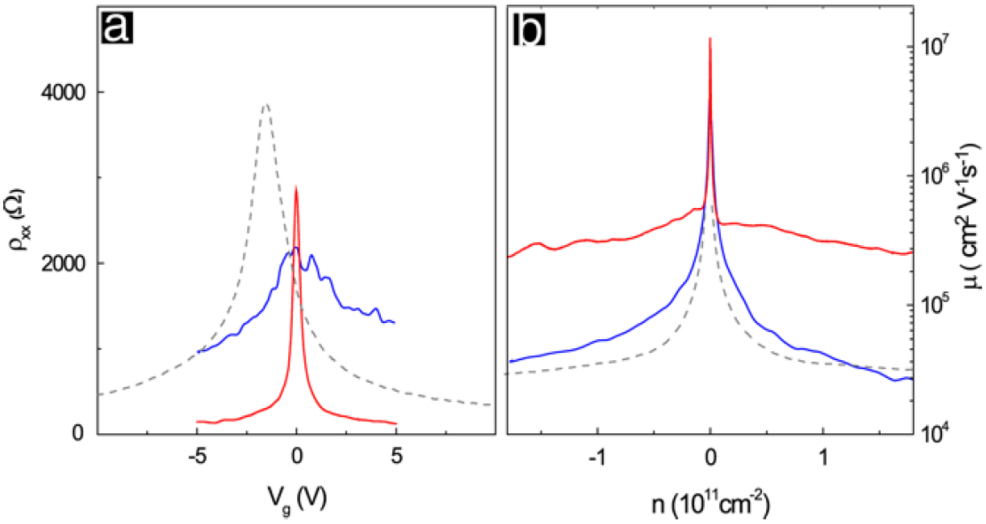

Fig. 1.11 (a) Measured resistivity of graphene: gray dashed curve is from the graphene on the substrate, the blue curve is from the suspended graphene before current annealing, the red curve is from the suspended graphene after current annealing. (b) is the corresponding mobility calculated by $\mu = 1/en\rho_{xx}$. From reference [28].

For the graphene on substrate (grey dashed curve in Fig. 1.11), the resistivity is high, and the Dirac point moves to a negative voltage, which is because of the natural doping from the substrate. For the suspended graphene before annealing, the resistivity is also high, because the scattering from residues is not reduced significantly. The curve is also in low quality with a lot of fluctuations, which tells us the quality of the suspended graphene is still low. However, the Dirac point happens at the zero-biasing voltage.

After current annealing, the quality of the suspended graphene is much better with a high-quality curve (red). Moreover, the resistivity is much lower and the Dirac point happens at exactly zero-biasing voltage. The mobility of graphene can be calculated from the resistivity as:

$$\mu = 1/en\rho_{xx} \qquad (1\text{-}8),$$

where e = 1.6×10^{-19} C, n is the density of the carrier. Then the mobility of the graphene can be obtained, as shown in Fig. 1.11 (b). It is concluded that the mobility of carriers in the suspended graphene after annealing can be as high as 200 000 cm^2/Vs which is one order higher than that of graphene on the substrate, which tells us that we can achieve high performance devices by suspending the devices.

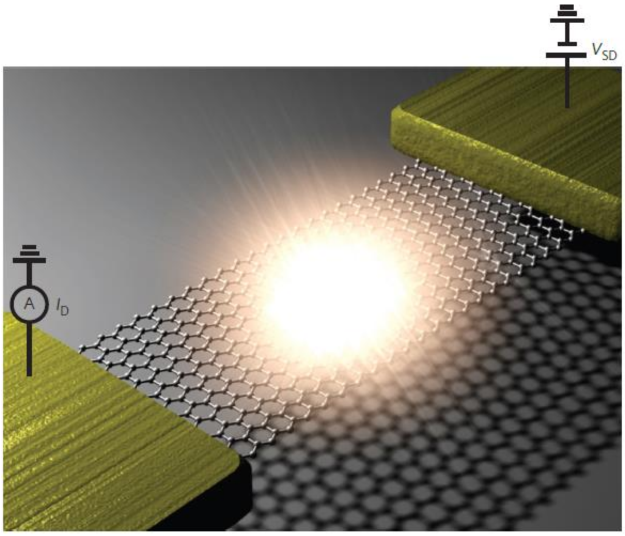

Fig. 1.12 Suspended graphene for thermal bright light emission. From reference [41].

There are also some other applications for suspended graphene, such as used for thermal light emission, as shown in Fig. 1.12, because of the high-temperature stability of graphene. However, the efficiency of light emission by graphene on a substrate is very low and the spectrum is limited to the infrared range, which is because of the high heat dissipation from the substrate and the significant hot electron relaxation caused by extrinsic impurity scattering. Nevertheless, the suspended graphene can overcome these problems and achieve high efficiency bright thermal light emission. We can achieve high-efficiency devices by suspending the devices.

1.2 Review of graphene modulators (part I)

Among most of the passive devices, modulator is a very common device and has been reported by numerous papers [2,9,26,27,34-39,43-59]. Before the development of graphene fabrication technology, the modulators were suffering from a large footprint, high-energy consumption, low operation speed, narrow bandwidth, and low modulation depth. Modulators based on traditional materials [43-45] have been developed to their performance limits. The first graphene modulator was reported [2] in 2011. Since then, many studies [26,27,34-38,46-59] have been performed and published on different graphene modulators with different structures, and the figure of merits (FOMs) have been improved significantly.

The structures of graphene modulators can be a monolayer graphene coated on top of semiconductor wafer [2,46], double-layer sandwiched by an insulator material such as Al_2O_3 [26,35,47], four [48] or more graphene layers [36] on wafer, graphene-coated cylinder dielectric wire [49-51], dielectric loaded plasmon waveguide [34], and Mach-Zehnder (M-Z) interferometer [36,46], for optical modulator [2,26,34-38,46-51,53-59] and THz modulator [27,52].

Among these graphene modulators, there are still a lot of challenges and problems to be overcome. In this section, first I will talk about the basic physics of modulator to address what a modulator is and what its function is (section 1.2.1). Then, I will talk about several examples to address the challenges and problems in this field (section 1.2.2). Third, I will record the state-of-the-art values in this field by studying most of the references reported graphene modulators (from section 1.2.3 to 1.2.6).

1.2.1 The basic physics of a modulator

In electronics and telecommunications, a modulator is used as a device to vary one or more properties of the carrier wave by an electronic or optical information signal. In this research, I will only consider the case when the carrier wave is an optical or THz wave. According to the different varying properties of the carrier waves, the modulators can be divided into amplitude modulator (AM), frequency modulator (FM), and phase modulator (PM). In this research, I will only consider amplitude modulator.

1.2.1.1 Types of modulator:

According to the different types of information signal, modulators can be divided into electro-optical, magnetic-optical, and all-optical types. In this research, I will only consider the electro-optical modulator. The electro-optical modulator can also be divided into electro-absorptive and electro-refractive types according to the difference of the changes of mode effective refractive index when a voltage is applied on the material. The modulator enabled by the change of imaginary part of the mode effective refractive index is defined as the electro-absorptive modulator, and the modulator enabled by the change of real part of the mode effective refractive index is defined as the electro-refractive modulator. The electro-refractive modulator is often used as a Mach-Zehnder (M-Z) interferometer. In this research, both the electro-absorptive modulator and the electro-refractive modulator will be considered.

1.2.1.2 FOMs of modulator:

There are several figure of merits (FOMs) need to be addressed for the electro-optical modulator, which include modulation depth, modulation speed, footprint, modulation bandwidth, operation bandwidth, and figure of merit (FOM).

The **modulation depth** is defined as the change of the amplitude of the carrier waves when a modulation is operating. The concept can be seen in Fig. 1.13.

From Fig. 1.13, we can see in the modulation, the amplitude of the carrier signal changes as the information signal changes, and the highest change of the amplitude is defined as the modulation depth. It can be written as:

$$h = \frac{m(t)}{A} \qquad (1\text{-}9),$$

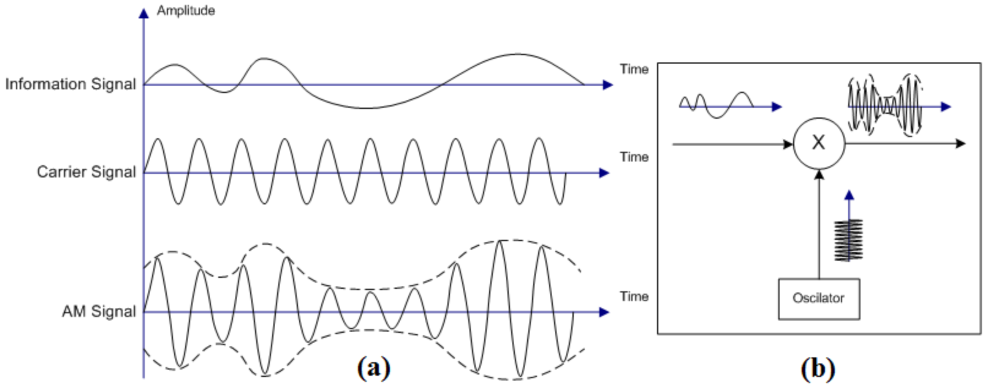

Fig. 1.13 (a) Schematic of the definition of modulation depth; (b) Schematic of the operation of a modulator. From Wikipedia.

where $m(t)$ is the amplitude of the information signal wave, A is the amplitude of the carrier wave. For a realized transmission-based modulator, the modulation depth can also be obtained as [26]:

$$M = \frac{T_{on} - T_{off}}{T_{on}} \qquad (1\text{-}10),$$

where T_{on} is the on-state transmittance, T_{off} is the off-state transmittance. The normalized modulation depth can also be defined as the extinction ratio which is [34]:

$$\text{extinction ratio} = \Delta\alpha = \alpha_{off} - \alpha_{on} \qquad (1\text{-}11),$$

where α_{off} is the off-state loss of the modulator, α_{on} is the on-state loss of the modulator.

The **modulation speed** is defined as the frequency of the information signal when 3-dB modulation amplitude is applied to the modulator. The equivalent circuit of the modulator can be simplified as a voltage source applied to a resistance and a capacitor, as shown in Fig. 1.14.

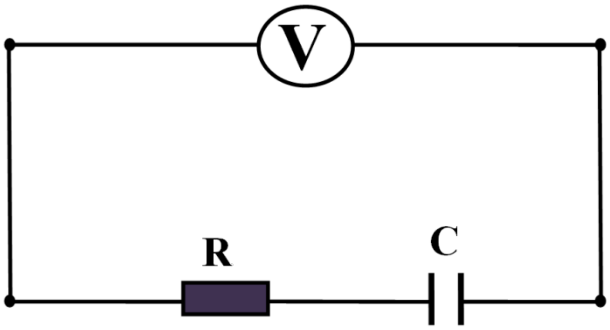

Fig. 1.14 Equivalent circuit of a modulator, which includes the applied voltage, the resistance of the modulator, and the capacitor of the modulator.

When the frequency of the applied voltage is higher, the resistance caused by the capacitor will be lower. Therefore, at a higher modulation frequency, the voltage will be mostly applied on R, and the modulator cannot be operated efficiently. When the modulator is operating, we should ensure enough energy is applied on the capacitor, so the modulation speed cannot be too high for the best performance of a fixed modulator. The modulation speed is the modulation frequency when 50 percentages (3-dB) of applied voltage is applied on the capacitor. We have a relation of:

$$R = \left| \frac{1}{i\omega C} \right| \tag{1-12}$$

Then we get the 3-dB modulation speed of:

$$f_{3\mathrm{dB}} = \frac{1}{2\pi RC} \tag{1-13}$$

In the graphene modulator, R includes the contact resistance between electrodes and graphene and the graphene sheet resistance, C is related to the footprint of the modulator.

The **footprint** of a modulator is defined as the active modulation area. In a waveguide-based modulator, it is the beam width multiply the interaction length of the light in the waveguides. There is also a modulation speed limit which is related to the interaction length, and it can be obtained as:

$$f_{\text{limit}} = \frac{\mathrm{c}}{4nL} \qquad (1\text{-}14),$$

where c is the velocity of light in vacuum, n is the effective refractive index of the mode, and L is the interaction length. This limit is to ensure the electric field in the material is a fixed value when the electro-magnetic wave is transmitting in the modulator.

The value of **modulation bandwidth** is often the same as the modulation speed because the lowest possible modulation speed is zero.

The **operation bandwidth** is the bandwidth of the carrier waves. If it is broader, more channels of the signal can be carried in the modulator.

The **figure of merit (FOM)** is defined as the ratio between extinction ratio and insertion loss. The insertion loss is the lowest loss of the modulator which cannot be tuned, and it can be calculated as:

$$L = -10\log[T_{\max}] \qquad (1\text{-}15)$$

The fundamental limit of a modulator is a relation between insertion loss and modulation depth as described in reference [39]. Therefore, the FOM can be an index of the fundamental limit of a modulator.

1.2.2 The graphene modulators

The first graphene-based modulator was reported in 2011 [2], where monolayer graphene is coated on the semiconductor wafer (Si bus waveguide with an Aluminum oxide), as shown in Fig. 1.15 (a). The voltage is applied between graphene and the Si. The Al_2O_3 is acting as an insulator. For the low thickness of the Al_2O_3 (only 7 nm here), the applied voltage on this modulator is very low, in the scale of -5 V ~ 5 V. The footprint of this modulator is 25 μm^2 (where the interaction length is 40 μm). The transmission is measured as a function of the drive voltage, as shown in Fig. 1.15 (c), the physics is to switch the interband transition threshold. The normalized modulation depth can be 0.1 dB/μm.

The authors further obtained the 3D transmission spectrum as functions of drive voltage and operation wavelength. They found that there is a sharper change of the transmission at the threshold points, as shown in Fig. 1.15 (d) (red dashed line). However, the highest modulation speed is only 1.2 GHz, which is because of the high contact resistance and graphene sheet resistance. Another problem is that, as seen in Fig. 1.15 (b), the light-graphene interaction is low, because the highest field amplitude is not happening at the position of graphene.

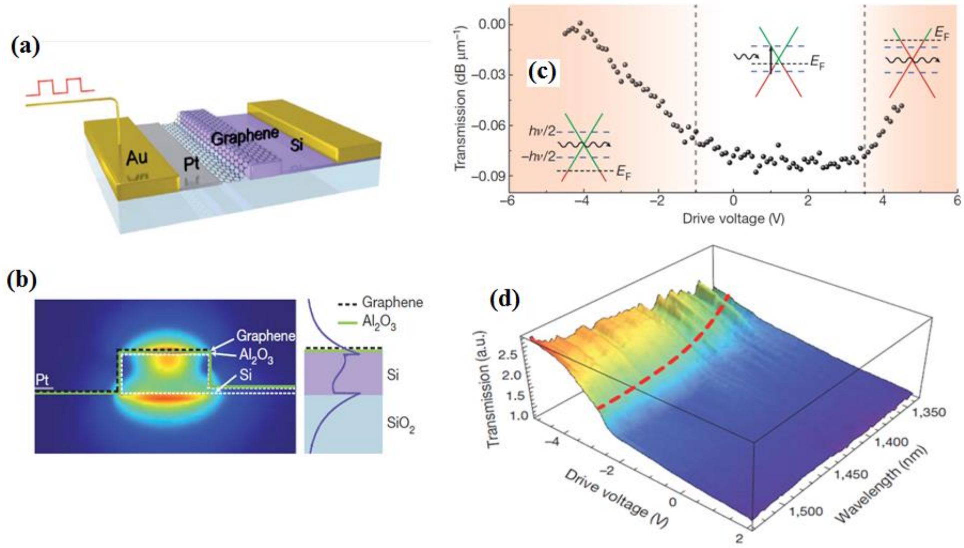

Fig. 1.15 Modulator from reference [2]. (a) 3D schematic of the modulator; (b) Field distribution of mode in the modulator; (c) Measured transmission of the modulator; (d) 3D spectrum of transmission as functions of drive voltage and operation wavelength.

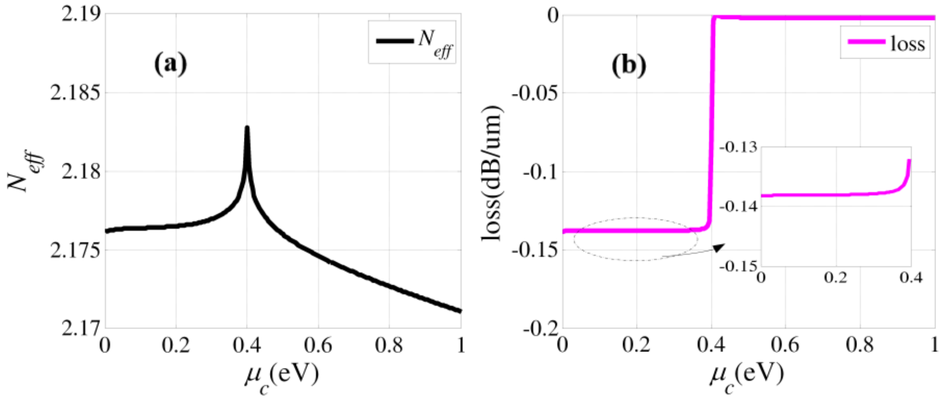

Fig. 1.16 Real part (a) and image part (b) of the mode index for the modulator in reference [46].

This modulator can also be used as a Mach-Zehnder modulator, and it has been reported by reference [46]. In their work by theoretical calculation, they found the real part of mode index has a significant change as a function of the chemical potential, as shown in Fig. 1.16.

They found the variation of the real part of the mode index (ΔN_{eff}) can be about 0.015. This is very good for Mach-Zehnder modulator, as shown in Fig. 1.17.

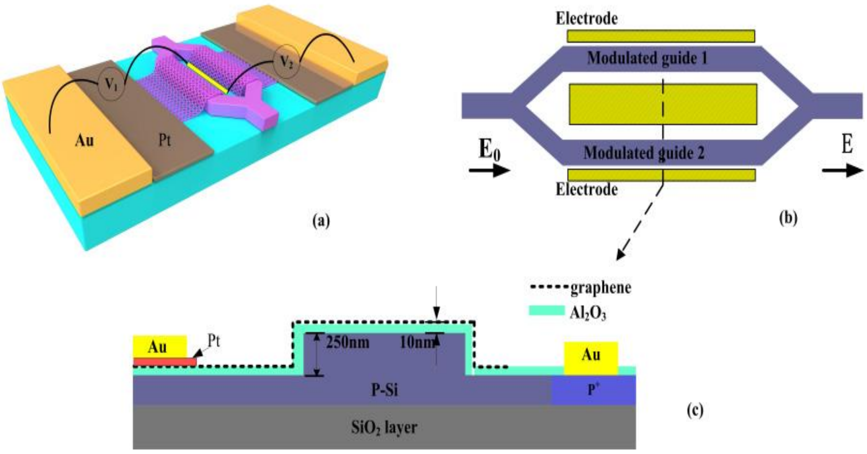

Fig. 1.17 Mach-Zehnder modulator in reference [46].

Two arms of the waveguides are used in this Mach-Zehnder modulator. One arm is biased by a fixed voltage to make the chemical potential to fix at 0.4 eV, and the other arm is biased by a changeable voltage (chemical potential). Therefore, the transmission of this modulator will depend on the chemical potential of the modulation arm, and can be calculated as:

$$T(\Delta\mu_c) = \frac{1}{4}\times[\exp(-\alpha_0 L)+\exp(-\alpha_1 L)+2\exp(-\frac{\alpha_0 L+\alpha_1 L}{2})\cos(\Delta\phi)] \qquad (1\text{-}16),$$

where $\Delta\phi = \frac{2\pi}{\lambda}\Delta N_{eff} L$, and α_0 and α_1 are the mode power attenuation (MPA) of the reference arms and the modulation arm, respectively.

The problem of this modulator is that the footprint is very large, and ΔN_{eff} is still very low.

A higher modulation speed was reported by reference [35] and it can be 150 GHz. In their work, they used one bus waveguide and one ring waveguide to couple with each other, as shown in Fig. 1.18.

The double graphene layers are coated on the ring waveguide, as shown in Fig. 1.18 (b) and detailed in Fig. 1.19 (a). When the interband transition of graphene takes place, the ring waveguide will be very lossy, and much less mode power will be coupled to the ring waveguide, so the transmittance in the bus waveguide will be very high. On the other way, if only the intraband transition take place, the ring waveguide will be transparent, and much more mode power will be coupled to the ring waveguide, so the transmittance in the bus waveguide will be very low.

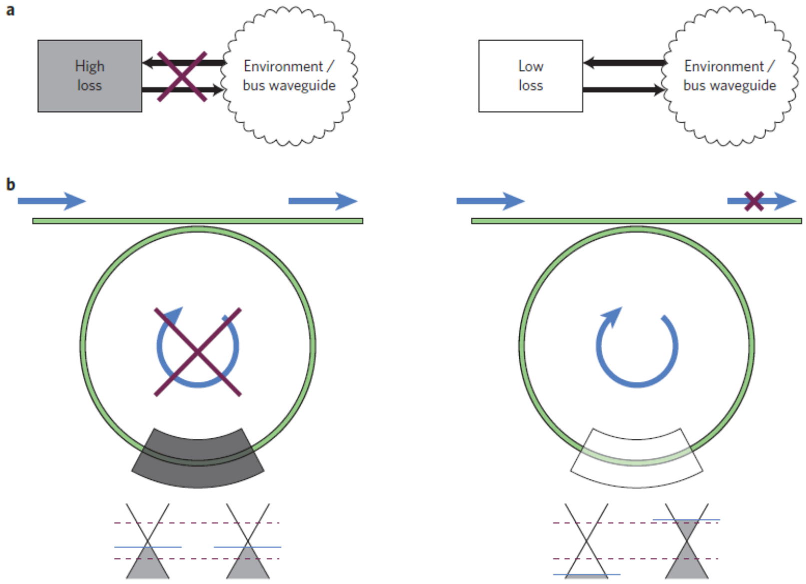

Fig. 1.18 Graphene modulator of one bus waveguide coupled by a ring waveguide: (a), Schematic concept. For a given coupling strength, a low-loss system will be more coupled to its environment than a high-loss system because of impedance matching. (b), Effect in a graphene-clad ring resonator and band diagrams for the two gated sheets of graphene in the parallel-plate capacitor structure. From reference [35].

In their fabrication, a very thick (65 nm) Al_2O_3 is deposited between two graphene layers, as seen in Fig. 1.19 (a). Then the voltage is applied between these two graphene layers. Because of the very thick insulator, the capacitance of this modulator is very small, which enhances the modulation speed (150 GHz). However, the applied voltage should be much higher (up to 50 V) for the thicker insulator, and the modulation efficiency should be lower.

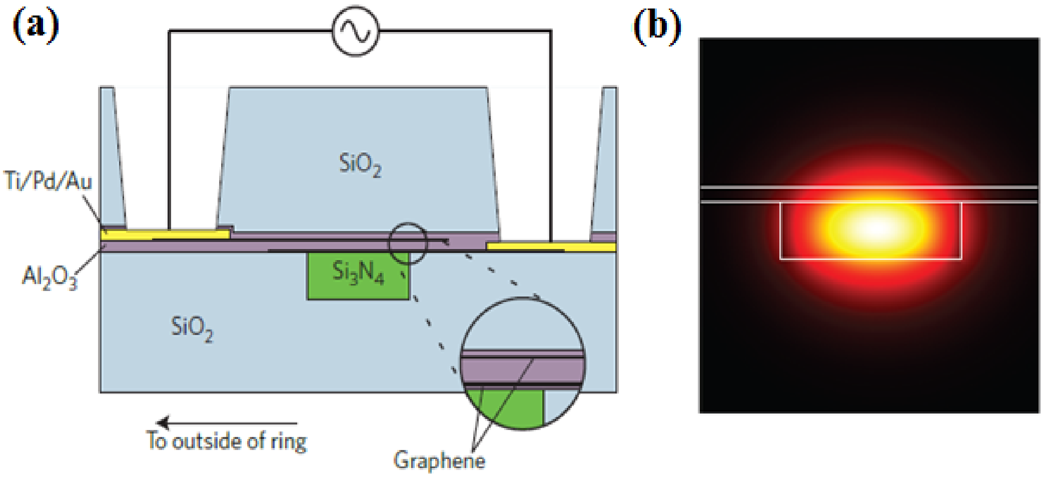

Fig. 1.19 (a) Structure of the graphene modulator placed on the ring waveguide, and (b) mode profile in the active area of the modulator. From reference [35].

Therefore, there is a compromise between modulation speed and modulation efficiency.

The high-κ dielectric material [60] has been used as an insulator in the graphene modulator [53]. The sub-wavelength thickness graphene modulator is shown in Fig. 1.20.

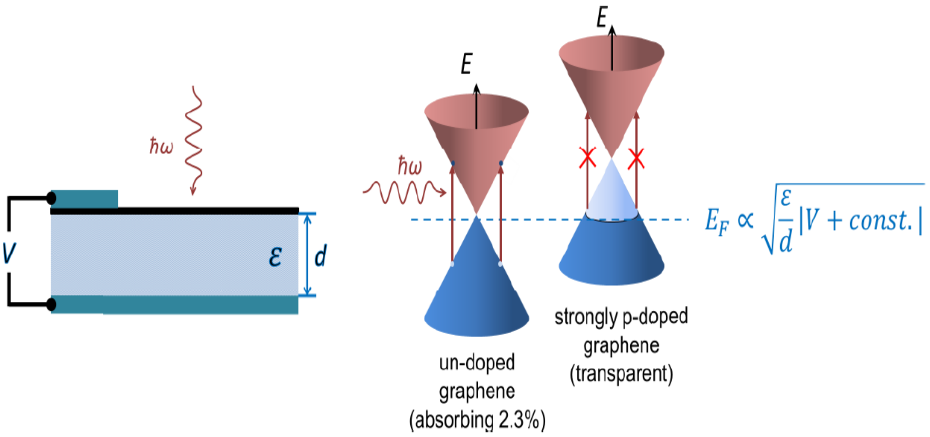

Fig. 1.20 Sub-wavelength thickness graphene modulator from reference [53].

In their work, a very thick high-κ gate material (Ta_2O_5) acts as an insulator between the upper-graphene layer and the low metal electrode. The light at λ = 1.55 μm incident at the perpendicular direction. The metal electrode also acts as a reflector. This modulation is also enabled by the interband transition, as seen the band structure in Fig. 1.20.

The performance of this modulator is shown in Fig. 1.21. Even though the thickness of the insulator is very high (~ 225 nm), the modulation area is also very large. Therefore, the modulation speed is limited to 100 MHz, as seen in Fig. 1.21.

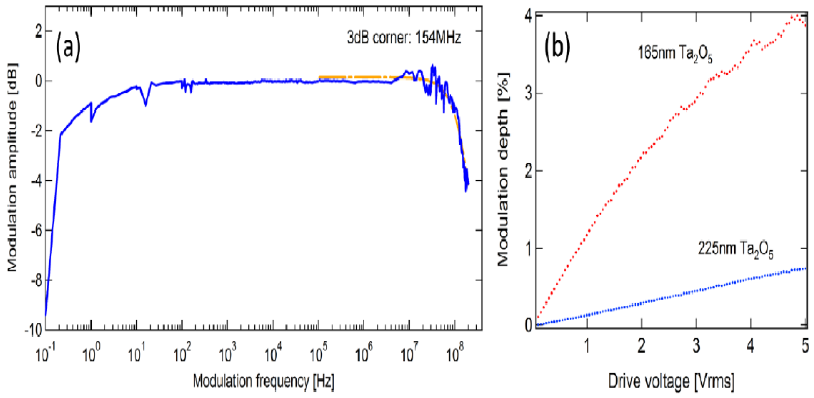

Fig. 1.21 Performance of the sub-wavelength thickness modulator in reference [53]: (a) response of the modulator (modulation speed), (b) modulation depth as a function of drive voltage.

Moreover, the light-graphene interaction is extreme low because the interaction length is only two of the thickness of the monolayer graphene. Therefore, the modulation depth is very low, which is on the scale of ~ 4%.

The above electro-optical modulators are operated at a wavelength of 1.55 μm. The THz graphene modulators which enabled by the intraband transition should be addressed accordingly as a comprehend review.

The THz graphene modulator was first demonstrated in reference [27]. In their work, they fabricated the modulator (as shown in Fig. 1.22 (a)) by using a single layer graphene coated on the top of SiO_2/p-Si substrate. The conductivity was measured as a function of applied voltage, as shown in Fig. 1.22 (c). We can see, as the voltage increase the conductivity decrease, which tells us the Dirac point happens at a higher voltage, so 50 V is closer to the Dirac point.

Fig. 1.22 (b) is the multiple-layer THz graphene modulator with several graphene pairs, which was not demonstrated by their work. In the pairs of graphene, if one is n-doped, the other one will be p-doped, as shown in the band structure.

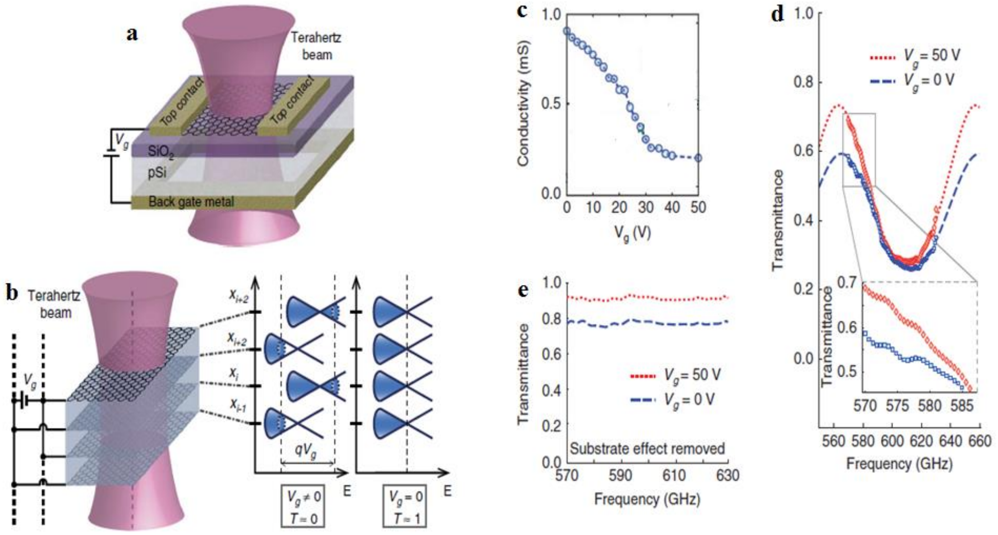

Fig. 1.22 THz graphene modulator based on transmission from reference [27]. (a) is the structure of single-layer graphene; (b) is the multiple-layer graphene and the band structure of different states; (c) is the measured conductivity of graphene as a function of applied voltage; (d) is the measured transmittance as a function of carrier THz wave frequency at different applied voltage 50 V (red) and 0 V (blue); (e) is the corresponding transmittance when the substrate effect is removed.

When the graphene is at the Dirac point, the density of state (DOS) for the interband transition is extreme low. The photon energy of THz wave is very low, so the interband transition can only happen near the Dirac point. Therefore, the intraband transition will dominate for the absorption mechanism. However, at the Dirac point, there is also no DOS for the intraband transition.

The transmittance will be very high when the graphene layers are at the Dirac point. When the graphene layers are biased to be away from the Dirac point, the intraband transition will take place and the absorption will be larger to make the transmittance lower. Therefore, the THz graphene modulator is enabled by the intraband transition of graphene.

From Fig. 1.22 (d) and (e), we can see the transmittance is higher at 50 V than at 0 V. There is a modulation depth of ~ 15%. The Dirac point happens at 50 V but not at 0 V, this is because the natural doping of graphene from the substrate is very high.

Another THz modulator was demonstrated by the same group [52]. This modulator is based on reflection, as shown in Fig. 1.23.

A monolayer graphene is coated on the SiO_2/p-Si substrate with a metal mirror on the bottom, as seen in Fig. 1.23 (a). The bottom metal mirror acts both as an electrode and a reflector. The THz wave incident at the perpendicular direction of the modulator and will interact with the monolayer graphene. The modulation is also enabled by the intraband transition which is the same as the modulator in reference [27].

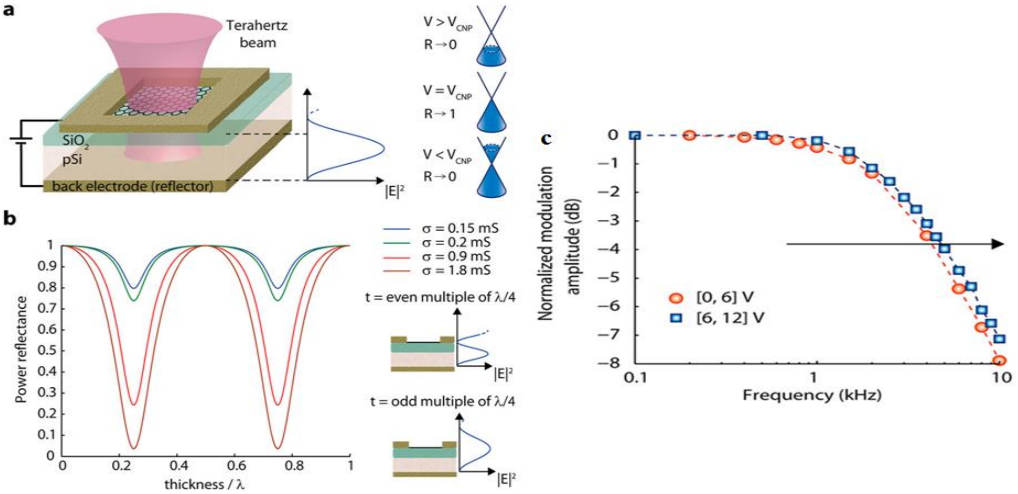

Fig. 1.23 (a) Structure of the THz reflection modulator; (b) Calculated power reflectance of the modulator as a function of the substrate optical thickness; (c) Measured normalized modulation amplitude as a function of modulation frequency. From reference [52].

Because of the Fabry-Perot etalon, the light-graphene interaction will be much higher at the resonance thickness of the substrate (an odd multiple of the quarter of the wavelength), as seen in Fig. 1.23 (b).

The modulation depth can be 95%, which is caused by the power of the mode is the peak at the position of graphene at the resonance condition. However, because the footprint of this modulator is very large, the capacitance of the modulator is very high, which makes the modulation speed of the THz modulator very low: 4 kHz in reference [52] as shown in Fig. 1.23 (c), and 20 kHz in reference [27].

1.2.3 State of the arts of graphene modulators

I study 29 references [2,26,27,34-59] firstly, which are about modulators: the scale of the years is from 2004 to 2016, and they include electro-optical modulator, all-optical modulator [49-51], THz modulator [27,52], and Mach-Zehnder modulator [36,43,46]. These modulators are studied firstly for examples to analyze the state of the arts and the research trend.

I record the state-of-the-art values of all the modulators for modulation depth, modulation speed, footprint, modulation bandwidth, operation bandwidth, and insertion loss, as shown in Table 2:

Table 2 State-of-the-art values of graphene modulator (part I)

Reference, and year	Where	If measured	Operation frequency	Modulation depth	Modulation Speed	Footprint	Modulation Bandwidth	Operation Bandwidth	Insertion Loss
[43], 2004	*Nature*	yes	1.55 μm	Maximized	1 GHz	0.03 mm^2	1 GHz	\	15.3 dB
[44], 2005	*Nature*	yes	1.5 μm	15 dB	\	5.4 μm^2	\	5.3 GHz	\
[45], 2011	*OE*	yes	1.55 μm	10 dB	60 GHz	~nm*mm	60 GHz	\	16 dB
[2], 2011	*Nature*	yes	1.53 μm	4 dB	1.2 GHz	25 μm^2	1.2 GHz	34.7 THz	\
[47], 2012	*NL*	yes	1.537 μm	6.4 dB	1 GHz	80 μm^2	1 GHz	\	\
[46], 2012	*OE*	no	1.55 μm	5.2 dB	\	100 μm^2	\	\	\
[26], 2012	*APL*	no	1.55 μm	7 dB	120 GHz	60 μm^2	120 GHz	\	2.5 dB
[38], 2012	*OE*	no	1.55 μm	3 dB	100 GHz	0.07 μm^2	100 GHz	\	3 dB
[53], 2012	*OE*	yes	1.55 μm	0.2 dB	0.1 GHz	10 mm^2	0.1 GHz	\	0.3 dB
[27], 2012	*Nature C*	yes	0.6 THz	0.8 dB	20 kHz	2.25 cm^2	20 kHz	100 GHz	0.2 dB
[52], 2012	*NL*	yes	0.63 THz	4.4 dB	4 kHz	1 cm^2	4 kHz	60 GHz	2 dB
[54], 2012	*OE*	no	1.55μm	30 dB	\	10 μm^2	\	100 GHz	0.5 dB
[36], 2013	*APL*	no	1.55 μm	35 dB	Fast	120 μm^2	larger	\	\
[49], 2013	*LPL*	yes	1.06 μm	13 dB	1 MHz	100 μm^2	1 MHz	13.35THz	0.1 dB
[34], 2013	*NanoT*	no	1.55 μm	16.8 dB	\	0.054μm^2	\	15 THz	13.5 dB
[55], 2013	*NL*	yes	1.57 μm	10 dB	1 GHz	0.5 μm^2	\	300 GHz	1.3 dB
[48], 2014	*OE*	no	1.55 μm	34 dB	100 GHz	5 μm^2	100 GHz	\	\
[56], 2014	*OE*	yes	1.55 μm	16 dB	0.67 GHz	\	0.67 GHz	225 THz	3.3 dB
[37], 2014	*APL*	no	40 THz	10 dB	\	\	\	15 THz	\
[57], 2014	*NL*	yes	1.55 μm	4.4 dB	4 GHz	90 μm^2	3 GHz	500 GHz	\
[50], 2014	*NL*	yes	1.55 μm	2.1 dB	200 GHz	28 μm^2	200 GHz	\	\
[58], 2014	LPR	no	40 THz	21.5 dB	\	\	\	15 THz	\
[35], 2015	*Nature P*	yes	1.55 μm	28 dB	150 GHz	45 μm^2	30 GHz	\	\
[59], 2015	*NL*	yes	1.55 μm	3.2 dB	1.2 GHz	0.5 μm^2	1.2 GHz	600 GHz	\
[51], 2016	*Optica*	yes	1.55 μm	3 dB	200 GHz	15 μm^2	200 GHz	73.5 THz	\

1.2.4 Supplementary information

1. References [43-45] are silicon modulators; References [2,26,34,35,38,47,48,53-59] are electro-optical graphene modulators; References [49-51] are all-optical graphene modulators; References [27,52] are THz graphene modulators; And references [36,46] are Mach-Zehnder graphene modulators.

2. All the references are recorded in the order as the paper publishing year increases (2004 to 2016).

3. The quality factor of a modulator is defined as $Q = \lambda/\Delta\lambda$, where λ is the operation wavelength and $\Delta\lambda$ is operation bandwidth. The Q factor in reference [43] is 39 350, which is not recorded in the table.

4. The modulation efficiency of Mach-Zehnder modulator is defined as $V_\pi * L$, where V_π is an applied voltage which should be enough for the π-phase shift, L is interaction length of the two arms of Mach-Zehnder modulator [36,43,46]. When the applied voltage for the π-phase shift is smaller and the interaction length is lower, the modulation efficiency should be higher, for lower energy consumption, and lower insertion loss. This is not recorded in the table.

5. The figure of merit $\Delta\alpha/\alpha$ is not recorded in the table, but the insertion loss α is recorded.

6. The footprint controls the modulation depth: when the interaction length is larger, the modulation depth should be higher. The modulation depth is also called as modulation index or extinction ratio.

7. The footprint of THz modulator is much larger because the diffraction limit of the THz wave makes the size of the device should be larger.

8. When the electric field at graphene is higher, the modulation depth will be higher. This is related to the light-graphene interaction.

9. The smaller the footprint is, the lower the applied voltage will be, the higher the modulation speed will be, and the energy consumption will

also be lower.

1.2.5 The results from review part I

1. The number of papers published each year is plotted as a function of the year, as shown in Fig. 1.24. Because the first graphene modulator was reported in 2011, there is no research on graphene modulator before 2011. The two papers in 2004 and 2005 were about silicon modulators, which are used here as a comparison. The reason why I choose these two papers from *Nature* in year 2004 and 2005 is that graphene is firstly fabricated in 2004, however graphene modulator is only firstly reported in 2011, and I want to show the research delay and time gap.

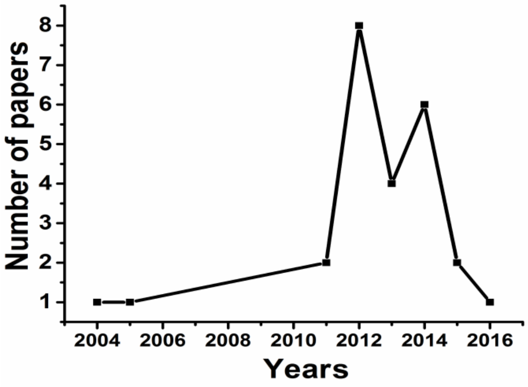

Fig. 1.24 Number of papers published each year.

In Fig. 1.24, there is a research peak for graphene modulator in the years from 2012 to 2014 (8 papers in 2012, 4 papers in 2013, and 6 papers in 2014). However, the number of papers decreases in the years from 2014 to 2016, which may tell us that the research on graphene modulator became less popular as the research problems on graphene modulators may be less at this stage. However, there are still some problems need to be solved, and new structures of graphene modulator are demanded.

2. The most popular journals for reporting graphene modulators are Optics Express (7 papers), Nano Letters (6 papers), Nature (3 papers), and Applied Physics Letters (3 papers) at this stage. The number of papers as a function of different journals is shown in Fig. 1.25. The impact factors (IF) of all the journals are above 3.

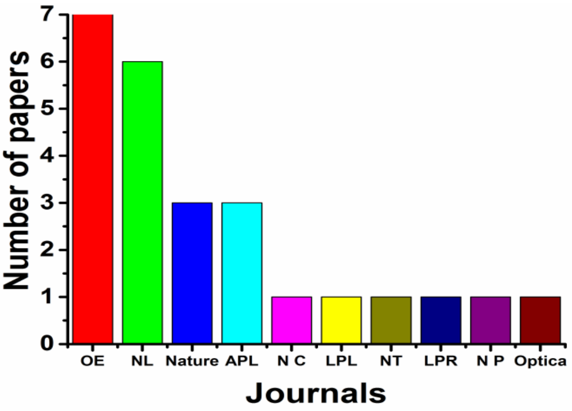

Fig. 1.25 Popularity of the journals on the research of graphene modulators (3 silicon modulators are included for comparison).

3. The number of papers as a function of if measured is shown in Fig. 1.26. We can see most of the papers (16 papers) are measured while only 9 papers (the number is about half of the number of measured papers) are pure theory research. We can do some theory research on this topic to balance the number of papers.

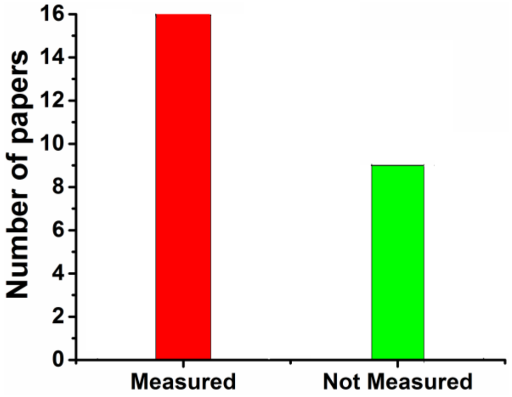

Fig. 1.26 Number of the papers on the graphene modulators as a function of if measured.

4. Most of the papers are focusing on the optical modulator which operating on wavelength $\lambda = 1.55$ μm. Only two papers are about THz graphene modulator at this stage.

5. The modulation depth as a function of paper number is shown in Fig. 1.27. The paper number is in the order of paper published year. The vertical line in the left down corner of Fig. 1.27 is the boundary line to separate Si modulator from graphene modulator. From Fig. 1.27, we can see in the first of the year 2011, the modulation depth of graphene

modulator is lower than the traditional Si-based modulator. However, the modulation depth of graphene modulator increased as the year passed, and it can be much higher than Si-based modulator. The highest modulation depth of the graphene-based modulator was first increasing then decreasing as the year passed. The highest value happens in the year of 2013 from reference [36], which is 35 dB. Moreover, there is no 100% modulation depth reported by 2016 at this stage.

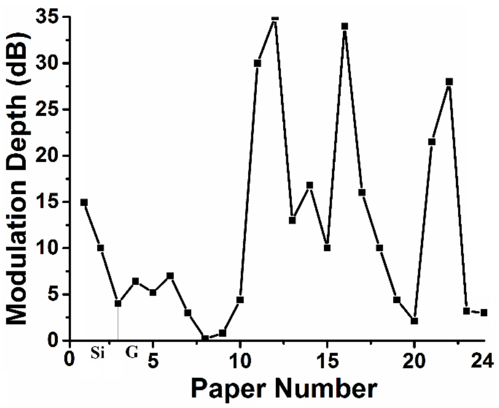

Fig. 1.27 Modulation depth as a function of paper number (in the order of publishing time increases). The first two data are from the Si-based modulators.

6. Fig. 1.28 shows the modulation speed (modulation bandwidth) as a function of the paper number (in the order of publishing time increases).

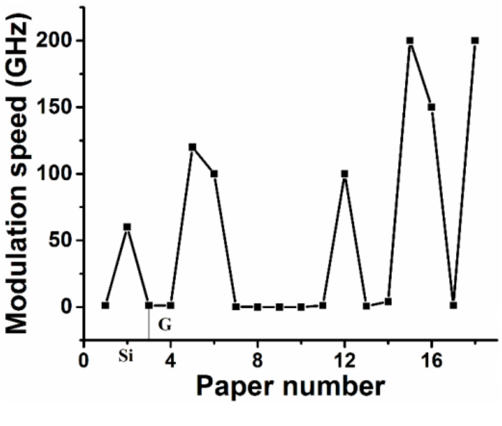

Fig. 1.28 Modulation speed as a function of the paper number in the order of published time increases. The first two data are from the Si-based modulators.

From the figure, we can see the highest modulation speed was increasing as the year passed. The modulation speed of graphene-based modulator can be much higher than that of the Si-based modulator. The highest value can be 200 GHz, but it is a not realized possible value. The demonstrated value can be 150 GHz, which was reported at 2015 in reference [35]. In the middle of Fig. 1.28, there are 5 much lower values, where two values are from graphene THz modulator. The very high modulation speed thanks to the high mobility of graphene which makes the total resistance very low, and the small footprints which make the capacitance of the modulator very low.

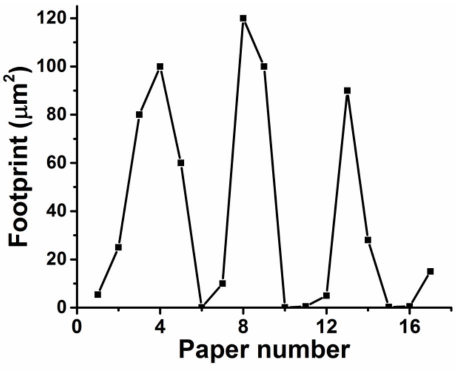

Fig. 1.29 Footprint of graphene modulator as a function of the paper number in the order of published time increases. Only the footprints of optical graphene modulators are considered.

7. The footprint of the graphene-based modulator can be very small. The smallest can be ~ 0.054 μm^2 reported in 2013 in reference [34]. The footprint (the large sizes of Si-based modulator and THz modulator are not included) as a function of the paper number is shown in Fig. 1.29. We can see all the sizes of graphene optical modulator are in the scale of μm^2. The highest values also decrease as the time passed.

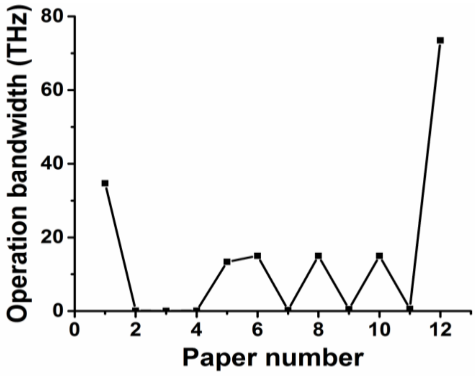

Fig. 1.30 Operation bandwidth as a function of the paper number. Only the graphene modulators are considered.

8. From Fig. 1.30, we can see the operation bandwidth of the graphene-based modulator can be very high ~ 73.5 THz [51], and most values are around 15 THz. So many channels of carrier waves can be processed in these modulators thanks to the broadband high tunable absorption loss of graphene.

9. Fig. 1.31 shows the insertion loss of graphene modulator can be much lower than Si-based modulator. Most of the values are below 4 dB, and the lowest insertion loss can be 0.1 dB in reference [49] in 2013. However, for some of the cases, the insertion loss is large, and the lowest value can still be lower.

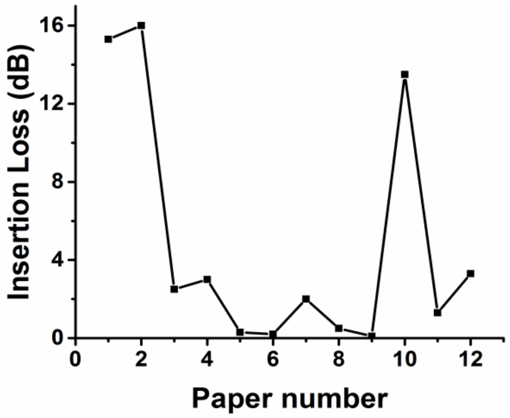

Fig. 1.31 Insertion loss of graphene modulators as a function of the paper number. The first two values are from Si-based modulators

1.2.6 The challenges and problems for graphene modulators

There are several existing challenges related to graphene modulators. My research aims to address a selection of these challenges, as follows:

1. The light-graphene interaction is always low for most of the cases of graphene modulators. If the light-graphene interaction can be enhanced, all the FOMs of the modulator can be improved.

2. There is a compromise between modulation speed and modulation efficiency. If the modulation speed is enhanced, the modulation efficiency will be lost accordingly. Therefore, we can have other designs of the graphene modulator to reduce this compromise.

3. The insertion loss is still very large for most of the cases.

4. The energy consumption is still very high.

5. The modulation speed is highly limited because of the high contact resistance between the electrode and graphene, and high sheet resistance of graphene. The mobility of graphene devices is always very low, which is caused by substrate impurity scattering.

6. For the graphene Mach-Zehnder modulator, the variance of the real part of mode index is still very low. The highest value is only 0.028 [36]. Therefore, the π-phase shift arm length should be very high, the smallest value is only 27.57 μm [36].

7. More 100% modulation depths still need to be realized. Even though there may have already been some works.

8. The FOM of graphene modulator is still low, ~72 [34], and still needs to be improved.

1.3 Review of THz waveguides

1.3.1 State of the arts of THz waveguides

Terahertz (THz) wave bridges the gap between microwave and optical wave. The exploration of THz wave with active detections by laboratory-based sources only began to emerge in the time of mid-1980s.

For waveguide in THz frequency, the principle is similar as the waveguide in other band of electromagnetic waves. To achieve greater confinement for THz wave guiding, researchers should lower the loss and dispersion to enable undistorted propagation.

The first application of waveguides is to transport electromagnetic waves from one point to another [61]. Till now, THz waveguides have also been used as sensors, or to guide waves in subwavelength range (which is beyond the diffraction limit), or to offer tight confinement of the THz waves to the structure which is beyond the Rayleigh range.

Selecting materials that are suitable for the fabrication of THz waveguides is the major barriers in this field. Metals function well at microwave frequencies, however, they have high Ohmic losses at THz frequencies. Polymers and glasses function well at infrared and optical frequencies, but have unacceptable frequency-dependent absorption losses for THz waves. Another barrier that limits the application of THz waveguides is the group-velocity dispersion.

The development of low-loss THz waveguides [62-64] is essential for facilitating terahertz science and applications [65-67]. THz waveguides have been investigated and play important roles in THz technology, among which the most important are as follows.

1.3.1.1 Parallel-plate THz waveguides

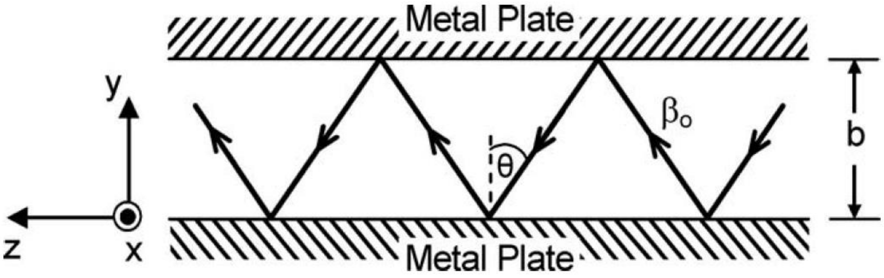

Fig. 1.32 THz wave in parallel-plate waveguide, cut from reference [68].

The parallel-plate waveguide [68,69] can guide the THz waves with very low loss. For TE mode, the loss coefficient can be as low as 2.6 dB/km [68]. However, the loss of TM mode is always 4-5 orders of magnitude larger than that of TE mode in this waveguide [69].

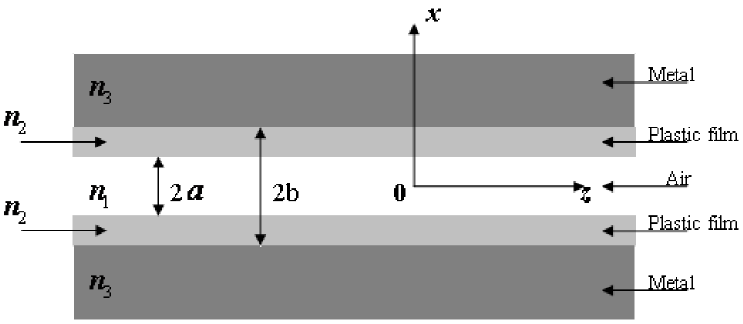

Fig. 1.33 Symmetrical plastic film coated parallel-plate waveguide structure. From reference [70].

Coating symmetrical plastic films on both sides on the two metal plates can make the loss of TM mode to be four orders of magnitude lower than the uncoated parallel-plate waveguides [70]. And the guiding mechanism of the coated parallel-plate waveguide changes to anti-resonant reflecting and the bandwidth can be as wide as 5.12 THz [70]. The structure of this waveguide is shown in Fig. 1.33.

The parallel-plate waveguides also have many applications, such as parallel-plate based filters [71-73], sensors [74], and switches.

Metal THz waveguides experience strong dispersion near the cut-off frequency of the guiding mode unless they support transverse electric and magnetic (TEM) modes which have no cut-off frequency. The cut-off frequency is used for tunable filter applications [75].

1.3.1.2 Metal wire THz waveguides

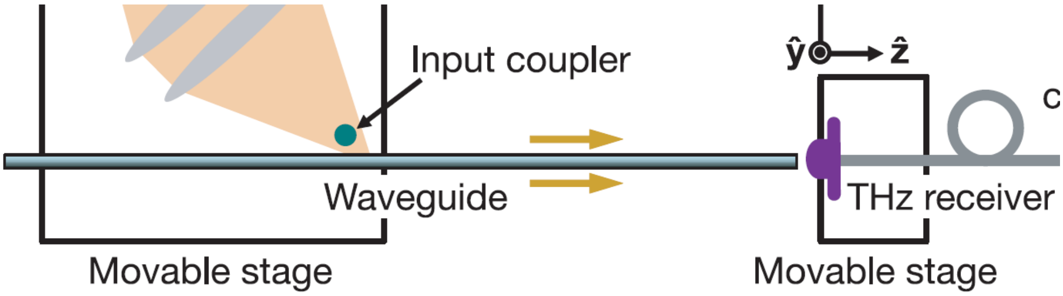

Fig. 1.34 Metal wire THz waveguide working as a role in the system, from reference [76].

The first paper which reported metal wire THz waveguide is published in *Nature* in 2004 by Mittleman et al. [76]. Broadband THz pulses can be guided on the metal wire in the form of THz Surface Plasmon Polaritons (THz SPPs) with nearly no dispersion and low loss coefficient (about 1 m^{-1}).

However, the THz waves on the metal wires are in radiation phase and the coupling efficiency is extreme low. This is because the coupling condition is hard to achieve. Moreover, the mode confinement is weak, which is the cause of low loss and low dispersion.

Since then, applications such as THz endoscope [76], sensors [77,78], transmitters, THz imaging [79], and THz nanofocusing [80] are proposed accordingly for THz wire. The mode characteristics of THz SPPs on metal wire are analyzed in detail [81]. The mode has π-phase differences on the opposite side of metal wire. Coating a dielectric film on the metal wire makes the loss much higher, but the confinement much better and the dispersion much higher [77,78], which is used for the sensor applications.

The coupling of THz waves from free air to metal wire have been researched. The coupling efficiency can be 43.5% [82].

One important application is the THz conical metal wire, the THz SPPs guided on it will be far beyond the diffraction limit, and it can be used for superfocusing [80].

1.3.1.3 Dielectric pipe waveguides

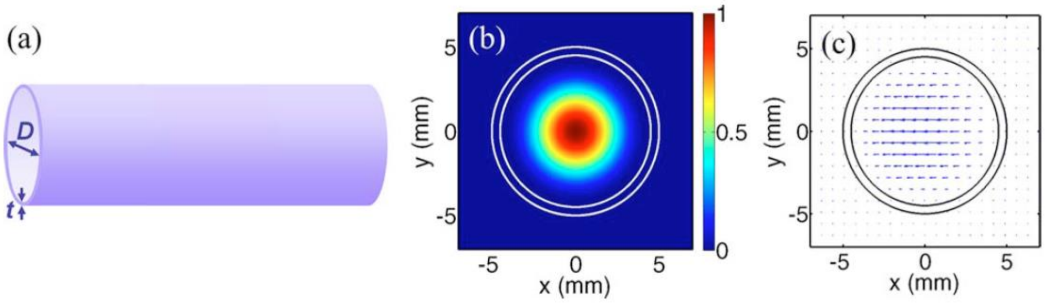

Fig. 1.35 THz pipe and the mode field, from reference [83].

This waveguide has been used in the THz region since 2009 [83]. A commercially available straw could guide THz wave effectively with low loss (as low as 0.0008/cm) and high coupling efficiency (as high as 80%) [83]. The guiding mechanism of this waveguide is anti-resonant reflecting because of the Fabry-Perot etalon. The losses will be at the peaks at the resonance frequencies. The bandwidth between loss peaks is very narrow because the thickness of the pipe wall cannot be very thin. The resonance frequencies can be predicted by the following equation:

$$f_m = \frac{mc}{2t\sqrt{n^2 - 1}} \qquad (1\text{-}17),$$

where m is the mode order, c is the speed of light in vacuum, t is the thickness of the pipe wall and n is the refractive index of the pipe material.

Research papers are focusing on to achieve broadband transmission of the anti-resonant reflecting mechanism. However, the highest bandwidth is only 1.1 THz [84]. Multiple applications also have followed for this waveguide, such as pipe-based THz sensors [85,86].

1.3.1.4 THz fibers

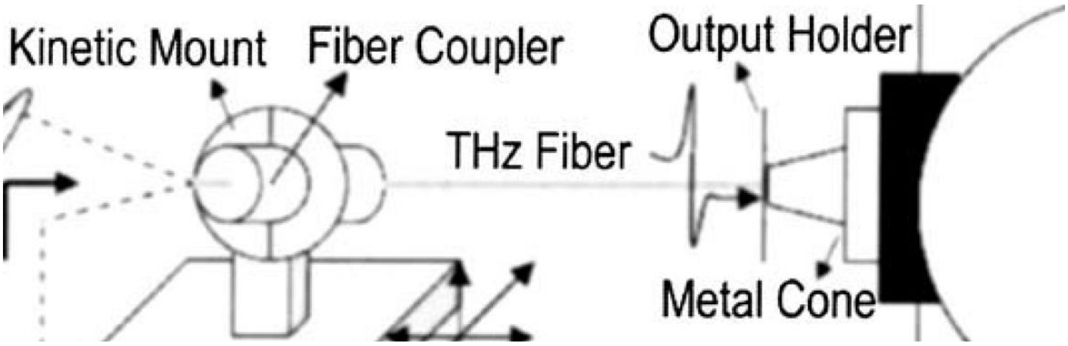

Fig. 1.36 THz fiber in system, cut from reference [87].

The research of THz fibers was just emerging in the period of 2006-2009. The low-loss subwavelength plastic fiber was firstly put forward in 2006 [87]. In this paper the mode field was analyzed, the mode transmission is based on a large part of energy distribute in the outside air. The loss of this THz fiber in measurement is low, and the coupling efficiency can be high, as high as 20% achieved in experiments.

Coating of metal films on THz fibers [88] was also studied, such as silver/PS-coated hollow waveguide, which exhibits a loss coefficient of 0.95 dB/m at the frequency of 2.5 THz [89].

1.3.1.5 Single metal plate THz waveguides

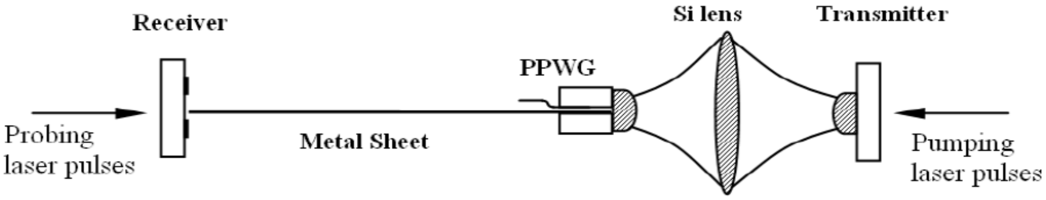

Fig. 1.37 Single metal plate in system, cut from reference [90].

THz single metal plate SPPs have been reported in papers [90-93]. These kinds of modes are suffering very large fields and extreme low coupling efficiency even though the loss is very low.

In reference [93], after coating a thin dielectric film on the surface of the metal plate, the loss and dispersion will be much higher and the mode field width will be much smaller. This can be very useful for sensing application [90-93]. And the coupling efficiency can be much higher after dielectric film coating. Therefore, single dielectric slab is used for coupling of SPPs mode on single metal plate, and the coupling efficiency in theory can be 45.64% [93].

1.3.1.6 Metal-clad hollow waveguides

In reference [94] in 2009 by Lu et al., this structure was reported firstly, as is shown in Fig. 1.38. The guiding of this waveguide is based on anti-resonant reflecting, and the loss is very high at the resonance frequencies. The most interesting thing is that the loss peaks can be moved when the distance between the dielectric slab and the side metal plate is changed.

Therefore, Lu et al. put forward the tunable filter application of this waveguide. However, their experiment work was limited for their tunable filter range is only 60 GHz, and the highest tune sensitivity is only 115 GHz/mm. And their theory analysis is not comprehensive.

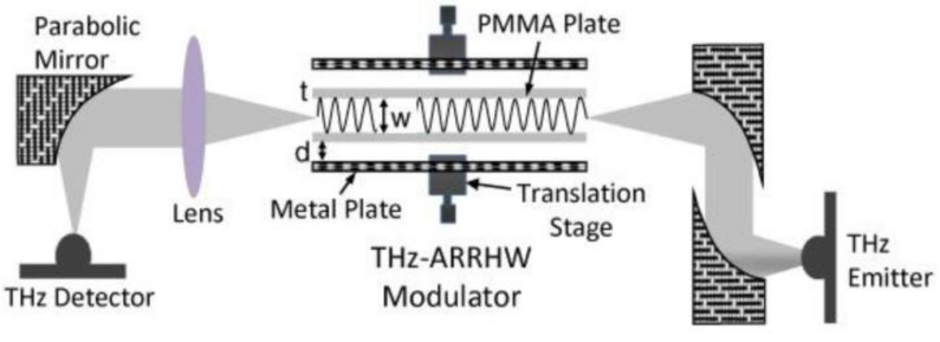

Fig. 1.38 Metal-clad anti-resonant reflecting hollow waveguide in system, cut from reference [94].

In reference [95], a comprehensive theoretical study on this waveguide was done. The blue-shift of the resonance frequency is strongly affected by the interval between two dielectric slabs. By changing the interval, the maximum frequency-tuning-range is up to 2030 GHz, and the maximum sensitivity of the resonance frequency shift is up to 6950 GHz/mm at the resonance order of $m = 1$.

1.3.1.7 Other THz waveguides

There are also a lot of other important THz waveguides, such as THz slabs [82,96], THz metal films [97], THz crystal waveguides. Since these THz waveguides were first reported, multiple applications such as THz imaging, THz coupling [82], THz switches have emerged in the research.

1.3.2 THz SPPs

THz wave as surface plasmon-polaritons (SPPs) have attracted extensive attention over the last several years. THz SPPs can be guided on metal wires [76-82], metal plates [90-93], or metal films [98].

It was first reported that THz SPPs can be guided along a metal wire with low losses (1 m^{-1}) and negligible group velocity dispersion (GVD) [76]. This is explained due to a large part of the wave energy being distributed in the air around the metal wire. Further researchers and scientists have continued this research into THz SPPs.

In the visible light range, there are three kinds of SPPs, which are pure SPPs, hybrid SPPs [99,100] and modified SPPs [101-103]. For hybrid modes, the effects of both the metal and dielectric should be considered. However, the hybrid SPPs modes in THz range is only discussed by a few papers [93] particularly.

The modified SPP modes in optical ranges were also discussed in several papers [101-103]. However, the modified SPPs modes at the THz range has not yet received significant attention.

These three kinds of SPP modes are discussed in detail as follows:

1.3.2.1 Pure SPPs

The basic demonstration of SPPs on metal dielectric surface is based on the theory of a single metal wire presented by Sommerfeld in 1899. Multiple works reported SPPs on metal wires, metal films, metal plates and thin metal tubes. And the topics on graphene-based [25,33] SPPs had been emerging since graphene was fabricated.

The surface wave is generated by the electromagnetic wave oscillated with the electron in the metal, which makes the electromagnetic waves propagate along the metal-dielectric surface. The super character of SPP mode is that it can confine the mode energy in only subwavelength area which is much beyond the diffraction limit [80]. However, the mode loss is very high, the mode will disappear in about several wavelengths' length.

Two classes of SPPs are currently being researched: 1. long-range (LR) SPPs, which can propagate over relatively long distances; 2. short-range (SR) SPPs, in which the propagation distance is short, with the advantage of the possibility of strong subwavelength localization.

1.3.2.2 Hybrid SPPs

In order to lower the loss of SPP mode on metal surfaces, Oulton et al. firstly put forward a hybrid plasmonic waveguide [99]. The structure is a dielectric cylinder wire above a metal plate, and they found that the mode field is confined in the small area of the dielectric gap between the cylinder wire and the metal plate, which is much smaller than the optical wavelength, moreover, the loss can be much lower than the pure SPPs on the metal surface.

After that, several works reported about the hybrid SPP modes [100] in the metal-dielectric waveguides. The difference is that these modes have three or more dielectric interfaces as propagated and mostly confined on the metal-dielectric interface. Nevertheless, the research on THz hybrid SPP modes is still minor to find [93].

1.3.2.3 Modified SPPs

Lowering the loss of SPP mode and not to increase the mode width is proposed by Liang et al. [101-103]. The modified SPP mode is a mode exist in the mental wire or film with two dielectric interfaces. Their proposed structure is a metal wire inserted to a dielectric hole [101] or the dielectric film coated metal film inserted to the infinity dielectric medium [102,103]. The loss of the modified SPPs decreases about 3 orders of magnitude, the mode width only increase slightly. This is because the infinity dielectric medium makes the mode energy in the metal decreases significantly. The sensing application [103] of this mode is followed. However, the modified THz SPPs have still not been reported yet at this stage.

1.3.2.4 Graphene SPPs

The graphene surface conductivity could be modulated by changing the chemical potential. As known, in the case of the chemical potential is greater than half the photon energy, intraband transitions dominate, and the graphene behaves like a metal. As a result, the graphene could support transverse magnetic (TM) polarized SPPs.

Graphene supported SPPs have unique properties comparing with which on metals. First, the field of SPPs supported by graphene is tightly confined on the graphene surface with a very high effective index [25] in optical range, comparing to a typical low value for SPPs on metals. Second, the damping loss of SPPs supported by graphene is relatively low. The propagation length could reach dozens of wavelengths of SPPs [33]. Finally, the propagation of SPPs in graphene can be dynamically tuned by external electric field, magnetic field, and gate voltage. Therefore, it is easy to modulate SPPs in real-time and even build modulator by spatially tuning the graphene.

1.3.3 The research work of THz waveguide

In this research, the modified THz SPPs on the double-dielectric-slab-coated metal-film waveguide will be presented. The effects of both the metal film and the dielectric slab on the modified SPP modes will be discussed. The double-coated metal-film waveguide can guide THz wave with ultra-low loss (2 orders of magnitude lower than the metal wires) and subwavelength beam width simultaneously (much lower than the beam width of the metal wires and the THz wavelength).

The triple-layer-dielectric-slab waveguide with high-low-high refractive indices distribution will be researched. This waveguide guides

THz wave as the anti-resonant reflecting mechanism.

The mode characteristics of the metal nanofilm-dielectric-plate waveguide will be discussed. The waveguide can guide TM mode with low loss, which is based on most of the energy propagate in the coated slabs. However, the losses of the TE modes are huge. The TE mode filter of this waveguide will be talked.

The mode characteristics of THz wave in the single-dielectric-slab-coated parallel-plate waveguide will also be discussed. The relationships between the propagating characteristics of the mode in this waveguide and the THz wave frequency, as well as the waveguide structure will numerically be studied. The GVD of the TM_0 mode and the low cut-off frequency of TE_1 mode are discussed in detail.

The hybrid THz SPPs on the double-dielectric-slab-coated metal plate waveguide will be presented. The structures of the l-h [low refractive index (inner) to high refractive index (outside)] coating and the h-l [high refractive index (inner) to low refractive index (outside)] coating will be studied. It shows anti-resonant reflection in the l-h coated metal plate and total internal reflection in the h-l coated metal plate. At the resonant silicon thicknesses or resonant frequencies for l-h coating, the hybrid SPP modes transfer to dielectric modes. However, for h-l coating, the hybrid modes are always SPP-like.

I believe that these results will be very important for hybrid THz SPPs in waveguides and the applications of sensors, filters and switches.

1.4 Review of graphene modulators (part II)

1.4.1 Graphene modulators (part II)

To the best of my knowledge, [104] is an early paper reported suspended graphene modulator. The structure is shown in Fig. 1.39.

In this structure, a big part is suspended in the air. The slot is between two top silicon waveguides. A monolayer graphene is transferred on the top of the slot. In my opinion, their structure is very complex and hard to fabricate even though they said “considering the easy and CMOS-compatible fabrication process of the design” in their paper.

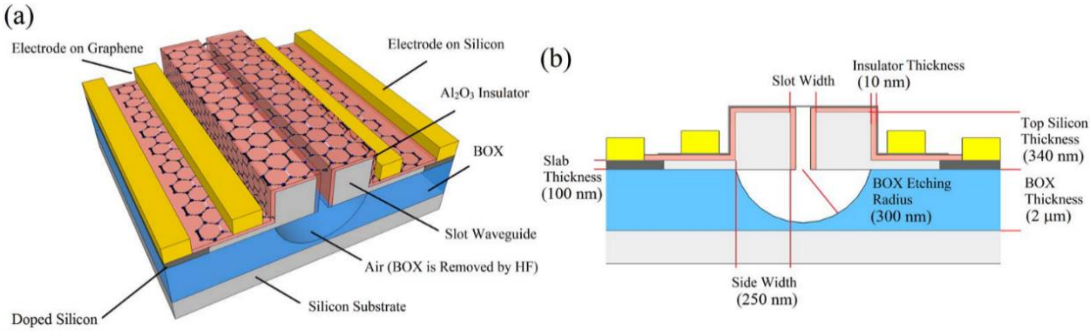

Fig. 1.39 Schematic of the (graphene-on-silicon) GoS-suspended vertical slot waveguide. (a) Three-dimensional view. (b) Cross-sectional view [104].

The mode is confined in the slot, the optical loss in waveguide is calculated as a function of the slot width, as shown in Fig. 1.40.

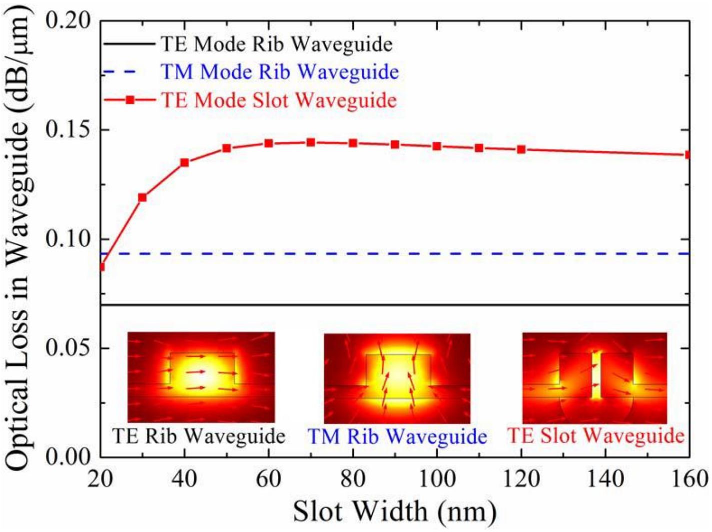

Fig. 1.40 Simulated optical absorption of GoS rib and slot waveguides [104].

The black solid line and the blue dashed line show the loss of graphene rib waveguides for TE mode and TM mode as a comparison. For the graphene slot waveguide, the loss is a function of the slot width. When the slot width is reduced, the light intensity is larger but the interaction area between graphene layer and propagating light will be smaller. When the slot width is larger, the interaction area will be larger, however, the light intensity is lower. Therefore, there is a trade-off between light intensity and interaction area to enhance the light-graphene interaction.

Even though the light-graphene interaction is larger than the rib waveguide, it is still very low.

The wave vector ($k = 2\pi\mathrm{Re}[N_{\mathrm{eff}}]/\lambda$) and loss of the slot waveguide are calculated as a function of the chemical potential, as shown in Fig. 1.41.

The change of wave vector k and optical loss of slot waveguide are much larger than those of rib waveguide. The change of wave vector k can be 0.0653 μm^{-1}, namely it is only 0.0161 for the change of refractive index (ΔN_{eff}), which is still a very low value.

Two arms of this slot waveguides are used to form an M-Z modulator and the normalized transmission as a function of the applied voltage is calculated, as shown in Fig. 1.42.

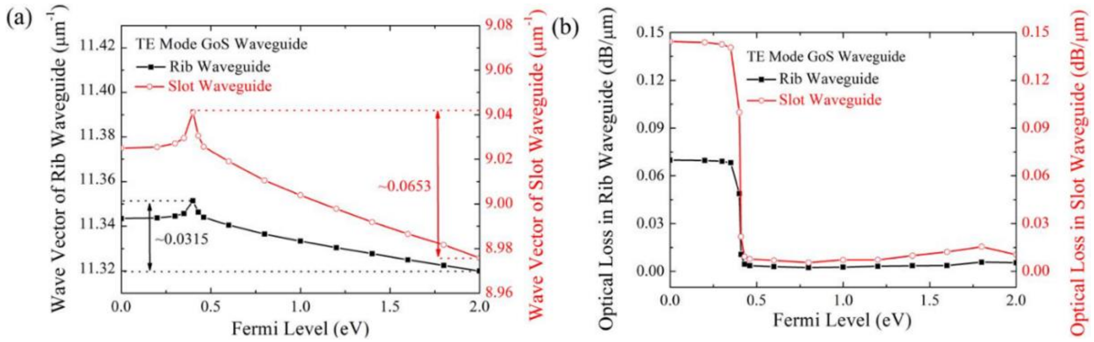

Fig. 1.41 Comparison in wave vector and optical loss between the GoS slot and rib waveguides [104].

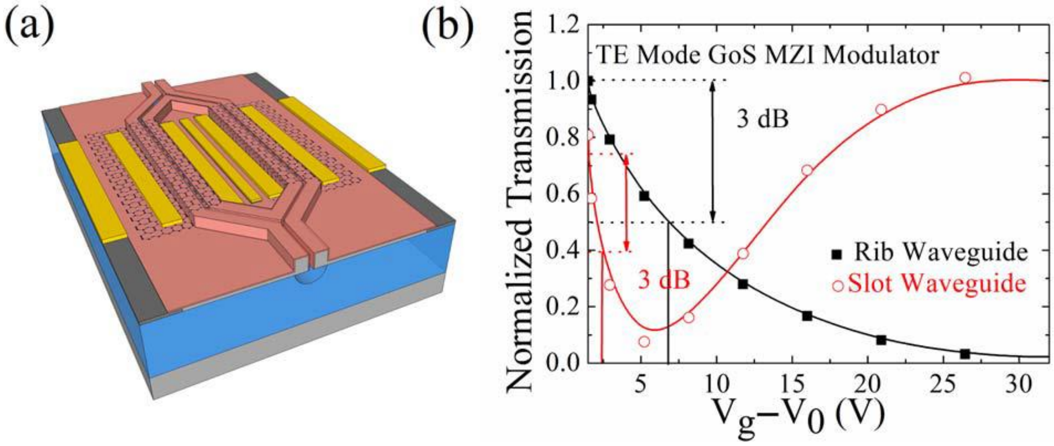

Fig. 1.42 M-Z modulators based on the GoS slot waveguide [104].

An experimental verification of electro-refractive phase modulation in graphene was reported by [105] in 2015. Their fabricated device structure is shown in Fig. 1.43. The relative difference between the lengths of two MZI arms is 91 μm. TE-polarized light is coupled in by using grating couplers. The authors simulated the waveguide structure, as shown in Fig. 1.44. We can see the graphene layer is located in the evanescent field. It is far away from mode amplitude center. The chemical potential of each graphene layer is changed electro-statically by biasing. Therefore, the effective refractive index of one MZI arm is changed, which causes a shift in phases.

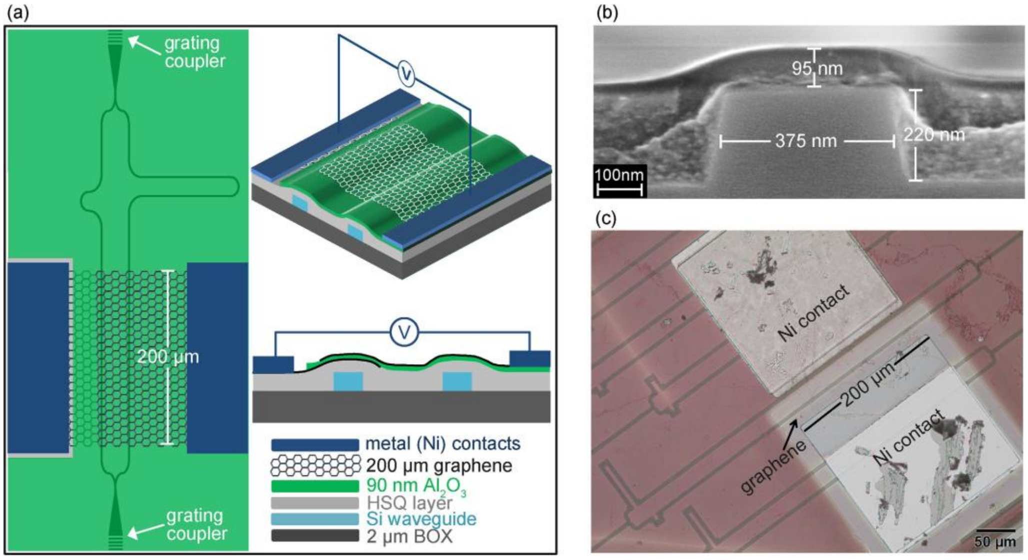

Fig. 1.43 Graphene based electro-refractive phase modulator [105].

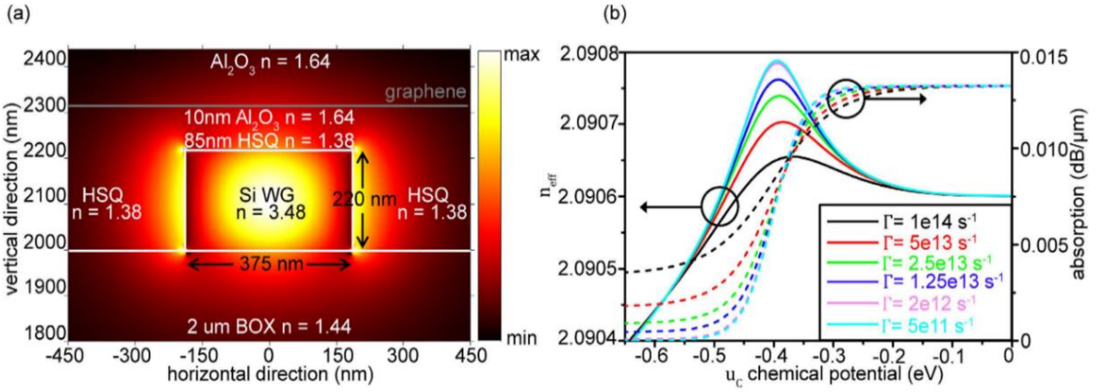

Fig. 1.44 Simulation results: (a) mode field, (b) N_{eff} and absorption of the modulator as a function of chemical potential of graphene [105].

From Fig. 1.44 (b), we can know for this case, the light-graphene interaction is very low and both the change of effective refractive index (ΔN_{eff}) and the absorption are still very low, which will cause very long

π-phase shift length and low modulation efficiency.

Fig. 1.45 shows another graphene phase modulator (GPM) [106] in 2017. This is with a phase-shifter length of 300 μm, and a 35 dB extinction ratio. The GPM has modulation efficiency of 0.28Vcm, it is one order of magnitude larger than the state-of-the-art value in p-n junction Si phase modulators. Even though their refractive index change is much larger than that in Si, it is still a very low value because of very low light-graphene interaction, and a better graphene phase modulator with higher refractive index change is still needed and has not been reported before this research.

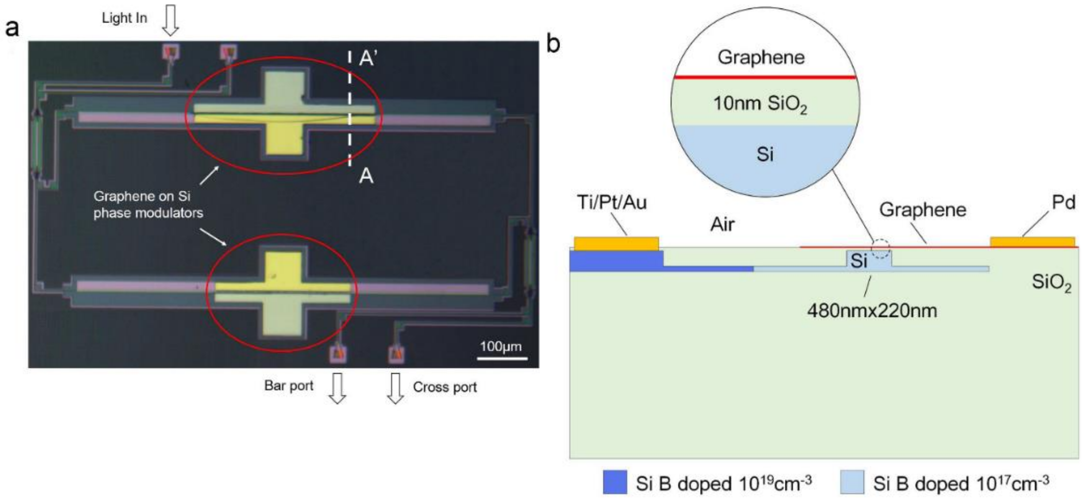

Fig. 1.45 (a) Optical micrograph of the MZI modulator. (b) Cross-section of the GPM in the section A-A' of (a) [106].

In [107], the authors reported a tunable graphene-based hybrid plasmonic modulator for subwavelength confinement. They have used two structures, one is an asymmetrical structure, as shown below in Fig. 1.46.

A silver cylindrical nanowire is put above a silicon-graphene-silica waveguide, the distance is *h*. They call it as “graphene-based hybrid plasmonic modulator (GHPM)”. The mode field is confined in the small dielectric gap. This hybrid mode can enhance the light-graphene interaction. The modulation depth is a trade-off between the mode field intensity and the distance of graphene layer to the center of mode field. In my opinion, their biasing of graphene is a problem.

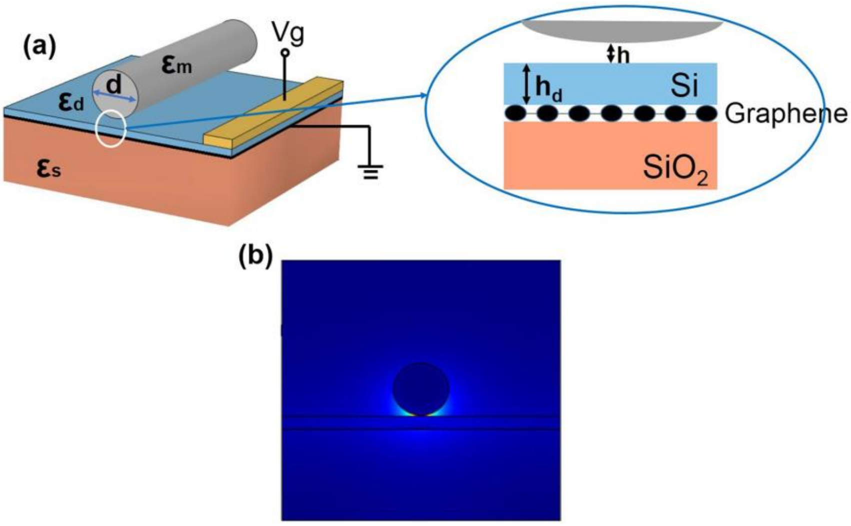

Fig. 1.46 Structure and mode distributions of the designed GHPM [107].

In order to further enhance the light-graphene interaction, the authors simulated a symmetrical structure, as shown in Fig. 1.47.

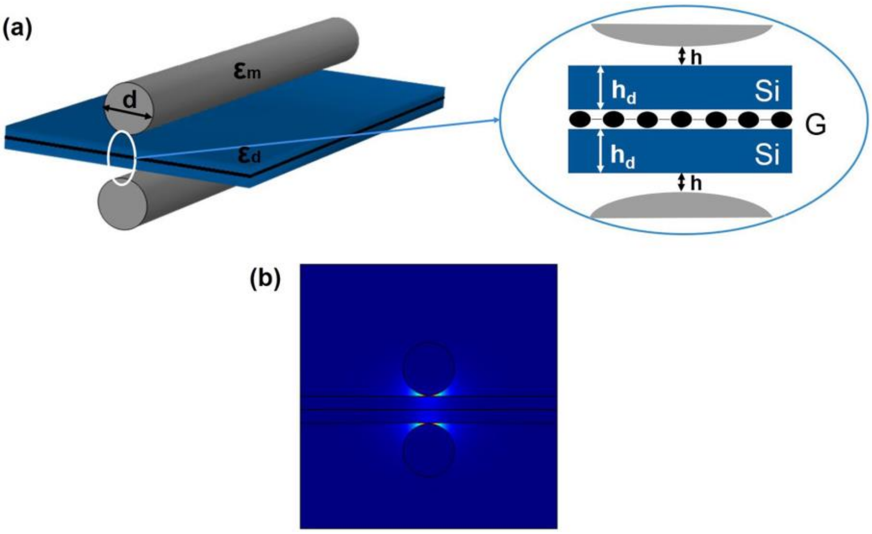

Fig. 1.47 Structure and mode distributions of SGHPM [107].

In this case, two silver cylindrical nanowires are symmetrically on both sides of the waveguide. They call it as "symmetrical graphene-based hybrid plasmonic modulator (SGHPM)". One can easily find tighter modes confinement than which is shown in Fig. 1.46.

In [108], the authors reported a multilayer graphene electro-absorption optical modulator based on double-stripe silicon nitride waveguide. They researched both graphene double-layer and four-layer structures, as shown in Fig. 1.48.

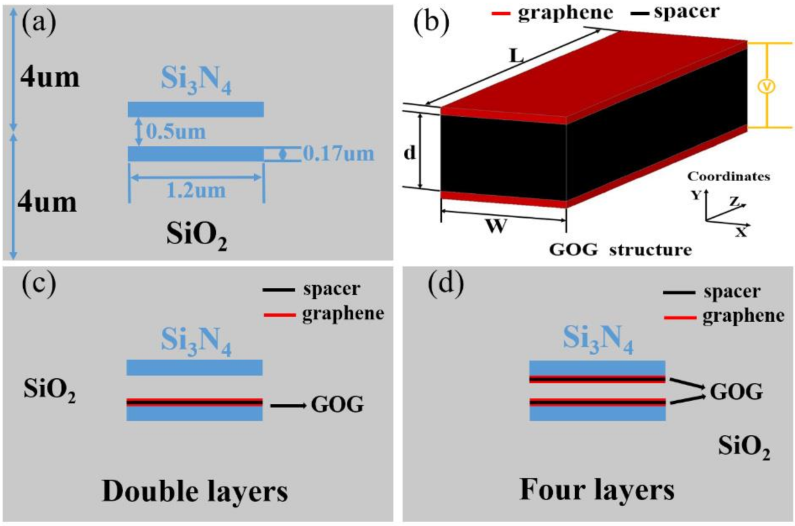

Fig. 1.48 (a) Cross section of the double-stripe Si_3N_4 waveguide. (b) Graphene-on-graphene (GOG) structure. (c) Double graphene layers configuration. (d) Four graphene layers configuration [108].

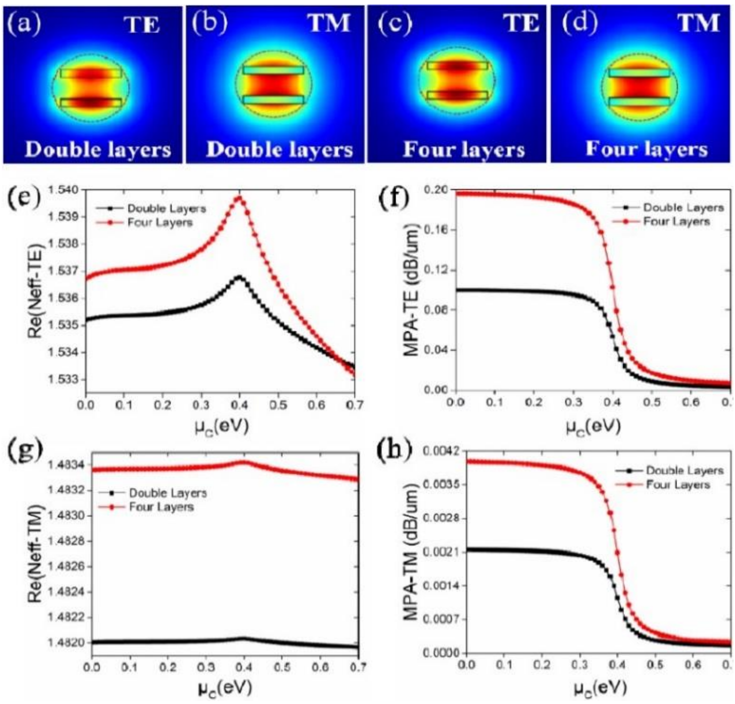

Fig. 1.49 (a)-(d) Electric field magnitude |E| distributions of the TE and TM modes at μ_c = 0 eV in the double and four graphene layers configurations. (e)-(h) Real(N_{eff}) and MPA of the TE and TM modes with different chemical potentials in both configurations [108].

Before this work, almost all the presented Si_3N_4/graphene modulators are based on the single stripe Si_3N_4 waveguide. Comparing to the single stripe Si_3N_4 waveguide, double-stripe Si_3N_4 waveguide will have much more symmetrical mode field distribution and lower polarization dependence. Therefore, the light-graphene interaction will be enhanced. They simulated both TE mode and TM mode on double-layer and four-layer, and got the N_{eff} and MPA, as shown in Fig. 1.49.

We can see the light-graphene interaction is much higher for TE mode and four-layer structure than TM mode and double-layer structure. This is due to the higher absorption of TE mode and the symmetrical structure of the four graphene layers configuration. The biasing of the four-layer graphene modulator is shown in Fig. 1.50.

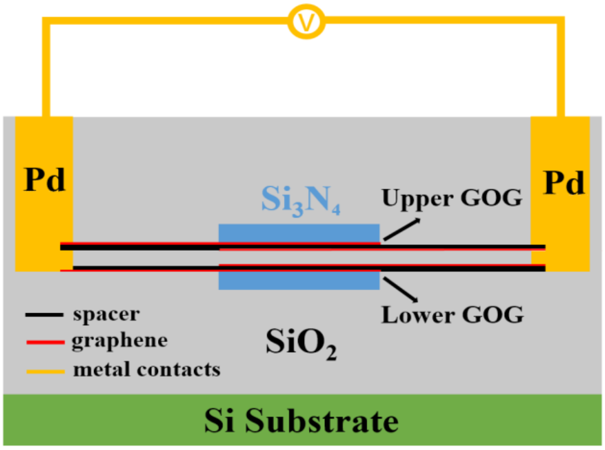

Fig. 1-50 Cross section of the four graphene layers modulator structure [108].

One graphene layer in the lower GOG and one graphene layer in the upper GOG are connected to the signal electrode, and the remaining two graphene layers in the two GOG structures are connected to the ground electrode. Due to this graphene layers co-electrode design, the series resistance of the modulator is reduced by 50%.

1.4.2 State of the arts of graphene modulators (part II)

According to the first part of the review, at this stage, I study the latest references which are all focusing on graphene modulators, and record their state-of-the-art values of every index as shown in Table 3.

In this table, I study 32 new references [104-135] to show how better FOMs of graphene modulators happen. The order of the references is strictly in the order of published year from 2012 to 2018. Among these references, references [115,126,133] are about all-optical graphene modulator; Reference [110] is about magneto-optical graphene modulator; The rest references are all about electro-optical graphene modulator. References [109,110,115,123,128] are about THz graphene modulator; The operation (carrier) wavelengths of the rest references are at 1.55 μm.

Table 3 State-of-the-art values of graphene modulator (part II)

Reference, and year	Where	If measured	Operation f or λ	Modulation depth	Modulation Speed	Footprint	Modulation Bandwidth	Operation Bandwidth	Insertion Loss
[109], 2012	ACS Nano	yes	0.2-2 THz	99%	\	\	\	1.8 THz	\
[110], 2013	PCCP	no	0-14 THz	15.7%	\	\	\	14 THz	\
[111], 2013	Nano Lett.	yes	450nm-2μm	35%	\	\	\	Broadband	\
[112], 2013	Sci. Reports	no	0.8-1.9μm	3 dB	850 GHz	0.72 μm	850 GHz	0.8-1.9μm	\
[113], 2014	Nano Lett.	yes	1.55 μm	40%	80 GHz	\	80 GHz	\	\
[114], 2014	Opt. Lett.	no	1.55 μm	9.5 dB	1 THz	0.01 μm^2	\	1.4-1.7 μm	−0.27 dB
[115], 2014	Sci. Reports	yes	0.25-1THz	94%	200 KHz	5 mm	200 kHz	0.75 THz	\
[116], 2015	Nanoscale	yes	1.55 μm	7 dB	\	10 μm^2	\	6.2 nm	\
[117], 2015	Nature C	yes	1.5 μm	50%	100 GHz	10 μm^2	\	\	\
[118], 2015	OE	no	1.55 μm	12.5 dB	133 GHz	20 μm^2	\	125.6 nm	\
[119], 2015	OE	yes	1.55 μm	2.5%	2.5 MHz	\	2.5 MHz	\	10%
[120], 2015	Opt. Lett.	no	1.55 μm	100%	\	\	\	\	6%
[121], 2015	J. Phys. D:	no	1.55 μm	3 dB	\	120 nm	\	62 THz	\
[122], 2015	small	no	0-10THz	76%	91 kHz	\	\	0.568 THz	17%
[105], 2015	Sci. Reports	yes	1.55 μm	22.5 dB	\	\	\	\	2 dB
[123], 2015	Nanotech	no	1.55 μm	21.7 dB	723 GHz	1.3 μm^2	\	\	2.18 dB
[124], 2016	ACS Photon	yes	1.55 μm	2 dB	35 GHz	18 μm^2	35 GHz	1.5-1.64 μm	\
[104], 2016	Opt. Lett.	no	1.55 μm	3 dB	\	100 μm	\	To 8.0 μm	\
[125], 2016	OE	yes	1.55 μm	11 dB	0.78GHz	1 mm^2	\	\	\
[126], 2016	Sci. Reports	yes	1.55 μm	9 dB	0.5 THz	\	0.5 THz	\	1 dB
[107], 2017	Sci. Reports	no	1.55 μm	3 dB	1.3 GHz	\	1.3 GHz	\	\
[127], 2017	IEEE	no	1.55 μm	5 dB	2.5 GHz	\	2.5 GHz	\	\
[128], 2017	Nanoscale	yes	0.6–1.6THz	15%	\	\	\	1 THz	\
[129], 2017	OE	yes	1.5 μm	3%	\	5 μm^2	\	900nm-1.5μm	10%
[130], 2017	OE	yes	1.55 μm	4.5 dB	5 GHz	\	5 GHz	\	5 dB
[108], 2017	OE	no	1.55 μm	3 dB	30.6GHz	18.04 μm	30.6GHz	\	\
[131], 2017	Opt. Lett.	yes	1.55 μm	1 dB	\	\	\	\	30 dB
[132], 2017	Opt. Lett.	no	1.55 μm	3 dB	0.48 THz	3.6 μm	0.48 THz	\	0.32 dB
[106], 2018	Nature P	yes	1.55 μm	35dB	5GHz	300μm	5GHz	\	\
[133], 2018	IEEE P. T.	yes	1.55 μm	7.3 dB	500 GHz	700 μm	\	970 nm	\
[134], 2018	Appl.Phy. E	no	1.55 μm	3 dB	120 GHz	\	120 GHz	\	1.5 dB
[135], 2018	Sci. Reports	yes	1.55 μm	3 dB	\	40 μm	\	15 nm	\

All these modulation depths are fulfilled, and it can be 100% [120].

The cause of this 100% modulation is the optical reflection using surface plasmon resonance in a graphene-embedded hybrid plasmonic waveguide. The structure is shown in Fig. 1.51.

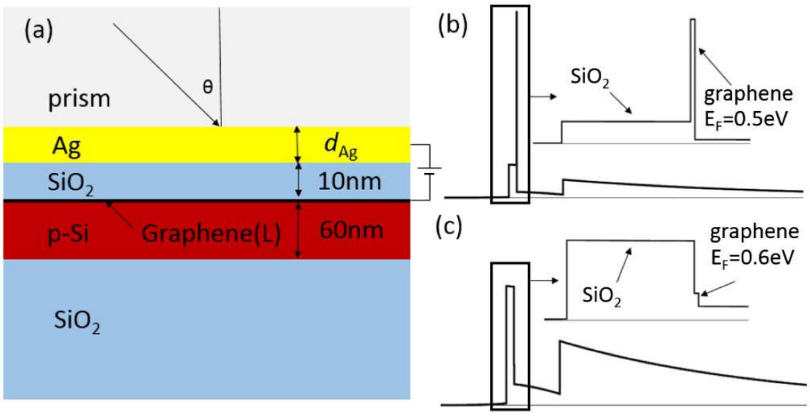

Fig. 1.51 (a) Schematic of the graphene-based optical modulator. The electric field distributions of the one-dimensional structure composed of Ag-SiO_2-graphene-Si-SiO_2 for (b) E_F = 0.5 eV, and (c) E_F = 0.6 eV. From reference [120].

In this modulator, when the light passes through the prism, it is totally reflected at the prism-A_g interface, and generates an evanescent wave. When the propagation constants of the evanescent wave and the hybrid plasmonic mode are matched, the evanescent wave couples to the hybrid plasmonic mode, resulting in a reflection dip at the incident angle for which the matching condition is satisfied.

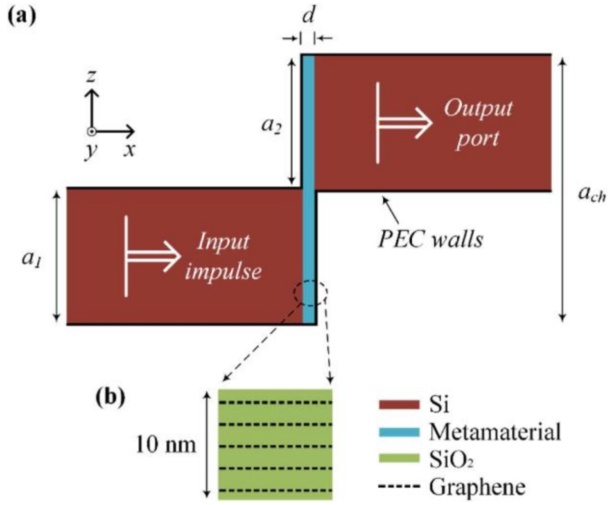

Fig. 1.52 Modulator's structure (a); (b) Metamaterial consists of graphene sheets and silica layers. From reference [114].

The highest modulation speed is 1 THz reported by [114], and 850

GHz reported by [112]. The footprint can be as low as 0.01 μm^2 by [114]. The structure of the modulator in [114] is shown in Fig. 1.52. This is an ultra-compact optical modulator based on graphene-silica metamaterial. The carrier light is input from the left port of the multilayer graphene metamaterial, and output port is on the right side of the thin modulator. The carrier wave is squeezed and tunneled through the metamaterial channel. This device is sealed with perfect electric conductor (PEC) walls for avoiding the leakage of the light energy.

The thickness of the graphene-silica metamaterial is only 0.015 μm and with a height of 0.68 μm, so they got a footprint of only 0.01 μm^2. Since the extremely high carrier mobility ensures the resistance of this modulator to be very small. Meanwhile, the small device area also leads to a tiny capacitance C (less than 0.1 fF). Thus, this modulator is estimated to have a modulation speed more than 1 THz.

The state-of-the-art value of insertion loss is still very high. The lowest one is 6% by reference [120]. The structure is shown in Fig. 1.51 (a). As the number of graphene increases, the insertion loss is lower, which is because of two factors: the increased resonant angle shift, and the lower loss of the hybrid plasmonic mode owing to the reduced sliver (A_g) thickness. This lower insertion loss can still be reduced significantly.

Reference [134] reported the latest ultra-high-speed graphene optical modulator design based on tight field confinement in a slot waveguide. Their structure is shown in Fig. 1.53.

The overlap of the two graphene sheets is suspended in the air slot. The partial graphene electrode overlap over the waveguide reduces the effective width of the capacitor, so capacitance is also reduced by more than one order of magnitude. Then the modulation speed is very high with lower overlap width, more than 800 GHz with the compromise of lower light-graphene interaction.

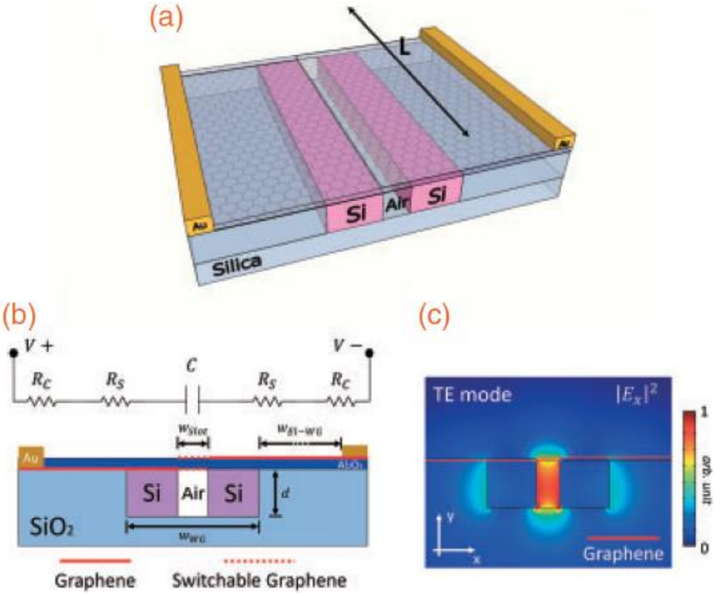

Fig. 1.53 (a) Three-dimensional schematic of the slot modulator design with the device length parameter L (not in scale). (b) Cross-section of the device with the equivalent RC circuit. (c) Mode profile of the device. From reference [134].

The authors find when the overlap width is at 50 nm, the light-graphene interaction is enhanced to its maximum and the modulation speed can be 120 GHz. At this point, the compromise between modulation speed and modulation efficiency is reduced significantly.

1.4.3 Conclusion of graphene modulators review

In this introduction, I study about 60 references on graphene modulators exampled from 2011 to 2018. Different graphene modulators have been well studied, such as all-optical, electro-absorption, electro-refractive, magneto-optical modulators, and THz modulators. Different structures are also included, such as monolayer, double-layer, four-layer and multi-layer graphene modulators, and suspended or slot graphene modulators. Among these different kinds of graphene modulators, most are focusing on optical communication wavelength at 1.55 μm, and most are electro-optical modulators. All the figure of merits of graphene modulators can be much better than the traditional silicon modulators, such as higher modulation depth, higher modulation speed, compacter footprints, broader bandwidth, and much lower insertion loss.

In the first 29 references, I have addressed the state-of-the-art values and the analyzed the trend of research of graphene modulators. The challenges and problems are also addressed. For the last 32 references I have addressed how the better FOMs happen.

However, these reported graphene modulators still can be improved and the design and fabrication of all these modulators are still very far away from the fundamental limits of graphene. Moreover, the compromise between the modulation speed and modulation efficiency is still a problem for designing better modulators, and it still needs to be reduced. I believe this review can be a good roadmap to develop graphene modulators and solve challenges and problems which are still there.

In this thesis, I show how graphene modulators are developing from low FOMs to high FOMs. I study four kinds of suspended graphene modulators. In chapter 2, I show the suspended self-biasing graphene modulator, which has been designed very close to the fundamental limits of graphene. Further, in chapter 3, the suspended triple-layer graphene modulator is studied, the light-graphene interaction is enhanced further with reduced compromise between modulation speed and modulation efficiency. In chapter 4, a comparison between suspended double-layer graphene modulator and sub-wavelength graphene modulator is presented. All the suspended graphene modulators are designed very near to the fundamental limits of graphene. In chapter 5, I show how near-fundamental-limit design of a graphene modulator is achieved through a research on metal-clad suspended self-biasing graphene modulator. Moreover, by suspending the graphene sheets for these modulators, we at least have three distinctive advantages:

(i). The structure can be design-free for the middle silicon slab or insulator slab acting as a bus waveguide to confine the mode. If we choose the right thickness of the middle slab, the light-graphene interaction will be enhanced to its maximum;

(ii). The modulator can be very clean, and we can achieve high quality devices. Moreover, the channel mobility reduction caused by graphene-dielectric interaction will be lower, and the graphene can achieve higher mobility;

(iii). The modes in this structure will be totally symmetrical, so the insertion loss can be much lower, and the two graphene layers will be always under the same ambient, the doping degree can be always the same.

1.5 Reason of the organization of reviews

The first part of graphene modulator review is done to address the research gap in this field which include 25 references published before 2016. In addition, the research trend for graphene modulators is predicted by this part. The second part is done particularly to address how the graphene modulators are developed from the low FOMs to the high FOMs.

For the review of THz waveguides, all the physics are related to my research of multiple-layer THz waveguides. The THz wave-graphene interaction is extreme low, which is almost zero because of the small size of graphene. The wavelength of THz wave is very large, which makes the beam width of THz wave is in millimeter scale caused by the diffraction limit. However, the interaction thickness of graphene is only a monolayer of graphene which is negligible compared by other materials. Moreover, the biasing is a problem if these structures in chapter 6 are made by graphene. Therefore, I do a research of multiple-layer THz waveguides by metal film to fill this structure gap and for a comprehensive research.

Chapter 2

Suspended Self-biasing Graphene Modulator

In this chapter, a theoretical investigation of a suspended self-biasing graphene waveguide for electro-optical modulators is presented. The light-graphene interaction can be enhanced by suspending the waveguide. For electro-absorptive modulation, the normalized modulation depth can be 0.54 dB/μm with a 3-dB footprint of only 1.5 μm^2. The insertion loss is extremely low ~ 0.002 dB, with a figure of merit of ~ 2700. For the electro-refractive modulation, a 100% modulation can be achieved with much smaller π-phase shift length of only 18.0 μm. The modulators also show great potential for high-speed (~ 559.2 GHz) modulation. The compromise between modulation speed and modulation efficiency is reduced significantly and the design is near-optimal to its fundamental limits. Moreover, a simulation by COMSOL is also conducted as a comparison. I believe this suspended graphene modulator can pave the way to practical high-speed, compact-footprint, and high-efficiency devices.

2.1 Introduction

To the best of my knowledge, the suspended self-biasing graphene waveguide has not been used as a modulator yet. By suspending the double self-biasing graphene layers, it has at least four distinctive advantages: i). We can design the modulator to realize the highest light-graphene interaction (in the cases of references [2,47], the modulators are not optimized when they just used the silicon waveguide to confine the fields). Then the modulation efficiency can be enhanced and the footprint can be smaller; ii). Since the self-biasing graphene waveguide is suspended in the air, the channel mobility reduction caused by graphene-dielectric interaction will be lower, the total resistance, including the graphene-metal contact resistance and graphene sheet resistance, of the modulator, can be even lower. Moreover, the capacitance will be lower with a thicker insulator. Therefore, the modulation speed and bandwidth can be enhanced. The compromise between modulation speed and modulation efficiency can be reduced; iii). The insertion loss will be extremely low, and the figure of merit (FOM) (defined as the ratio of modulation depth to insertion loss) can be even better; iv). Since the two graphene layers are under the same ambient, the modulation curves will be totally symmetrical.

In this chapter, I present a theoretical study of practical modulators based on this suspended self-biasing graphene waveguide for both electro-absorptive and -refractive types. In section 2.2, I analyze the model and derive the dispersion equation. In section 2.3.1, the modulator is designed and the effects on light-graphene interaction are discussed and analyzed in detail. The performance of the modulator is shown in section 2.3.2. For electro-absorptive type, the insertion loss is extremely low ~ 0.002 dB, with the figure of merit of ~ 2700. For electro-refractive type, a 100% modulation can be achieved with much smaller π-phase shift length of 18.0 μm. The modulator also shows great potential for high-speed modulation with a predicted 3-dB modulation bandwidth of 559.2 GHz and a speed limit of 4.29 THz. The compromise between modulation speed and modulation efficiency is reduced significantly. The design of this modulator is also near-optimal to its fundamental limits [39]. Moreover, the applied voltage can be lower than 5 V, and the energy consumption can be as low as 1.23 fJ/bit. In section 2.3.3, the simulation by COMSOL is given, which shows perfect agreements with my calculation results. In section 2.4, I will do a comparison with the not suspended structures. With all these advantages, the suspended modulator has great potentials for realizing practical high-speed, compact-footprint, and high-efficiency devices.

2.2 Models and theoretical method

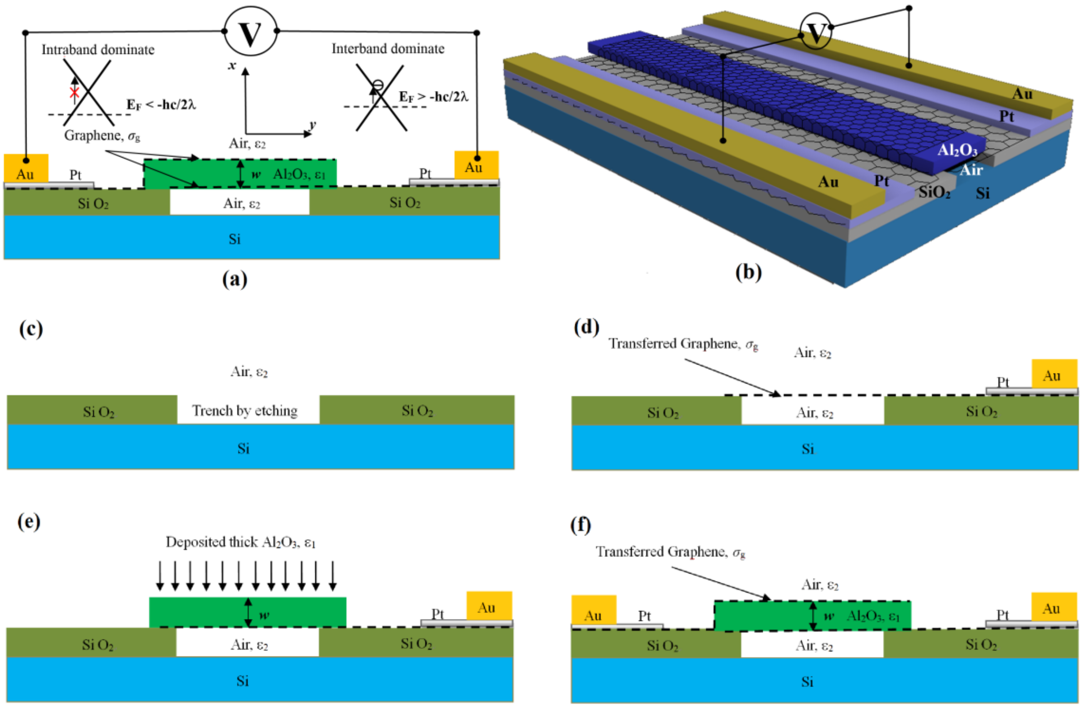

Fig. 2.1 Structure of suspended self-biasing graphene modulator (a) and the schematic of the 3D view (b). (c)~(f) show the fabrication steps of the device. The fabrication starts from the silicon waveguide with a trench in the middle caused by etching, as shown in (c). In (d), mechanical transfer of prepared graphene sheet. (e) Deposit of Al_2O_3. (f) Mechanical transfer of the second graphene sheet.

The side-view for the modulator structure and the coordinate system are shown in Fig. 2.1 (a). Here the two graphene sheets sandwiched by the insulator are biased simultaneously by each other to form a p-n junction:

one is p-doped and the other n-doped with the same carrier density. That is why the modulator is called as a self-biasing graphene modulator.

Thus, the chemical potentials of these two graphene sheets have the same absolute values, and these two graphene sheets share the same permittivity. Here the insulator slab between the two graphene sheets has two functions: i) It is used for generating electrons and holes to realize self-biasing; ii) It is used for confining the mode to enhance the light-graphene interaction.

Fig. 2.1 (b) shows the 3D schematic of the modulator. The active region of the modulator is suspended in the air over the semiconductor wafer. The air interval between the active region and the Si substrate is large enough, so the optical modes remain undisturbed from the substrate. The thickness of the graphene in the calculation is $\delta = 0.33$ nm, and the thickness of the insulator slab is w.

Figs. 2.1 (c) ~ (f) illustrate a possible way to fabricate the suspended self-biasing graphene modulator. First a trench is made in the semiconductor wafer by etching (c); then an annealed graphene is transferred [136] on the trench (d); after that a thick insulator slab should be deposited on the suspended first layer graphene (e); at last another annealed graphene is transferred on the top of the insulator slab (f).

The equivalent permittivity of graphene can be written as $\varepsilon_g = i\sigma_g/\omega\varepsilon_0\delta$ [137], where δ is the thickness of monolayer graphene, ω is the angular frequency of carrier wave, and ε_0 is the permittivity of vacuum. In the optical range, the surface conductivity σ_g of graphene can be predicted by the Kubo formula, seen as Eqs. (1-1, 1-2 and 1-3).

The suspended self-biasing graphene waveguide may support transverse magnetic (TM) and transverse electric (TE) modes simultaneously. For TM mode, the light-graphene interaction is much more complex than that of TE mode, because it has two components of the electric field (E_x and E_z). The one-atom-layer thick graphene's periodicity is in the two-dimensional lattice plane, and it reveals anisotropic material properties: the in-plane permittivity ($\varepsilon_g = i\sigma_g/\omega\varepsilon_0\delta$) can be actively tuned by the chemical potentials (the Fermi level), whereas the out-of-plane permittivity ($\varepsilon_\perp$, in the direction perpendicular to the graphene sheet) does not vary with the external parameters. Only the electric field can interact with graphene, so the dispersion relation of TM mode cannot be derived directly. However, for TE mode, it only has an in-plane component E_y which interacts with the graphene. I discuss the symmetric TE mode here. The mode propagates along the z-direction, and the TE mode field distribution in each area can be assumed as the following form [138]:

$$E_y(x) = \begin{cases} A_6 \exp[-h_3(x - w/2 - \delta)] & x \ge w/2 + \delta \\ A_2 \cos h_2(x - w/2) + A_3 \sin h_2(x - w/2) & w/2 \le x \le w/2 + \delta \\ A_1 \cos(h_1 x) & -w/2 \le x \le w/2 \\ A_4 \cos h_2(x + w/2) + A_5 \sin h_2(x + w/2) & -(w/2 + \delta) \le x \le -w/2 \\ A_6 \exp[h_3(x + w/2 + \delta)] & x \le -(w/2 + \delta) \end{cases} \quad (2\text{-}1),$$

where $A_1 \sim A_6$ are unsolved mode coefficients in different regions. The permittivity is $\varepsilon_n = \varepsilon_1$, $\varepsilon_n = \varepsilon_g$ or $\varepsilon_n = \varepsilon_2 = 1$ of the dielectric insulator slab, graphene, or outside air, respectively. The complex propagation constant is $\beta = \beta_1 + i\beta_2$ where β_1 is related to the effective refractive index ($N_{eff} = \beta_1/k_0$, k_0 is the wave vector in vacuum), and β_2 is related to the mode power attenuation (MPA) $\alpha = 20\beta_2 * \log_{10}(e)$. $h_1 = \sqrt{\varepsilon_1 k_0^2 - \beta^2}$, $h_2 = \sqrt{i\sigma_g \omega \mu_0 / \delta - \beta^2}$, $h_3 = \sqrt{\beta^2 - \varepsilon_2 k_0^2}$. As the tangential electro-magnetic fields are continuous on the interfaces, I have derived the dispersion equations of TE mode as follows [138]:

$$\tan(h_1 w/2) = (1 - i\sigma_g k_0^{\,2} / h_3 \omega \varepsilon_0 + \beta^2 \delta / h_3) / (h_1 \delta + h_1 / h_3) \qquad (2\text{-}2)$$

2.3 Results and discussions

2.3.1 Mode characteristics

When $w = 100$ nm, I use the material of Aluminum Oxide ($\varepsilon_1 = 3.06$ at $\lambda = 1.55$ µm) to calculate Eq. (2-2), and obtain the MPA (α) and effective refractive index (N_{eff}) of TE mode as a function of μ_c at wavelengths of 1.55 µm, as shown in Fig. 2.2.

The MPA has an abrupt change at the threshold of interband transition, and similar results have been found in [46,104,108]. When the chemical potential is between $-\pi\hbar c/\lambda$ and $\pi\hbar c/\lambda$, the interband transition takes place. The loss will be more than 2000 times lower when the chemical potential is beyond this scale: The loss is 0.258 dB/µm at μ_c = 0.40 eV, however, the loss is only 0.00097 dB/µm at μ_c = 0.41 eV, 266 times lower; 0.0001 dB/µm at 0.8 eV, 2580 times lower, which makes a normalized modulation depth of 0.257 dB/µm. It is worthy to point out that if the cladding layer is not air, namely the waveguide is not suspended, the modulation depth will be extreme low, such as it is only 0.0052 dB/µm for ε_2 = 3.0, and no mode will be supported when ε_2 is equal or higher than 3.06. Beyond this absorption threshold, $\mu_c > \pi\hbar c/\lambda$, the intraband contribution of conductivity dominates for all electron states in resonance with incident photons are occupied, and the interband transition is forbidden, or there are no electrons available for interband transitions ($\mu_c < -\pi\hbar c/\lambda$). This huge and sudden change in MPA can be very useful for electro-absorptive modulators.

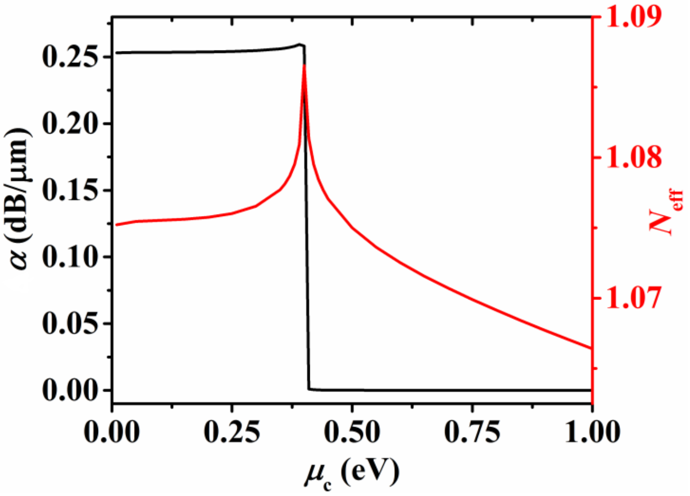

Fig. 2.2 MPA (black line) and mode index (red line) of TE mode in the self-biasing graphene waveguide as a function of chemical potential μ_c of graphene.

There is also a sharp change at this threshold point for the real part of the effective refractive index. It increases to the peak point N_{eff} = 1.0865 at μ_c = 0.4 eV then decreases to a lower value N_{eff} = 1.0664 at μ_c = 1.0 eV, which makes a $\Delta N_{\mathrm{eff}} = 0.02$. This is very useful for realizing practical electro-refractive modulators.

For the electro-absorptive case, the normalized modulation depth $\Delta\alpha$, defined as the off-state MPA minus the on-state MPA, is gotten as a function of dielectric insulator thickness w at $\lambda = 1.55$ μm, as shown in Fig. 2.3 (main panel).

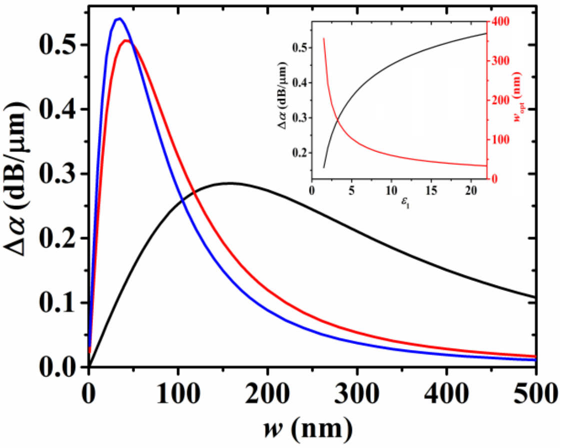

Fig. 2.3 Normalized modulation depth changes as a function of dielectric insulator thickness w at $\lambda = 1.55$ μm for different dielectric: $\varepsilon_1 = 3.06$ (black line), $\varepsilon_1 = 16$ (red line), $\varepsilon_1 = 22$ (blue line). Inset: The highest normalized modulation depth (black line) for different dielectric (ε_1), and the corresponding optimized dielectric thickness (red line).

There is a peak for normalized modulation depth at the optimized thickness w_{opt}, where the light-graphene interaction can be enhanced. The highest normalized modulation depth can be 0.54 dB/μm (which is only 0.16 dB/μm for the similar modulator in reference [47]) at $\varepsilon_1 = 22$, and $w_{\mathrm{opt}} = 33.2$ nm, which makes a 3-dB footprint of 0.272×5.556 μm^2 = 1.5 μm^2. ΔN_{eff}, defined as the peak N_{eff} at $\mu_c = 0.4$ eV minus the lowest N_{eff} at $\mu_c = 1.0$ eV, have the totally same changing law as $\Delta\alpha$ as a function of w. The highest ΔN_{eff} can be 0.043 at $\varepsilon_1 = 22$, and $w_{\mathrm{opt}} = 33.2$ nm, which is much larger than the state-of-the-art value of 0.028 in reference [36]. If we use two of these waveguides to form two arms of a Mach-Zehnder (M-Z) modulator, the required arm length (L_π) to achieve the π-phase shift, which can be calculated through $\lambda/2 = \Delta N_{\mathrm{eff}} * L_\pi$, will be only 18.0 μm, while it is 27.57 µm in reference [36]. Therefore, the footprint of the M-Z modulator based on this waveguide can be even smaller.

The inset of Fig. 2.3 shows the highest normalized modulation depth at different permittivities ε_1 of the insulators and the corresponding w_{opt}. As the permittivity increases, the highest normalized modulation depth also increases and the optimized thickness decreases, which tells us that the modulation depth can be higher and the footprint can be smaller for higher permittivity insulator materials. According to my calculation, I find the highest ΔN_{eff} have the totally same law as $\Delta\alpha$ as a function of ε_1.

For TE mode, the electric field E_y is in the plane of the graphene, so the amplitude of E_y which interacts with graphene will determine the interaction strength of one photon, and the confinement of the mode will determine the photon number which interact with the graphene. The normalized mode field distribution profiles and the associated electric field amplitudes in the graphene layer are obtained by calculating Eq. (2-1), as shown in Fig. 2.4.

Fig. 2.4 (a) is obtained when $\varepsilon_1 = 22$ at different insulator thickness w = 10 nm, 33.2 nm (w_{opt}), and 100 nm. The mode index N_{eff} is 1.087, 1.69, or 3.14, separately.

When the mode index is low, the amplitude of E_y in the graphene layer is high ~ 0.996 (panel a_1). However, the mode will be very leaky for most of the field will distribute in the outside air.

When $N_{\mathrm{eff}} = 1.69$, the amplitude of E_y in the graphene layer is also very high ~ 0.957 (panel a_2), moreover the confinement of the mode will be much better, so the light-graphene interaction is enhanced at this point, and both the $\Delta\alpha$ and ΔN_{eff} will be higher.

For $N_{\mathrm{eff}} = 3.14$, the confinement of the mode is much better, but the amplitude of E_y in the graphene layer decreased significantly to only ~ 0.76 (panel a_3).

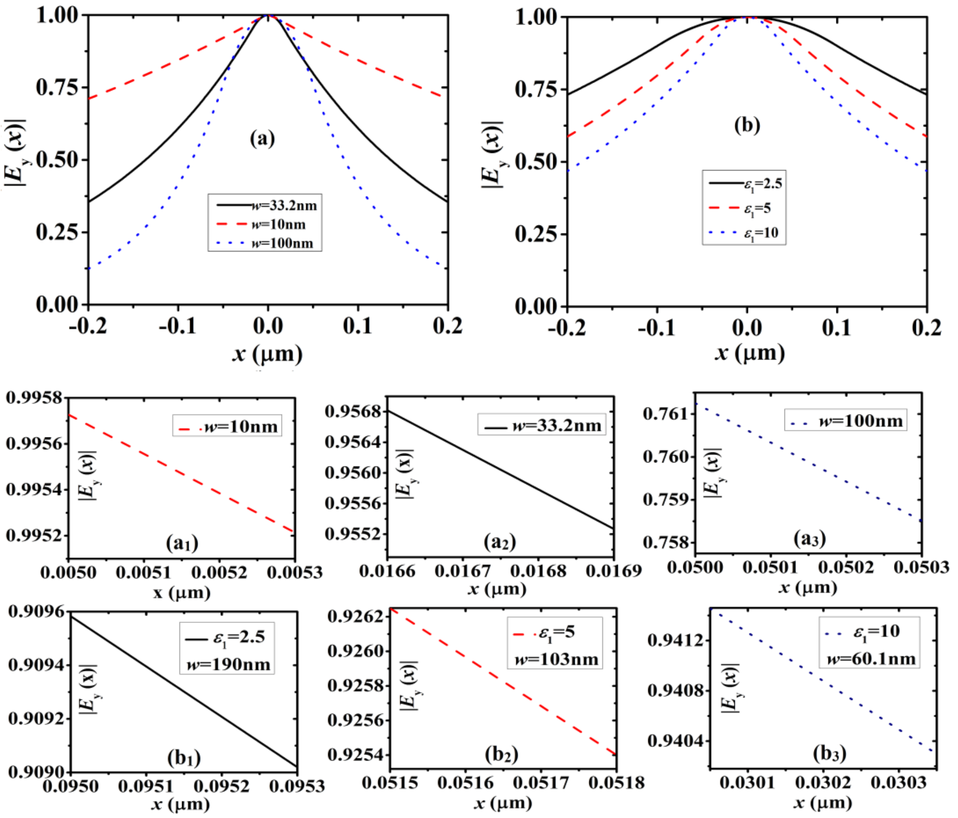

Fig. 2.4 Mode field amplitude as a function of coordinate x when $\mu_c = 0.3$ eV at $\lambda = 1.55$ μm: (a) $\varepsilon_1 = 22$: $w_{\text{opt}} = 33.2$ nm (black solid line), $w = 10$ nm (red dashed line), and $w = 100$ nm (blue dotted line), (b) $\varepsilon_1 = 2.5$, $w_{\text{opt}} = 190$ nm (black solid line), $\varepsilon_1 = 5$, $w_{\text{opt}} = 103$ nm (red dashed line), $\varepsilon_1 = 10$, $w_{\text{opt}} = 60.1$ nm (blue dotted line). The panels (a_1) ~ (a_3) show the amplitude of E_y in the graphene layer for (a) accordingly. The panels (b_1) ~ (b_3) show the amplitude of E_y in the graphene layer for (b) accordingly.

Fig. 2.4 (b) is obtained from different dielectrics at the w_{opt} points: $\varepsilon_1 = 2.5$, $w_{\text{opt}} = 190$ nm (black solid line), $\varepsilon_1 = 5$, $w_{\text{opt}} = 103$ nm (red dashed line), and $\varepsilon_1 = 10$, $w_{\text{opt}} = 60.1$ nm (blue dotted line). From the panels (b_1) ~ (b_3), we can see when the permittivity is higher, the amplitude of E_y in the graphene layer will be higher. It is 0.909, 0.926, or 0.941 for $\varepsilon_1 = 2.5$, 5, or 10 respectively. The confinement of the mode is also better for higher insulator permittivity. Therefore, the light-graphene interaction is absolutely better for high-κ gate dielectric materials [60]. For the case of $\varepsilon_1 = 22$ (Ta_2O_5), the light-graphene interaction is enhanced, and this causes higher modulation efficiency.

The material h-BN shows weak interaction with graphene, which will reduce the channel mobility reduction of graphene layers. For this modulator, it shows the highest normalized modulation depth of 0.294 dB/μm with a thickness of w_{opt} = 149 nm by using h-BN as the insulator slab.

2.3.2 Modulation performance

For the electro-absorptive modulator, the total power transmittance through a transmission length L in the modulator can be expressed as $T(\lambda)$ = Exp[-α*L]. The power transmittance spectrum of this modulator is obtained at different chemical potentials with a propagation length of L = 10 μm when ε_1 = 22, w_{opt} = 33.2 nm, as shown in Fig. 2.5 (a).

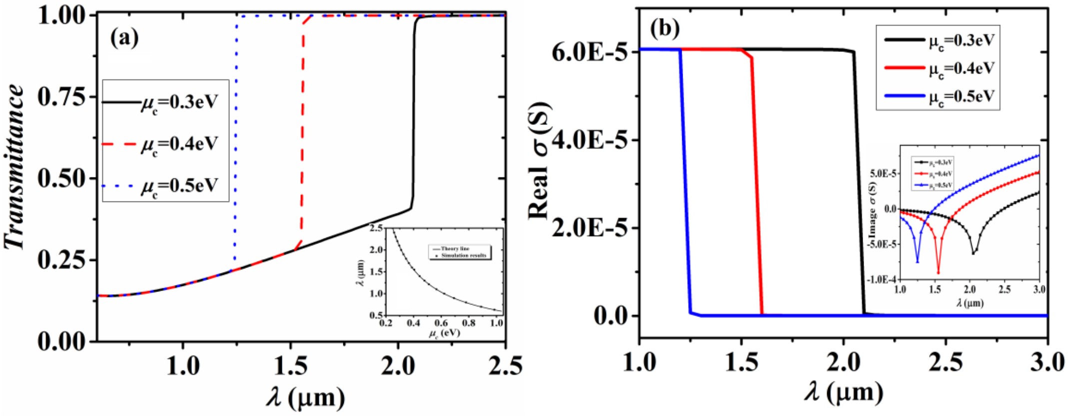

Fig. 2.5 (a) Power transmittance of the modulator as a function of wavelength, inset is the sharp turn point wavelength as a function of chemical potential. (b) and (inset) are real and imaginary part of the graphene conductivity as a function of wavelength, respectively.

From Fig. 2.5 (a), we can see there is a sharp change of the transmittance for different chemical potentials separately, and it always happens at the wavelength $\lambda = \pi\hbar c/\mu_c$, which is exactly the sudden turn point of MPA, as seen in Fig. 2.2 (black line). I simulate the MPA sudden turn points (square points) at different wavelengths and obtain the theoretical line (solid line) from $\lambda = \pi\hbar c/\mu_c$ as shown in Fig. 2.5 (a) inset. The simulation results are in good agreement with the theoretical line.

We can see when the chemical potentials change from 0.25 eV (applied voltage is 0.287 V) to 1.0 eV (applied voltage is 4.447 V), the modulator operation carrier wave spectrum ranges from 0.6 µm to 2.5 µm which covers the spectrum from visible light to near-infrared.

After a 10 µm propagating, a modulation depth of 71.24% is achieved at $\lambda = 1.55$ µm. The insertion loss, which is defined as $\alpha = -10\mathrm{Log}[T_{\max}]$, is also extreme low ~ 0.002 dB ($T_{\max} = 0.9995$). Therefore, the figure of merit (FOM) $\Delta\alpha/\alpha$ of this modulator is ultrahigh ~ 2706.

The conductivity of graphene is also calculated as a function of the wavelength, as shown in Fig. 2.5 (b) and the inset. Both the real part and imaginary part of σ_g are very sensitive to the wavelength when the chemical potential is equal to the half photon energy $\pi\hbar c/\lambda$, for example $\mu_c = 0.3$ eV at $\lambda = 2.07$ µm, $\mu_c = 0.4$ eV at $\lambda = 1.55$ µm, $\mu_c = 0.5$ eV at $\lambda = 1.24$ µm.

When the wavelength is smaller, the tuning points of the conductivity will move to the larger chemical potential, which makes graphene a constant absorber in the visible range. However, when the wavelength is much larger, such as in the THz range, the sensitive points disappear, and graphene behaves like a metal. It is worthy to point out that the small real part of the conductivity after the sharp turning points makes the on-state MPA very low because the imaginary part of graphene permittivity will be very small.

For the M-Z modulator, the schematic is shown in Fig. 2.6. I make one waveguide as a reference arm and the chemical potential is fixed at $\mu_{c0} = 1.0$ eV due to its smaller MPA and not very high applied voltage. The length of the two arms should be chosen carefully because it should be several times of L_π, but lower than the maximum allowed length $L_{\max}$ ($L_{\max} = 1/\alpha$) to make sure there is enough power at the output port.

I change the chemical potential of the modulation arm. According to my calculation, I find that $L_{\max}$ is on the scale of ~ cm, which is more than

1800 times larger than L_π ~ µm. This is because of the ultrahigh FOM of this modulator. So I choose an arm length of L = 100 µm is reasonable.

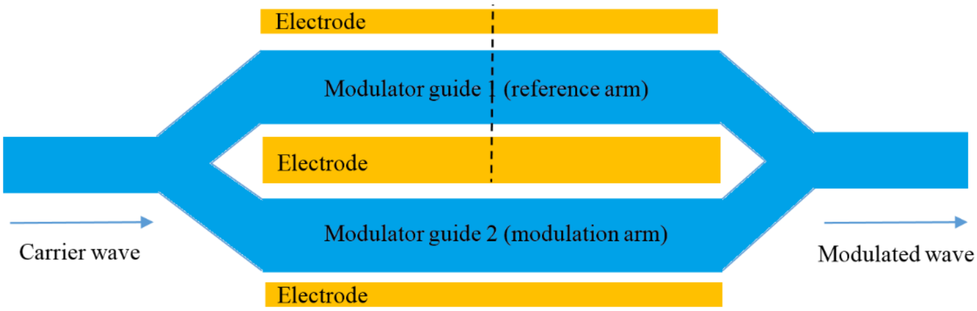

Fig. 2.6 The schematic of the M-Z modulator.

The normalized power transmittance, $T(\Delta\mu_c)$, of this M-Z modulator can be expressed as follows:

$$T(\Delta\mu_c)=\frac{1}{4}\times[\exp(-\alpha_0 L)+\exp(-\alpha_1 L)+2\exp(-\frac{\alpha_0 L+\alpha_1 L}{2})\cos(\Delta\phi)] \qquad (2\text{-}3),$$

where $\Delta\phi=\frac{2\pi}{\lambda}\Delta N_{eff}L$, α_0, α_1 is the MPA of the reference arms and the modulation arm, respectively. I calculate Eq. (2-3), and plot the transmittance $T(\Delta\mu_c)$ of this M-Z modulator in Fig. 2.7.

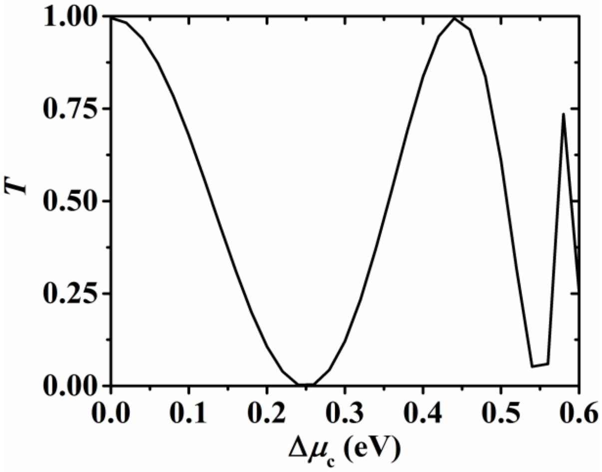

Fig. 2.7 Transmittance of the M-Z modulator as a function of the difference of the chemical potentials ($\Delta\mu_c$) of two arms when L = 100 µm.

One can see that there is one 100% modulation depth ($[T_{on} - T_{off}]/T_{on}$) and three π phase shifts. These are because of the high FOM and L is chosen 5 times larger than L_π.

The 3-dB modulation bandwidth can be calculated by:

$$f_{3dB} = 1/2\pi R_{\text{total}} C \qquad (2\text{-}4),$$

where R_{total} is the total resistance of the modulator, which includes the contact resistance (between electrode metal and graphene) and the graphene sheet resistance. Both of these two resistances are highly related to the mobility of graphene. According to reference [139], for my advantage of suspending structure, choosing contact resistance of 300 Ω·μm and a sheet resistance of 300 Ω/sq is reasonable, so R_{total} = 300/10+300 Ω = 330 Ω. $C = \varepsilon_1 \varepsilon_0 S / w$ is the capacitance of the active area of the modulator. Here I choose that S is equal to 0.5 μm × 10 μm, where 0.5 μm is the width of the modulator in the y-axis [140]. So the capacitance is C = 29.32 fF for ε_1 = 22, w_{opt} = 33.2 nm, then a 3-dB modulation bandwidth of 16.45 GHz is obtained. For lower permittivity material, the modulation bandwidth can be enhanced, for example, it is 559.2 GHz for ε_1 = 3.06 (Al_2O_3), w_{opt} = 157 nm, which is much higher than reported 35 GHz with the same insulator material Al_2O_3. The limit of the modulation speed is $c/4\sqrt{\varepsilon_1}d$, which I get is 1.6 THz (Ta_2O_5), or 4.29 THz (Al_2O_3).

Such a high value of the modulation bandwidth and speed is contributed by the lower total resistance and the much smaller footprint. However, when the modulation speed is higher, the permittivity of the insulator should be lower and the modulation efficiency is lower (lower light-graphene interaction and higher applied voltage). So there is a compromise between modulation speed and modulation efficiency. When the permittivity ε_1 of the insulator is around 5, the modulation speed can be around 500 GHz, and the normalized modulation depth is around 0.35 dB/μm simultaneously. It is worthy to point out that when the light-graphene interaction is enhanced, the insulator is much thicker than other graphene modulators, and both the modulation speed and modulation efficiency can be enhanced simultaneously, so the compromise between modulation speed and modulation efficiency is always reduced compared with other modulators.

The fundamental limits of graphene modulators in transmission can be expressed as [39]:

$$\gamma_{\mathrm{mod}} = \frac{(h \cdot T_{on})^2}{(1-T_{on}{}^2)[1-(1-h)^2 T_{on}{}^2]} \le \gamma_M \qquad (2\text{-}5),$$

where $h = (T_{\mathrm{on}} - T_{\mathrm{off}})/T_{\mathrm{on}}$ is the modulation depth, $\gamma_{\mathrm{M}} = |\sigma_{\mathrm{on}} - \sigma_{\mathrm{off}}|/4\mathrm{Re}(\sigma_{\mathrm{on}})\mathrm{Re}(\sigma_{\mathrm{off}})$ is the upper bounded quantity of graphene modulator, which depends only on graphene conductivity (on-state σ_{on} and off-state σ_{off}). I calculate Eq. (2-5), and get the fundamental limit of this modulator, as shown in Fig. 2.8.

We can see the performance of this modulator is very near the fundamental limit. This is because the high light-graphene interaction makes the modulation depth much higher, and the suspended structure makes the insertion loss much lower.

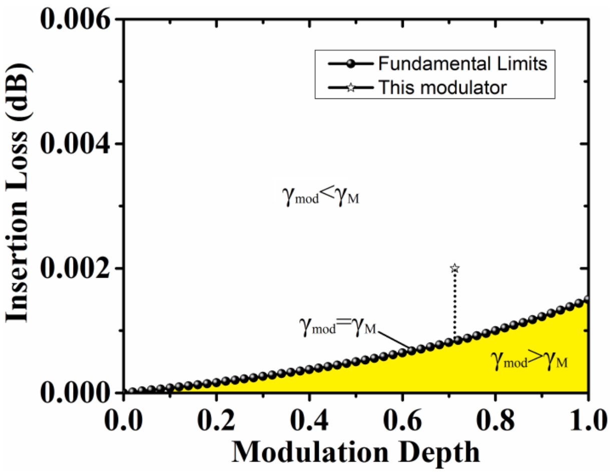

Fig. 2.8 Fundamental limit and the performance of this modulator. Yellow area is the forbidden area.

The chemical potential μ_c can be tuned by applying voltage V_g [141]:

$$V_g = \frac{\mathrm{e}w}{\pi \varepsilon_1 \varepsilon_0 \hbar^2 v_F{}^2} \int_0^{\infty} \varsigma[(\mathrm{e}^{\frac{\varsigma-\mu_c}{k_B \mathrm{T}}}+1)^{-1} - (\mathrm{e}^{\frac{\varsigma+\mu_c}{k_B \mathrm{T}}}+1)^{-1}]\mathrm{d}\varsigma \qquad (2\text{-}6),$$

where ς is energy. According to the theory in reference [142], in my case, since the two graphene layers have energy coupling from each other, the equivalent permittivity of the device should be $\varepsilon = (\varepsilon_1 + 2\varepsilon_{\mathrm{air}})/3$ and the choosing of an average Fermi velocity v_F = 1.5×10^6 m/s is reasonable. When the chemical potential is from -1 eV to 1 eV, I calculate Eq. (2-6) and obtain the applied voltage as a function of μ_c, as shown in Fig. 2.9 (a).

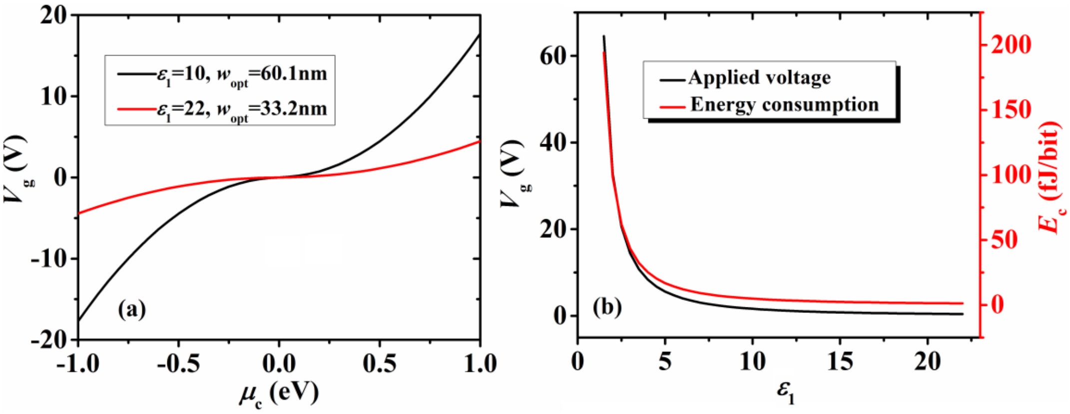

Fig. 2.9 (a) Applied voltage as a function of chemical potential μ_c: black line: ε_1 = 10, w_{opt} = 60.1 nm, red line: ε_1 = 22, w_{opt} = 33.2 nm; (b) Applied voltage and corresponding energy consumption as a function of permittivity ε_1 of the insulator when w is at w_{opt} and μ_c = 0.3 eV.

The applied voltage is always smaller than 5.0 V for ε_1 = 22, w_{opt} = 33.2 nm when the chemical potential is changing from -1eV to 1eV. But for ε_1 = 10, w_{opt} = 60.1 nm, the applied voltage should be larger (< 20 V). For h-BN, ε_1 = 3.24, w_{opt} = 149 nm, the applied voltage should be ~ 100 V.

I also obtain the optimized (w = w_{opt}) applied voltage and the corresponding energy consumption as a function of insulator permittivity ε_1 when μ_c = 0.3 eV, as shown in Fig. 2.9 (b). It shows that the optimized voltage and energy consumption will be lower when the permittivity is larger. The applied voltage is on the scale of 0.4 V ~ 5.6 V, and the energy consumption is on the scale of 1.23 fJ/bit ~ 16.8 fJ/bit when ε_1 is changing from 22 to 5. The energy consumption is comparable to the smallest reported value (0.482 fJ/bit) [38].

2.3.3 Full-wave simulation by COMSOL

My results have been compared by full-wave simulation using commercial software (COMSOL). In the simulation, I set ε_1 = 22, μ_c = 0.3 eV, the thickness of graphene is δ = 0.33 nm, insulator thickness of h_core =

0.0332 µm with a solving area of h_cladding = 7 µm and L = 10 µm. The transmittance of E_y is gotten at the different wavelengths, as shown in Fig. 2.10. We can see the transmittance is very high at λ = 2.5 µm and there is almost no decay along the transmission length. However, the transmittance is decayed significantly at λ = 0.6 µm. All of these results agree well with the calculation results.

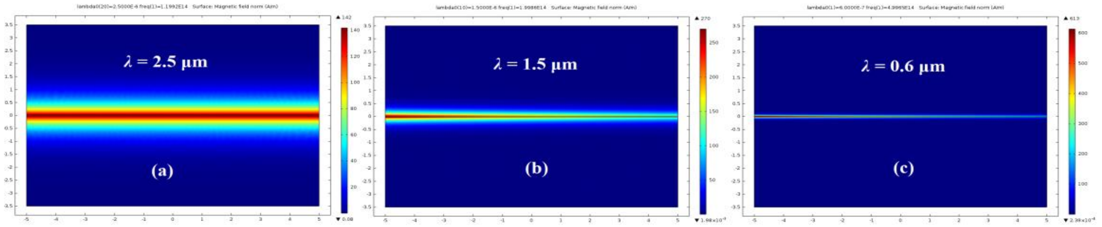

Fig. 2.10 Transmittance of E field at different wavelength: λ = 2.5 µm (a), λ = 1.5 µm (b), and λ = 0.6 µm (c) when ε_1 = 22, μ_c = 0.3 eV. The solving area width h_cladding = 7 µm, length d = 10 µm, and core width h_core = 0.0332 µm. Simulated by COMSOL.

In order to know the transmittance as a function of the wavelength, I retrieve the scattering parameter S_{21} as a function of the carrier wavelength, as shown in Fig. 2.11.

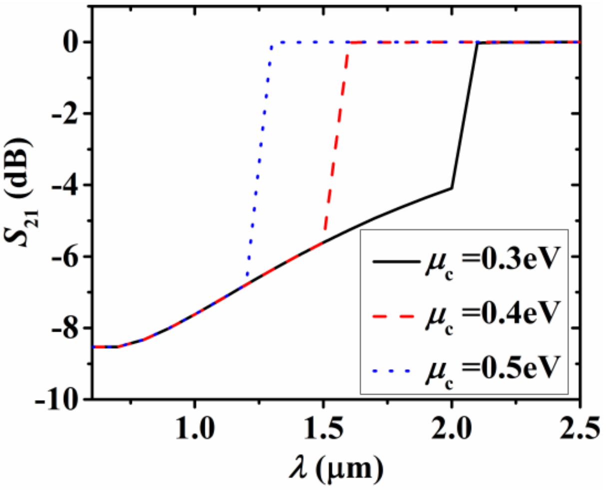

Fig. 2.11 Scattering parameter S_{21} as function of wavelength at μ_c = 0.3 eV (black solid line), μ_c = 0.4 eV (red dashed line) or μ_c = 0.5 eV (blue dotted line). Simulated by COMSOL.

By comparing Fig. 2.11 and Fig. 2.5 (a), we can see the results obtained from these two different methods are matched exactly well. The only difference is that in the case of COMSOL results, I have considered the reflection, which makes the insertion loss a slightly larger, and the difference is lower than 0.001, which tells us that the reflection of this modulator is very low. The insertion loss is of ~ 0.002 dB, the modulation depth is of 5.430 dB at $\lambda = 1.55$ µm. Then we can achieve a FOM of 2715.

After my simulation, I find that if the lower air layer (the etched layer) is filled with silica ($\varepsilon_2 = 4$), namely the modulator is put directly on the semiconductor wafer, the modulation depth of this case will be only 3.125 dB, which is much lower than the suspended case. It will be extreme lower if the insulator is the optimized materials (ε_1 is around 5).

2.3.4 Comparison with other graphene modulators

In order to get a better knowledge of the high performance of this modulator, I summarize the FOMs of different graphene modulators as a comparison, as seen Table 4:

Table 4. Comparison with other modulators

Ref.	Modulation Speed	Modulation Bandwidth	Operation Bandwidth	Modulation Depth	FOM $\Delta\alpha/\alpha$	Footprint
[2]	1.2 GHz	1.2 GHz	1.35~1.6μm	4 dB	NA	25 μm^2
[35]	30 GHz	30 GHz	NA	28 dB	NA	45 μm^2
[124]	35 GHz	35 GHz	1.5~1.64μm	2 dB	NA	18 μm^2
[34]	NA	NA	15 THz	16.83 dB	72	0.05μm^2
[47]	1 GHz	1 GHz	NA	6.5 dB	NA	40 μm^2
[26]	120 GHz	120 GHz	NA	80%	NA	60 μm^2
This work	559.2 GHz	559.2 GHz	0.6~2.5μm	5.430 dB	2700	1.5 μm^2

2.4 Comparison with the not suspended graphene structure

2.4.1 Modulation curve

The modulation curve of a graphene modulator is the transmittance as a function of applied voltage [2,47]. The modulation curve has been measured by many papers [2,47,56,124]. However, the theory modulation curve of a graphene modulator has not been reported yet. Here I calculate the modulation curve of my suspended self-biasing graphene modulator when Al_2O_3 is working as the insulator with a thickness of $w = 100$ nm, at the communication wavelength 1.55 µm, for 10 µm long device, as shown in Fig. 2.12.

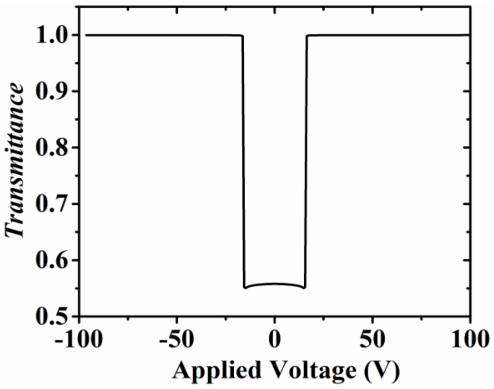

Fig. 2.12 Modulation curve of the suspended self-biasing graphene modulator.

Since the two graphene layers are under the same ambient, the impurity doping will be the same. Actually, for the suspended structure, the impurity doping will be much lower. When the modulator is self-biased, the two graphene layers will be doped simultaneously with the same degree of density. The only difference is that one is p-doped and the other one is n-doped. Therefore, the two graphene layers have the same permittivity. The Dirac point of the two graphene layers will happen at the zero-biasing voltage, the modulation curve will be totally symmetrical, as seen in Fig. 2.12.

The modulation curves of [2,47,56,124] are not symmetrical, which is caused by serious natural doping from the substrate. However, there is a difference between theoretical modulation curve and the experimental one. The experimental curves change gradually as the intraband transition turn to the interband transition. However, we can see the very clear sudden change of the transmittance at the absorption threshold for theoretical modulation curve. For quantum physics prediction, there must be a sudden change of the modulation curve at the threshold turn point. The gradually changing of the experimental modulation curve may be caused by the dissipation from the substrate.

2.4.2 Modulation depth comparison between suspended modulator and modulator with cladding

In order to know the difference between modulation depths of suspended case and unsuspended case, and to address the strong point of suspending, the modulation depths of these two different cases are calculated as a function of insulator width w when ε_1 = 22, ε_2 = 1 (suspended) or 3.06 (Al_2O_3 cladding), at λ = 1.55 μm, as shown in Fig. 2.13.

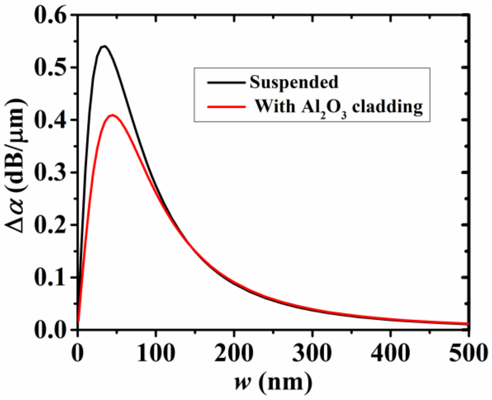

Fig. 2.13 Modulation depth of the suspended case (black line) and unsuspended case (red line) as a function of insulator thickness w.

From Fig. 2.13 we can see when the modulator is filled with Al_2O_3 cladding, the highest modulation depth is much lower (only 0.409 dB/μm) than the suspended case (0.541 dB/μm), and the optimal thickness w_{opt} is slightly thicker (45 nm). For the same modulation, the length of the unsuspended case should be 1.32 times longer than the suspended case, so the footprint (thickness multiply length) should be about 2 times larger. For the modulation speed, these two cases are almost the same, since the ratio of graphene overlap area to insulator thickness is almost unchanged.

I also calculate the mode power attenuation (MPA) as a function of chemical potential when ε_1 = 22, ε_2 = 1 (suspended) or 3.06 (Al_2O_3 cladding), w_{opt} = 33.2 nm, at λ = 1.55 μm, as shown in Fig. 2.14.

For this case, I do not consider the absorption loss of the substrate. From Fig. 2.14, we can see the on-state attenuations of these two cases are almost the same, both are very small. However, the off-state loss of the suspended case is 0.15 dB/μm larger, which tells us a larger modulation depth can be achieved by suspending.

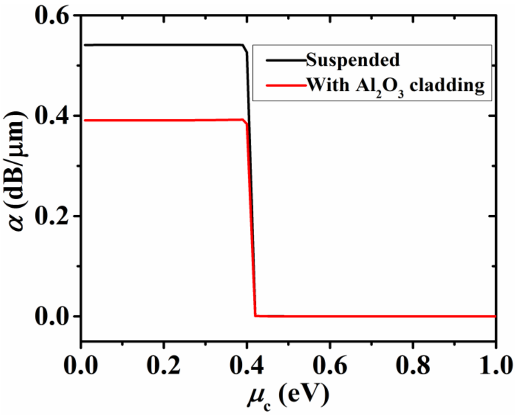

Fig. 2.14 MPA of the suspended case (black line) and unsuspended case (red line) as a function of chemical potential of graphene.

This is because a higher permittivity of the cladding material causes lower mode amplitude in the graphene and make the mode field leakier, which causes lower light-graphene interaction.

For the unsuspended case, different cladding materials cause different modulation depth reduction. I obtain the modulation depth as a function of the permittivity of the cladding material when $\varepsilon_1 = 22$ (high-κ material), $w_{opt} = 33.2$ nm, at $\lambda = 1.55$ μm, as shown in Fig. 2.15.

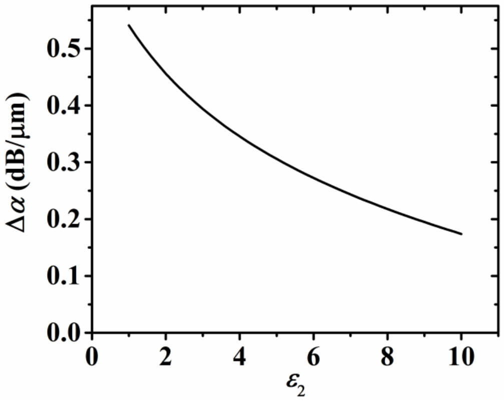

Fig. 2.15 Modulation depth of the unsuspended case as a function of the permittivity of the cladding material.

From Fig. 2.15, we can see the modulation depth decrease from 0.54 dB/μm to 0.17 dB/μm when ε_2 is changing from 1 to 10. It is worthy to point out that when the permittivity of the cladding material is larger than that of the middle insulator, no mode will be supported in the waveguide. For low-κ materials (such as Al_2O_3, and h-BN), the modulation depth will be very low if the waveguide is not suspended.

2.4.3 Insertion loss comparison

In this case, I consider a loss tangent of 0.001 of the cladding substrates (ε_2 = 3.06 Al_2O_3) to calculate the insertion loss for 10 µm long device. The unsuspended insertion loss at the optimized device structure is obtained as a function of the permittivity of the middle insulator, as shown in Fig. 2.16.

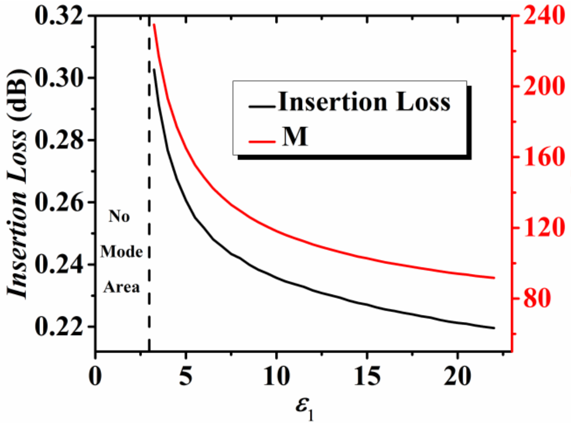

Fig. 2.16 Unsuspended insertion loss (black line) and the ratio M (red line) of unsuspended insertion loss to suspended insertion loss as a function of the permittivity of the middle insulator.

From Fig. 2.16, we can see the insertion loss of the unsuspended case is on the scale of 0.2 dB ~ 0.3 dB for a 10 µm long device. The ratio M of unsuspended insertion loss to the suspended insertion loss is also shown in Fig. 2.16 (red line). M is more than 100, which tells us that the insertion loss of the suspended case can be 100 times lower and a much higher figure of merit (FOM) can be achieved. For example, the FOM of the suspended case can be 2700, however, it is only 24 for the unsuspended case. There also shows a no mode area for lower ε_1.

The best insulator material for fabricating this suspended self-biasing graphene modulator is the material with permittivity around 5. I obtain the scattering parameter S_{21} from simulation by commercial software COMSOL. In the simulation, I set ε_1 = 5, the thickness of graphene is 0.33

nm, insulator thickness of h_core = 0.103 μm with a solving area of h_cladding = 7 μm and L = 10 μm. The relation between S_{21} and carrier wavelength is shown in Fig. 2.17.

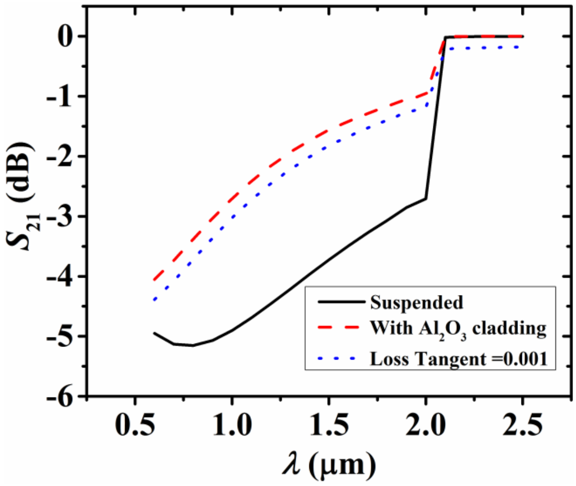

Fig. 2.17 Scattering parameter S_{21} as a function of carrier wavelength at μ_c = 0.3 eV when the modulator is suspended (black solid line), with Al_2O_3 cladding (red dashed line) and the with cladding loss tangent of 0.001 (blue dotted line).

From Fig. 2.17, we can see the modulation depth of the suspended case at λ = 1.55 μm is 3.6 dB which is much larger than that (1.5 dB) of the unsuspended case. If the loss is considered, the highest transmittance will be decreased to - 0.18 dB, which causes larger insertion loss. This is due to a significant proportion of the mode energy being distributed in the cladding material.

2.4.4 The difference between bilayer graphene and self-biasing graphene

First, the structure is totally different: The bilayer is two graphene layers stacked together; The self-biasing graphene is two graphene layers sandwiched by a gate material.

Second, the purpose is different: For bilayer, it is to change the quantum physics of graphene, such as to create a bandgap; For self-biasing, it is to cause higher light-graphene interaction.

Third, the bilayer cannot confine the mode, so it cannot be used as a waveguide.

Fourth, the bilayer cannot be biased by itself.

2.5 Summary

In my theoretical analysis, a suspended self-biasing graphene waveguide is used for both electro-absorptive and electro-refractive modulators. The device is then designed to achieve the highest light-graphene interaction. For electro-absorptive modulation, the normalized modulation depth can be 0.54 dB/μm and the 3-dB footprint can be only 1.5 μm^2. The performance of the modulator with a propagation length of 10 μm is also analyzed. A modulation depth of 71.24% can be achieved with a small footprint. A FOM of ~ 2700 is achievable and it also shows a great potential for very high modulation speed ~ 559.2 GHz. The compromise between modulation speed and modulation efficiency is reduced significantly. For electro-refractive modulation, a 100% modulation is achieved with a very small π-phase shift length of 18.0 μm. The performance of this modulator is also near-optimal to its fundamental limits. Moreover, the lowest energy consumption of 1.23 fJ/bit is also obtained. A full-wave simulation by COMSOL is also given as a comparison, which shows perfect agreement with my calculation results. All of these sounding results are contributed by the suspended graphene structure and the highest light-graphene interaction, as known from the comparison.

Chapter 3

Suspended Triple-layer Graphene Modulator

In this chapter, the suspended triple-layer graphene modulator is firstly investigated theoretically. There appear two modulation depths for electro-absorption modulation. And the light-graphene interaction is enhanced to its maximum by this design. The highest modulation depth for electro-absorption modulation can be 0.834 dB/μm causing a 3-dB footprint of only 0.94 μm^2. For electro-refractive modulation, there appear several 100% modulations with a much smaller π-phase shift length of only 11.3 μm. This modulator also shows great potential for high-speed modulation with a prediction value of 759.85 GHz, while the switch energy can be as low as 0.61 fJ/bit with low applied voltage. Moreover, the simulation by COMSOL is also presented as a comparison, which agrees well with my calculation results. And the figure of merit of this modulator can be 2105. I believe these results can pave the way to design practical high-speed, compact-footprint, and high-efficiency devices.

3.1 Introduction

The compromise between modulation speed and modulation efficiency is always an issue which limits a better modulator: When the modulation speed is higher, the capacitance of the modulator should be lower, hence the thickness of the insulator between the two electrodes should be thicker and the active area smaller. This will make the modulation efficiency much lower for higher applied voltage, demanding a smaller footprint, and lower modulation depth.

An improved suspending self-biasing graphene modulator [143] has been proposed in a previous chapter. By suspending the modulator, I design it to have much higher modulation speed, as high as 559.2 GHz. The footprint for electro-absorption modulation is only 1.5 μm^2. The modulation depth can also be 100% for electro-refractive modulation. The most important is the figure of merit (FOM) (defined as the ratio of modulation depth to insertion loss) can be to ~ 2700. These good results are contributed by three reasons: First, the modulator can be designed to realize the highest light-graphene interaction; Second, the suspending structure makes the channel mobility reduction caused by graphene-dielectric interaction much lower; Third, the suspending of the modulator makes the insertion loss much lower. This suspended self-biasing graphene modulator has been developed to very near the fundamental limits. However, the applied voltage is still large and the modulation depth for the electro-absorption modulation is still low. Moreover, the light-graphene interaction can be enhanced further by suspending triple graphene layers, which has not been researched yet.

In this chapter, I discuss a new graphene modulator: the suspended triple-layer graphene modulator. In this case, three graphene layers are interleaved by two insulator slabs, and the modulator is suspended. The three graphene layers are biased simultaneously by each other, which makes the middle layer double doped as each of the two side layers. The light-graphene interaction will be enhanced significantly for there are three graphene layers and the middle layer is always at the highest mode energy distribution center. Moreover, two insulator slabs make the confinement of the mode better and the parallel connection of the two capacitors makes the total resistance lower, and the applied voltage will also be lower for a thinner insulator slab at the best light-graphene interaction points.

In section 3.2, the mode profile equations and the dispersion equation of the TE mode are derived and the waveguide structure model is analyzed. In section 3.3.1, the mode characteristics in this waveguide are analyzed. There appear two modulation depths and two mode index peaks, which are caused by the middle graphene layer and the two side graphene layers, respectively. The waveguide is designed to the highest light-graphene interaction condition for the highest modulation depth at the optimized insulator thickness. The mode profiles are analyzed to explain how the highest light-graphene interaction happens. In section 3.3.2, the performance of this modulator is described and the physics are discussed. The transmittance for electro-absorption type shows two modulations.

For the electro-refractive type, the π-phase shift length is only 11.3 μm, and it shows several 100% modulations. The modulation speed can be as high as 759.85 GHz. Moreover, the applied voltage and energy consumption is lower than the suspending self-biasing graphene modulator. In section 3.3.3, the full-wave simulation by COMSOL is given as a comparison, which matches very well with my calculation. I propose that this modulator can be widely used in many applications, and the results presented here give promise that it can be used to design graphene modulators and other optical devices.

3.2 Model and dispersion equation

The waveguide structure is shown in Fig. 3.1 (a). Three graphene layers are sandwiched by two insulator slabs which have the same material and a thickness of w. The thickness of a graphene layer is $\delta = 0.33$ nm. The waveguide is suspended in the air for three reasons: First, by suspending, the mode will be confined in the graphene center, the mode confinement will also be better, and the light-graphene interaction will be enhanced; Second, the mode profile will be totally symmetrical, and the insertion loss will be lower; Third, the waveguide will be away from any other disturbance which effects the quality of the device, so the mobility of graphene will be better.

The voltage is applied between the middle layer and the two side layers. If the middle layer is connected to the negative electrode of the voltage source, the electrons from the middle graphene layer will move to the two side layers, as shown in Fig. 3.1 (b).

The middle graphene layer will be doped with holes, and the two side layers will be doped with electrons. Moreover, the doping degree in the middle layer will be two times that of each side layer. If each of the two side layers has a chemical potential of μ_c, the middle layer will have a chemical potential of $\sqrt{2}\mu_c$. The equivalent circuit of this modulator is shown in Fig. 3.1 (c).

From Fig. 3.1 (c), we can know the equivalent circuit of this modulator is two modulators parallel connected to each other and biased simultaneously. So the total resistance and capacitance will be:

$$\frac{1}{R_{total}} = \frac{1}{1.5R} + \frac{1}{1.5R} = \frac{4}{3R} \tag{3-1}$$

$$C_{total} = 2C \tag{3-2}$$

The modulation speed will be:

$$f_{3\text{dB}} = \frac{1}{2\pi R_{\text{total}} C_{\text{total}}} = \frac{1}{3\pi RC} \tag{3-3}$$

The modulation speed is larger than that of the suspended self-biasing graphene modulator which is $1/4\pi RC$. Moreover, the light-graphene interaction will be enhanced further because the mode amplitude will be the peak at the middle graphene layer for the symmetrical mode profile. The compromise between modulation speed and modulation efficiency will be reduced further.

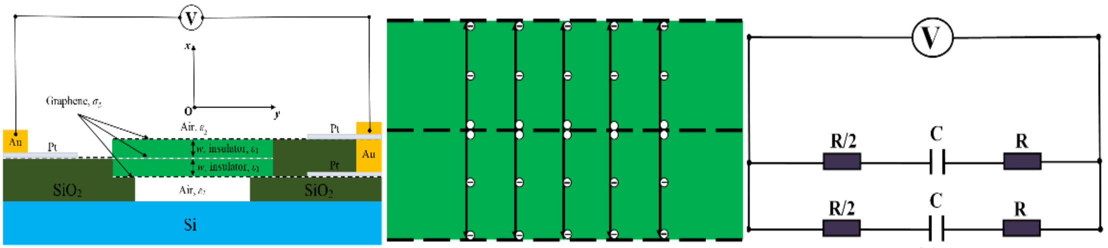

(a) (b) (c)

Fig. 3.1 (a) Structure of suspended triple-layer graphene waveguide modulator. (b) Movement of carriers when the triple-layer graphene modulator is biased. (c) Equivalent circuit of the suspended triple-layer graphene modulator.

According to the well-known two-dimensional analysis [144], the dimension of the waveguide in *y*-direction can be assumed as large enough for not disturbing the mode configuration. The suspended triple-layer graphene waveguide may support transverse magnetic (TM) and transverse electric (TE) modes simultaneously. I discuss the symmetric TE mode here. The mode profile can be assumed as [138]:

$$E_y(x)=\begin{cases} A_{10}e^{-h_4(x-3\delta/2-w)} & x\geq 3\delta/2+w \\ A_6e^{-h_3(x-\delta/2-w)}+A_7e^{-h_3(x-\delta/2-w)} & \delta/2+w\leq x\leq 3\delta/2+w \\ A_2\cos h_2(x-\delta/2)+A_3\sin h_2(x-\delta/2) & \delta/2\leq x\leq \delta/2+w \\ A_1\cos(h_1x) & -\delta/2\leq x\leq \delta/2 \\ A_4\cos h_2(x+\delta/2)+A_5\sin h_2(x+\delta/2) & -\delta/2-w\leq x\leq -\delta/2 \\ A_8e^{-h_3(x+\delta/2+w)}+A_9e^{-h_3(x+\delta/2+w)} & -3\delta/2-w\leq x\leq -\delta/2-w \\ A_{10}e^{-h_4(x+3\delta/2+w)} & x\leq -3\delta/2-w \end{cases} \quad (3\text{-}4),$$

where A_1 ~ A_{10} are unsolved mode coefficients in different regions, $h_1=(\varepsilon_g k_0^2-\beta^2)^{1/2}$, $h_2=(\varepsilon_1 k_0^2-\beta^2)^{1/2}$, $h_3=(\beta^2-\varepsilon_g k_0^2)^{1/2}$, and $h_4=(\beta^2-\varepsilon_2 k_0^2)^{1/2}$. The wave vector in vacuum is $k_0=2\pi/\lambda$. ε_g, ε_1 or ε_2 is relative permittivity of graphene (ε_g = $i\sigma_g/\omega\varepsilon_0\delta$), insulator slab or the outside air, respectively. According to Eq. (3-4), the longitudinal magnetic field of the modes is derived by using $H_z(x)=\frac{j}{\omega\mu}\frac{\partial}{\partial x}E_y(x)$. Based on the continuities of tangential field components at the interfaces, the dispersion equation is further derived as follows [138]:

$$\tan(h_1\delta / 2) = \frac{P_1 + P_2}{P_3 + P_4} \qquad (3\text{-}5),$$

where $P_1 = [1 + \frac{h_2}{h_3}\tan(h_2 w) - \frac{h_3}{h_4} - \frac{h_2}{h_4}\tan(h_2 w)]e^{-h_3\delta}$, $P_2 = [1 - \frac{h_2}{h_3}\tan(h_2 w) + \frac{h_3}{h_4} - \frac{h_2}{h_4}\tan(h_2 w)]e^{h_3\delta}$, $P_3 = [-\frac{h_3}{h_4}\frac{h_1}{h_2}\tan(h_2 w) + \frac{h_1}{h_4} + \frac{h_1}{h_2}\tan(h_2 w) - \frac{h_1}{h_3}]e^{-h_3\delta}$, and $P_4 = [\frac{h_3}{h_4}\frac{h_1}{h_2}\tan(h_2 w) + \frac{h_1}{h_4} + \frac{h_1}{h_2}\tan(h_2 w) + \frac{h_1}{h_3}]e^{h_3\delta}$.

However, in this modulator, both TE mode and TM mode may be stimulated. These two kinds of modes have totally orthogonality electric and magnetic field polarity. In order to stimulate pure TE mode in experimental system, we only need to set the optical laser source to make sure the mode electric polarity is in the plane of the waveguide in y-axis direction. In this way, the TM mode will be forbidden for the totally orthogonality polarity.

3.3 Results and discussions

3.3.1 Physics of the mode

Firstly, I choose Aluminum Oxide (ε_1 = 3.06 at λ = 1.55 μm) as the insulator material. When w = 100 nm, I calculate Eq. (3-5) and get the MPA (α) and effective refractive index (N_{eff}) of the mode as a function of μ_c (the chemical potential of each side graphene layer) at λ = 1.55 μm, as shown in Fig. 3.2.

The figure shows that the MPA has two abrupt turn points. The first turn point happens at 0.2835 eV: the MPA changes from 0.453 dB/μm to 0.274 dB/μm causing a normalized modulation depth $\Delta\alpha$ of 0.179 dB/μm. At this point, the chemical potential of the middle graphene layer is 0.401 eV, which is exactly half of the photon energy.

Before this point the interband absorption of both the middle graphene layer and two side graphene layers happens, the MPA is very high. After this point the absorption of the middle layer turns to intraband absorption which causes the first modulation depth. So the first modulation depth is caused by the middle graphene layer, which is 0.179

dB/μm.

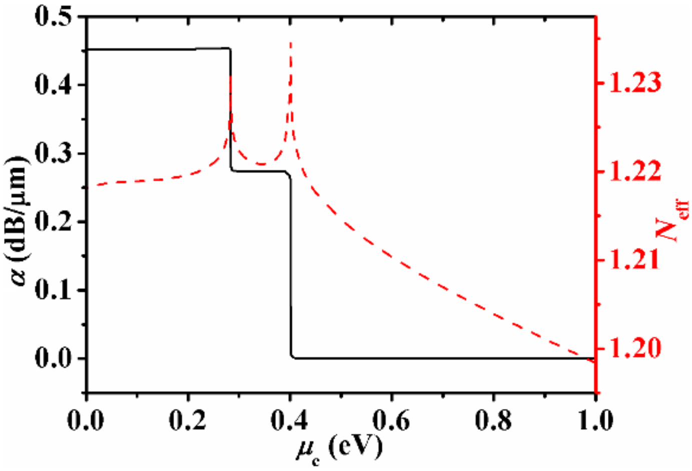

Fig. 3.2 MPA (black line) and mode index (red dash line) of TE mode in the suspended triple-layer graphene modulator as a function of chemical potential μ_c of the side graphene layers.

The second turn point happens at 0.401 eV: the MPA changes from 0.274 dB/μm to 0.0005 dB/μm causing a normalized modulation depth of 0.274 dB/μm. This modulation depth is caused by the two side layers which I call as modulation depth 1 ($\Delta\alpha_1$). Modulation depth 1 is larger than the first modulation depth, which is because both the two side layers turn from interband absorption to intraband absorption. There is a total normalized modulation depth which is 0.453 dB/μm, I call it as modulation depth 2 ($\Delta\alpha_2$).

There are two peaks for effective refractive index (N_{eff}) which happen at exactly the two MPA turn points respectively. The maximum ΔN_{eff} is 0.036. Both the modulation depths and ΔN_{eff} are much better than those of the self-biasing case [143] which I have discussed in the former chapter.

I get both modulation depth 1 and 2 as a function of the insulator thickness w, as shown in Fig. 3.3 (a). The changing law of modulation depth to w is similar as that of the self-biasing graphene modulator. There are $\Delta\alpha$ peaks happening at the optimized insulator thickness w_{opt}, which shows the highest light-graphene interaction. The maximum $\Delta\alpha_1$ are 0.286 dB/μm, 0.506 dB/μm, 0.539 dB/μm, and the corresponding w_{opt1} are

77.8 nm, 20.9 nm, 16.5 nm, for ε_1 = 3.06, 16 (a possible middle value at wavelength 1.55 μm), 22 (permittivity of Ta_2O_5 at wavelength 1.55 μm), respectively. The maximum $\Delta\alpha_2$ are 0.460 dB/μm, 0.786 dB/μm, 0.834 dB/μm, and the corresponding w_{opt2} are 85.6 nm, 22.4 nm, 17.6 nm, for ε_1 = 3.06, 16, 22, respectively. The highest modulation depth (0.834 dB/μm) is much higher than that of the self-biasing graphene modulator which is only 0.54 dB/μm [143] at the same conditions. Therefore, the 3-dB footprint of this modulator will be only 0.26 μm (half-maximum width of the mode profile) × 3.597 μm (3 dB/(0.834 dB/ μm)) = 0.94 μm^2.

The maximum values of $\Delta\alpha_1$ and $\Delta\alpha_2$ and the corresponding w_{opt1} and w_{opt2} are gotten as a function of ε_1, as shown in Fig. 3.3 (b). These two modulation depths increase monotonously as ε_1 increases. w_{opt1} and w_{opt2} decrease monotonously as ε_1 increases. And w_{opt2} is always slightly larger than w_{opt1}. When ε_1 = 22, I find w_{opt1} = 16.5 nm and w_{opt2} = 17.6 nm.

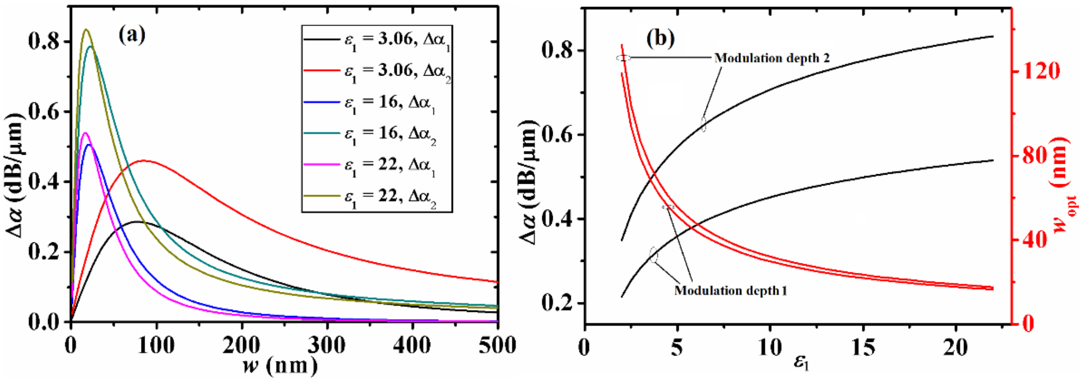

Fig. 3.3 (a) Modulation depths (both $\Delta\alpha_1$ and $\Delta\alpha_2$) change as a function of insulator thickness w at λ =1.55 μm for different dielectric: ε_1 = 3.06, 16, and 22, respectively. (b) The highest modulation depth (black line) for different insulator permittivity ε_1 and the corresponding optimized dielectric thickness (red line) for both modulation depth 1 and 2, respectively.

For TE mode, the electric field E_y is in the plane of graphene, so the amplitude of E_y which interacts with graphene will determine the interaction strength of one photon, and the confinement of the mode will determine the photon number which interact with graphene. I have obtained the normalized mode profile as a function of vertical axis x when

$\varepsilon_1 = 22$, and $w = 17$ nm (w_{opt}), 5 nm, and 50 nm, as shown in Fig. 3.4 (a).

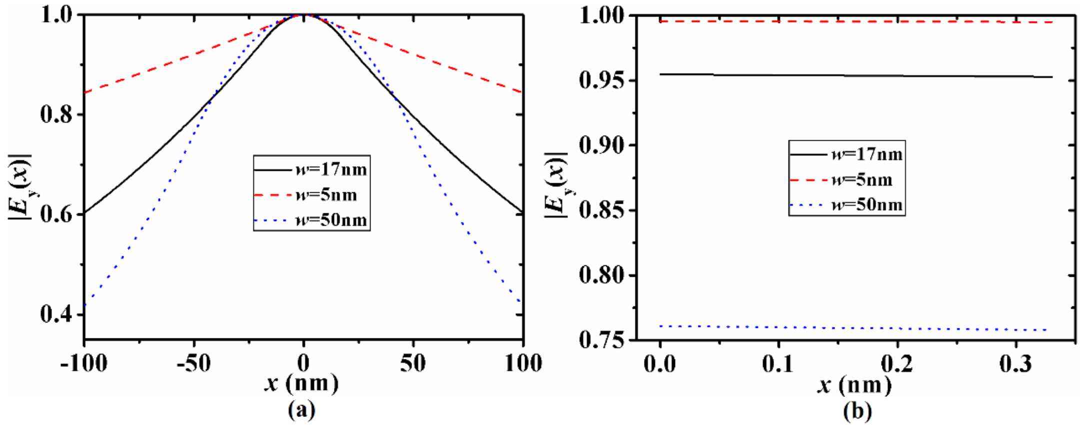

Fig. 3.4 (a) Mode profile as a function of coordinate x when $\mu_c = 0.3$ eV at $\lambda = 1.55$ m, $\varepsilon_1 = 22$, and $w = 17$ nm (black line), 5 nm (red dashed line) and 50 nm (blue dotted line). (b) The corresponding mode amplitude in the side graphene layers.

The mode confinement increases when w is changing from 5 nm to 50 nm. So the interaction photon number with graphene will increase as w is changing from 5 nm to 50 nm. After my calculation, I find that the mode amplitude in the middle graphene layer is always 1. Therefore, the mode confinement will determine the light-graphene interaction for the middle graphene layer. This is why w_{opt2} is always slightly larger than w_{opt1} (modulation depth 2 is caused by the middle graphene layer).

I also get the mode amplitude in each of the two side graphene layers, as shown in Fig. 3.4 (b). We can see that as w increases, the mode amplitude in the side graphene layers decreases (it is 0.995, 0.954 and 0.760 for $w = 5$ nm, 17 nm and 50 nm, respectively). So there is a trade-off between mode confinement and mode amplitude in graphene to realize the highest light-graphene interaction. For different insulator materials, I also have found that when the permittivity is higher, the mode confinement is absolutely better and the mode amplitude in graphene is also larger. Therefore, high-κ materials [60] are absolutely better for higher light-graphene interaction.

3.3.2 Modulation performance

I have obtained the mode power transmittance spectrum of the modulator at chemical potentials of 0.3 eV, 0.4 eV and 0.5 eV, with a propagation length of $L = 5$ μm when $\varepsilon_1 = 22$, $w_{\text{opt}} = 17$ nm, as shown in Fig. 3.5.

From Fig. 3.5, we can see there are two sharp changes of the transmittance for each chemical potential. The first one happens at $\lambda = \pi\hbar c/\mu_c$, the second happens at $\lambda = \pi\hbar c/2^{0.5}\mu_c$, both of which are at the two MPA turn points, respectively. This will be very important for two signal modulation for controlling the modulation depth.

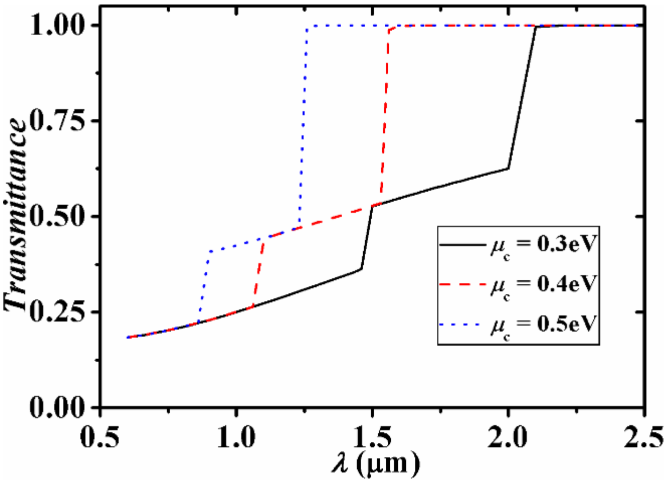

Fig. 3.5 Mode power transmittance of the modulator as a function of incident wavelength when $\mu_c = 0.3$ eV (black line), 0.4 eV (red dashed line) and 0.5 eV (blue dotted line).

After 5 μm propagating, a modulation depth of 61.66% can be achieved at $\lambda = 1.55$ μm. The insertion loss can be calculated as:

$$\alpha = -10\text{Log}[T_{\max}] \quad (3\text{-}6)$$

And the figure of merit (FOM) can be expressed as:

$$\text{FOM} = \Delta\alpha / \alpha \quad (3\text{-}7)$$

I get an insertion loss of only 0.00166 dB ($T_{\max} = 0.999618$), and the FOM of this modulator is also ultrahigh ~ 1265.

After calculation, I find that the highest ΔN_{eff} happens at $\varepsilon_1 = 22$, $w_{\text{opt}} = 17$ nm can be 0.0685, which is much larger than the state-of-the-art value of 0.043 [143]. Therefore, the π-phase shift arm length for this kind of M-Z modulator can be only 11.3 μm, which is much lower than the value of 18.0 μm [143]. For the M-Z modulator, I make the side-layer chemical potential of the reference arm fixed at μ_c = 1.0 eV and add voltage signal on the modulation arm. The side-layer chemical potential of the modulation arm can be changed from 0.2 eV to 1 eV. The normalized power transmittance $T(\Delta\mu_c)$ of this M-Z modulator can be expressed by Eq. (1-16) and Eq. (2-3). I calculate Eq. (1-16) or Eq. (2-3) when L = 12 μm (one π-phase shift), 34 μm (three π-phase shifts), 68 μm (six π-phase shifts), and plot the transmittance $T(\Delta\mu_c)$ of this M-Z modulator in Fig. 3.6.

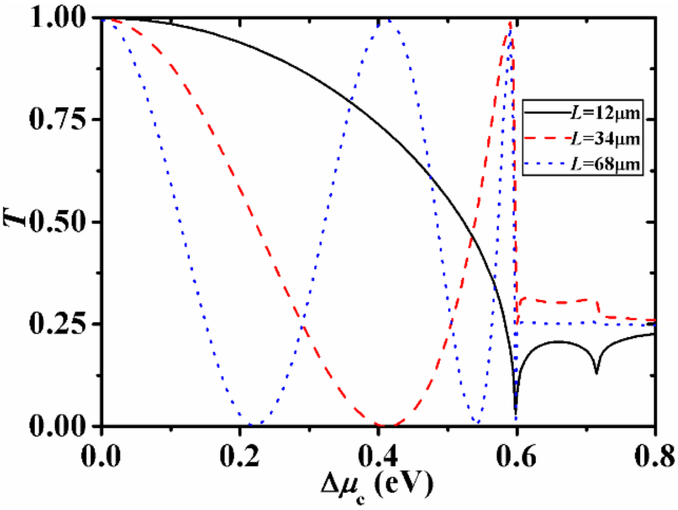

Fig. 3.6 Transmittance of the M-Z modulator as a function of the difference of the side-layer chemical potential ($\Delta\mu_c$) between two arms when L = 12 μm (black line), 34 μm (red dashed line), and 68 μm (blue dotted line).

From Fig. 3.6, we can see when $\Delta\mu_c$ is lower than 0.6 eV, there is one 100% modulation for L = 12 μm, two 100% modulations for L = 34 μm, three 100% modulations for L = 68 μm. These 100% modulations are caused by the two side graphene layers which cause the second N_{eff} peak as shown in Fig. 3.2. For this ΔN_{eff}, the insertion loss is low for it is modulation depth 1 (after this point all the three graphene layers will only cause intraband absorption) which is in operation. The waveguide maximum allowed length $L_{\max}$ ($L_{\max} = 1/\alpha$) is much longer (on the scale of ~ cm), and there is surely always enough energy at the output port.

We can also see that when $\Delta\mu_c$ is larger than 0.6 eV, there is no 100%

modulation, and the output energy is much lower. This is because now it is modulation depth 2 (after this point only the middle graphene layer will only cause intraband absorption) which is in operation, and the insertion loss is very high (α = 0.539 dB/μm), and L_{max} = 1/α = 1.86 μm is very low. The choosing of L > 1.86 μm makes almost no energy can get out from the modulation arm, and only the reference arm can put out energy which is 25% of the total energy. The small nadir in this region when L = 12 μm is caused by the first N_{eff} peak.

The 3-dB modulation bandwidth can be calculated by Eq. (3-3), where R is the total resistance caused by one graphene layer. According to reference [143], I choose R = 165 Ω is reasonable. $C = \varepsilon_1\varepsilon_0 S/w$ is one capacitance of the active area of the modulator. Here I choose that S = 0.5 μm × 5 μm = 2.5 μm^2, where 0.5 μm is the width of the modulator in y-axis, 5 μm is the length of the modulator. So the capacitance is C = 28.63 fF for ε_1 = 22, w_{opt} = 17 nm, then a 3-dB modulation bandwidth of 22.46 GHz is obtained, which is larger than that of reference [143] (16.45 GHz). I find that the modulation bandwidth can be 759.85 GHz for ε_1 = 3.06 (Al_2O_3), w_{opt} = 80 nm, which is much larger than 559.2 GHz reported in [143].

The side-layer chemical potential μ_c can be tuned by applying voltage V_g [141]. I also choose an average Fermi velocity of $v_F = 1.5\times10^6$ m/s. When the chemical potential is changing from -1 eV to 1 eV, I calculate Eq. (2-6) and obtain the applied voltage as a function of side-layer chemical potential μ_c, as shown in Fig. 3.7 (a).

We can see the applied voltage is always smaller than 2.3 V for ε_1 = 22, w_{opt} =17 nm when the chemical potential is changing from -1eV to 1eV. For ε_1 = 10, w_{opt} = 30 nm, the applied voltage should be larger (< 9.0 V).

I also have obtained the optimized ($w = w_{opt}$) applied voltage and the corresponding energy consumption as a function of insulator permittivity ε_1 when μ_c = 0.3 eV, as shown in Fig. 3.7 (b). It shows that the optimized voltage and energy consumption will be smaller when the permittivity is larger. The applied voltage is on the scale of 0.2 V ~ 2.8 V, and the energy consumption is on the scale of 0.61 fJ/bit ~ 8.3 fJ/bit when ε_1 is changing from 22 to 5. The energy consumption is lower than the values (larger than 1.23 fJ/bit) reported in my former work [143].

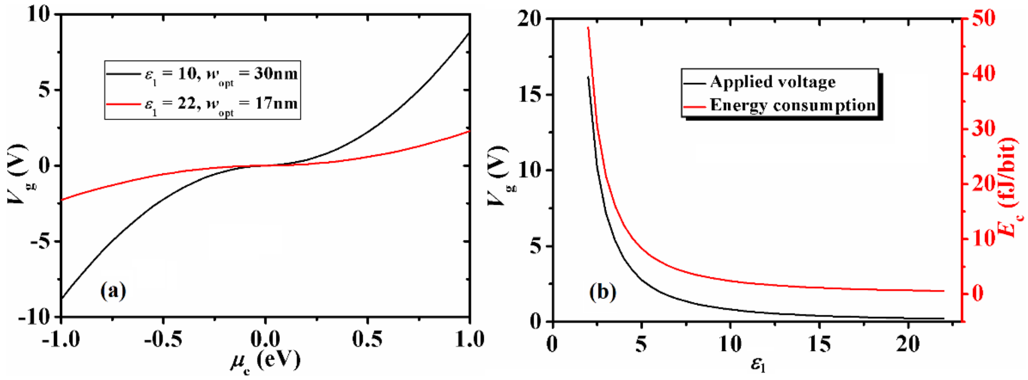

Fig. 3.7 (a) Applied voltage as a function of side-layer chemical potential μ_c: black line: ε_1 = 10, w_{opt} = 30 nm, red line: ε_1 = 22, w_{opt} = 17 nm; (b) Applied voltage and corresponding energy consumption as a function of permittivity ε_1 of the insulator when w is at w_{opt} and μ_c = 0.3 eV.

3.3.3 Full-wave simulation by COMSOL

My results have been compared by full-wave simulation using commercial software (COMSOL). In the simulation, I set ε_1 = 22, the thickness of graphene is 0.33 nm, double of insulator thickness is h_core = 0.034 μm with a solving area of h_cladding = 2 μm and L = 5 μm. The mode profile in the longitudinal transmission direction is obtained, as shown in Fig. 3.8. We can see the decay of the mode amplitude is negligible for λ = 2.5 μm and μ_c = 0.3 eV, however it is significant for λ = 0.6 μm and μ_c = 0.3 eV.

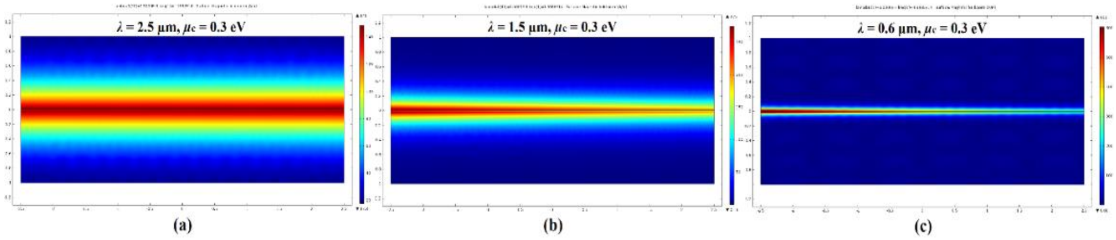

Fig. 3.8 Mode profile in the longitudinal transmission direction at different wavelength: λ = 2.5 μm (a), λ = 1.5 μm (b), λ = 0.6 μm (c) when ε_1 = 22, μ_c = 0.3 eV. Simulated by COMSOL.

I also retrieve the scattering parameter S_{21} as a function of the carrier wavelength, as shown in Fig. 3.9.

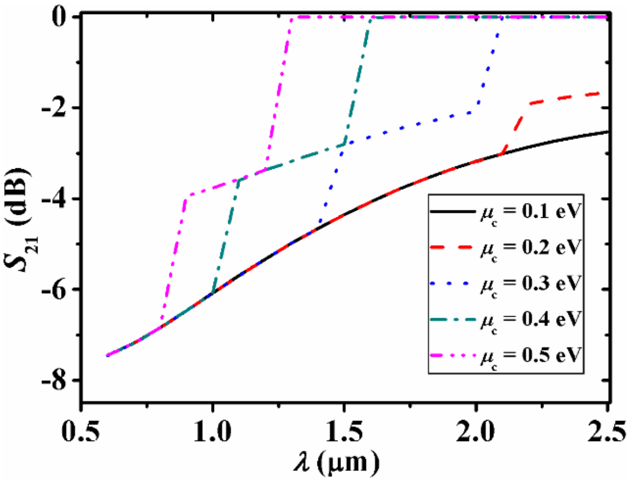

Fig. 3.9 Scattering parameter S_{21} as a function of wavelength at μ_c = 0.1 eV (black solid line), 0.2 eV (red dashed line), 0.3 eV (blue dotted line), 0.4 eV (green dashed dotted line), and 0.5 eV (pink dashed dotted dotted line). Simulated by COMSOL.

By comparing Figs. 3.9 and 3.5, we can see the results obtained from these two different methods are matched exactly well for μ_c = 0.3 eV, 0.4 eV and 0.5 eV. The difference from S_{21} and the transmittance T is only 0.001. S_{21} is slightly larger, because of the small reflection which has been considered in the COMSOL simulation. In this case the insertion loss is of ~ 0.002 dB. I also get S_{21} when μ_c = 0.1 eV, and 0.2 eV. There is no abrupt turn point for μ_c = 0.1 eV and only one for μ_c = 0.2 eV, because the considered wavelength scale is only up to 2.5 μm whose photon energy is 0.50 eV. The total modulation depth at λ = 1.55 μm is 4.21 dB, and we can achieve a FOM of 2105. This value is much larger than the value by calculation, because here I have considered the S_{21} of μ_c = 0.1 eV, and 0.2 eV which will cause modulation depth 2 (happen at μ_c = 0.2835 eV when λ = 1.55 μm).

3.4 Summary

In this chapter, a suspended triple-layer graphene modulator is discussed and reported for the first time. The model structure and corresponding physics are analyzed. There appear two modulation depths for electro-absorption modulation. After my design, the total modulation depth can be 0.834 dB/μm and a 3-dB footprint is only 0.94 μm^2. The light-graphene interaction will be enhanced at the optimized insulator thickness w_{opt} and the mechanism is analyzed by the mode field distribution in the waveguide. For electro-refractive modulation, I have achieved a very high (highest up to date) change of mode index (ΔN_{eff}) of 0.0685 causing a π-phase shift length of only 11.3 μm. Several 100% modulations are found in the M-Z modulator. The most sounding result is that I predict a very high modulation speed of as high as 759.85 GHz, while the switch energy can be as low as 0.61 fJ/bit with low applied voltage (< 9.0 V). The simulation by COMSOL is also conducted as a comparison, which has very good agreement with my calculation results. Moreover, the FOM of this modulator can be 2105. I believe these results are very useful for designing graphene-based devices.

Chapter 4

Suspended Graphene Double-layer Modulator and Sub-wavelength Thickness Modulator

In this chapter, a comparison between graphene suspended double-layer modulator (SDM) and sub-wavelength thickness modulator (STM) is presented. The physics of both are analyzed in detail which show a confined mode in suspended modulator but a leaky mode in sub-wavelength modulator. The leaky mode shows zero light-matter interaction and zero modulation depth which should be avoided in designing. The suspended modulator can achieve much lower insertion loss and extraordinary higher figure of merit (FOM) (~ 2480) than sub-wavelength modulator. Both are with high modulation efficiency and comparable modulation speed. I believe these designs will pave the way to realize high-efficiency, near-fundamental-limits graphene modulators.

4.1 Introduction

A suspended self-biasing [143] and a suspended triple-layer [145] graphene modulator were discussed in previous chapters. These two modulators are designed to get much higher light-graphene interaction, and the design is much near the fundamental limits of graphene. The figure of merit (FOM, defined as the ratio of modulation depth to insertion loss) of both are the highest up to date theoretically. And the compromise between modulation speed and modulation efficiency is reduced significantly. These good results are contributed by the suspended structure and the design-free light-matter interaction. However, in these much better graphene modulators, the applied voltage is still higher than no-suspending modulators and a comparison between suspending and no-suspending ones need to be done.

The suspended graphene-on-silicon slot waveguides [104] have been used as electro-optic modulators. They use the slot to confine the mode to enhance the light-graphene interaction. To the best of my knowledge, this is the first suspended graphene modulator. Even though the light-graphene interaction has been enhanced, the change of the mode index (ΔN_{eff}) is still very low, only 0.0161, which causes a very large π-shift length for Mach-Zehnder (M-Z) modulator. Moreover, their fabrication will be very difficult.

And the reflecting sub-wavelength thickness graphene modulators are researched by several papers [53]. But the light-graphene interaction is very low for the interaction thickness is only a monolayer graphene. Moreover, the waveguide-based sub-wavelength thickness graphene modulator is still not researched particularly in detail.

In this chapter, I report two kinds of new graphene modulators, the graphene suspended double-layer modulator (SDM) and sub-wavelength thickness modulator (STM). In section 4.2, the physics of these two modulators are analyzed and compared. The insertion loss is much higher for sub-wavelength one and the figure of merit is very low. However, the modulation depth is comparable in these two cases. There shows a leaky mode for sub-wavelength one where zero modulation depth happens. The field is totally leaky and no light-matter interaction happens at that point which should be avoided. However, the suspended one shows near fundamental limits design. In section 4.3, I show the modulation performance and the modulation efficiency and get a conclusion. The FOM of suspended one can be ~ 2480, while that of sub-wavelength one is only 1.28. The modulation efficiency is 0.792 dB/V and 0.456 dB/V, and the corresponding modulation speed is 54.85 GHz and 61.39 GHz, for suspended one and sub-wavelength one, respectively. I believe these results are very important to realize much better graphene modulators.

4.2 Mode physics

The structure of graphene suspended double-layer modulator (SDM) is shown in Fig. 4.1 (a): the active area has seven layers in x-axis direction, the double graphene layers are transferred under or on the insulator with a thickness of t = 7 nm and a permittivity of ε_2 = 3.06 (permittivity of Al_2O_3 at λ = 1.55 μm), in the middle, a transferred silicon slab with a thickness of w and a permittivity of ε_1 = 11.7 is used to confine the mode and as an electric pole to add voltage between silicon and the two side graphene layers. The fabrication is much easier than the suspended self-biasing [143] and triple-layer [145] graphene modulators.

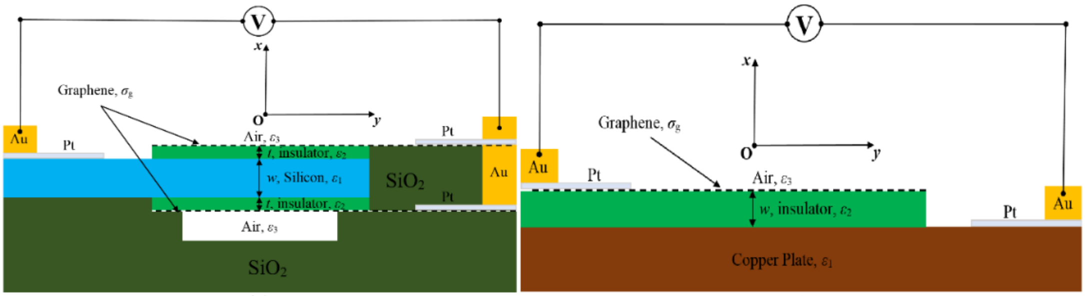

(a) (b)

Fig. 4.1 Structures of graphene suspended double-layer modulator (a) and sub-wavelength thickness graphene modulator (b).

Fig. 4.1 (b) shows the structure of graphene sub-wavelength thickness modulator (STM): an insulator with thickness w and permittivity of ε_2 = 22 is transferred on the copper plate (ε_1 by Drude model), the graphene layer is transferred on the top, the voltage is applied between the upper graphene layer and the bottom copper plate. The fabrication is much easier and have been demonstrated [53].

The methodology here is to derive the mode field equations and dispersion equations using Maxwell theory and Helmholtz equation, this is the well-known two-dimensional analysis [144]. For suspended double-layer modulator, it is a symmetrical seven-layer structure, the boundary condition makes seven mode field distribution equations and the corresponding dispersion equation for TE mode have been derived and used in reference [145]. For sub-wavelength thickness modulator, it has an asymmetrical four-layer structure. For TE mode, its mode field distribution equation can be written as:

$$E_y(x)=\begin{cases} A[(\cos h_2w+\frac{h_1}{h_2}\sin h_2w)\cos h_3\delta-(\frac{h_2}{h_3}\sin h_2w-\frac{h_1}{h_3}\cos h_2w)\sin h_3\delta]e^{-h_4(x-w-\delta)} & x\geq w+\delta \\ A[(\cos h_2w+\frac{h_1}{h_2}\sin h_2w)\cos h_3(x-w)-(\frac{h_2}{h_3}\sin h_2w-\frac{h_1}{h_3}\cos h_2w)\sin h_3(x-w)] & w\leq x\leq w+\delta \\ A[\cos h_2x+\frac{h_1}{h_2}\sin h_2x] & 0\leq x\leq w \\ Ae^{h_1x} & x\leq 0 \end{cases} \quad (4\text{-}1)$$

The corresponding dispersion equation can be derived as:

$$\tan h_2w=\frac{h_4+h_1+(\frac{h_4h_1}{h_3}-h_3)\tan h_3\delta}{(\frac{h_3h_1}{h_2}+\frac{h_4h_2}{h_3})\tan h_3\delta+h_2-\frac{h_4h_1}{h_2}} \quad (4\text{-}2),$$

where $h_1=(\beta^2-\varepsilon_1k^2)^{1/2}$, $h_2=(\varepsilon_2k^2-\beta^2)^{1/2}$, $h_3=(\varepsilon_gk^2-\beta^2)^{1/2}$, $h_4=(\beta^2-\varepsilon_3k^2)^{1/2}$; $\beta=\beta_1-j*\beta_2$ is the complex variable, in which the real part β_1 is related to the effective refractive index ($N_{\mathrm{eff}}=\beta_1/\mathrm{k}$) and the imaginary part β_2 is the amplitude loss coefficient of the guiding mode. $k=2\pi/\lambda$ is the wave vector in vacuum. ε_g is the permittivity of graphene. $\delta=0.33$ nm is the thickness of graphene.

Fig. 4.2 shows the mode power attenuation (MPA, $\alpha=20\beta_2*\log_{10}(\mathrm{e})$) (black solid line) as a function of chemical potential (μ_c) of graphene: (a) is the MPA of SDM at the condition of $w=100$ nm, $t=7$ nm, the inset shows the normalized modulation depth as a function of silicon thickness w when $t=7$ nm; (b) is the MPA of STM at the condition of $w=100$ nm; both are at the wavelength $\lambda = 1.55$ μm.

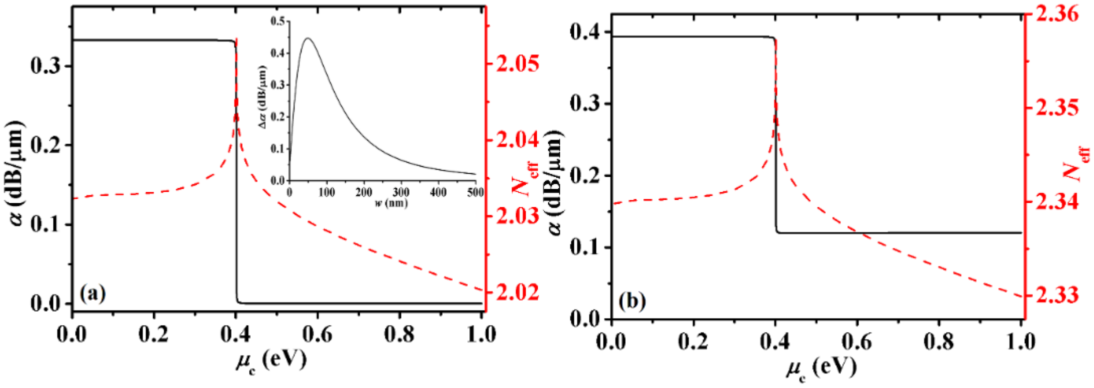

Fig. 4.2 MPA α (black solid line) and effective refractive index N_{eff} (red dashed line) of SDM (a) and STM (b) as a function of chemical potential μ_c of graphene. The inset shows the normalized modulation depth of SDM as a function of silicon thickness w.

Both cases show an on-state MPA (α_{on}), an off-state MPA (α_{off}) and a modulation depth of $\alpha_{\text{off}} - \alpha_{\text{on}}$. For SDM, the α_{on} is very low which is in the scale of 0.0002 dB/μm, causing a modulation depth of 0.333 dB/μm. However, for STM, the α_{on} is very high (~ 0.12 dB/μm), and the modulation depth is 0.274 dB/μm. The basic loss is caused by the metal plate. The modulation depth of SDM is larger because two graphene layers cause larger light-graphene interaction.

The effective refractive index (N_{eff}) of the corresponding mode is also gotten as shown in Fig. 4.2, the red dashed line. At the half photon energy point, there is an index peak, causing a change of N_{eff} (ΔN_{eff}) of 0.0335 (SDM) and 0.0276 (STM). This is very useful for Mach-Zehnder (M-Z) modulator. We can know even though the STM only has one graphene layer to interact with the light, the modulation depth and the change of N_{eff} is only slightly lower than those of SDM which has two interacting graphene layers. This is because I use Ta_2O_5 ($\varepsilon_2 = 22$ at $\lambda = 1.55$ μm), a high-κ material, as the insulator for STM. The high-κ material will enhance the light-graphene interaction and confine the mode. However, silicon can only confine the mode in SDM, and its permittivity is only 11.7.

From the inset in Fig. 4.2 (a), we can see there is an optimized w (w_{opt})

for the highest modulation depth, namely the highest light-graphene interaction. At $w_{opt} = 48.8$ nm, the highest modulation depth can be 0.4474 dB/μm and the corresponding highest ΔN_{eff} can be 0.0451. In order to get the modulation depth of STM as a function of insulator thickness w, I calculate Eq. (4-2) and get the off-state MPA and on-state MPA as a function of w, as shown in Fig. 4.3 (a).

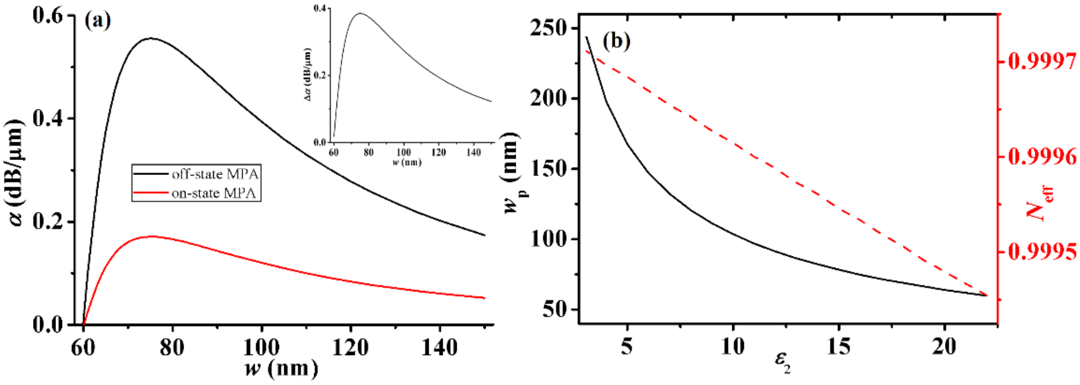

Fig. 4.3 (a) Off-state MPA and on-state MPA of STM as function of insulator thickness w, the inset shows the corresponding modulation depth α_{off} - α_{on}; (b) Position w_p of the leaky mode as a function of the permittivity ε_2 of the insulator material (black solid line) and the corresponding effective refractive index (N_{eff}).

The on-state loss is almost all caused by the copper plate, because on this state, the graphene only causes intraband absorption which is negligible compared with the Ohmic loss of the metal plate. However, the modulation depth is only caused by the graphene layer. From the inset, we can see at $w_{opt} = 75.1$ nm, the highest modulation depth is 0.385 dB/μm and the corresponding highest ΔN_{eff} can be 0.0387. We can also see when $w < 60$ nm, this mode is forbidden. At $w = 60$ nm, the modulator causes zero off-state MPA and on-state MPA and zero modulation depth. The mode here is totally leaky and cannot be guided on the waveguide effectively. This leaky mode has been found in reference [93]. I get the leaky mode position (the thickness of insulator w_p) as a function of permittivity (ε_2) of the insulator material, as shown in Fig. 4.3 (b). As ε_2 decreases, the w_p increases. We should know when $w < w_p$, this mode is forbidden, other modes may replace. So, for single mode stimulation, we should avoid this leaky mode. w_p = 243.76 nm when ε_2 = 3.06. I also get the corresponding N_{eff}, as shown the red dashed line in Fig. 4.3 (b). The effective indices of all the leaky mode is below 1, which shows no light-matter interaction because all the energy is distributed in the outside air.

In order to get a better knowledge of the mode discussed above, I calculate the mode field distribution of both SDM and STM, as shown in Fig. 4.4.

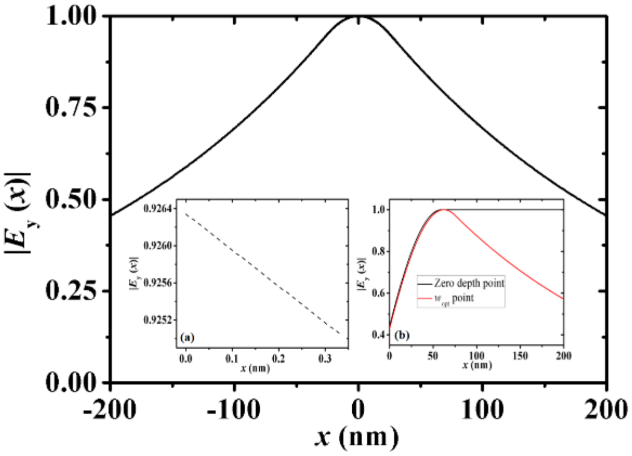

Fig. 4.4 Normalized mode field distribution as a function of x-axis of SDM when w_{opt} = 48.8 nm. Inset (a) shows the mode amplitude in the corresponding graphene layer of SDM. Inset (b) shows the mode field distribution of STM at zero depth point (w_p = 60 nm, black line) and w_{opt} = 75.1 nm point (red line).

The mode field distribution and light-graphene interaction of SDM is similar as the reported suspended self-biasing [143] and triple-layer [145] graphene modulators. For STM, at w_p = 60 nm, the field is maximum and has no decay in the infinity outside air, which tells us there is no light-matter interaction in the waveguide. However, at w_{opt}, the decay is significant in the outside air. For this case, the amplitude peak point (normalized to 1) happens at w = 62.3 nm, however, the graphene layer is put at w_{opt} = 75.1 nm, where the amplitude is 0.973. After my calculation, I find when w is smaller than w_{opt}, the confinement of the mode is much worse, when w is larger than w_{opt}, the amplitude in graphene layer is much lower. Therefore, I enhance the light-graphene interaction to the most at w_{opt}.

4.3 Discussions and conclusions

The mode power transmittance and the modulation performance are gotten as a function of carrier wavelength according to $T(\lambda) = \mathrm{Exp}[\alpha L]$ when $L = 10$ μm is the modulator length, as shown in Fig. 4.5.

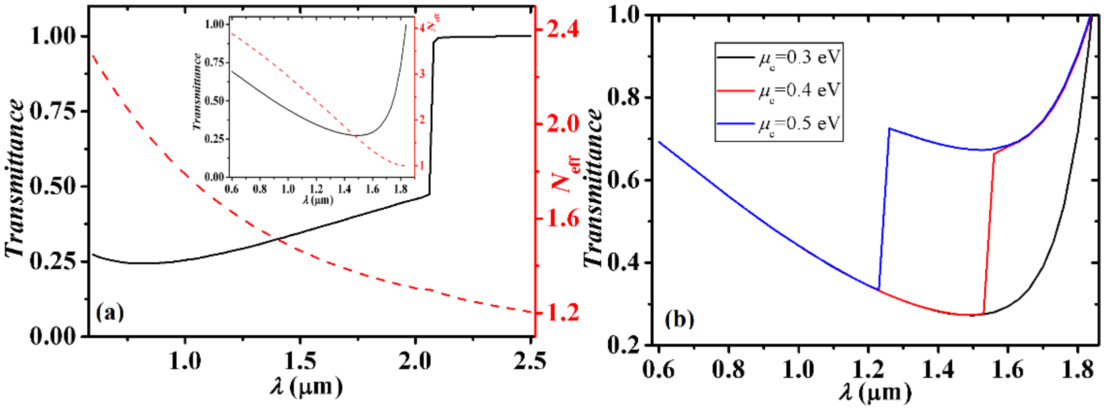

Fig. 4.5 (a) is the transmittance of SDM at the condition of $w_{\mathrm{opt}} = 48.8$ nm, $\mu_c = 0.3$ eV, the inset shows the transmittance of STM at the condition of $w_{\mathrm{opt}} = 75.1$ nm, $\mu_c = 0.1$ eV, the red dashed line is the corresponding effective refractive index of the mode; (b) is the transmittance of STM at the condition of $w_{\mathrm{opt}} = 75.1$ nm, $\mu_c = 0.3$ eV (black), 0.4 eV (red) and 0.5 eV (blue).

As clear in Fig. 4.5 (a), the transmittance of SDM is similar as [143,145]. Here we can get a modulation depth of 75.61% and an insertion loss α of 0.00247 dB ($T_{\max} = 0.999432$), with a FOM of ~ 2480, which is a comparable value as the reported one in reference [143,145]. For STM, performance shown in the inset of Fig. 4.5 (a), the mode is forbidden when $\lambda > 1.84$ μm. The transmittance is 1 at that forbidden point, however the modulation depth is zero there. From the red dashed line, we can know the mode is always a confined mode for SDM ($N_{\mathrm{eff}} > 1$), however the leaky mode appears when the wavelength come to the forbidden point ($N_{\mathrm{eff}} < 1$) for STM. We should avoid this forbidden point when design STM.

I calculate the transmittance of STM as a function of carrier wavelength λ at different chemical potential (μ_c), as shown in Fig. 4.5 (b). The forbidden point does not move for different μ_c, this is why the modulation depth is zero at that point. At the modulation wavelength as μ_c changes from 0.3 eV to 0.5 eV, we can get a modulation depth of 39.51% and an insertion loss of 1.704 dB ($T_{\max}$ = 0.6754), so the FOM is only 1.28, which is significantly below the FOM of the suspended one.

At last, I get the applied voltage of these two modulators, as shown in Fig. 4.6.

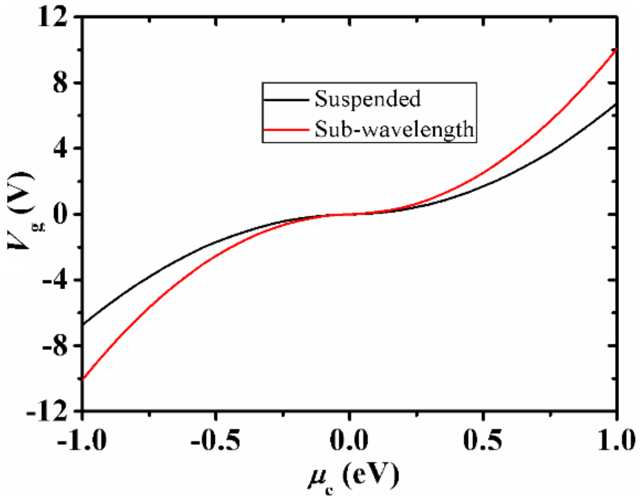

Fig. 4.6 Applied voltage of SDM (black line) and STM (red line) as a function of chemical potential (μ_c) of graphene, at the condition of insulator thickness t = 7 nm, ε_2 = 3.06 for black line, and w_{opt} = 75.1 nm and ε_2 = 22 for red line. The Fermi velocity is $v_F = 1.5\times10^6$ m/s.

The applied voltage is related to the modulation efficiency which is defined as [110]:

$$M = \frac{(\alpha_{\text{off}} - \alpha_{\text{on}}) * L}{V_{\text{on}} - V_{\text{off}}} \qquad (4\text{-}3),$$

where L = 10 μm is the length of the modulator, I choose V_{on} at μ_c = 1 eV, V_{off} at MPA abrupt turn point (namely 0.4 eV when λ = 1.55 μm). When the applied voltage is low, the switch energy will be lower and the modulation efficiency will be higher. According to Eq. (4-3), I get the modulation efficiency at this condition for SDM is M = 0.792 dB/V, for STM is M = 0.456 dB/V. However, at larger modulation efficiency, the modulation speed will be reduced for larger capacitance. The compromise between modulation speed and modulation efficiency is significantly reduced by my former work [143,145], and the design is very near the fundamental limits [39] of graphene. Here, the applied voltage of SDM is in the scale of < 7 V (< 11 V for STM) when chemical potential is changing from -1 eV to 1 eV. I consider the modulator width in y-direction is 0.5 μm, using total resistance R_1 = 150 Ω [143] for SDM and R_2 = 200 Ω for STM, I get the modulation speed of 54.85 GHz for SDM, and 61.39 GHz for STM.

In conclusion, I have researched two kinds of graphene modulators. For suspended double-layer modulator (SDM), the insertion loss is very low with an ultrahigh FOM. The physics of the modes are discussed by analyzing the MPA and the mode field distribution. For sub-wavelength thickness modulator (STM), I find the leaky mode which causes zero light-matter interaction and should be avoided when designing. The FOM of STM is very low for much larger insertion loss caused by the metal plate. Moreover, these two modulators have high modulation efficiency and comparable modulation speed. According to my knowledge, these modulators can also be fabricated by other 2D materials, such as black phosphorus. However, the mobility of other 2D material is much lower than graphene, so the modulation speed will be lower than that of graphene. And for their large band gap, their modulator operation bandwidth (the bandwidth of carrier waves) maybe narrower. I believe these results are very important for realizing practical graphene modulators and related devices.

Chapter 5

Metal-clad Suspended Self-biasing Graphene Modulator

In this chapter, a research on the metal-clad suspended self-biasing graphene modulator is conducted theoretically. The results reveal higher light-graphene interaction with smaller size of this modulator. In addition, when the light-graphene interaction is enhanced, the light-metal interaction is also stronger, which causes larger insertion loss and makes the FOM lower. The length of π-phase shift is reduced to 6.35 μm for this M-Z modulator which is the smallest size achieved up to date. The modulator's FOM can be tuned by changing the air gap (d) between the moveable metal plates and the suspended structure. In the case when this air gap increases, the configuration represents closer fundamental limits design. Moreover, the cut-off mode is discussed, and it has potential to be used in the tunable filter application. This tunable configuration of modulator is believed to have potential that can pave the way to design tunable light-matter interaction device and has evaluated for the near fundamental limits design.

5.1 Introduction

In this field, in order to realize near fundamental limits design, different modulator structures are put forward. The main purpose is to enhance the light-graphene interaction. Researchers have found that the symmetrical structure can make the mode with lower insertion loss and higher modulation depth, so the light-graphene interaction is enhanced further. The figure of merit (FOM) of graphene modulator is defined as the ratio of modulation depth to insertion loss. And the FOM can be an index of how the design is approaching the fundamental limits of graphene [39].

In my former work [143,145,146], I have reported the suspended graphene modulators which is already much near the fundamental limits of graphene [39]. The FOMs of these cases are in the order of 2000 and the compromise between modulation speed and modulation efficiency is reduced significantly. These results are contributed by that the devices are with much less residues on graphene sheets and the modes are symmetrical. However, the modulator which is between low-level design and near fundamental limits design is still a gap which should be addressed.

In this chapter, I show how near fundamental limits design happens. Here, a suspended self-biasing graphene modulator with tunable metal-cladding is researched. The light-graphene interaction is very complex and can be enhanced and tuned significantly by very small modulation size. The modulation depth and insertion loss are increasing with considered smaller modulation size. The FOM is changeable by different insulator thicknesses and tunable by moveable metal-cladding. However, when the modulation size is too small, the mode will be cut-off and the loss is huge. The trade-off between modulation depth and FOM is analyzed and the filter application by cut-off wavelength is also discussed. I find that when the air gap (d) between moveable metal-cladding and suspended structure is larger, the design is nearer fundamental limits of graphene. However, we can control the tunable light-graphene interaction by smaller air gap (d).

5.2 Results and discussions

The structure of metal-clad suspended self-biasing graphene modulator is shown in Fig. 5.1.

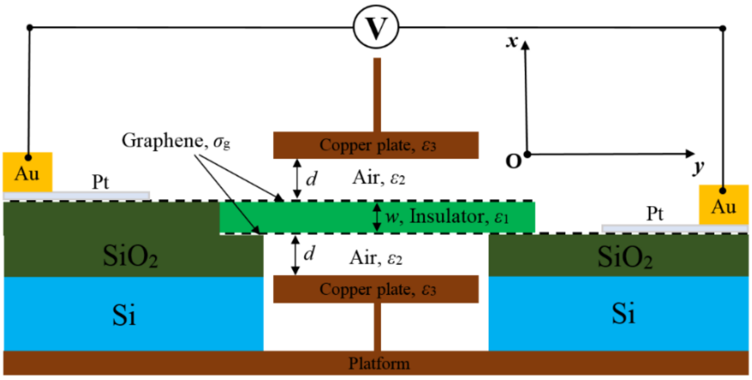

Fig. 5.1 Cross section schematic of the structure of metal-clad suspended self-biasing graphene modulator.

For this structure, two monolayer graphene sheets are sandwiched by an insulator slab (here Aluminum Oxide Al_2O_3, $\varepsilon_1 = 3.06$ at $\lambda = 1.55$ μm). These two graphene sheets are biased by each other and suspended in the air. Two moveable metal plates (here copper is adopted, the permittivity ε_3 is got from Drude model [147]) are cladding above or below both sides of the suspended structure.

The active area of the modulator includes seven layers: the moveable up and below metal plates (ε_3), the two air gaps (ε_2) with distance d shown in the figure, two graphene sheets (permittivity is $\varepsilon_g = i\sigma_g/\omega\varepsilon_0\delta$, where the surface conductivity σ_g is calculated from Kubo formula, $\delta = 0.33$ nm is the thickness of the monolayer graphene), and the middle insulator slab (Al_2O_3) with thickness w.

Here the air gap (d) between metal-cladding and the suspended structure is tunable by moving the metal plates. The according axis system is also shown in Fig. 5.1, the modulator width in y-direction is large enough for the beam width diffraction which doesn't have boundary condition and can be assumed to be the same as in free-space. The optical wave (here $\lambda = 1.55$ μm) incidents in z-direction which is perpendicular to *x*-*y* plane.

The methodology here is to derive the mode field equations and the dispersion equation of this symmetrical seven-layer structure for TE mode which has been used and discussed in detail in reference [145]. This is the well-known two-dimensional analysis [144].

Fig. 5.2 shows the mode power attenuation (MPA, α) as a function of chemical potential of graphene (μ_c) when insulator (Al_2O_3) slab thickness is w = 100 nm and air gap width is d = 500 nm (black solid line), 300 nm (red dashed line) or 250 nm (blue dotted line) at λ = 1.55 μm.

There shows an off-state MPA (α_{off}) and an on-state MPA (α_{on}) and a modulation depth of $\Delta\alpha = \alpha_{off} - \alpha_{on}$. At the absorption threshold point of graphene (μ_c = 0.4 eV here), the mode transfers from off-state to on-state when the chemical potential is slightly larger. This is because when the chemical potential is lower than half photon energy (0.4 eV for λ = 1.55 μm), the graphene causes interband absorption, otherwise, only intraband absorption happens which causes very small loss.

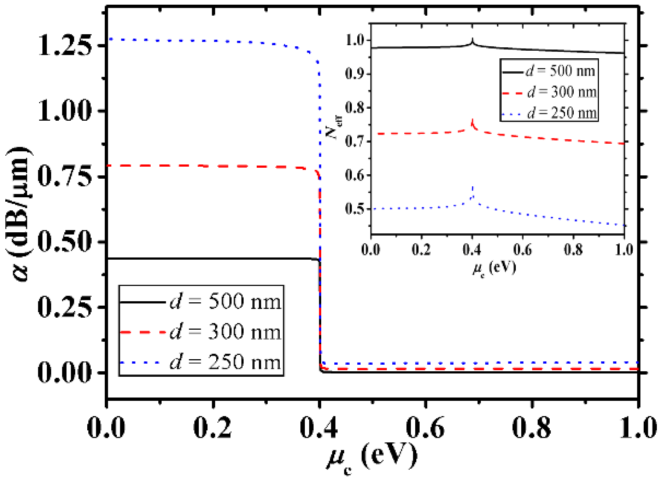

Fig. 5.2 MPA α of the modulator is gotten as a function of chemical potential μ_c when w = 100 nm and d = 500 nm (black solid line), 300 nm (red dashed line) and 250 nm (blue dotted line) at wavelength λ = 1.55 μm. The inset shows the corresponding effective refractive index (N_{eff}) of the mode as a function of μ_c.

Here, the insulator slab has a thickness of w = 100 nm. However, when the air gap width changes from d = 500 nm to d = 250 nm the modulation depth increase from 0.4339 dB/μm (α_{off} = 0.4368 dB/μm, α_{on} = 0.0029 dB/μm for d = 500 nm) to 1.2388 dB/μm (α_{off} = 1.2754 dB/μm, α_{on} = 0.0366 dB/μm for d = 250 nm). The light-graphene interaction is much better enhanced when the air gap width d is smaller. The normalized insertion loss is α_{on}, so the FOM of this modulator can be defined as:

$$\text{FOM} = \Delta\alpha / \alpha_{\text{on}} \qquad (5\text{-}1)$$

Here, for d = 500 nm I get a FOM of 150, and a FOM of 34 for d = 250 nm. Therefore, when the light-graphene interaction is enhanced, I get the modulation depth but loss the FOM for much larger insertion loss caused by the metal plate (larger light-metal interaction).

From the inset of Fig. 5.2, we can see the corresponding mode index (N_{eff}) for each case. When d is smaller, N_{eff} is much lower than 1 for much larger light-metal interaction. The change of mode index (ΔN_{eff}) is 0.04365, 0.07736, and 0.12200 for d = 500 nm, 300 nm, and 250 nm respectively. If two of this modulator are used as two arms of Mach-Zehnder (M-Z) modulator, the π-phase shift length will be only 17.75 μm, 10.02 μm, and 6.35 μm accordingly at λ = 1.55 μm. This is a great improvement for M-Z modulator.

Fig. 5.3 shows the modulation depth and FOM as a function of insulator thickness w when air gap width d = 500 nm (a) and 300 nm (b) at wavelength λ = 1.55 μm.

From Fig. 5.3, we can see for both cases, the modulation depth decreases and FOM increases as w is becoming larger, so the thinner w can cause higher light-graphene interaction, but it also causes higher insertion loss for higher light-metal interaction. For d = 500 nm, the modulation depth is in the scale of 0.54 ~ 0.22 dB/μm (1.94 ~ 0.24 dB/μm for d = 300 nm) and the corresponding FOM is in the scale of 70 ~ 400 (25 ~ 92 for d = 300 nm) when w is changing from 10 nm to 300 nm (50 nm to 300 nm for d = 300 nm).

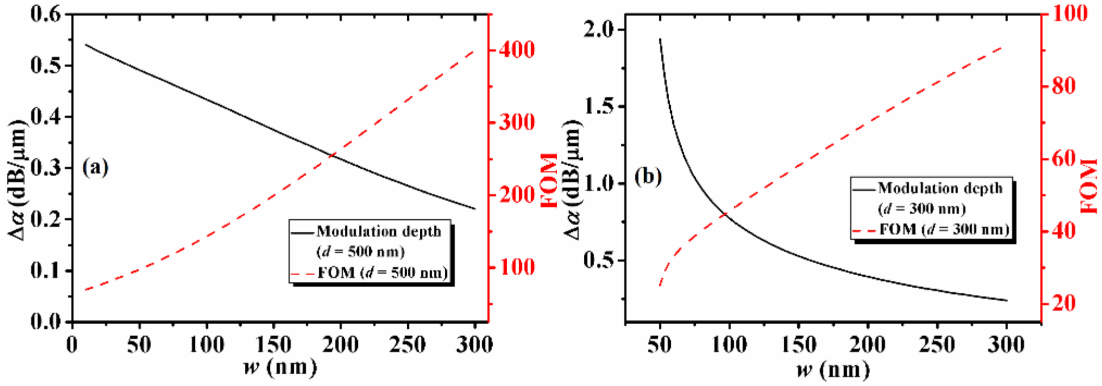

Fig. 5.3 Modulation depth (black solid line) and FOM (red dashed line) as a function of insulator thickness w when air gap width d = 500 nm (a) and 300 nm (b) at wavelength λ = 1.55 μm.

So, there is a trade-off between higher modulation depth and higher FOM. If the modulation depth is got, the modulation efficiency will loss for larger insertion loss and the design will be further away from the fundamental limits of graphene. According to my calculation, I find for d = 300 nm, the mode is cut-off when w is lower than 50 nm. The cut-off wavelength (λ_c) has a relation of:

$$f_c = \frac{c}{\lambda_c} = \frac{c}{2(n_1 w + 2d)} \tag{5-2}$$

Here c = 3×10^8 m/s is velocity of light in vacuum, $n_1 = \sqrt{\varepsilon_1}$ is the refractive index of the insulator material (n_1 = 1.75 for ε_1 = 3.06), ($n_1 w$ + 2d) is the optical interval between two metal plates. From Eq. (5-2), I can change it to:

$$w_c = \frac{\lambda}{2n_1} - \frac{2d}{n_1} \tag{5-3}$$

I submit λ = 1.55 μm, n_1 = 1.75 and d = 300 nm to Eq. (5-3), and get w_c = 100 nm, which is why when w < 50 nm, the loss become huge. When the mode is cut-off, the light-metal interaction will be extremely high which will cause much higher insertion loss and much lower FOM even though the modulation depth may be enhanced.

I get the modulation depth and FOM as a function of air gap width d

when $w = 100$ nm at $\lambda = 1.55$ μm, as shown in Fig. 5.4.

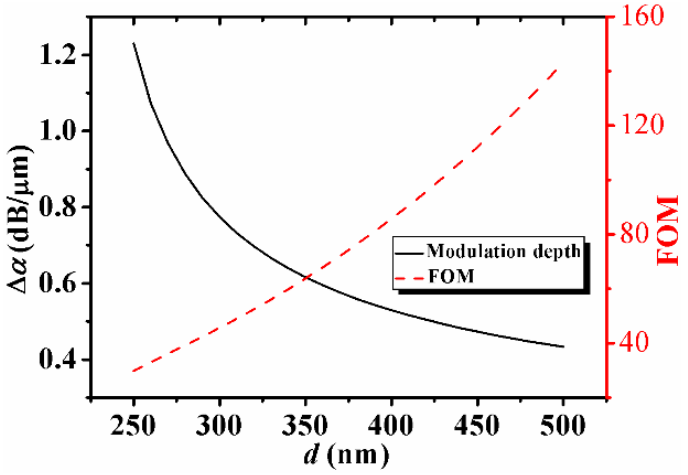

Fig. 5.4 Modulation depth (black solid line) and FOM (red dashed line) as a function of air gap width d when insulator thickness $w = 100$ nm at wavelength $\lambda = 1.55$ μm.

As we can see the modulation depth is much higher at lower d which enhances the light-graphene interaction. However, the light-metal interaction is also enhanced which causes higher insertion loss and lower FOM. Since d is changeable by moving the metal-cladding, we can achieve tunable FOM for this modulator. When d is too small, the mode will also be cut-off. From Eq. (5-2), we can derive the relation of cut-off d_c as:

$$d_c = \frac{\lambda}{4} - \frac{n_1 w}{2} \tag{5-4}$$

When $\lambda = 1.55$ μm, $n_1 = 1.75$ and $w = 100$ nm, I get $d_c = 300$ nm. When d is even lower, the loss will be even huge. Therefore, when d is larger, we can achieve nearer fundamental limits design of graphene.

In order to get a better knowledge of light-matter interaction, I calculate the mode fields of the modulator as a function of x-axis, as shown in Fig. 5.5.

We can see the mode confinement will be absolutely better when d is lower. This is because for TE mode, the metal plate will confine the field for it is always E-field nadir at the interface of metal. When w is lower, according to my calculation, I find the mode amplitude (A) in graphene layer is higher (A is 0.948 for $w = 100$ nm, and 0.985 for $w = 50$ nm).

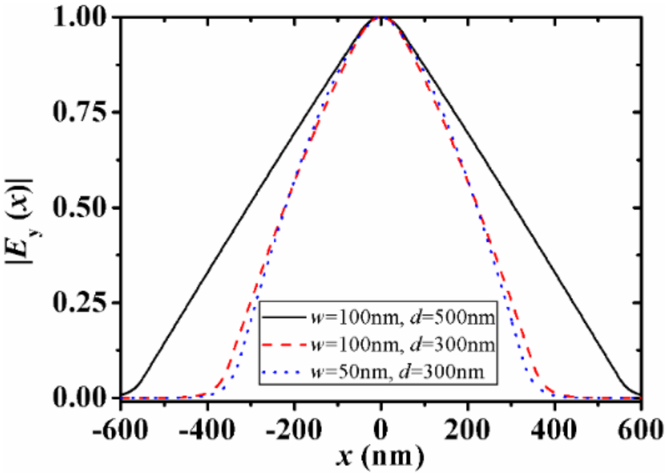

Fig. 5.5 Mode field distributions as a function of x-axis when $w = 100$ nm, $d = 500$ nm (black solid line); $w = 100$ nm, $d = 300$ nm (red dashed line); $w = 50$ nm, $d = 300$ nm (blue dotted line) at wavelength $\lambda = 1.55$ μm.

As the confinement of the mode will enhance the photon number which interact with graphene and the amplitude in graphene layer may enhance the interaction strength of one photon, the light-graphene interaction will absolutely be enhanced by lower d and lower w. However, the light-metal interaction is also enhanced by lower d and lower w for larger evanescent depth.

The transmittance and the modulation performance are gotten as a function of carrier wavelength according to $T(\lambda) = Exp[-\alpha L]$ when $L = 5$ μm is the modulator length, as shown in Fig. 5.6.

For $w = 100$ nm and $d = 500$ nm, the insertion loss can be very low ($T_{\max} = 0.995$) at the interested wavelength, but the modulation depth is lower for this case (only ~ 50%). However, for other two cases, the modulation depth can be higher (~ 77%) but the insertion loss is also higher. When the wavelength is too large, the mode will be cut-off, here we can see the calculated cut-off wavelength is $\lambda_c = 2.68$ μm, 1.89 μm and 1.62 μm for these three cases accordingly. The wavelength which is larger than λ_c will be filtered accordingly.

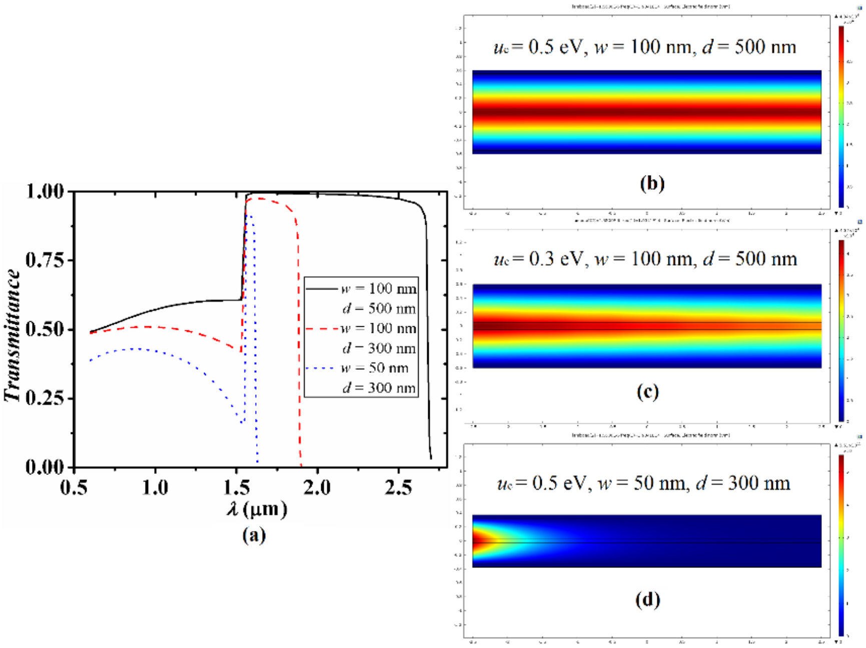

Fig. 5.6 (a) Transmittance as a function of carrier wavelength when $w = 100$ nm, $d = 500$ nm (black solid line); $w = 100$ nm, $d = 300$ nm (red dashed line); $w = 50$ nm, $d = 300$ nm (blue dotted line), which are all at modulator length $L = 5$ μm and chemical potential of $\mu_c = 0.4$ eV. (b) ~ (d) are the mode profiles in the longitudinal direction at different structure parameters: (b) $w = 100$ nm, $d = 500$ nm at $\mu_c = 0.5$ eV; (c) $w = 100$ nm, $d = 500$ nm at $\mu_c = 0.3$ eV; (d) $w = 50$ nm, $d = 300$ nm at $\mu_c = 0.5$ eV.

According to Eq. (5-2), we can change it to λ_c form as:

$$\lambda_c = 2(n_1 w + 2d) \qquad (5\text{-}5)$$

For these three cases, I get the theoretical cut-off wavelength is λ_c = 2.35 μm, 1.55 μm and 1.375 μm. The calculation results show slightly red shift but agree with the theory value very well.

The full-wave simulation is conducted, which shows good agreement with my calculation results. The mode profiles in the longitudinal transmission direction are shown in Fig. 5.6 (b) ~ (d). In this simulation, I set insulator permittivity ε_1 = 3.06, graphene monolayer thickness δ = 0.33 nm, insulator thickness $w = 0.1$ μm [(b) and (c)] or 0.05 μm (d) with a cladding air area of $d = 0.5$ μm [(b) and (c)] or 0.3 μm (d) and modulation length of $L = 5$ μm at chemical potentials of $\mu_c = 0.5$ eV [(b) and (d)] or 0.3 eV (c). The decay of the mode amplitude is negligible for the case of $w = 0.1$

μm, $d = 0.5$ μm and $\mu_c = 0.5$ eV, however it is significant for the case of $w = 0.1$ μm, $d = 0.5$ μm and $\mu_c = 0.3$ eV. We can also know the mode is totally cut off for the case of $w = 0.05$ μm, $d = 0.3$ μm and $\mu_c = 0.5$ eV.

5.3 Conclusions

In this chapter, I have done a theoretical research on the metal-clad suspended self-biasing graphene modulator. The light-graphene interaction can be enhanced by smaller size of this modulator, such as lower insulator slab thickness w and lower air gap width d. However, the light-metal interaction is also stronger with smaller size which causes larger insertion loss and makes lower FOM. The change of mode index (ΔN_{eff}) can be as high as 0.122 causing a π-phase shift length of only 6.35 μm for M-Z modulator which is the best value up to date. The FOM is tunable by changing the air gap (d) between the moveable metal plates and the suspended structure. When the air gap is larger, this configuration shows nearer fundamental limits design. The mechanism of light-graphene interaction is analyzed by the mode field distribution. Moreover, the cut-off mode is discussed by showing w_c, d_c and λ_c, and the tunable filter application is mentioned. The full-wave simulation is also conducted. I believe these results are very useful to design tunable light-matter interaction devices and contribute to tunable FOM physics.

Chapter 6

Multiple-layer Terahertz Waveguides

In this chapter, theory of five kinds of layered structure THz waveguides is presented. In these waveguides, the modified and hybrid THz surface plasmon-polaritons (SPPs) are researched in detail. On these modes, the effects of material in each layer are discussed. The anti-resonant reflecting mechanism is also discussed in these waveguides. The mode characteristics of both TM mode and TE mode are analyzed for guiding TM mode with low loss and TE modes with huge loss in one waveguide: the TE modes filter application is put forward. The mode characteristics for one waveguide have useful sensor applications: for TE_1 mode, I find that the low cut-off frequency has a sensitivity (S) to the refractive index of the dielectric slab. The highest S can be 666.7 GHz/RIU when $n_2 = 1.5$, $w = 0$ and $t = 0.1$ mm. I believe these results are very useful for designing practical THz devices for SPPs, filter and sensor applications.

6.1 Introduction

Terahertz (THz) wave as surface plasmon-polaritons (SPPs) has attracted extensive attention over the last several years. THz SPPs can be guided on metal wires, metal plates, or metal films. Wang and Mittleman reported the first THz SPPs on metal wires with low losses (experimental 1 m^{-1}) and negligible group velocity dispersion (GVD). Before Wang's work, the SPP mode is only researched on optical ranges. Researchers have followed to study THz SPPs on metal wires. The basic demonstration is based on the theory presented by Sommerfeld in 1899. In recent years, the modified SPP modes in optical ranges are discussed in several papers. However, the modified SPPs in THz range are still not discussed particularly.

The hybrid plasmonic mode is a hybrid mode of the SPP mode and the dielectric mode. This hybrid mode exhibits lower loss than the SPP mode and better confinement than the dielectric mode. However, the hybrid SPP mode in THz range is only discussed by a few papers particularly. The hybrid THz SPP mode on double-dielectric-slab-coated metal plate waveguide (DMPW) have not been discussed yet.

For ordinary THz waveguides, planar waveguides are acting important roles in many applications because of their simple structure, low loss, high coupling efficiency and good confinement. Planar THz waveguides, such as parallel-plate waveguides, metal film coated double-dielectric-slab waveguides, single metal plate waveguides, and metal-clad hollow waveguides are reported. Anti-resonant reflecting mechanism is discovered in the plastic coated parallel-plate waveguide and metal-clad hollow waveguides. And applications of tunable terahertz filters based on planar structures are reported by many papers.

In this chapter, the physics and potential applications of five types of layered THz waveguides are analyzed. In section 6.2, all the structures and the dispersion equations are derived. In section 6.3, the modified THz SPPs in the dielectric-slab-coated metal-film waveguide (DMW) is discussed. In section 6.4, the triple-layer-dielectric-slab waveguide (TW) with high-low-high refractive indices is discussed. In section 6.5, the mode characteristics of the metal nanofilm-dielectric-plate waveguide (MNW) of both TM mode and TE mode are discussed. I put forward the application of a TE modes filter of this waveguide. In section 6.6, I discuss the mode characteristics in the single-dielectric-slab-coated parallel-plate waveguide (SPW). In section 6.7, the hybrid THz SPPs on the double-dielectric-slab-coated metal plate waveguide (DMPW) is presented. At the resonant frequencies, the hybrid SPP modes transfer to dielectric modes. However, for the high-low indices coating, the hybrid mode is always a SPP-like mode. To the best of my knowledge, these layered THz waveguides are still not researched in detail and I believe these results are useful in designing THz waveguides and the according applications such as THz SPPs, filters, and sensors.

6.2 The waveguide structures and the dispersion equations

The structures of these layered THz waveguides are shown in Fig. 6.1: (a) is the dielectric-slab-coated metal-film waveguide (DMW); (b) is the triple-layer-dielectric-slab waveguide (TW); (c) is the metal nanofilm-dielectric-plate waveguides (MNW). They are all five-layer symmetrical structures (a, b, c).

(d) is the single-dielectric-slab-coated parallel-plate waveguide (SPW), and (e) is the double-dielectric-slab-coated metal plate waveguide (DMPW). They are four-layer structures (d, e).

The TM mode and TE mode of the THz wave is guided in *z*-direction, the width in *y*-direction is large enough. This is the well-known two-dimensional analysis [144]. The field equations of the even guiding mode in each layer are similar for the first three five-layer structures. Take the metal nanofilm-dielectric-plate waveguides (MNW) as an example, the mode field equations can be written as [138]:

TM mode:

$$H_y(x)=\begin{cases} A\cos(h_1 x) & |x|\le\frac{t}{2} \\ A[\cos(h_1\frac{t}{2})\cos h_2(|x|-\frac{t}{2})-\frac{h_1\varepsilon_2}{h_2\varepsilon_1}\sin(h_1\frac{t}{2})\sin h_2(|x|-\frac{t}{2})] & \frac{t}{2}\le|x|\le\frac{t}{2}+d \\ A[\cos(h_1\frac{t}{2})\cos h_2 d-\frac{h_1\varepsilon_2}{h_2\varepsilon_1}\sin(h_1\frac{t}{2})\sin h_2 d]e^{-h_3(|x|-\frac{t}{2}-d)} & |x|\ge\frac{t}{2}+d \end{cases} \tag{6-1}$$

TE mode:

$$E_y(x)=\begin{cases} A\cos(h_1 x) & |x|\le\frac{t}{2} \\ A[\cos(h_1\frac{t}{2})\cos h_2(|x|-\frac{t}{2})-\frac{h_1}{h_2}\sin(h_1\frac{t}{2})\sin h_2(|x|-\frac{t}{2})] & \frac{t}{2}\le|x|\le\frac{t}{2}+d \\ A[\cos(h_1\frac{t}{2})\cos h_2 d-\frac{h_1}{h_2}\sin(h_1\frac{t}{2})\sin h_2 d]e^{-h_3(|x|-\frac{t}{2}-d)} & |x|\ge\frac{t}{2}+d \end{cases} \quad (6\text{-}2)$$

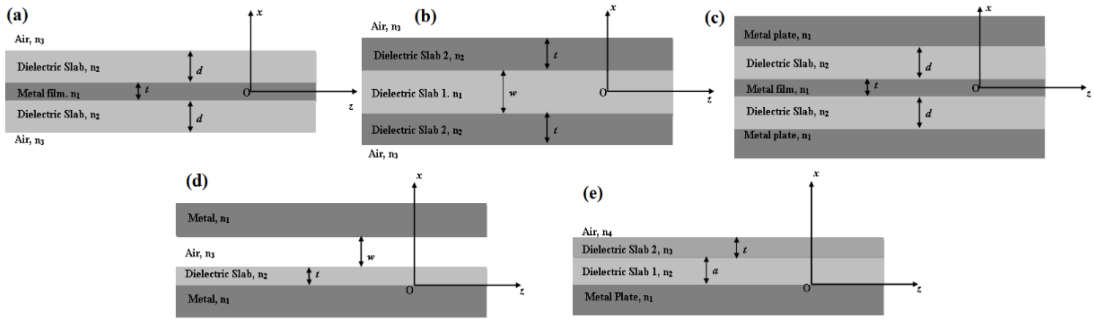

Fig. 6.1 Structures of these five kinds of multiple-layer THz waveguides. The material of each layer is shown in the figure. n_1, n_2, and n_3 are the refractive index accordingly. In (a), d is the thickness of the coating dielectric slab with a refractive index of n_2, and t is the thickness of the metal film with a refractive index of n_1. In (b), the materials of the two coating slabs are the same and with a refractive index of n_2 and a thickness of t. The middle dielectric slab has a different material with a refractive index of n_1 and a width of w. In (c), the middle metal film has a thickness of t and a refractive index of n_1; the two coated dielectric slabs have a thickness of d and a refractive index of n_2; and the outside metal plates have a refractive index of n_1. In (d), t is the thickness of the dielectric slab, w is the width of the air gap. In (e), the structure has four layers: the first layer is the metal plate with a refractive index of n_1; the second layer is dielectric slab 1 with a refractive index of n_2 and a thickness of a; the third layer is dielectric slab 2 with a refractive index of n_3 and a thickness of t; the fourth layer is the outside air with a refractive index of n_4.

The dispersion equations of the guiding modes (five-layered) can be written as [138]:

TM mode: $$h_1\frac{t}{2}=\tan^{-1}\left[\frac{1-\frac{h_2\varepsilon_3}{h_3\varepsilon_2}\tan h_2 d}{\frac{h_1\varepsilon_3}{h_3\varepsilon_1}+\frac{h_1\varepsilon_2}{h_2\varepsilon_1}\tan h_2 d}\right] \quad (6\text{-}3)$$

TE mode: $$h_1\frac{t}{2}=\tan^{-1}\left[\frac{1-\frac{h_2}{h_3}\tan h_2 d}{\frac{h_1}{h_3}+\frac{h_1}{h_2}\tan h_2 d}\right] \quad (6\text{-}4)$$

where $h_1=(n_1^2k^2-\beta^2)^{1/2}$, $h_2=(n_2^2k^2-\beta^2)^{1/2}$, $h_3=(\beta^2-n_1^2k^2)^{1/2}$; $\beta=\beta_1-j*\alpha$ is the complex variable, in which the real part β_1 is related to the effective refractive index ($n_{\mathrm{eff}} = \beta_1/k$) and the imaginary part α is the amplitude loss coefficient of the guiding mode. $k = 2\pi/\lambda$ is the wave vector in vacuum. $\varepsilon_1 = n_1^2$ and $\varepsilon_2 = n_2^2$ are relative permittivities of the metal and dielectric slab, respectively.

For structures in Fig. 6.1 (a) and (b), Eqs. (6-1) - (6-4) only need slightly changes, for example, we should use $h_3 = (\beta^2 - \varepsilon_3 k_0{}^2)^{1/2}$ and the according refractive index of the according materials for (a) and use w to replace t, t to replace d for (b).

In the similar way, the dispersion equations of the guiding modes in the single-dielectric-slab-coated parallel-plate waveguide (SPW) (4-layered, Fig. 6.1 (d)) can be written as [138]:

TM mode:

$$\tan h_2 t = \frac{\dfrac{2h_1}{\varepsilon_1} + (\dfrac{h_1{}^2\varepsilon_3}{h_3\varepsilon_1{}^2} - \dfrac{h_3}{\varepsilon_3})\tan h_3 w}{(\dfrac{h_3 h_1 \varepsilon_2}{h_2\varepsilon_1\varepsilon_3} + \dfrac{h_1 h_2 \varepsilon_3}{h_3 \varepsilon_2 \varepsilon_1})\tan h_3 w + \dfrac{h_2}{\varepsilon_2} - \dfrac{h_1{}^2\varepsilon_2}{h_2\varepsilon_1{}^2}} \qquad (6\text{-}5)$$

TE mode:

$$\tan h_2 t = \frac{2h_1 + (\dfrac{h_1{}^2}{h_3} - h_3)\tan h_3 w}{(\dfrac{h_3 h_1}{h_2} + \dfrac{h_1 h_2}{h_3})\tan h_3 w + h_2 - \dfrac{h_1{}^2}{h_2}} \qquad (6\text{-}6)$$

As shown in Fig. 6.1 (e), the waveguide has a low-high refractive indices (l-h) coating ($n_2 < n_3$) structure and a high-low refractive indices (h-l) coating ($n_2 > n_3$) structure. The hybrid THz SPPs modes are transverse magnetic (TM) polarized THz waves and transmit in z-direction, the width in y-direction is large enough. The mode field equations of the guiding mode in each layer can be written as [138]:

$$H_y(x) = \begin{cases} A[(\cos h_2 a + \dfrac{h_1\varepsilon_2}{h_2\varepsilon_1}\sin h_2 a)\cos h_3 t - (\dfrac{h_2\varepsilon_3}{h_3\varepsilon_2}\sin h_2 a - \dfrac{h_1\varepsilon_3}{h_3\varepsilon_1}\cos h_2 a)\sin h_3 t]e^{-h_4(x-a-t)} & x \geq a+t \\ A[(\cos h_2 a + \dfrac{h_1\varepsilon_2}{h_2\varepsilon_1}\sin h_2 a)\cos h_3(x-a) - (\dfrac{h_2\varepsilon_3}{h_3\varepsilon_2}\sin h_2 a - \dfrac{h_1\varepsilon_3}{h_3\varepsilon_1}\cos h_2 a)\sin h_3(x-a)] & a \leq x \leq a+t \\ A[\cos h_2 x + \dfrac{h_1\varepsilon_2}{h_2\varepsilon_1}\sin h_2 x] & 0 \leq x \leq a \\ Ae^{h_1 x} & x \leq 0 \end{cases} \qquad (6\text{-}7)$$

As the tangential components of the electromagnetic fields on interfaces are continuous, we can obtain the dispersion equation of the guiding TM mode [138]:

$$\tan h_2 a = \frac{\frac{h_4}{\varepsilon_4} + \frac{h_1}{\varepsilon_1} + (\frac{h_4 h_1 \varepsilon_3}{h_3 \varepsilon_1 \varepsilon_4} - \frac{h_3}{\varepsilon_3}) \tan h_3 t}{(\frac{h_3 h_1 \varepsilon_2}{h_2 \varepsilon_1 \varepsilon_3} + \frac{h_4 h_2 \varepsilon_3}{h_3 \varepsilon_2 \varepsilon_4}) \tan h_3 t + \frac{h_2}{\varepsilon_2} - \frac{h_4 h_1 \varepsilon_2}{h_2 \varepsilon_1 \varepsilon_4}} \qquad (6\text{-}8)$$

By dispersion Eqs. (6-3), (6-4), (6-5), (6-6), and (6-8), we can calculate the propagation constant β of the waveguide for TM mode and TE mode respectively. Pursuantly, we can get the loss coefficients and effective refractive indices of these patterns. Further, according to the propagation constant and Eqs. (6-1), (6-2), and (6-7), we can find out the field distributions of mode patterns.

6.3 Modified THz SPPs on dielectric-slab-coated metal-film waveguide (DMW)

The material of the metal is chosen as copper for all the cases. For this case, the waveguide structure is shown in Fig. 6.1 (a). The parameter of copper film in THz region can be gotten from the Drude mode [147]:

$$\varepsilon_3 = \varepsilon_\infty - \frac{\omega_p^{\,2}}{\omega^2 - i\omega\omega_\tau} \qquad (6\text{-}9)$$

where ε_∞ is the high frequency permittivity of copper which is always negligible in THz region, ω_p = 1.1234×10^{16} rad/s [147] is the plasma oscillation frequency of copper, ω_τ = 1.3798×10^{13} rad/s [147] is the damping frequency of copper, and ω is the angular frequency of the THz wave.

The material of the dielectric slab is chosen as the silicon here, in Drude mode: $\varepsilon_\infty = 11.7$ is the high frequency dielectric constant. I adopt the doped silicon which has parameters of ω_p = 0.01×10^{12} rad/s, ω_τ = 0.67×10^{12} rad/s. $\varepsilon_3 = n_3^2 = 1$ is the relative permittivity of air. The modified plasmonic modes are transverse magnetic (TM) polarized THz waves.

I calculate Eq. (6-3) at the condition of t = 10 nm and d = 0.1 mm, and get the changing law of guiding mode loss (solid line) to THz frequency f, as shown in Fig. 6.2 (a). The corresponding effective refractive index (dashed line) and group velocity ($\frac{v_g}{\mathrm{c}} = \frac{1}{n_{eff}\left(1+\frac{k_0}{n_{eff}}\frac{\mathrm{d}n_{eff}}{\mathrm{d}k_0}\right)}$ [70], dotted line) are also shown.

From Fig. 6.2 (a), we can see that the law of loss to *f* has three segments. In the region of 0.1 THz ~ 0.23 THz, the loss increases sharply as *f* increases. The changing slopes of effective refractive index and group velocity to *f* are much sharper in this region which tells us that both the phase velocity dispersion (PVD) and the group velocity dispersion (GVD) are much higher in this region. When the THz frequency is very low, the wavelength is much larger, and the diffraction limit of the THz wave make the beam width larger. As the waveguide size is fixed here, the metal film and the coated silicon slab cannot cause too much loss. In this range as the frequency increases, the mode confinement will be better and better, and the effects of the metal film and the coated silicon slab on the mode will become more and more important.

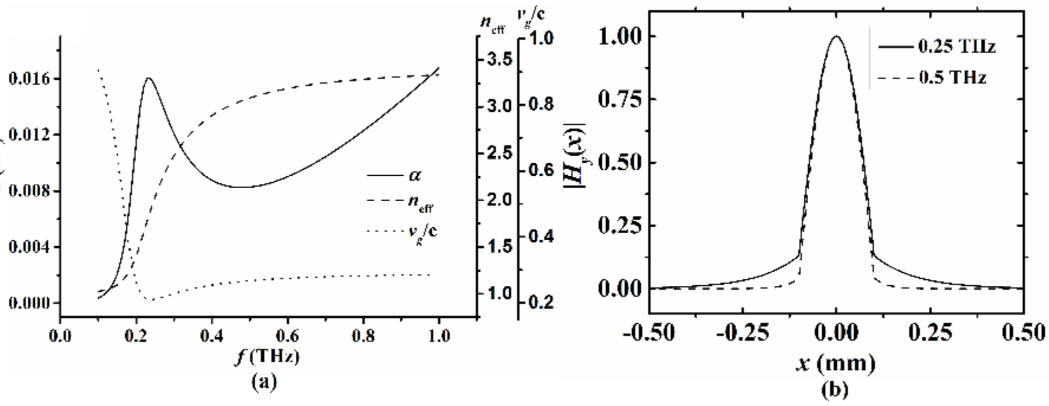

Fig. 6.2 (a) Guiding mode loss (solid line), effective refractive index (dashed line) and group velocity (dotted line) of the dielectric-coated metal-film waveguide as a function of THz frequency *f* at the condition of t = 10 nm and d = 0.1 mm, (b) The corresponding mode field distribution at f = 0.25 THz (solid line) and f = 0.5 THz (dashed line).

In the region of 0.23 THz ~ 0.48 THz, the loss decreases as *f* increases, and both the PVD and GVD are lower, which tells us that the effects of metal film are lower. This is because more energy will be confined in the coated slabs. According to my calculation by Drude mode, the loss caused by silicon decreases as *f* increase in this region.

In the region of higher than 0.48 THz, the loss increases monotonously and the dispersion is almost zero. When the THz wavelength becomes even lower, the confinement of the mode will make even more energy interact with the metal film. The loss of this dielectric-coated film is extreme low (lower than 0.016 m^{-1}), which is one order of magnitude lower than the theoretical loss of THz SPPs on metal wires [81]. This is because the metal film is much thinner than the penetration depth of THz waves to metal wires (about 100 nm) even though the THz wavelength is the same as reference [81].

According to Eq. (6-1), I get the mode field at 0.25 THz (solid line) and 0.5 THz (dashed line) at the condition of $t = 10$ nm and $d = 0.1$ mm, as shown in Fig. 6.2 (b). We can see that the mode energy is almost concentrated in the dielectric slab and the beam width is only about 0.2 mm while the wavelength of THz wave is 1.2 mm at 0.25 THz. The degree of the energy concentration is higher at the larger *f*, as can be seen from the mode field at 0.5 THz (dashed line) in Fig. 6.2 (b). For THz metal wires, the mode field amplitude is still strong at the distance of 10 mm [81] from the metal wire surface at the same condition.

The silicon coating makes the confinement of this modified SPP mode much better. After my calculation, I find that the pure SPP mode on this metal film is very leaky, the mode confinement is too weak and the mode cannot be guided effectively, because the wavelength of THz wave is much larger than the thickness of the metal film, the diffraction limit makes almost no electric-matter interaction between TM mode and the much thinner metal film.

The loss and effective refractive index of modified THz SPP mode on this waveguide are gotten as a function of *d*, as shown in Fig. 6.3 (a).

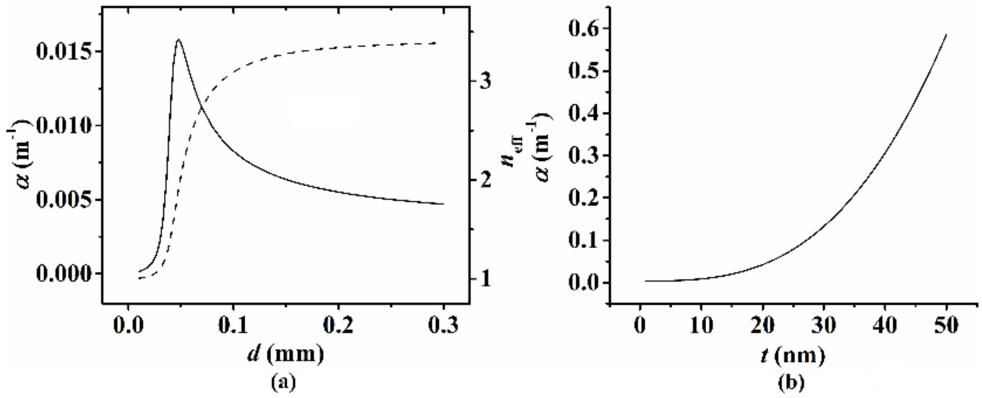

(a) (b)

Fig. 6.3 (a) is the changing law of mode loss (solid line) and effective refractive index (dashed line) of the modified SPP mode to the coated slab thickness *d* at the condition of *t* = 10 nm and *f* = 0.5 THz. (b) is the changing law of mode loss to the thickness *t* of the metal film at the condition of *d* = 0.1 mm and *f* = 0.5 THz.

The loss is extreme low when the thickness *d* of the slab is much thinner. However, in that case, the effective refractive index is almost 1, most of the energy is in the air and the beam width is much larger. When *d* increases, the loss has a maximum point and then decreases significantly. At the maximum point, the electric-metal interaction is enhanced to its maximum. The effective refractive index increases monotonously to that of the silicon, the energy will be distributed more in the dielectric slab and the beam width will be smaller as *d* is even larger after the maximum point, and the electric-metal interaction is lower. The loss is lower for larger *d*. Therefore, the larger the *d* is, the longer the THz waves can transmit and the smaller the beam width is. This is because the effect of the slab on the mode is more obvious for larger *d*.

I also get the loss changing as a function of metal film thickness *t*, as shown in Fig. 6.3 (b). The loss of the modified THz SPP mode increases monotonously as *t* increases. The effects of metal film to the modified THz SPPs will be obviously larger when *t* is larger.

6.4 THz triple-layer-dielectric-slab waveguide (TW) with anti-resonant reflecting

The waveguide structure is shown in Fig. 6.1 (b). The waveguide has high-low-high refractive indices ($n_1 < n_2$) here. Silicon with $\mathrm{Real}[n_2] = \sqrt{11.7} = 3.42$ and an absorption loss by Drude model (as seen above) is chosen as n_2. Polystyrene (PS) with a parameter of $n_1 = \sqrt{\varepsilon_1} = 1.58 - j0.0036$ [89] is chosen as n_1. The absorption loss of the PS is much larger than that of the silicon. I only consider TM mode here.

By Eq. (6-3), the loss, effective refractive index and group velocity are gotten as a function of the THz wave frequency f, as shown in Fig. 6.4.

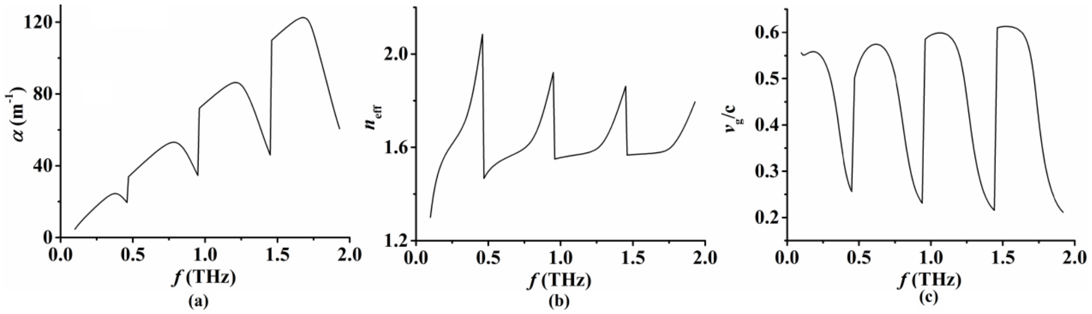

Fig. 6.4 Loss (a), effective refractive index (b) and group velocity (c) of the triple-layer-dielectric-slab waveguide with high-low-high refractive indices change as a function of THz frequency f when $t = 0.1$ mm, $w = 0.5$ mm.

The loss of the guiding mode appears nadirs at the frequencies of 0.46 THz, 0.95 THz and 1.45 THz. They are caused by the anti-resonant reflection mechanism. The loss nadir points can be predicted by the following relation, namely the relation of the resonant frequency [70]:

$$f_m = \frac{m\mathrm{c}}{2t\sqrt{n_2^{\ 2} - n_1^{\ 2}}} \qquad (6\text{-}10)$$

$m = 1, 2, 3\ldots$ is the resonance order. I substitute $\mathrm{c} = 3\times10^8$ m/s, $t = 0.1$ mm, $n_2 = 3.42$ and $n_1 = 1.58$ to Eq. (6-10) and get $f_1 = 0.49$ THz, $f_2 = 0.99$ THz and $f_3 = 1.48$ THz. The numerical calculation values appear a little red-shift comparing with the theory values, which is caused by the approximating of Eq. (6-10).

When f is at the resonant frequencies, the energy of THz wave will transmit through the interfaces between the core PS and the coated silicon, and more energy will distribute in the lower loss silicon. However, anti-resonant reflections happen when f is not the resonant frequencies and most of the energy will be confined in the high loss PS slab. In Fig. 6.4 (b) and (c), the effective refractive index of the guiding mode appears peaks and the group velocity of the guiding mode appears nadirs at the resonant frequencies.

In order to get a better understanding of the mode in the waveguide with the anti-resonant guiding mechanism, I calculate the mode field of the guiding mode at the anti-resonant frequency 0.96 THz and the resonant frequency 1.45 THz when $t = 0.1$ mm and $w = 0.5$ mm, as shown in Fig. 6.5.

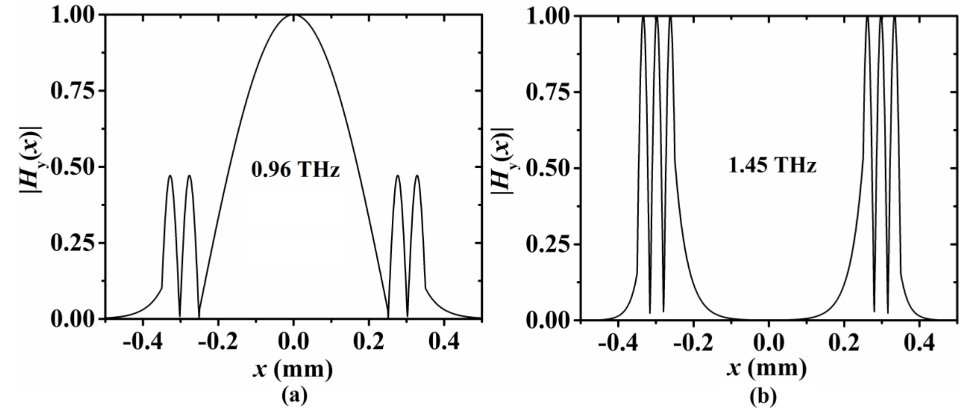

Fig. 6.5 Mode field distribution at the anti-resonant frequency 0.96 THz (a) and the resonant frequency 1.45 THz (b) when $t = 0.1$ mm and $w = 0.5$ mm.

Fig. 6.5 shows the evidence of less energy distributing in lower loss silicon at the anti-resonant frequency (0.96 THz) and more at the resonant frequency (1.45 THz). We can also see that the phase in one coating silicon slab is about 2π at 0.96 THz (the start frequency of resonant mode order $m = 3$) and 3π at 1.45 THz (resonant order $m = 3$), which has been discussed in reference [70].

At $f = 1.0$ THz and $w = 0.5$ mm, the loss (a) and the corresponding effective refractive index (b) of the guiding mode are gotten as a function of t, as shown in Fig. 6.6.

When the thicknesses of the silicon slabs are close to 0.044 mm, 0.096

mm, 0.146 mm and 0.194 mm, the loss coefficient decreases sharply. When 1.0 THz becomes the resonant frequency for the coated silicon thickness, much more energy will distribute in the low loss silicon, and the effective refractive index will also be larger as can be seen in Fig. 6.6 (b). The resonant silicon thicknesses can be predicted by the following relation:

$$t_m = \frac{mc}{2f\sqrt{n_2^{\,2} - n_1^{\,2}}} \qquad (6\text{-}11)$$

I substitute c = 3×10^8 m/s, f = 1.0 THz, n_2 = 3.42 and n_1 = 1.58 to Eq. (6-11), and get t_1 = 0.049 mm, t_2 = 0.099 mm, t_3 =0.148 mm and t_4 =0.198 mm. The numerical values are in good agreement as the theoretical values.

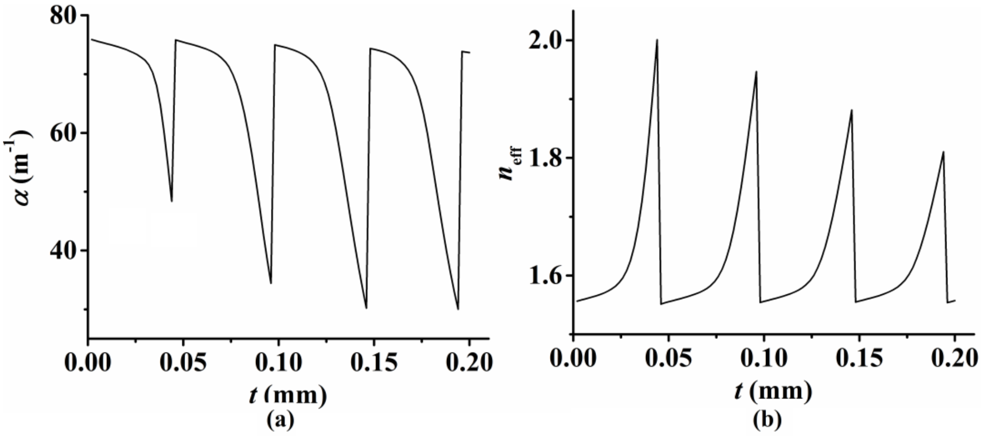

Fig. 6.6 Laws of loss (a) and the corresponding effective refractive index (b) of the guiding mode changing as a function of t when f = 1.0 THz and w = 0.5 mm.

When f = 1.0 THz and t = 0.1 mm, the loss and the corresponding effective refractive index of the guiding mode are gotten as a function of w, as shown in Fig. 6.7.

Both the loss and the effective refractive index (to that of PS) are increasing monotonously. When w is larger, the energy of the THz wave will distribute more in the high loss PS slab and less in the low loss silicon and outside air. According to my calculation, if chosen $n_1 > n_2$ the mode will show total internal reflecting (TIR) which is not so interesting.

For TIR case, this triple-layer THz waveguide is like a traditional optical fiber if the central layer is thick enough.

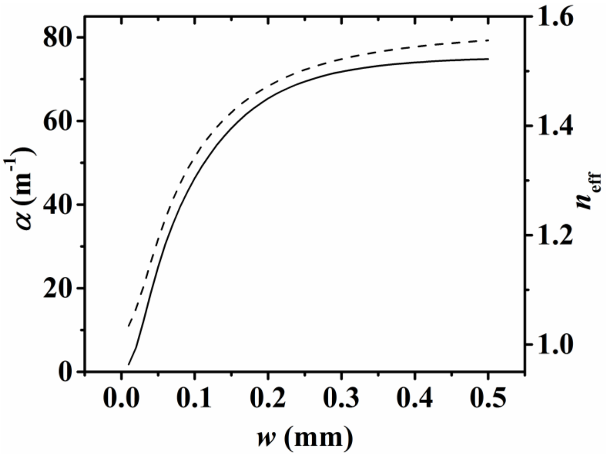

Fig. 6.7 Law of loss (solid line) of the guiding mode changing as a function of w when f = 1 THz, t = 0.1 mm. The dashed line is the corresponding effective refractive index of the guiding mode.

6.5 THz wave in metal nanofilm-dielectric-plate waveguide (MNW)

The waveguide structure is shown in Fig. 6.1 (c). The material of the metal nanofilm and the metal plate is chosen as copper. The material of the two coated dielectric slabs is chosen as silicon. The parameters of copper and silicon in THz region are seen above. I consider both TM and TE mode here.

When the thickness of the nanofilm is t = 10 nm and the thickness of the two coated dielectric slabs is d = 0.5 mm, I calculate Eq. (6-3) and get the loss (solid line) and the corresponding effective refractive index (dashed line) of TM mode in the waveguide as a function of THz frequency f, as shown in Fig. 6.8.

The loss of the TM mode of the waveguide increases monotonously as f increases. In the range of 0.1 THz ~ 0.5 THz, the loss is below 1.29 m^{-1} and at 0.1 THz the loss can be as low as 0.66 m^{-1}. The effective refractive index of the mode is always about 3.42, the mode is based on most of the energy propagates in the coated silicon slabs. The slope of the effective refractive index to the frequency is almost zero which tells us the GVD of the TM mode is almost 0. This is because in the waveguide, only the electric field amplitude will have interaction with the metal. However, the electric field amplitude in TM mode is very small. So the interaction of TM mode with metal in this waveguide is very small.

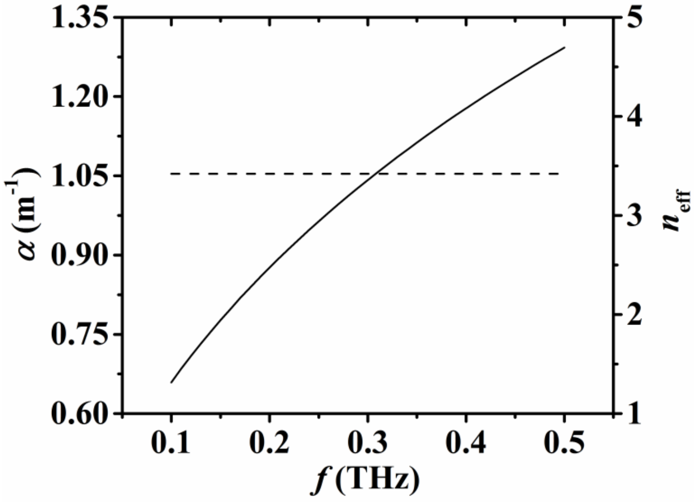

Fig. 6.8 Loss (solid line) and the corresponding effective refractive index (dashed line) of TM mode in the waveguide change as a function of THz frequency f when $t = 10$ nm and $d = 0.5$ mm.

I calculate Eq. (6-4) and get the losses (a) and the corresponding effective refractive indices (b) of TE modes in the waveguide as a function of THz frequency f when $t = 10$ nm and $d = 0.5$ mm, as shown in Fig. 6.9.

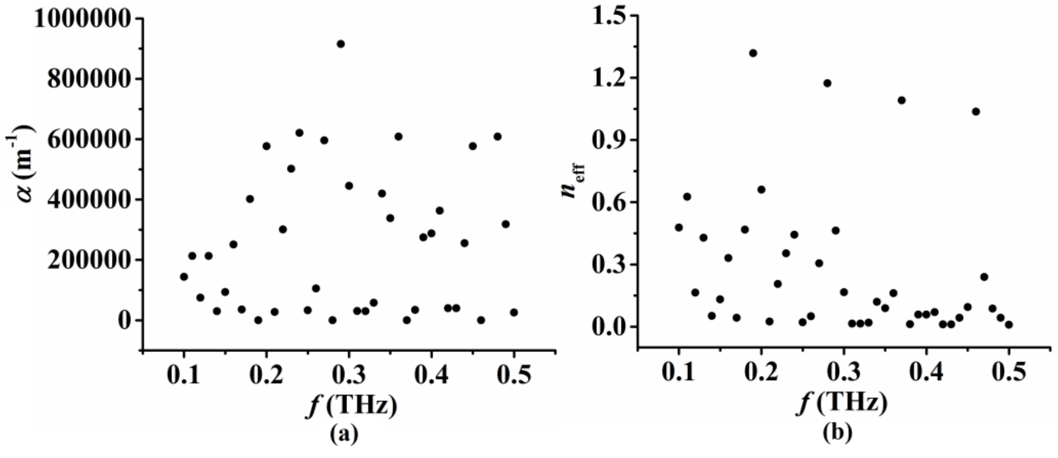

Fig. 6.9 Losses (a) and the corresponding effective refractive indices (b) of TE modes in the waveguide changing as a function of THz frequency f when $t = 10$ nm and $d = 0.5$ mm.

Multiple TE modes appear in the waveguide since the losses and the effective refractive indices are discontinuous at every frequency. The losses of the TE modes can be as high as 1.42×10^6 m^{-1} which is 6 orders of magnitude higher than the loss of TM mode when the waveguide has the same structure. So this waveguide can be used as a filter of the TE modes and pass the TM mode.

The effective refractive indices are in the range of 0 ~ 1.3, which is much lower than that of the silicon. This is because that the modes interaction with the metal is huge for the electric field amplitude of TE mode (E_y) is very large.

In order to get a better understanding of the TE modes, I get the mode fields of a TE mode in the waveguide at $f = 0.3$ THz, $t = 10$ nm and $d = 0.5$ mm according to Eq. (6-2), as shown in Fig. 6.10.

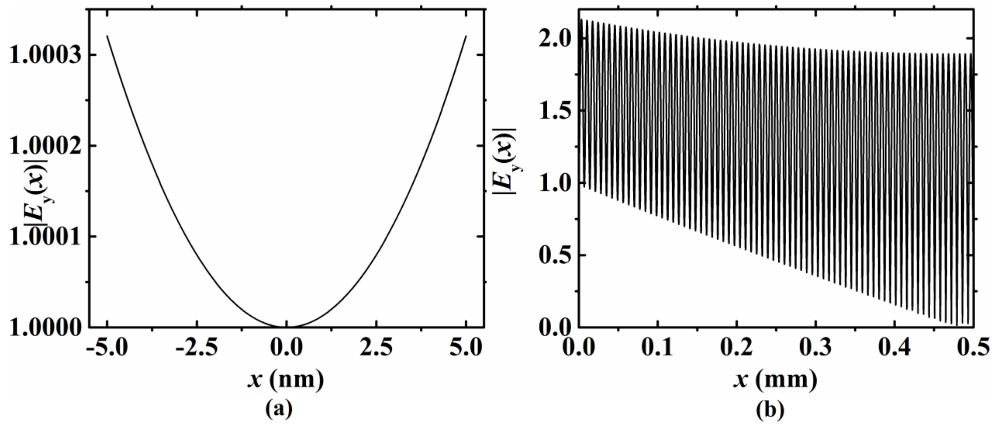

Fig. 6.10 Not normalized mode field of a TE mode in the metal nanofilm-dielectric-plate waveguide at the frequency 0.3 THz and $t = 10$ nm, $d = 0.5$ mm. (a) is the field in the metal nanofilm; (b) is the field in the coated silicon slab.

At this condition, the loss of the considered mode is 445374 m^{-1}, which is more than 5 orders of magnitude higher than the loss of TM mode. A considerable field is distributed in the nanofilm, which causes the huge electric-metal interaction. Fig. 6.10 (b) shows the phase in the coated silicon slabs which is more than 50π, the order of the mode is very large.

I also calculate the field of a lower mode at 0.19 THz, as shown in Fig. 6.11. At this condition the loss of the considered mode is 102.89 m^{-1}, which is about only 2 orders of magnitude higher than the loss of TM mode.

From Fig. 6.11, we can see the relative percentage of energy in the metal nanofilm is much lower (the field amplitude is 1 in the metal film but it is 50 in the silicon slab). The phase in the coated silicon slab is only 2π, which tells us that the order of the mode is 2.

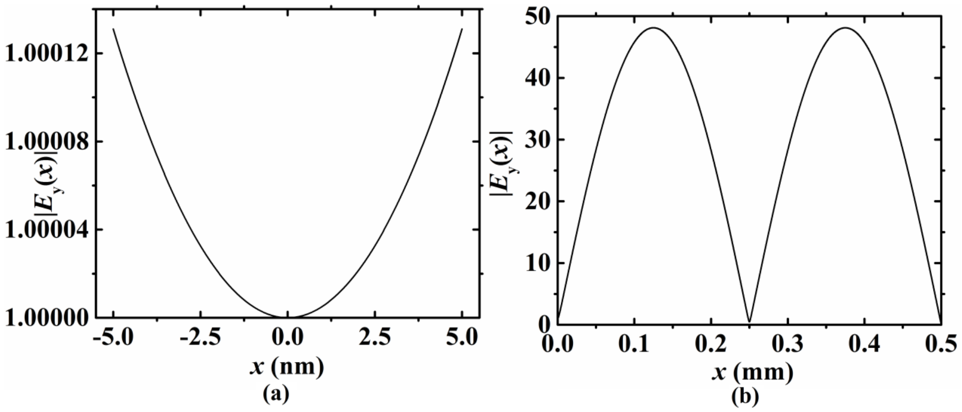

Fig. 6.11 Not normalized mode field of a TE mode in the metal nanofilm-dielectric-plate waveguide at the frequency 0.19 THz and $t = 10$ nm, $d = 0.5$ mm. (a) is the field in the metal nanofilm; (b) is the field in the coated silicon slab.

The TE modes in the parallel-plate waveguide have low cut-off frequencies, and the losses near the low cut-off frequencies are huge. The adding of the metal film in the middle cause the low cut-off frequencies to be complex, so the losses of TE modes in the metal nanofilm-dielectric-plate waveguide are huge and multiple modes appear.

When $t = 10$ nm and $f = 0.5$ THz, I calculate Eq. (6-3) and get the loss of TM mode in the waveguide as a function of silicon slab thickness d, as shown in Fig. 6.12 (a). As d increases, the loss of TM mode decreases monotonously. The loss changes from 63.2 m^{-1} (at $d = 0.01$ mm) to 1.29 m^{-1} (at $d = 0.5$ mm). The increasing of d has significance influence on the mode loss, which tells us the effects of coated silicon slabs on the TM mode are larger.

I also get the loss of TM mode in the waveguide as a function of t according to Eq. (6-3), at $d = 0.5$ mm and $f = 0.5$ THz, as shown in Fig. 6.12 (b). As t increases from 1 nm to 50 nm, the loss increases slightly (from 1.29 m^{-1} at $t = 1$ nm to 1.34 m^{-1} at $t = 50$ nm), which tells us the effects of the nanofilm on the TM mode are much lower. However, as discussed above, the effects of the nanofilm on the TE modes are huge.

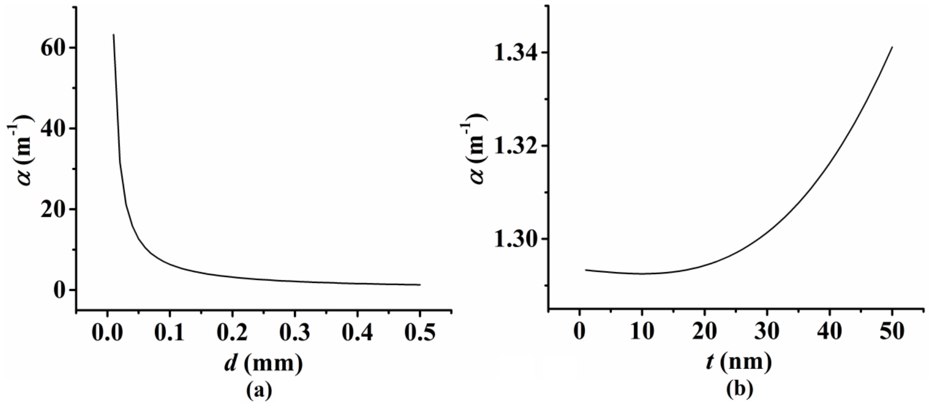

Fig. 6.12 (a) Loss of TM mode in the metal nanofilm-dielectric-plate waveguide changing as a function of coated silicon thickness d when $t = 10$ nm and $f = 0.5$ THz; (b) Loss of TM mode in the metal nanofilm-dielectric-plate waveguide changing as a function of nanofilm thickness t when $d = 0.5$ mm and $f = 0.5$ THz.

6.6 THz single-dielectric-slab-coated parallel-plate waveguide (SPW)

6.6.1 Mode characteristics of the waveguide

Fig. 6.1 (d) shows the structure of this case. Copper is adopted as the material of the metal plates. The material of the dielectric slab is chosen as the silicon or plastic. When $t = 0.1$ mm, $w = 0.1$ mm, I calculate Eqs. (6-5) and (6-6), and get the loss (solid line) and the effective refractive index (dashed line) of the different slab material (silicon or plastic) waveguide at different THz frequencies, as shown in Fig. 6.13. The group velocity of the guiding modes is shown in dotted line.

Both of the loss and effective refractive index of TM$_0$ mode (which is also called as the transverse-electromagnetic (TEM) mode) of the waveguide are increasing monotonously. When f is larger, more THz energy will distribute in the lossy dielectric slab and less in the air interval. The loss changing law of TM$_0$ mode is the same as described in reference [69]. After coating a dielectric slab, the group velocity of TM$_0$

mode in the waveguide is only 0.23 ~ 0.64 (for silicon slab) or 0.64 ~ 0.84 (for plastic slab) of the light velocity in vacuum.

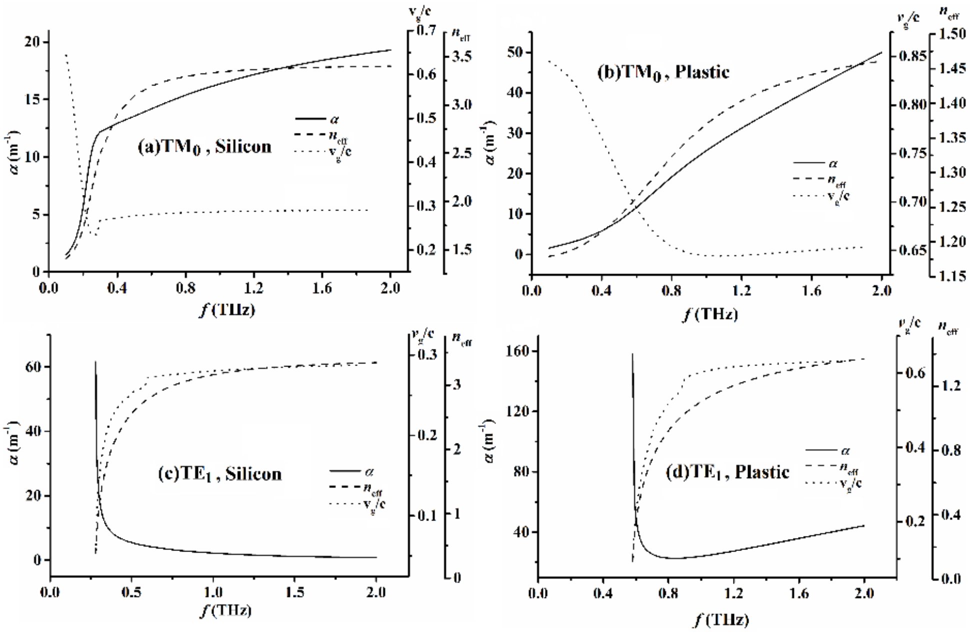

Fig. 6.13 Dependence of loss (solid line), effective refractive index (dashed line) and group velocity (dotted line) of the waveguide with the parameters of $t = 0.1$ mm, $w = 0.1$ mm on THz frequency. (a) is TM$_0$ mode with a silicon slab; (b) is TM$_0$ mode with a plastic slab; (c) is TE$_1$ mode with a silicon slab; (d) is TE$_1$ mode with a plastic slab.

The changing slope of group velocity is much sharper in the lower frequency. For silicon slab coated waveguide, the GVD is much larger than that of plastic slab coated waveguide in the narrow lower frequency region, which can be seen from the less sharp and wider sharp region of the group velocity of the plastic-coated waveguide.

In the region of higher than 0.30 THz (silicon coated waveguide) and 0.80 THz (plastic coated waveguide), the GVD of the waveguide is much lower. When the GVD of the waveguide is larger, the changing of the effective refractive index is also sharper. The refractive index of silicon is 3.42 (1.5 for plastic), so the effective refractive index of silicon coated waveguide is in the region of 1 ~ 3.42 (1 ~ 1.5 for plastic coating). After coating, the TM mode loss is in the region 1.5 m^{-1} ~ 50 m^{-1}, which is only 1 order of magnitude larger than that of uncoated waveguide.

From Fig. 6.13 (c) and (d), we can see that there appears a low cut-off frequency for TE_1 mode. Both the loss and the GVD are much larger near the low cut-off frequency. The low cut-off frequency of silicon-coated waveguide is about 0.28 THz (0.58 THz for plastic coating). According to reference [68], we can know the low cut-off frequency for TE_1 mode of this waveguide is:

$$f_c = \frac{c}{2(n_2 t + w)} \qquad (6\text{-}12),$$

where $(n_2 t + w)$ is the optical width between the two parallel plates. I substitute the values ($t = 0.1$ mm, $w = 0.1$ mm, c = 3×10^8 m/s, $n_2 = 3.42$ or 1.5) to Eq. (6-12) and get $f_c = 0.34$ THz for silicon-coated waveguide, and $f_c = 0.60$ THz for plastic-coated waveguide. We can know that the low cut-off frequency is strongly affected by the refractive index of the slab.

When $f = 1$ THz, $t = 0.1$ mm, I get the loss (solid line) and the effective refractive index (dashed line) of the different slab material (silicon or plastic) waveguide at the different air interval w, as shown in Fig. 6.14.

For TM_0 mode, the loss increases slightly to a stable value in silicon-coated waveguide, while there is a minim loss in plastic-coated waveguide when w changes from 0 to 0.1 mm. The effective refractive index also only has slightly changing. For the same parameters of the structure, the optical width between the two parallel plates of the silicon-coated waveguide is much larger than that of the plastic-coated waveguide.

For TE_1 mode at $f = 1$ THz, $t = 0.1$ mm, there is a cut-off w_c for plastic-coated waveguide ($w_c = 0$ mm according to Eq. (6-12)), while it is absence for silicon-coated waveguide. We can modify the low cut-off frequency of the waveguide by changing the width of the air interval, which has been discussed in reference [75], however the sensitivity is much lower for silicon-coating waveguide.

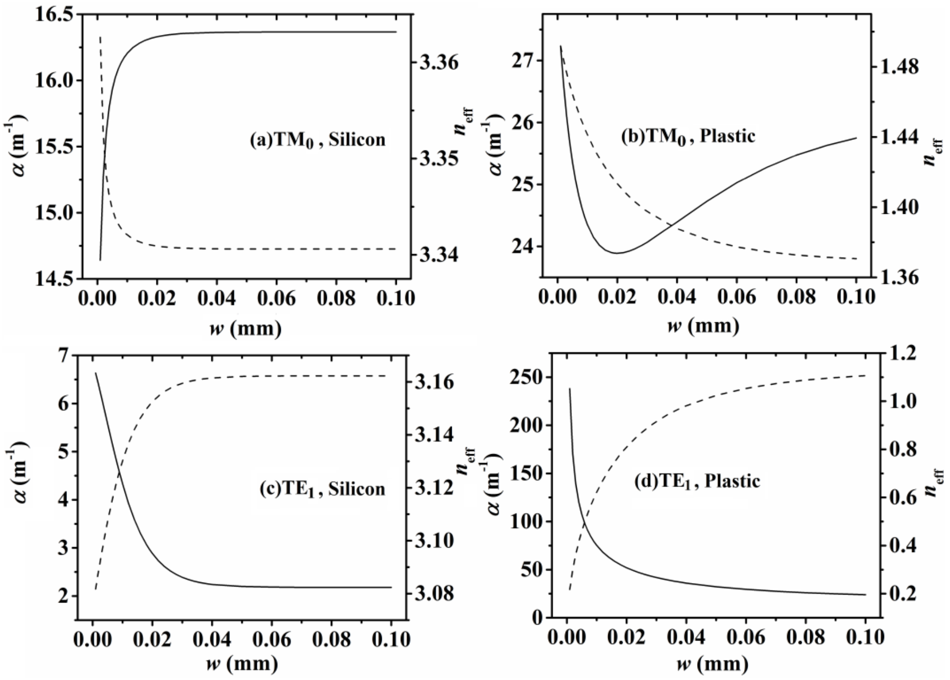

Fig. 6.14 Dependence of loss (solid line) and effective refractive index (dashed line) of the waveguide with the parameter of $t = 0.1$ mm, and frequency $f = 1$ THz on air interval w. (a) is TM_0 mode with a silicon slab; (b) is TM_0 mode with a plastic slab; (c) is TE_1 mode with a silicon slab; (d) is TE_1 mode with a plastic slab.

When $f = 1$ THz, $w = 0.1$ mm, I get the changing laws of loss (solid line) and the effective refractive index (dashed line) of the different slab material waveguide to t, as shown in Fig. 6.15.

There is a loss peak for TM_0 mode in silicon-coated waveguide while it increases monotonously for plastic-coated waveguide. The effective refractive index increases monotonously from 1 to the dielectric refractive index, which is the evidence for more energy in the dielectric slab. And the GVD will be higher for larger t, which is because GVD is a relation between group velocity and THz wave frequency, the coated dielectric slab is a dispersion medium.

There is a low cut-off t_c for TE_1 mode (it is 0.015 mm for silicon waveguide, and 0.033 mm for plastic waveguide, according to Eq. (6-12)). However, when w is large enough, t_c will disappear. The low cut-off t_c is caused for lower optical interval between the two metal plates.

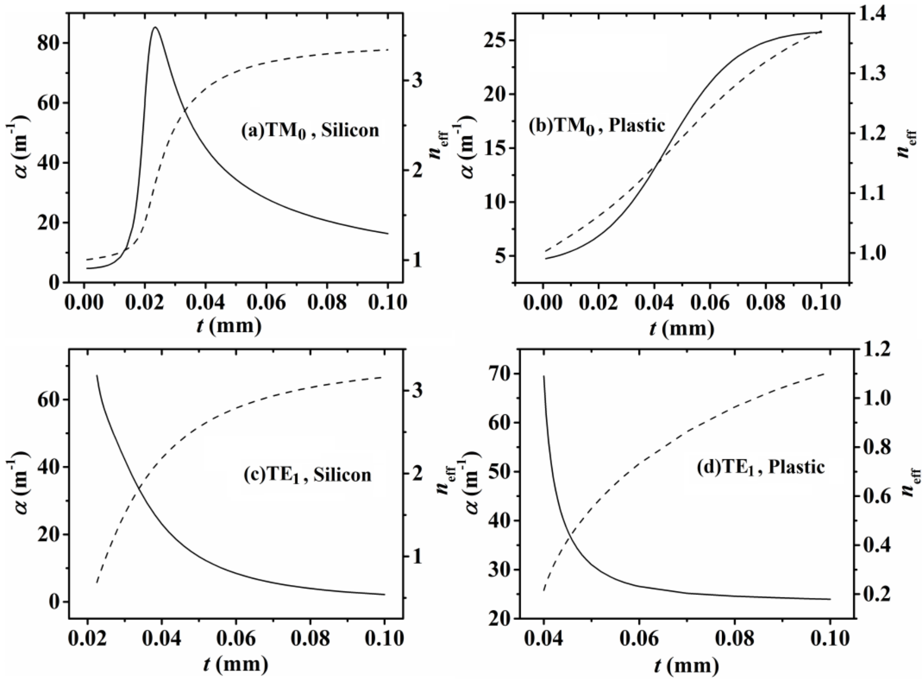

Fig. 6.15 Dependence of loss (solid line) and effective refractive index (dashed line) of the waveguide with the parameter of $w = 0.1$ mm, and frequency $f = 1$ THz on slab thickness t. (a) is TM$_0$ mode with a silicon slab; (b) is TM$_0$ mode with a plastic slab; (c) is TE$_1$ mode with a silicon slab; (d) is TE$_1$ mode with a plastic slab.

6.6.2 The application of refractive index sensing

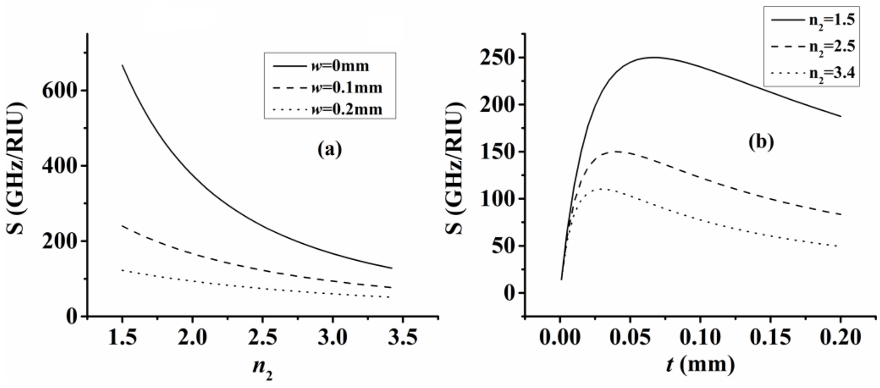

Fig. 6.16 (a) Sensitivities of f_c to refractive index n_2 of the coating slab at different values of n_2 for different waveguide structure. Solid line is at the condition of $w = 0$ mm, dashed line is at the condition of $w = 0.1$ mm, dotted line is at the condition of $w = 0.2$ mm, and $t = 0.1$ mm for all cases; (b) Sensitivities of f_c to n_2 at different values of t for different refractive index of the dielectric slab. Solid line is at the condition of $n_2 = 1.5$, dashed line is at the condition of $n_2 = 2.5$, dotted line is at the condition of $n_2 = 3.4$, and $w = 0.1$ mm for all cases.

According to Eq. (6-12), the low cut-off frequency of TE_1 mode is determined by n_2, t and w. In case of fixed t and w, the changing of n_2 will move the cut-off frequency. So the changing of f_c has a sensitivity to the changing of n_2, and it can be represented as:

$$S = \left|\frac{\partial f_c}{\partial n_2}\right| = \frac{\mathrm{c}t}{2(n_2 t + w)^2} \qquad (6\text{-}13)$$

According to Eq. (6-13), I get the sensitivities of f_c to n_2 at different value of n_2 and t for different waveguide structure, as shown in Fig. 6.16. We can know that the sensitivity decreases monotonously as n_2 increases, and it is larger when w is smaller. When $w = 0$ mm, $n_2 = 1.5$ and $t = 0.1$ mm, the highest sensitivity is up to S = 666.7 GHz/RIU (refractive-index-unit). While there is a peak for S changing to t. When n_2 is smaller, the peak of S appears at larger t (for example the peak appears at $t = 0.065$ mm for $n_2 = 1.5$, while at $t = 0.03$ mm for $n_2 = 3.4$).

6.7 Hybrid THz SPPs in double-dielectric-slab-coated metal plate waveguide (DMPW)

Fig. 6.1 (e) shows the structure of this case. The materials of the coating dielectric slabs are chosen as Polystyrene (PS) and silicon. Copper is adopted as the material of metal plate. When $t = 0.1$ mm, $a = 0.5$ mm, I get the loss (a) and effective refractive index (b) of the l-h coated (silicon is the out-coating) metal plate waveguide and the loss ((c) solid line) and effective refractive index ((c) dashed line) of the h-l coated (silicon is the inner-coating) metal plate waveguide as a function of the THz wave frequency f, as shown in Fig. 6.17.

From Fig. 6.17 (a), we can see even though the basic loss increase monotonously, there are loss nadirs at the frequencies of 0.45 THz, 0.94 THz, 1.42 THz and 1.89 THz. This is also because THz waves appear anti-resonant reflecting. The resonance frequency can also be predicted by Eq. (6-10). I substitute $\mathrm{c} = 3\times10^8$ m/s, $t = 0.1$ mm, $n_3 = 3.42$ and $n_2 = 1.58$ to the equation and get $f_1 = 0.49$ THz, $f_2 = 0.99$ THz, $f_3 = 1.48$ THz and $f_4 = 1.98$ THz, which show good agreements with the calculation results. The peaks of the corresponding effective refractive index at the resonant frequencies (as seen in Fig. 6.17 (b)) tell us that much more energy comes to the low loss and high index silicon. However, in the h-l coated metal plate, the loss (as seen in Fig. 6.17 (c) solid line) and effective index (as seen in Fig. 6.17 (c) dashed line) increase monotonously. This is because when $n_2 > n_3$, THz waves appear total internal reflecting (TIR) on the interface between the inner-coating silicon slab and the out-coating PS slab.

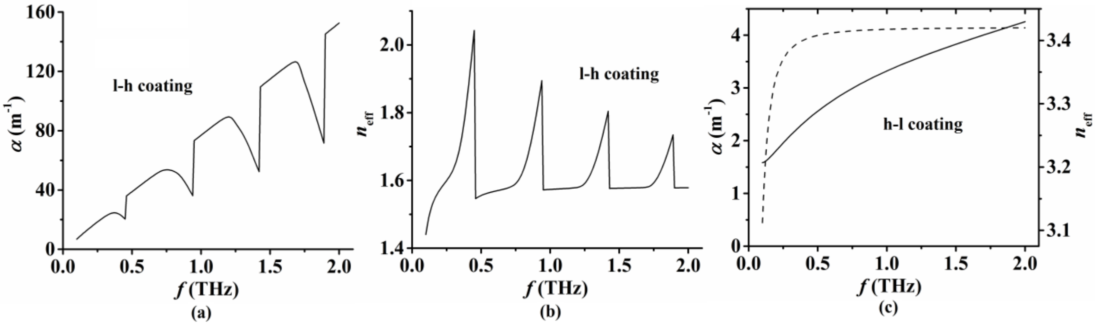

(a) (b) (c)

Fig. 6.17 Laws of the loss (a) and effective refractive index (b) of the l-h coated metal plate waveguide, and the loss ((c) solid line) and effective refractive index ((c) dashed line) of the h-l coated metal plate waveguide changing as a function of the THz wave frequency f.

The THz SPPs are the modes confined on the surface of the metal plate. After double dielectric coating, the modes become hybrid THz SPPs. The modes propagate in the waveguide with the effects of the two coating dielectric slabs and the metal plate. The effects of the l-h coating on the hybrid modes are related to the frequencies. When f is closer to the resonant frequencies, the effects of the out-coating is much stronger than the inner-coating and the hybrid SPP modes are transferring to dielectric modes. However, when f is at the anti-resonant frequencies, the effects of the inner-coating and the metal plate are much stronger than the out-coating and the hybrid modes maintain the characteristics of the

SPP-like modes. In the h-l coating metal plate, the effects of the metal plate and the inner-coating slab are always higher than the out-coating slab, and the hybrid modes are always the SPP-like modes.

I also get the corresponding group velocity of the waveguide when t = 0.1 mm, a = 0.5 mm, as a function of f, as shown in Fig. 6.18. We can see there are nadirs of the group velocity of the l-h coated waveguide, while the group velocity of the h-l coated waveguide changes slightly. This tells us that the GVD of these two waveguides is totally different. The GVD of the l-h coated waveguide is much higher and more complex. This phenomenon is useful for the application as a THz sensor.

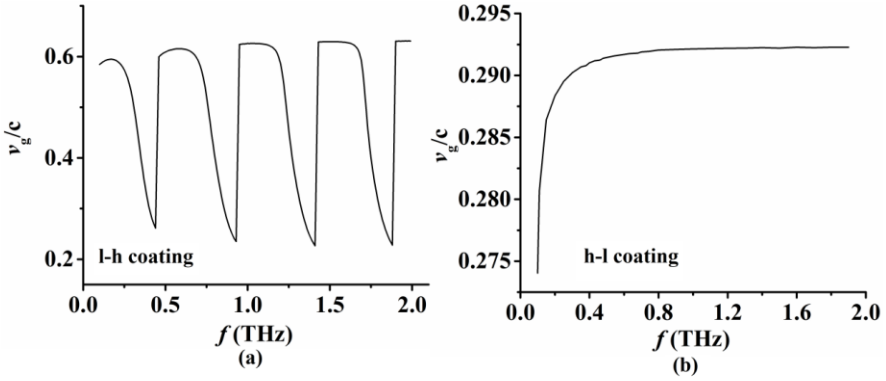

Fig. 6.18 Law of the group velocity changing as a function of f when t = 0.1 mm, a = 0.5 mm of the l-h coated waveguide (a) and the h-l coated waveguide (b).

In order to get a better understanding of the hybrid modes, I get the mode fields of both the l-h coated waveguide and the h-l coated waveguide at f = 1.0 THz or 1.42 THz, t = 0.1 mm and a = 0.5 mm according to Eq. (6-7), as shown in Fig. 6.19. For the l-h coated waveguide, we can see that at the anti-resonant frequency 1.0 THz, THz wave amplitude peak is at the metal plate interface which tells us that at this condition the metal plate still has significant effects on the hybrid modes and the hybrid mode is still SPP-like. From Fig. 6.19 (b), we can see at the resonant frequency 1.42 THz, almost no energy is distributed in the metal plate and only some in the inner-coating PS slab. Most of the energy is distributed in the out-coating silicon slab, which tells us that the hybrid SPPs modes transfer to dielectric modes totally, and the out-coating has the largest effect at this condition.

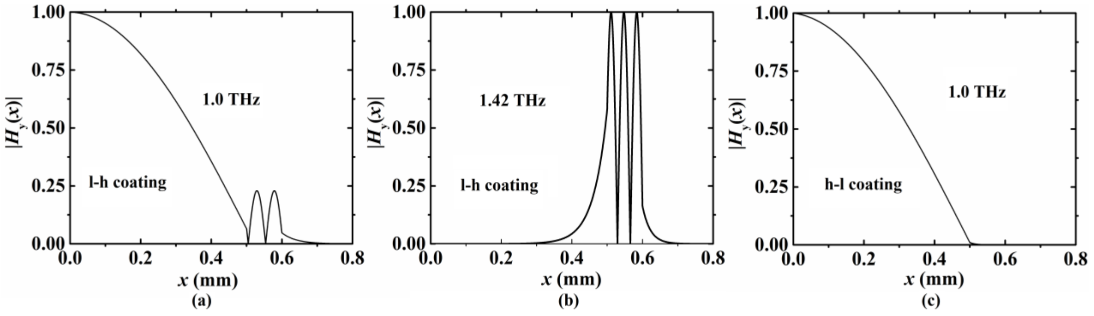

Fig. 6.19 Normalized mode field of l-h coated metal plate at the anti-resonant frequency 1.0 THz (a) and resonance frequency 1.42 THz (b), and the normalized mode field of h-l coated metal plate at 1.0 THz (c).

For the h-l coated waveguide, we can see that at the frequency 1.0 THz, it appears TIR on the interface between the inner-coating silicon and the out-coating PS. The waves in the out-coating PS and the outside air are evanescent waves, and most of the energy is distributed in the inner-coating silicon which has the largest effects on the hybrid modes. For the h-l coating, there is a considerable energy in the metal plate at every frequency which tells us that the metal plate always has significant effects on the hybrid modes and the hybrid mode is always SPP-like.

At $f = 1.0$ THz and $a = 0.5$ mm, I get the loss (a) and the corresponding effective refractive index (b) of the guiding mode in the l-h coated metal plate and the losses in the h-l coated metal plate (c) as a function of t, as shown in Fig. 6.20.

We can see there are loss nadirs at the thicknesses of 0.044 mm, 0.094 mm, 0.144 mm and 0.192 mm in Fig. 6.20 (a). When 1.0 THz becomes the resonant frequency for the out-coating silicon thickness, much more energy will be distributed in the low loss high index silicon. The resonant silicon thicknesses can be predicted by Eq. (6-11). I substitute $c = 3\times10^8$ m/s, $f = 1.0$ THz, $n_2 = 3.42$ and $n_1 = 1.58$ to the equation, and get $t_1 = 0.049$ mm, $t_2 = 0.099$ mm, $t_3 = 0.148$ mm and $t_4 = 0.198$ mm. The numerical values are in good agreement with the theoretical values.

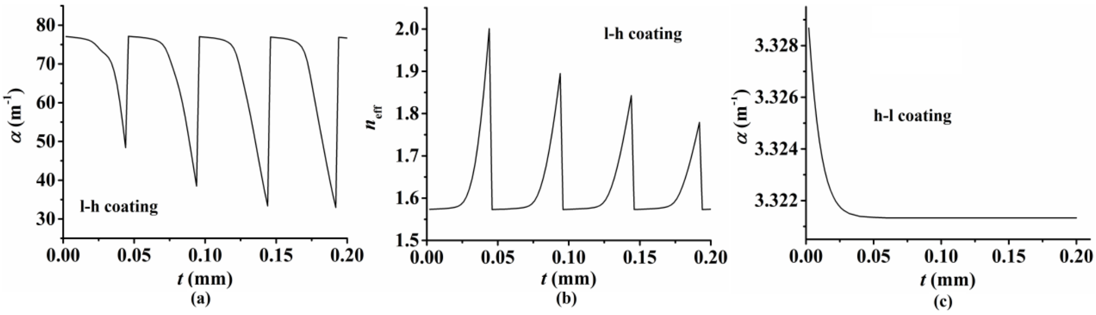

Fig. 6.20 Laws of the loss (a) and the corresponding effective refractive index (b) of the guiding mode in the l-h coated metal plate and the loss in the h-l coated metal plate (c) changing as a function of *t*.

We can know the effects of the two coating dielectric slabs of the l-h coating metal plate on the hybrid THz SPPs is strongly affected by the out coating silicon thickness. At the resonant silicon thicknesses, the effects of the out coating are much more obviously, while at the anti-resonant silicon thicknesses, the effects of the inner coating are much more obviously. However, the loss of the h-l coated metal plate decreases monotonously and change slightly, as can be seen in Fig. 6.20 (c), which tells us that even though the thickness of the out coating PS slab is increasing, its effects on the hybrid modes are much smaller. This is because of the TIR on the interface.

When f = 1.0 THz and t = 0.1 mm, I get the loss (solid line) of the l-h coated metal plate waveguide (a) and the h-l coated metal plate waveguide (b) as a function of *a*, as shown in Fig. 6.21. The dashed line is the corresponding effective refractive index of the guiding mode.

In Fig. 6.21, the loss of the l-h coated waveguide increases monotonously while the loss of the h-l coated waveguide decreases monotonously. And the corresponding effective refractive index increases monotonously to the effective refractive index of the inner-coating material (1.58 for PS, 3.42 for silicon). At a = t = 0.1 mm, the effective refractive index of the l-h coated waveguide is 1.47, and the effective refractive index of the h-l coated waveguide is 3.34, which tells us that in the range of $a > 0.1$ mm, the effects of the inner coating on the hybrid THz SPPs is much more important. When $a < 0.1$ mm, the effective refractive index increases sharply as a increases, which tells us the effects of the inner coating increase quickly.

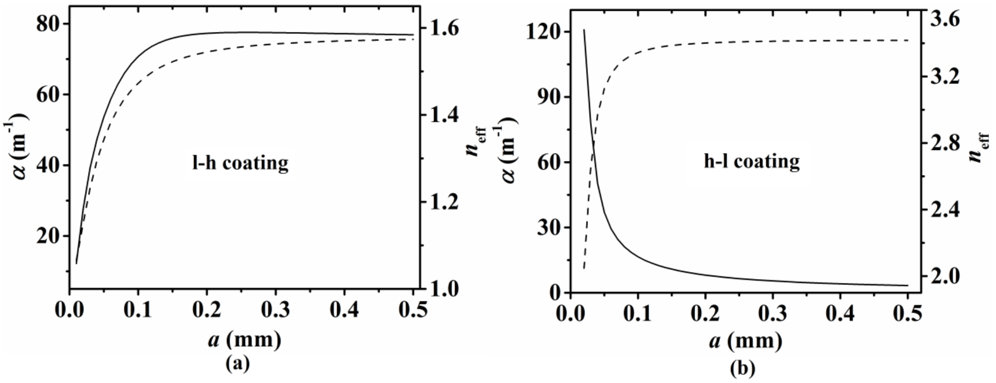

(a) (b)

Fig. 6.21 Laws of loss (solid line) of the l-h coated metal plate waveguide (a) and the h-l coated metal plate waveguide (b) changing as a function of a, the dashed line is the corresponding effective refractive index of the guiding mode.

6.8 Summary

In summary, I have presented five kinds of layered THz waveguides. The modified THz SPPs are guided on DMW. For TW, the waveguide with high-low-high refractive indices guides THz wave as the anti-resonant reflecting. The mode characteristics of both TM and TE mode are shown in MNPW. A TE modes filter for this waveguide is put forward. The GVD of TM_0 mode in SPW is shown. The characteristics of the TE_1 mode low cut-off frequency are given. It shows a sensitivity (S) to the refractive index of the dielectric slab. The highest S can be 666.7 GHz/RIU when $n_2 = 1.5$, $w = 0$ and $t = 0.1$ mm. Moreover, the hybrid THz SPPs on DMPW have been presented. At the resonant frequencies and resonant silicon thicknesses, the hybrid SPP modes transfer to dielectric modes. However, for the h-l coating, the hybrid mode is always a SPP-like mode. I believe that these results are very useful for designing of THz waveguides, sensors, and filters, and for modified and hybrid THz SPPs in waveguides.

Chapter 7

Methodology and Derivations

7.1 Methodology

Different layered graphene waveguides are analyzed and simulated theoretically. Models are developed for structures of suspended two to three graphene layers as well as some other structures. Their performance as the building blocks of various passive components is evaluated in comparisons with other bench-marking technologies.

The dispersion equations of these graphene modulators and multiple-layer THz waveguides are derived. The mode characteristics of these waveguides are obtained from calculation. The structures of the modulators are designed to maximize light-graphene interaction. The performances of these modulators are derived. The applications of these THz waveguides are also put forward.

Third, the mode profile equations of graphene modulators and THz waveguides are calculated and the mode profiles are derived for the analysis and explanation of the results of the mode characteristics. Moreover, the full-wave simulations by COMSOL are followed as a comparison.

7.2 Derivations

7.2.1 Derive of dispersion equations of asymmetrical 4-layer waveguides

The structure of the universe asymmetrical 4-layer waveguides is shown in Fig. 7.1. Four different materials fill in four layers, the side two layers have an infinity thickness, and the middle two layers have a thickness of a and $(b - a)$, respectively. The coordinate system is shown in the figure, the $x = 0$ plane is in the interface between material 1 and material 2. For materials, they have a refractive index which is set to as n_1, n_2, n_3, or n_4 respectively. The width in y-direction is assumed as infinity and doesn't have boundary condition. The modes transmit in z-direction which is perpendicular to the x-y-plane.

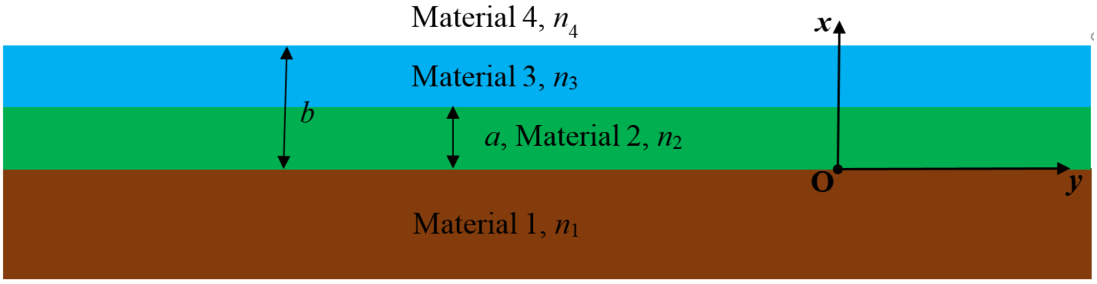

Fig. 7.1 Universe asymmetrical 4-layer waveguides structure.

7.2.1.1 TE mode

As electro-magnetic waves propagate in these materials of this kind of structure, the physics in each layer obey the Maxwell equation and Helmholtz equation. For transverse electric (TE) mode, it only has three components: the transverse electric field E_y (x), the tangential magnetic field H_z (x), and transverse magnetic field H_x (x). The transverse electric field E_y (x) in each layer can be solved by Helmholtz equation as shown below [138]:

$$\frac{\partial^2 E_y(x)}{\partial x^2} + (n_l{}^2 k_0{}^2 - \beta^2) E_y(x) = 0 \qquad (l = 1, 2, 3, 4) \qquad (7\text{-}1),$$

where n_l is the refractive index of material in each layer (l = 1, 2, 3, 4), k_0 is the wave vector in vacuum, and β is the complex propagation constant which includes the effective refractive index (real part) and amplitude loss (imaginary part) of the mode which need to be solved. By solving this equation, then we can get the whole electric field for TE mode, and it can be written as:

$$E_y(x,y,z,t) = E_y(x)e^{-i(\omega t-\beta z)} \tag{7-2}$$

I generally set $n_1k_0, n_4k_0 < \beta < n_2k_0, n_3k_0$, so we can get the wave vector in each layer as:

$h_1 = (\beta^2 - n_1^2k^2)^{1/2}$, $h_2 = (n_2^2k^2 - \beta^2)^{1/2}$, $h_3 = (n_3^2k^2 - \beta^2)^{1/2}$, $h_4 = (\beta^2 - n_4^2k^2)^{1/2}$.

Then the *E* field can be gotten as:

$$E_y(x) = \begin{cases} A_1e^{-h_4(x-b)} & x \ge b \\ A_2\cos h_3(x-a) + A_3\sin h_3(x-a) & a \le x \le b \\ A_4\cos h_2x + A_5\sin h_2x & 0 \le x \le a \\ A_6e^{h_1x} & x \le 0 \end{cases} \tag{7-3}$$

At $x = 0$, $E_y(x)$ is continuous, so we can get:

$$A_6 = A_4 \tag{7-4}$$

At $x = a$, $E_y(x)$ is also continuous, we can get:

$$A_4\cos h_2a + A_5\sin h_2a = A_2 \tag{7-5}$$

At $x = b$:

$$A_2\cos h_3(b-a) + A_3\sin h_3(b-a) = A_1 \tag{7-6}$$

The tangential magnetic field $H_z(x)$ and the transverse electric field $E_y(x)$ has a relation of:

$$H_z(x) = \frac{j}{\omega\mu}\frac{\partial}{\partial x}E_y(x) \tag{7-7}$$

By Eq. (7-7), we can derive the mode field components of $H_z(x)$ in each layer as:

$$H_z(x) = \begin{cases} -A_1h_4e^{-h_4(x-b)} & x \ge b \\ -A_2h_3\sin h_3(x-a) + A_3h_3\cos h_3(x-a) & a \le x \le b \\ -A_4h_2\sin h_2x + A_5h_2\cos h_2x & 0 \le x \le a \\ A_6h_1e^{h_1x} & x \le 0 \end{cases} \tag{7-8}$$

At $x = 0$, $H_z(x)$ is continuous, so we can get:

$$A_6h_1 = A_5h_2 \tag{7-9}$$

At $x = a$, $H_z\,(x)$ is also continuous, we can get:

$$-A_4 h_2 \sin h_2 a + A_5 h_2 \cos h_2 a = A_3 h_3 \qquad (7\text{-}10)$$

At $x = b$:

$$-A_2 h_3 \sin h_3 (b-a) + A_3 h_3 \cos h_3 (b-a) = -A_1 h_4 \qquad (7\text{-}11)$$

By using Eqs. (7-4), (7-5), (7-6), (7-9), (7-10), and (7-11), we can get:

$$-A_4(\cos h_2 a + \frac{h_1}{h_2}\sin h_2 a) h_3 \sin h_3(b-a) - A_4(\frac{h_2}{h_3}\sin h_2 a - \frac{h_1}{h_3}\cos h_2 a) h_3 \cos h_3 (b-a) =$$

$$-(A_4(\cos h_2 a + \frac{h_1}{h_2}\sin h_2 a)\cos h_3(b-a) - A_4(\frac{h_2}{h_3}\sin h_2 a - \frac{h_1}{h_3}\cos h_2 a)\sin h_3(b-a)) h_4$$

=>

$$h_3 \tan h_3 (b-a) + \frac{h_3 h_1}{h_2}\tan h_2 a \tan h_3 (b-a) + h_2 \tan h_2 a - h_1 =$$

$$h_4 + \frac{h_4 h_1}{h_2}\tan h_2 a - \frac{h_4 h_2}{h_3}\tan h_3 (b-a)\tan h_2 a + \frac{h_4 h_1}{h_3}\tan h_3 (b-a)$$

Then we can derive the dispersion relation as:

$$\tan h_2 a = \frac{h_4 + h_1 + (\frac{h_4 h_1}{h_3} - h_3)\tan h_3 (b-a)}{(\frac{h_3 h_1}{h_2} + \frac{h_4 h_2}{h_3})\tan h_3 (b-a) + h_2 - \frac{h_4 h_1}{h_2}} \qquad (7\text{-}12)$$

The mode amplitude coefficients in each layer can be solved accordingly. So, we can derive the mode field distribution equation for TE mode as:

$$E_y(x) = \begin{cases} A[(\cos h_2 a + \frac{h_1}{h_2}\sin h_2 a)\cos h_3 (b-a) - (\frac{h_2}{h_3}\sin h_2 a - \frac{h_1}{h_3}\cos h_2 a)\sin h_3 (b-a)]e^{-h_4 (x-b)} & x \ge b \\ A[(\cos h_2 a + \frac{h_1}{h_2}\sin h_2 a)\cos h_3 (x-a) - (\frac{h_2}{h_3}\sin h_2 a - \frac{h_1}{h_3}\cos h_2 a)\sin h_3 (x-a)] & a \le x \le b \\ A[\cos h_2 x + \frac{h_1}{h_2}\sin h_2 x] & 0 \le x \le a \\ Ae^{h_1 x} & x \le 0 \end{cases} \qquad (7\text{-}13)$$

7.2.1.2 TM mode

For transverse magnetic (TM) mode, it only has three components: the transverse magnetic field $H_y\,(x)$, the tangential electric field $E_z\,(x)$, and transverse electric field $E_x\,(x)$. The transverse magnetic field $H_y\,(x)$ in each layer can be solved by Helmholtz equation.

In general, here I set:

$h_1=(\beta^2-n_1^{\,2}k^2)^{1/2}$, $h_2=(n_2^{\,2}k^2-\beta^2)^{1/2}$, $h_3=(n_3^{\,2}k^2-\beta^2)^{1/2}$, $h_4=(\beta^2-n_4^{\,2}k^2)^{1/2}$, The transverse magnetic field $H_y(x)$ in each layer can be written as:

$$H_y(x)=\begin{cases} A_1e^{-h_4(x-b)} & x\geq b \\ A_2\cos h_3(x-a)+A_3\sin h_3(x-a) & a\leq x\leq b \\ A_4\cos h_2x+A_5\sin h_2x & 0\leq x\leq a \\ A_6e^{h_1x} & x\leq 0 \end{cases} \tag{7-14}$$

At $x = 0$, $H_y(x)$ is continuous, so we can get:

$$A_6=A_4 \tag{7-15}$$

At $x = a$, $H_y(x)$ is also continuous, we can get:

$$A_4\cos h_2a+A_5\sin h_2a=A_2 \tag{7-16}$$

At $x = b$:

$$A_2\cos h_3(b-a)+A_3\sin h_3(b-a)=A_1 \tag{7-17}$$

The transverse magnetic field $H_y(x)$ and the transverse electric field $E_z(x)$ has a relation of:

$$H_z(x)=-\frac{j}{\omega\varepsilon}\frac{\partial}{\partial x}E_y(x) \tag{7-18}$$

$$E_z(x)=-\frac{i}{\omega}\begin{cases} -A_1\dfrac{h_4}{\varepsilon_4}e^{-h_4(x-b)} & x\geq b \\ -A_2\dfrac{h_3}{\varepsilon_3}\sin h_3(x-a)+A_3\dfrac{h_3}{\varepsilon_3}\cos h_3(x-a) & a\leq x\leq b \\ -A_4\dfrac{h_2}{\varepsilon_2}\sin h_2x+A_5\dfrac{h_2}{\varepsilon_2}\cos h_2x & 0\leq x\leq a \\ A_6\dfrac{h_1}{\varepsilon_1}e^{h_1x} & x\leq 0 \end{cases} \tag{7-19}$$

where $\varepsilon_1=n_1^2$, $\varepsilon_2=n_2^2$, $\varepsilon_3=n_3^2$, $\varepsilon_4=n_4^2$. At $x = 0$, $E_z(x)$ is continuous, so we can get:

$$A_6\frac{h_1}{\varepsilon_1}=A_5\frac{h_2}{\varepsilon_2} \tag{7-20}$$

At $x = a$, $E_z(x)$ is also continuous, we can get:

$$-A_4\frac{h_2}{\varepsilon_2}\sin h_2a+A_5\frac{h_2}{\varepsilon_2}\cos h_2a=A_3\frac{h_3}{\varepsilon_3} \tag{7-21}$$

At $x = b$:

$$-A_2\frac{h_3}{\varepsilon_3}\sin h_3(b-a)+A_3\frac{h_3}{\varepsilon_3}\cos h_3(b-a)=-A_1\frac{h_4}{\varepsilon_4} \qquad (7\text{-}22)$$

By using Eqs. (7-15), (7-16), (7-17), (7-20), (7-21), and (7-22), we can get:

$$-A_4(\cos h_2a+\frac{h_1\varepsilon_2}{h_2\varepsilon_1}\sin h_2a)\frac{h_3}{\varepsilon_3}\sin h_3(b-a)-A_4(\frac{h_2\varepsilon_3}{h_3\varepsilon_2}\sin h_2a-\frac{h_1\varepsilon_3}{h_3\varepsilon_1}\cos h_2a)\frac{h_3}{\varepsilon_3}\cos h_3(b-a)=$$
$$-(A_4(\cos h_2a+\frac{h_1\varepsilon_2}{h_2\varepsilon_1}\sin h_2a)\cos h_3(b-a)-A_4(\frac{h_2\varepsilon_3}{h_3\varepsilon_2}\sin h_2a-\frac{h_1\varepsilon_3}{h_3\varepsilon_1}\cos h_2a)\sin h_3(b-a))\frac{h_4}{\varepsilon_4}$$

$$=>$$

$$\frac{h_3}{\varepsilon_3}\tan h_3(b-a)+\frac{h_3h_1\varepsilon_2}{h_2\varepsilon_1\varepsilon_3}\tan h_2a\tan h_3(b-a)+\frac{h_2}{\varepsilon_2}\tan h_2a-\frac{h_1}{\varepsilon_1}=$$
$$\frac{h_4}{\varepsilon_4}+\frac{h_4h_1\varepsilon_2}{h_2\varepsilon_1\varepsilon_4}\tan h_2a-\frac{h_4h_2\varepsilon_3}{h_3\varepsilon_2\varepsilon_4}\tan h_3(b-a)\tan h_2a+\frac{h_4h_1\varepsilon_3}{h_3\varepsilon_1\varepsilon_4}\tan h_3(b-a)$$

Then we can derive the dispersion relation as:

$$\tan h_2a=\frac{\frac{h_4}{\varepsilon_4}+\frac{h_1}{\varepsilon_1}+(\frac{h_4h_1\varepsilon_3}{h_3\varepsilon_1\varepsilon_4}-\frac{h_3}{\varepsilon_3})\tan h_3(b-a)}{(\frac{h_3h_1\varepsilon_2}{h_2\varepsilon_1\varepsilon_3}+\frac{h_4h_2\varepsilon_3}{h_3\varepsilon_2\varepsilon_4})\tan h_3(b-a)+\frac{h_2}{\varepsilon_2}-\frac{h_4h_1\varepsilon_2}{h_2\varepsilon_1\varepsilon_4}} \qquad (7\text{-}23)$$

The mode amplitude coefficients in each layer can be solved accordingly. And the field distribution equation for TM mode in each layer can be written as:

$$H_y(x)=\begin{cases} A[(\cos h_2a+\frac{h_1\varepsilon_2}{h_2\varepsilon_1}\sin h_2a)\cos h_3(b-a)-(\frac{h_2\varepsilon_3}{h_3\varepsilon_2}\sin h_2a-\frac{h_1\varepsilon_3}{h_3\varepsilon_1}\cos h_2a)\sin h_3(b-a)]e^{-h_4(x-b)} & x\geq b \\ A[(\cos h_2a+\frac{h_1\varepsilon_2}{h_2\varepsilon_1}\sin h_2a)\cos h_3(x-a)-(\frac{h_2\varepsilon_3}{h_3\varepsilon_2}\sin h_2a-\frac{h_1\varepsilon_3}{h_3\varepsilon_1}\cos h_2a)\sin h_3(x-a)] & a\leq x\leq b \\ A[\cos h_2x+\frac{h_1\varepsilon_2}{h_2\varepsilon_1}\sin h_2x] & 0\leq x\leq a \\ Ae^{h_1x} & x\leq 0 \end{cases}$$

(7-24)

7.2.2 Derive of dispersion equations of symmetrical 5-layer waveguides

The structure of the universe symmetrical 5-layer waveguides is shown in Fig. 7.2. Three different materials fill in symmetrical 5 layers, the side two layers have an infinity thickness, and the middle three layers have a thickness of $2a$, $(b-a)$, and $(b-a)$, respectively. The coordinate system is shown in the figure, the $x = 0$ plane is in the middle of the symmetrical structure. For materials, they have a refractive index which is set to as n_1, n_2, or n_3, respectively. The width in y-direction is assumed as infinity and doesn't have boundary condition. The modes are guided in z-direction.

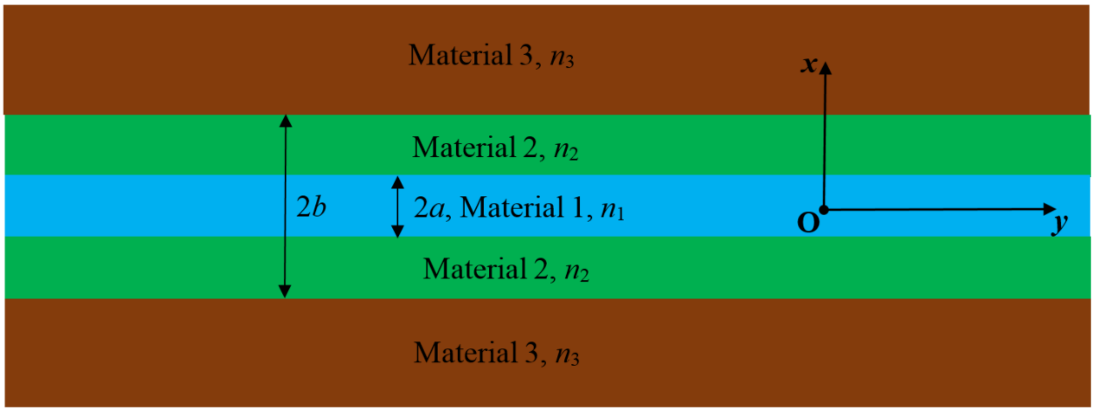

Fig. 7.2 Universe symmetrical 5-layer waveguides structure.

7.2.2.1 TE mode

For TE mode, the whole electric field can be written as: $E_y(x,y,z,t) = E_y(x)e^{-i(\omega t-\beta z)}$.

Here is the same as above to solve the Helmholtz equation:

$$\frac{\partial^2 E_y(x)}{\partial x^2} + (n_l{}^2 k_0{}^2 - \beta^2)E_y(x) = 0 \qquad (l = 1,\ 2,\ 3)$$

In generally, I set: $n_3 k_0 < n_2 k_0 < \beta < n_1 k_0$

When $l = 1$, I set $h_1 = (n_1{}^2 k_0{}^2 - \beta^2)^{\frac{1}{2}}$, by Helmholtz equation, we can get:

$$E_y(x) = A_1 \cos(h_1 x) \qquad -a \le x \le a \qquad (7\text{-}25)$$

When $l = 2$, I set $h_2 = (\beta^2 - n_2{}^2 k_0{}^2)^{\frac{1}{2}}$, by Helmholtz equation, we can get:

$$E_y(x) = \begin{cases} A_2 e^{-h_2(x-a)} + A_3 e^{h_2(x-a)} & a \le x \le b \\ A_4 e^{-h_2(x+a)} + A_5 e^{h_2(x+a)} & -b \le x \le -a \end{cases} \qquad (7\text{-}26)$$

When $l = 3$, I set $h_3 = (\beta^2 - n_3{}^2 k_0{}^2)^{\frac{1}{2}}$, by Helmholtz equation, we can get:

$$E_y(x) = \begin{cases} A_6 e^{-h_3(x-b)} & x \ge b \\ A_6 e^{h_3(x+b)} & x \le -b \end{cases} \qquad (7\text{-}27)$$

At $x = a$, $E_y(x)$ is continuous, so we can get:

$$A_1 \cos(h_1 a) = A_2 + A_3 \tag{7-28}$$

At $x = b$:

$$A_2 e^{-h_2(b-a)} + A_3 e^{h_2(b-a)} = A_6 \tag{7-29}$$

At $x = -a$:

$$A_1 \cos(h_1 a) = A_4 + A_5 \tag{7-30}$$

At $x = -b$:

$$A_4 e^{-h_2(-b+a)} + A_5 e^{h_2(-b+a)} = A_6 \tag{7-31}$$

At $x = a$, $\dfrac{\partial E_y(x)}{\partial x}$ is continuous, so we can get:

$$-A_1 \sin(h_1 a) \cdot h_1 = -A_2 h_2 + A_3 h_2 \tag{7-32}$$

At $x = b$:

$$-A_2 e^{-h_2(b-a)} h_2 + A_3 e^{h_2(b-a)} h_2 = -A_6 h_3 \tag{7-33}$$

At $x = -a$:

$$A_1 \sin(h_1 a) \cdot h_1 = -A_4 h_2 + A_5 h_2 \tag{7-34}$$

At $x = -b$:

$$-A_4 e^{-h_2(-b+a)} h_2 + A_5 e^{h_2(-b+a)} h_2 = A_6 h_3 \tag{7-35}$$

For even mode, we have:

$$A_3 = A_4 \ \text{ and } A_2 = A_5 \tag{7-36}$$

We substitute (7-36) to (7-28) and (7-30), we can get:

$$A_2 + A_3 = A_1 \cos(h_1 a) \tag{7-37}$$

We substitute (7-36) to (7-32) and (7-34), we can get:

$$-A_2 h_2 + A_3 h_2 = -A_1 \sin(h_1 a) \cdot h_1 \tag{7-38}$$

We substitute (7-36) to (7-29) and (7-31), we can get:

$$A_2 e^{h_2(-b+a)} + A_3 e^{-h_2(-b+a)} = A_6 \tag{7-39}$$

We substitute (7-36) to (7-33) and (7-35), we can get:

$$A_2 e^{h_2(-b+a)} h_2 - A_3 e^{-h_2(-b+a)} h_2 = A_6 h_3 \qquad (7\text{-}40)$$

By (7-37) to (7-40), for there is a No-zero solution, we can have:

$$\begin{bmatrix} -\mathrm{Cos}[ah_1], & 1, & 1, & 0 \\ \mathrm{Sin}[ah_1]*h_1, & -h_2, & h_2, & 0 \\ 0, & e^{h_2(a-b)}, & e^{-h_2(a-b)}, & -1 \\ 0, & e^{h_2(a-b)}h_2, & -e^{-h_2(a-b)}h_2, & -h_3 \end{bmatrix} = 0 \quad (7\text{-}41)$$

To solve this Matrix, we can get:

$$h_1 a = \tan^{-1}\left[\frac{h_2}{h_1}\frac{h_2 + h_3 + (-h_2 + h_3)e^{2h_2(-b+a)}}{h_2 + h_3 - (-h_2 + h_3)e^{2h_2(-b+a)}}\right] \qquad (7\text{-}42)$$

This is the dispersion equation.

If I set $n_3 k_0 < \beta < n_2 k_0 < n_1 k_0$, we can get another version of this dispersion equation as:

$$h_1 a = \tan^{-1}\left[\frac{1 - \frac{h_2}{h_3}\tan h_2(b-a)}{\frac{h_1}{h_2}\tan h_2(b-a) + \frac{h_1}{h_3}}\right] \qquad (7\text{-}43),$$

where $h_2 = (n_2{}^2 k_0{}^2 - \beta^2)^{\frac{1}{2}}$, h_1 and h_3 are the same. These two equations have the same solution. I only use one version of this equation.

We can derive the TE mode field distribution equation for case $n_3 k_0 < \beta < n_2 k_0 < n_1 k_0$ as:

$$E_y(x) = \begin{cases} A_1[\cos(h_1 a)\cos h_2(b-a) - \frac{h_1}{h_2}\sin(h_1 a)\sin h_2(b-a)]e^{-h_3(x-b)} & x \ge b \\ A_1[\cos(h_1 a)\cos h_2(x-a) - \frac{h_1}{h_2}\sin(h_1 a)\sin h_2(x-a)] & a \le x \le b \\ A_1\cos(h_1 x) & -a \le x \le a \\ A_1[\cos(h_1 a)\cos h_2(x+a) + \frac{h_1}{h_2}\sin(h_1 a)\sin h_2(x+a)] & -b \le x \le -a \\ A_1[\cos(h_1 a)\cos h_2(b-a) - \frac{h_1}{h_2}\sin(h_1 a)\sin h_2(b-a)]e^{h_3(x+b)} & x \le -b \end{cases}$$

(7-44)

7.2.2.2 TM mode

Here I set: $h_1 = (n_1^2 k_0^2 - \beta^2)^{1/2}$, $h_2 = (n_2^2 k_0^2 - \beta^2)^{1/2}$, $h_3 = (\beta^2 - n_3^2 k_0^2)^{1/2}$ for the condition of $n_3k_0 < \beta < n_2k_0 < n_1k_0$.

So, the field distribution for TM mode is:

$$H_y(x) = \begin{cases} A_1\cos(h_1x) & -a \le x \le a \\ A_2\cos h_2(x-a) + A_3\sin h_2(x-a) & a \le x \le b \\ A_4\cos h_2(x+a) + A_5\sin h_2(x+a) & -b \le x \le -a \\ A_6e^{-h_3(x-b)} & x \ge b \\ A_6e^{h_3(x+b)} & x \le -b \end{cases} \tag{7-45}$$

At x = a, $H_y(x)$ is continuous, we can have:

$$A_1\cos(h_1a) = A_2 \tag{7-46}$$

At x = b:

$$A_2\cos h_2(b-a) + A_3\sin h_2(b-a) = A_6 \tag{7-47}$$

At x = -a:

$$A_1\cos(h_1a) = A_4 \tag{7-48}$$

At x = -b:

$$A_4\cos h_2(-b+a) + A_5\sin h_2(-b+a) = A_6 \tag{7-49}$$

Then $E_z(x)$ can be derived as by using equation:

$$E_z(x) = -\frac{i}{\omega}\begin{cases} -A_1\frac{h_1}{\varepsilon_1}\sin(h_1x) & -a \le x \le a \\ -A_2\frac{h_2}{\varepsilon_2}\sin h_2(x-a) + A_3\frac{h_2}{\varepsilon_2}\cos h_2(x-a) & a \le x \le b \\ -A_4\frac{h_2}{\varepsilon_2}\sin h_2(x+a) + A_5\frac{h_2}{\varepsilon_2}\cos h_2(x+a) & -b \le x \le -a \\ -A_6\frac{h_3}{\varepsilon_3}e^{-h_3(x-b)} & x \ge b \\ A_6\frac{h_3}{\varepsilon_3}e^{h_3(x+b)} & x \le -b \end{cases} \quad (7\text{-}50),$$

where $\varepsilon_1 = n_1^2$, $\varepsilon_2 = n_2^2$, $\varepsilon_3 = n_3^2$.

At x = a, E_z(x) is continuous, we can have:

$$-A_1\frac{h_1}{\varepsilon_1}\sin(h_1a) = A_3\frac{h_2}{\varepsilon_2} \tag{7-51}$$

At x = b:

$$-A_2\frac{h_2}{\varepsilon_2}\sin h_2(b-a)+A_3\frac{h_2}{\varepsilon_2}\cos h_2(b-a)=-A_6\frac{h_3}{\varepsilon_3} \quad (7\text{-}52)$$

At x = -a:

$$A_1\frac{h_1}{\varepsilon_1}\sin(h_1a)=A_5\frac{h_2}{\varepsilon_2} \quad (7\text{-}53)$$

At x = -b:

$$-A_4\frac{h_2}{\varepsilon_2}\sin h_2(-b+a)+A_5\frac{h_2}{\varepsilon_2}\cos h_2(-b+a)=A_6\frac{h_3}{\varepsilon_3} \quad (7\text{-}54)$$

By (7-46) and (7-48), we can get:

$$A_2=A_4=A_1\cos(h_1a) \quad (7\text{-}55)$$

By (7-51) and (7-53), we can get:

$$A_3=-A_5=-A_1\frac{h_1\varepsilon_2}{h_2\varepsilon_1}\sin(h_1a) \quad (7\text{-}56)$$

Substitute (7-55) and (7-56) to (7-47), (7-49), (7-52), and (7-54), we can get:

$$\cos(h_1a)\cos h_2(b-a)-\frac{h_1\varepsilon_2}{h_2\varepsilon_1}\sin(h_1a)\sin h_2(b-a)=A_6/A_1 \quad (7\text{-}57)$$

$$\cos(h_1a)\frac{h_2\varepsilon_3}{h_3\varepsilon_2}\sin h_2(b-a)+\frac{h_1\varepsilon_2}{h_2\varepsilon_1}\sin(h_1a)\frac{h_2\varepsilon_3}{h_3\varepsilon_2}\cos h_2(b-a)=A_6/A_1 \quad (7\text{-}58)$$

By (7-57) and (7-58), we can get:

$$1-\frac{h_1\varepsilon_2}{h_2\varepsilon_1}\tan(h_1a)\tan h_2(b-a)=\frac{h_2\varepsilon_3}{h_3\varepsilon_2}\tan h_2(b-a)+\frac{h_1\varepsilon_2}{h_2\varepsilon_1}\frac{h_2\varepsilon_3}{h_3\varepsilon_2}\tan(h_1a) \quad (7\text{-}59)$$

Simplify (7-59), we can get:

$$\tan(h_1a)=\frac{1-\dfrac{h_2\varepsilon_3}{h_3\varepsilon_2}\tan h_2(b-a)}{\dfrac{h_1\varepsilon_3}{h_3\varepsilon_1}+\dfrac{h_1\varepsilon_2}{h_2\varepsilon_1}\tan h_2(b-a)} \quad (7\text{-}60)$$

This is the dispersion relation.

We can derive the mode field distribution equation as:

$$H_y(x) = \begin{cases} A_1 \cos(h_1 x) & -a \le x \le a \\ A_1[\cos(h_1 a)\cos h_2(x-a) - \dfrac{h_1 \varepsilon_2}{h_2 \varepsilon_1}\sin(h_1 a)\sin h_2(x-a)] & a \le x \le b \\ A_1[\cos(h_1 a)\cos h_2(x+a) + \dfrac{h_1 \varepsilon_2}{h_2 \varepsilon_1}\sin(h_1 a)\sin h_2(x+a)] & -b \le x \le -a \\ A_1[\cos(h_1 a)\cos h_2(b-a) - \dfrac{h_1 \varepsilon_2}{h_2 \varepsilon_1}\sin(h_1 a)\sin h_2(b-a)]e^{-h_3(x-b)} & x \ge b \\ A_1[\cos(h_1 a)\cos h_2(b-a) - \dfrac{h_1 \varepsilon_2}{h_2 \varepsilon_1}\sin(h_1 a)\sin h_2(b-a)]e^{h_3(x+b)} & x \le -b \end{cases}$$

(7-61)

7.2.3 Derive of dispersion equations of symmetrical 7-layer waveguides

The structure of the universe symmetrical 7-layer waveguides is shown in Fig. 7.3. Four different materials fill in symmetrical 7 layers, the outside two layers have an infinity thickness, and the middle five layers have a thickness of $2a$, $(b - a)$, $(b - a)$, $(c - b)$, and $(c - b)$, respectively. The coordinate system is shown in the figure, the $x = 0$ plane is in the middle of the symmetrical structure. For materials, they have a refractive index which is set to as n_1, n_2, or n_3, n_4, respectively. The width in y-direction is assumed as infinity and doesn't have boundary condition. The modes are guided in z-direction.

TE mode:

The start of the derivation is still to solve the Helmholtz equation:

$$\frac{\partial^2 E_y(x)}{\partial x^2} + (n_l^2 k_0^2 - \beta^2) E_y(x) = 0 \qquad (l = 1, 2, 3, 4)$$

I set: $n_4 k_0 < n_3 k_0 < \beta < n_2 k_0 < n_1 k_0$

When $l = 1$, I set $h_1 = (n_1^2 k_0^2 - \beta^2)^{\frac{1}{2}}$, and by Helmholtz equation, we can get:

$$E_y(x) = A_1 \cos(h_1 x) \qquad -a \le x \le a \qquad (7\text{-}62)$$

When $l = 2$, I set $h_2 = (n_2^2 k_0^2 - \beta^2)^{\frac{1}{2}}$, and get:

$$E_y(x)=\begin{cases}A_2\cos h_2(x-a)+A_3\sin h_2(x-a) & a\le x\le b\\ A_4\cos h_2(x+a)+A_5\sin h_2(x+a) & -b\le x\le -a\end{cases}\tag{7-63}$$

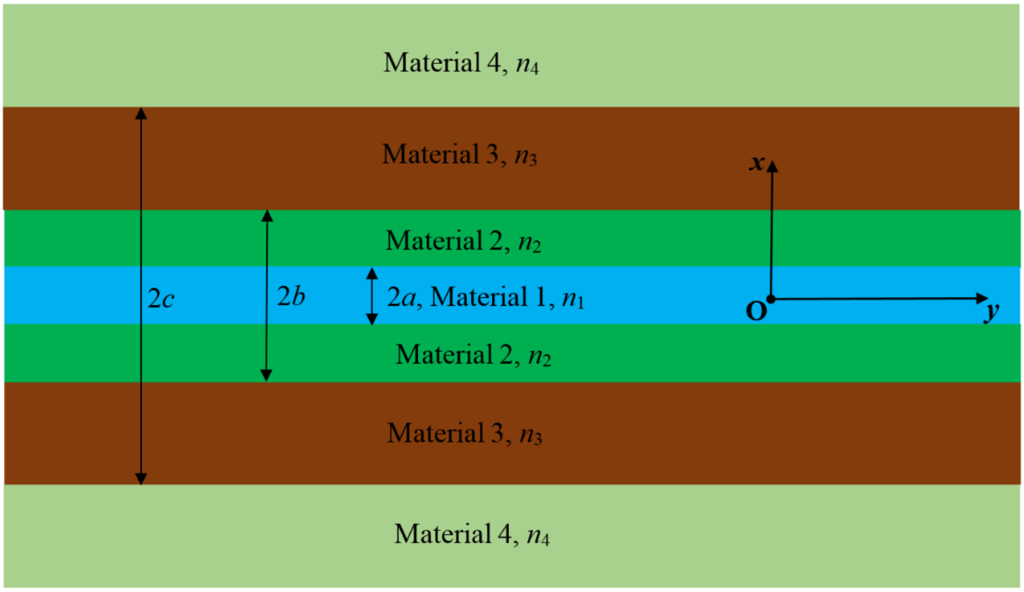

Fig. 7.3 Universe symmetrical 7-layer waveguides structure.

When l = 3, I set $h_3=(\beta^2-n_3{}^2k_0{}^2)^{\frac{1}{2}}$, and get:

$$E_y(x)=\begin{cases}A_6e^{-h_3(x-b)}+A_7e^{h_3(x-b)} & b\le x\le c\\ A_8e^{-h_3(x+b)}+A_9e^{h_3(x+b)} & -c\le x\le -b\end{cases}\tag{7-64}$$

When l = 4, I set $h_4=(\beta^2-n_4{}^2k_0{}^2)^{\frac{1}{2}}$, and get:

$$E_y(x)=\begin{cases}A_{10}e^{-h_4(x-c)} & x\ge c\\ A_{10}e^{h_4(x+c)} & x\le -c\end{cases}\tag{7-65}$$

By the steps shown above, the dispersion equation of this symmetrical 7-layer waveguides can be gotten as:

$$\tan(h_1a)=\frac{\begin{array}{c}[1+\tan h_2(b-a)\cdot\frac{h_2}{h_3}-\frac{h_3}{h_4}-\frac{h_2}{h_4}\tan h_2(b-a)]e^{-h_3(c-b)}\\ +[1-\tan h_2(b-a)\cdot\frac{h_2}{h_3}+\frac{h_3}{h_4}-\frac{h_2}{h_4}\tan h_2(b-a)]e^{h_3(c-b)}\end{array}}{\begin{array}{c}[-\frac{h_3}{h_4}\frac{h_1}{h_2}\tan h_2(b-a)+\frac{h_1}{h_4}+\frac{h_1}{h_2}\tan h_2(b-a)-\frac{h_1}{h_3}]e^{-h_3(c-b)}\\ +[\frac{h_3}{h_4}\frac{h_1}{h_2}\tan h_2(b-a)+\frac{h_1}{h_4}+\frac{h_1}{h_2}\tan h_2(b-a)+\frac{h_1}{h_3}]e^{h_3(c-b)}\end{array}}\tag{7-66}$$

Chapter 8

Summary and Future Work

In this thesis, two main topics were presented, analyzed and discussed: one is the suspended graphene modulators and one is the multiple-layer THz waveguides. A comprehensive literature review was conducted on graphene modulators and THz waveguides to identify the current research challenges and gaps.

8.1 The achieved research objectives

The first objective of this research is to develop high performance graphene-based modulators. The project focuses on suspended waveguide-based modulators: both electro-absorptive and -refractive types. The FOMs of a graphene modulator are improved by this research: footprint (of the scale of 0.94 μm^2), modulation speed (competitive values of the order 759.85 GHz), modulation depth (greater than 90% for electro-absorptive type, 100% for electro-refractive type), operation bandwidth (greater than 15 THz), and energy consumption (on the scale of 0.61 fJ/bit). The design of the suspended graphene modulators is very near the fundamental limits of graphene.

The second objective of this research is to develop THz waveguides. Five types of layered THz waveguides for different applications. The project focuses on 4 and 5 layers planar THz waveguides. The physics of these layered THz waveguides are developed and different applications are put forward for the first time.

8.2 Summary

In **chapter 1**:

A very detailed review about graphene modulators and THz waveguides is conducted. The basic physics (such as conductivity and mobility) of graphene are analyzed. The suspended graphene with high quality and much less impurity residues is reported to achieve much lower impurity scattering and ultrahigh mobility.

Particularly, a very detailed review of graphene modulators were thoroughly conducted. The first part of state of the arts of graphene modulators have been done by studying 25 references about modulators in the time scale from 2004 to 2016. The problems in graphene-based modulators which this research based are listed.

Different THz waveguides have been talked. Different kinds of SPP modes have been discussed.

The second part of review of graphene modulators is shown. The state-of-the-art values of every FOM parameter is recorded in Table 3 to show how low FOMs are developing to high FOMs.

In **chapter 2**:

An ultra-fast suspended self-biasing graphene modulator is researched. The light-graphene interaction is enhanced significantly by this symmetrical structure. The insertion loss is very low for the suspended symmetrical structure, and the FOM is ultrahigh.

The electro-absorption modulation shows a FOM of ~ 2700. The electro-refractive modulation shows one 100% modulation depth. The compromise between modulation speed and modulation efficiency is reduced significantly and this design is very near the fundamental limits of graphene. With all these merits, the modulation efficiency is also very high.

In **chapter 3**:

The suspended triple-layer graphene modulator which shows two modulation depths and high modulation speed is presented. These two modulation depths are caused by the two side graphene layers and the middle graphene layer separately. The light-graphene interaction is enhanced further by the middle graphene layer is always put in the mode center (mode energy peak).

The FOM of electro-absorption modulation can also be 2105. And there show several 100% modulations for electro-refractive modulation. The modulation speed can be 759.85 GHz with very low applied voltage and very low energy consumption. And the compromise between modulation speed and modulation efficiency is reduced further.

In **chapter 4**:

A comparison between suspended double-layer graphene modulator and sub-wavelength thickness graphene modulator is presented. A leaky mode in the sub-wavelength thickness graphene modulator is found, which should be avoid when designing. The basic MPA for STM is very high, causing a very high insertion loss. The FOM of SDM can be ultrahigh (~ 2480), however, for STM, it is only 1.28. They both show reducing of the compromise between modulation speed and modulation efficiency.

In **chapter 5**:

A design of metal-clad suspended self-biasing graphene modulator is shown. With metal-cladding, the light-graphene interaction can be enhanced with lower insulator slab thickness w and lower air gap width d between metal plates and the suspended structure. However, the light-metal interaction is also stronger for smaller size which causes larger insertion loss. The FOM of this modulator is tunable by moveable metal-cladding. The design is nearer fundamental limits of graphene when the metal-cladding is further away the suspended structure. However, we can control the tunable light-graphene interaction by smaller size (lower w and d) of this modulator. The cut-off mode is also discussed for tunable filter application.

In **chapter 6**:

Five kinds of layered THz waveguides were presented. The modified THz SPPs on DMW is discussed. For TW, the waveguide with high-low-high refractive indices guides THz wave as the anti-resonant reflecting mechanism. The mode characteristics of both TM mode and TE mode in MNW are presented, and the application of a TE modes filter for this waveguide is put forward. The GVD of TM_0 mode in SPW is discussed. For TE_1 mode, the characteristics of the low cut-off frequency are given. The low cut-off frequency has a sensitivity (S) to the refractive index of the dielectric slab. The highest S can be 666.7 GHz/RIU when $n_2 = 1.5$, $w = 0$ and $t = 0.1$ mm. Moreover, the hybrid THz SPPs on DMPW have been presented. At the resonant frequencies and resonant silicon thicknesses of the l-h coating, the hybrid SPP modes transfer to dielectric modes. However, for the h-l coating, the hybrid mode is always a SPP-like mode. I believe that these results are very useful for designing of THz waveguides, sensors, and filters, and for modified and hybrid THz SPPs in waveguides.

In **chapter 7**, the applied methodology of this research and the derivations are shown.

8.3 Future work and perspectives

8.3.1 Future work

According to my knowledge, the tolerance analyzing for these waveguides is very important for future fabrication. These fabrications will require a precision to the nanometer scale for the low error and high sensitivity for these physics in these waveguides.

For **chapter 2**:

The suspended self-biasing graphene modulator will need to be fabricated at the parameters of: 1. insulator material h-BN (ε_1 = 3.24), insulator thickness w_{opt} = 149 nm, modulator length L = 10 μm; and 2. insulator material Ta_2O_5 (ε_1 = 22), insulator thickness w_{opt} = 33.2 nm, modulator length L = 10 μm.

The high modulation speed of case 1; high modulation depth and low applied voltage of case 2; and compact footprint, low insertion loss, broad operation bandwidth, and ultra-high FOM of both cases will need to be experimentally validated.

For **chapter 3**:

The suspended triple-layer graphene modulator will need to be measured at the parameters of: 1. insulator material h-BN (ε_1 = 3.24), insulator thickness w_{opt} = 78 nm, modulator length L = 5 μm; and 2. insulator material Ta_2O_5 (ε_1 = 22), insulator thickness w_{opt} = 17 nm, modulator length L = 5 μm.

In addition, the high modulation speed of case 1; two high modulation depths and low applied voltage of case 2; and compact footprint, low insertion loss, broad operation bandwidth, and ultra-high FOM of both cases will need to be measured.

For **chapter 4**:

The suspended double-layer graphene modulator at the condition: silicon (ε_1 = 11.7) thickness of w_{opt} = 48.8 nm, insulator (Al_2O_3, ε_2 = 3.06) thickness of t = 7 nm, modulator length L = 10 μm will require fabrication followed by experimental validation.

For sub-wavelength thickness modulator, it will be fabricated at insulator (Ta_2O_5, ε_2 = 22) thickness of w_{opt} = 75.1 nm and 60 nm, modulator length L = 10 μm.

The high modulation speed and large modulation efficiency at w_{opt} = 75.1 nm, and the leaky mode at w_{p} = 60 nm will be validated.

For **chapter 5**:

Fabrication of the metal-clad suspended self-biasing graphene modulator to measure the tunable light-graphene interaction and FOM will be conducted. The M-Z modulator with small π-phase shift length (as low as 6.35 μm) will be demonstrated. The filter application of this modulator will also be demonstrated.

For **chapter 6**:

The layered THz waveguides at the optimized designed structures [144] will require fabrication and validation.

8.3.2 Future perspectives for graphene modulator

The main purpose of researches on graphene modulator is to develop a modulator closer to the fundamental limits of graphene. In some cases, higher light-graphene interaction can enhance the modulator to be closer to the fundamental limits of graphene. The compromise is that the light interaction with other materials should be lower, so fewer materials in the fabrication of graphene modulator can make the modulator better. In the cases of references [52,53], metal or other higher lossy materials are included in the active area, which definitely causes much higher insertion loss with lower modulation depth. For future perspectives, graphene and other 2D materials based modulators are to develop higher FOMs.

8.3.2.1 Modulation depth

In reference [116], the modulation depth of electro-absorption modulation of graphene can be 100%. The higher coupling between different modes can enhance the modulation depth. In reference [52,113], the resonant mode is used to enhance the modulation depth. By suspending the graphene structures [143,145,146,149,150], the modulation depth can be designed to the highest for these simpler structures with much fewer materials.

For future fabrications, the modulation depth of graphene modulators can be enhanced by: i). Coupling between different modes; ii). Using resonant modes; iii). Suspending structures; iv). Designing for higher light-graphene interaction; v). Fabricating with fewer materials.

For electro-refractive modulation, the 100% modulations can be realized with much lower π-phase shift length than that of silicon modulators. Higher light-graphene interaction can enhance the change of refractive index, which will cause even lower π-phase shift length. The π-phase shift length has been reduced to 11.3 μm by [145] and 6.35μm by [150].

8.3.2.2 Modulation speed

The compromise between modulation speed and modulation efficiency is always a problem which stops a better modulator. In order to get higher modulation speed, the capacitor of modulators should be lower, and the resistances caused by contact or graphene sheet should be lower. So higher modulation speed can be realized by: i). Using thicker gate material; ii). Making the modulation area smaller; iii). Improving the mobilities of graphene by cleaning graphene sheets; iv). Lower the electrode-graphene contact area.

For the trade-off between modulation speed and modulation efficiency, methods 1 and 2 may cause lower modulation efficiency. By designing the suspended graphene modulators [143,145,146,149,150], thicker gate material can be found which will enhance the light-graphene interaction simultaneously. In short, the suspended structures can be good candidates for future applications.

8.3.2.3 Footprint

For graphene modulator, the footprint is much smaller than that of traditional modulator which is because of much higher absorption of graphene with small area. Different structures have different footprints. Higher light-graphene interaction can further enhance the footprint.

8.3.2.4 Operation bandwidth

Because of the broadband absorption of graphene, the operation bandwidth of graphene modulator is always very high. Originally, the

3-dB bandwidth can be from visible light to near THz band. The waveguide-base modulator has very small wave-graphene interaction in THz ranges, so the 3-dB bandwidth may not reach THz ranges. The most interesting operation bandwidth for research is in the scale of 15 THz [34,37].

8.3.2.5 Insertion loss

Fewer the materials in the modulator, much lower will be the insertion loss. The insertion loss of suspended graphene modulator has been developed very near to the fundamental limits of graphene which is in the range of 0.002 dB [143,145,146,149,150].

8.3.3 Future perspectives for THz waveguide

Since graphene cannot be used in THz waveguide with effectively light-matter interaction, novel larger materials for THz waveguide are demanding. Maybe in the coming future, the novel materials with excellent properties like graphene will be fabricated and used in THz waveguide and then there will be a spring for THz waveguide-based modulator.

Reference:

[1] K. S. Novoselov, A. K. Geim, S. V. Morozov, D. Jiang, Y. Zhang, S. V. Dubonos, I. V. Grigorieva, and A. A. Firsov, "Electric field effect in atomically thin carbon films," Science, 306(5696), 666–669 (2004).

[2] M. Liu, X. Yin, E. Ulin-Avila, B. Geng, T. Zentgraf, L. Ju, F. Wang, and X. Zhang, "A graphene-based broadband optical modulator," Nature, 474, 64-67 (2011).

[3] J. Tian, A. Katsounaros, D. Smith, and Y. Hao, "Graphene field-effect transistor model with improved carrier mobility analysis," IEEE Transactions on Electron Devices, 62(10), 3433-3440 (2015).

[4] R. Filter, M. Farhat, M. Steglich, R. Alaee, C. Rockstuhl, and F. Lederer, "Tunable graphene antennas for selective enhancement of THz-emission," Opt. Express, 21(3), 3737-3745 (2013).

[5] Z. Fang, Y. Wang, A. E. Schlather, Z. Liu, P. M. Ajayan, F. Javier García de Abajo, P. Nordlander, X. Zhu, and N. J. Halas, "Active tunable absorption enhancement with graphene nanodisk arrays," Nano Lett., 14, 299-304 (2014).

[6] H.-J. Li, L.-L. Wang, H. Zhang, Z.-R. Huang, B. Sun, X Zhai, and S.-C. Wen, "Graphene-based mid-infrared, tunable, electrically controlled plasmonic filter," Appl. Phys. Express, 7, 024301 (2014).

[7] B. Standley, W. Bao, H. Zhang, J. Bruck,C. N. Lau, and M. Bockrath, "Graphene-based atomic-scale switches," Nano Lett., 8(10), 3345-3349 (2008).

[8] D. Akinwande, N. Petrone and J. Hone, "Two-dimensional flexible nanoelectronics," Nat. Communications, 5: 5678 (2014).

[9] C. Lin, R. Grassi, T. Low, and A. S. Helmy, "Multilayer black phosphorus as a versatile mid-infrared electro-optic material," Nano Lett., 16, 1683-1689 (2016).

[10] K. F. Mak, C. Lee, J. Hone, J. Shan, and T. F. Heinz, "Atomically thin MoS_2: a new direct-gap semiconductor," Phys. Rev. Lett. 105(13), 136805 (2010).

[11] Z. Yin, H. Li, H. Li, L. Jiang, Y. Shi, Y. Sun, and H. Zhang, "Single-layer MoS_2 phototransistors," ACS Nano, 6(1), 74-80 (2011).

[12] W. Wu, D. De, S. C. Chang, Y. Wang, H. Peng, J. Bao, and S. S. Pei, "High mobility

and high on/off ratio field-effect transistors based on chemical vapor deposited single-crystal MoS_2 grains," Appl. Phys. Lett. 102(14), 142106 (2013).

[13] W. Liu, J. Kang, D. Sarkar, Y. Khatami, D. Jena, and K. Banerjee, "Role of metal contacts in designing high-performance monolayer n-type WSe_2 field effect transistors," Nano Lett. 13(5), 1983-1990 (2013).

[14] H. Fang, S. Chuang, T. C. Chang, K. Takei, T. Takahashi, and A. Javey, "High-performance single layered WSe_2 p-FETs with chemically doped contacts," Nano Lett. 12(7), 3788-3792 (2012).

[15] L. P. Feng, N. Li, M. H. Yang, and Z. T. Liu, "Effect of pressure on elastic, mechanical and electronic properties of WSe_2: A first-principles study," Materials Research Bulletin, 50, 503-508 (2014).

[16] K. Watanabe, T. Taniguchi, and H. Kanda, "Direct-bandgap properties and evidence for ultraviolet lasing of hexagonal boron nitride single crystal," Nat. Materials, 3(6), 404-409 (2004).

[17] Y. Shi, C. Hamsen, X. Jia, K. K. Kim, A. Reina, M. Hofmann, and M. S. Dresselhaus, "Synthesis of few-layer hexagonal boron nitride thin film by chemical vapor deposition," Nano Lett. 10(10), 4134-4139 (2010).

[18] L. Song, L. Ci, H. Lu, P. B. Sorokin, C. Jin, J. Ni, A. G. Kvashnin, D. G. Kvashnin, J. Lou, B. I. Yakobson, and P. M. Ajayan, "Large scale growth and characterization of atomic hexagonal boron nitride layers," Nano Lett. 10(8), 3209-3215 (2010).

[19] H. Liu, A. T. Neal, Z. Zhu, Z. Luo, X. Xu, D. Tománek, and P. D. Ye, "Phosphorene: an unexplored 2D semiconductor with a high hole mobility," ACS Nano 8(4), 4033-4041 (2014).

[20] R. Fei, A. Faghaninia, R. Soklaski, J. A. Yan, C. Lo, and L. Yang, "Enhanced thermoelectric efficiency via orthogonal electrical and thermal conductances in phosphorene," Nano Lett. 14(11), 6393-6399 (2014).

[21] Q. Wei, and X. Peng, "Superior mechanical flexibility of phosphorene and few-layer black phosphorus," Appl. Phys. Lett. 104(25), 251915 (2014).

[22] L. Li, Y. Yu, G. J. Ye, Q. Ge, X. Ou, H. Wu, D. Feng, X. H. Chen and Y. Zhang, "Black phosphorus field-effect transistors," Nat. Nanotech. 9 372-377 (2014).

[23] K. S. Novoselov, D. Jiang, F. Schedin, T. J. Booth, V. V. Khotkevich, S. V. Morozov, and A. K. Geim, "Two-dimensional atomic crystals," PNAS 102(30), 10451-10453 (2005).

[24] V. P. Gusynin, S. G. Sharapov, and J. P. Carbotte, "Magneto-optical conductivity in graphene," J. Phys.: Condens. Matter, 19, 026222 (2007).

[25] H. Liang, S. Ruan, M. Zhang, H. Su, and I. L. Li, "Graphene surface plasmon polaritons with opposite in-plane electron oscillations along its two surfaces," Appl. Phys. Lett., 107, 091602 (2015).

[26] S. J. Koester, and M. Li, "High-speed waveguide-coupled graphene-on-graphene optical modulators," Appl. Phys. Lett., 100(17), 171107 (2012).

[27] B. Sensale-Rodriguez, R. Yan, M. M. Kelly, T. Fang, K. Tahy, W. S. Hwang, D. Jena, L. Liu and H. G. Xing, "Broadband graphene terahertz modulators enabled by intraband transitions," Nat. Communications, 3: 780 (2012).

[28] K.I. Bolotin, K.J. Sikes, Z. Jiang, M. Klima, G. Fudenberg, J. Hone, P. Kim, H.L. Stormer, "Ultrahigh electron mobility in suspended graphene," Solid State Communications, 146, 351–355 (2008).

[29] Min Shi, Semiconductor devices: Physics and Technology, (Suzhou University, 2009)

[30] X. Zeng, X. Cheng, R. Yu, G. D. Stucky "Electromagnetic microwave absorption theory and recent achievements in microwave absorbers" Carbon, 168, 606-623 (2020).

[31] P. Salén, M. Basini, S. Bonetti, J. Hebling, M. Krasilnikov, A. Y. Nikitin, G. Shamuilov, Z. Tibai, V. Zhaunerchyk, V. Goryashko, "Matter manipulation with extreme terahertz light: Progress in the enabling THz technology" Phys. Reports, 836–837, 1-74 (2019).

[32] L. Tong, R. Gattass, J. B. Ashcom, S. He, J. Lou, M. Shen, I. Maxwell and E. Mazur, "Subwavelength-diameter silica wires for low-loss optical wave guiding," Nature, 426, 816-819 (2003).

[33] B. Wang, X. Zhang, X. Yuan, and J. Teng, "Optical coupling of surface plasmons between graphene sheets," Appl, Phys. Lett., 100, 131111 (2012).

[34] J. Gosciniak, and D. T. Tan, "Graphene-based waveguide integrated dielectric-loaded plasmonic electro-absorption modulators," Nanotechnology, 24(18), 185202 (2013).

[35] C. T. Phare, Y. H. D. Lee, J. Cardenas, and M. Lipson, “Graphene electro-optic modulator with 30 GHz bandwidth,” Nat. Photonics, 9(8), 511-514 (2015).

[36] R. Hao, W. Du, H. Chen, X. Jin, L. Yang, and E. Li, “Ultra-compact optical modulator by graphene induced electro-refraction effect,” Appl. Phys. Lett., 103(6), 061116 (2013).

[37] C. Zeng, J. Guo, and X. Liu, “High-contrast electro-optic modulation of spatial light induced by graphene-integrated Fabry-Pérot microcavity,” Appl. Phys. Lett., 105, 121103 (2014).

[38] S. J. Koester, H. Li, and M. Li, “Switching energy limits of waveguide-coupled graphene-on-graphene optical modulators,” Opt. Express, 20(18), 20330-20341 (2012).

[39] M. Tamagnone, A. Fallahi, J. R. Mosig, J. Perruisseau-Carrier, “Fundamental limits and near-optimal design of graphene modulators and non-reciprocal devices,” Nat. Photonics, 8(7), 556-563 (2014).

[40] J. S. Bunch, A. M. van der Zande, S. S. Verbridge, I. W. Frank, D. M. Tanenbaum, J. M. Parpia, H. G. Craighead, P. L. McEuen, “Electromechanical resonators from graphene sheets,” Science, 315, 490–493 (2007).

[41] Y. D. Kim, H. Kim, Y. Cho4, J. H. Ryoo, C.-H. Park, P. Kim, Y. S. Kim, S. Lee, Y. Li, S.-N. Park, Y. S. Yoo, D. Yoon, V. E. Dorgan, E. Pop, T. F. Heinz, J. Hone, S.-H. Chun, H. Cheong, S. W. Lee, M.-H. Bae, and Y. D. Park, “Bright visible light emission from graphene,” Nat. Nanotechnol., 10, 676-682 (2015).

[42] X. Du, I. Skachko, A. Barker, and E. Andrei, “Approaching ballistic transport in suspended graphene,” Nat. Nanotechnol., 3, 491- 495 (2008).

[43] A. Liu, R. Jones, L. Liao, D. Samara-Rubio, D. Rubin, O. Cohen, R. Nicolaescu, and M. Paniccia, “A high-speed silicon optical modulator based on a metal–oxide–semiconductor capacitor,” Nature, 427, 615-618 (2004).

[44] Q. Xu, B. Schmidt, S. Pradhan, and M. Lipson, “Micrometre-scale silicon electro-optic modulator,” Nature, 435, 325-327 (2005).

[45] L. Alloatti, D. Korn, R. Palmer, D. Hillerkuss, J. Li, A. Barklund, R. Dinu, J. Wieland, M. Fournier, J. Fedeli, H. Yu, W. Bogaerts, P. Dumon, R. Baets, C. Koos, W. Freude, and J. Leuthold, “42.7 Gbit/s electro-optic modulator in silicon technology,” Opt. Express, 19(12), 11841-11851 (2011).

[46] C. Xu, Y. Jin, L. Yang, J. Yang, and X. Jiang, “Characteristics of electro-refractive modulating based on Graphene-Oxide-Silicon waveguide,” Opt. Express, 20(20), 22398-22405 (2012).

[47] M. Liu, X. Yin, and X. Zhang, “Double-layer graphene optical modulator,” Nano Lett., 12(3), 1482-1485 (2012).

[48] S. Ye, Z. Wang, L. Tang, Y. Zhang, R. Lu, and Y. Liu, “Electro-absorption optical modulator using dual-graphene-on-graphene configuration,” Opt. Express, 22(21), 26173-26180 (2014).

[49] Z.-B. Liu, M. Feng, W.-S. Jiang, W. Xin, P. Wang, Q.-W. Sheng, Y.-G. Liu, D. N. Wang, W.-Y. Zhou and J.-G. Tian, “Broadband all-optical modulation using a graphene-covered-microfiber,” Laser Phys. Lett., 10, 065901 (2013).

[50] W. Li, B. Chen, C. Meng, W. Fang, Y. Xiao, X. Li, Z. Hu, Y. Xu, L. Tong, H. Wang, W. Liu, J. Bao, and Y. R. Shen, “Ultrafast all-optical graphene modulator,” Nano Lett., 14, 955-959 (2014).

[51] S. Yu, X. Wu, K. Chen, B. Chen, X. Guo, D. Dai, L. Tong, W. Liu, and Y. R. Shen, “All-optical graphene modulator based on optical Kerr phase shift,” Optica, 3(5), 541-544 (2016).

[52] B. Sensale-Rodriguez, R. Yan, S. Rafique, M. Zhu, W. Li, X. Liang, D. Gundlach, V. Protasenko, M. M. Kelly, D. Jena, L. Liu, and H. G. Xing, “Extraordinary control of terahertz beam reflectance in graphene electro-absorption modulators,” Nano Lett., 12, 4518-4522 (2012).

[53] C.-C. Lee, S. Suzuki, W. Xie, and T. R. Schibli, “Broadband graphene electro-optic modulators with sub-wavelength thickness,” Opt. Express, 20(5), 5264-5269 (2012).

[54] M. Midrio, S. Boscolo, M. Moresco, M. Romagnoli, C. D. Angelis, A. Locatelli, and A.-D. Capobianco, “Graphene–assisted critically–coupled optical ring modulator,” Opt. Express, 20(21), 23144-23155 (2012).

[55] X. Gan, R.-J. Shiue, Y. Gao, K. F. Mak, X. Yao, L. Li, A. Szep, D. Walker, Jr., J. Hone, T. F. Heinz, and D. Englund, “High-contrast electrooptic modulation of a photonic crystal nanocavity by electrical gating of graphene,” Nano Lett., 13, 691-696 (2013).

[56] M. Mohsin, D. Schall, M. Otto, A. Noculak, D. Neumaier, and H. Kurz, “Graphene

based low insertion loss electro-absorption modulator on SOI waveguide," Opt. Express, 22(12), 15292-15297 (2014).

[57] N. Youngblood, Y. Anugrah, R. Ma, S. J. Koester, and M. Li, "Multifunctional graphene optical modulator and photodetector integrated on silicon waveguides," Nano Lett., 14, 2741-2746 (2014).

[58] J. Lao, J. Tao, Q. J. Wang, and X. G. Huang, "Tunable graphene-based plasmonic waveguides: nano modulators and nano attenuators," Laser & Photonics Review, 8(4), 569-574 (2014).

[59] Y. Gao, R.-J. Shiue, X. Gan, L. Li, C. Peng, I. Meric, L. Wang, A. Szep, D. Walker, Jr., J. Hone, and D. Englund, "High-speed electro-optic modulator integrated with graphene-boron nitride heterostructure and photonic crystal nanocavity," Nano Lett., 15, 2001-2005 (2015).

[60] G. D. Wilk, R. M. Wallace, and J. M. Anthony, "High-κ gate dielectrics: Current status and materials properties considerations," Journal of Appl. Phys., 89(10), 5243-5275 (2001).

[61] G. Keiser, Optical Fiber Communications, 2nd ed. (McGraw-Hill, 1991).

[62] G. Gallot, S. P. Jamison, R.W. McGowan, and D. Grischkowsky, "Terahertz waveguides," J. Opt. Soc. Am. B, 17, 851-863 (2000).

[63] S. Atakaramians, S. Afshar V., T. M. Monro, and D. Abbott, "Terahertz dielectric waveguides," Advances in Optics and Photonics, 5, 169–215 (2013).

[64] M. Nagel, A. Marchewka, and H. Kurz, "Low-index discontinuity terahertz waveguides," Opt. Express, 14, 9944-9954 (2006).

[65] R. W. McGowan, G. Gallot, and D. Grischkowsky, "Propagation of ultra-wideband short pulses of THz radiation through submillimeter-diameter circular waveguides," Opt. Lett., 24, 1431-1433 (1999).

[66] S. P. Jamison, R. W. McGown, and D. Grischkowsky, "Single-mode waveguide propagation and reshaping of sub-ps terahertz pulses in sapphire fiber," Appl. Phys. Lett., 76, 1987-1989 (2000).

[67] H. Han, H. Park, M. Cho, and J. Kim, "Terahertz pulse propagation in a plastic photonic crystal fiber," Appl. Phys. Lett., 80, 2634-2636 (2002).

[68] R. Mendis and D. M. Mittleman, “An investigation of the lowest-order transverse-electric (TE_1) mode of the parallel-plate waveguide for THz pulse propagation,” J. Opt. Soc. Am. B, 26, A6-A13 (2009).

[69] R. Mendis and D. M. Mittleman, “Comparison of the lowest-order transverse-electric (TE_1) and transverse-magnetic (TEM) modes of the parallel-plate waveguide for terahertz pulse applications,” Opt. Express, 17, 14839-14850 (2009).

[70] J. Liu, H. Liang, M. Zhang, and H. Su, “Broadband terahertz transmission within the symmetrical plastic film coated parallel-plate waveguide,” App. Opt., 53(26), 6008-6012 (2014).

[71] I. J. H. McCrindle, J. Grant, T. D. Drysdale, and D. R. S. Cumming, “Hybridization of optical plasmonics with terahertz metamaterials to create multi-spectral filters,” Opt. Express, 21(16), 19142-19152 (2013).

[72] R. Mendis, A. Nag, F. Chen, and D. M. Mittleman, “A tunable universal terahertz filter using artificial dielectrics based on parallel-plate waveguides,” Appl. Phys. Lett., 97(13), 131106 (2010).

[73] B. S. Phillips, P. Measor, Y. Zhao, H. Schmidt, and A. R. Hawkins, “Optofluidic notch filter integration by lift-off of thin films,” Opt. Express, 18(5), 4790–4795 (2010).

[74] R. Mendis, V. Astley, J. Liu, and D. M. Mittleman, “Terahertz microfluidic sensor based on a parallel-plate waveguide resonant cavity,” Appl. Phys. Lett., 95 (17), 171113 (2009).

[75] J. Liu, H. Liang, M. Zhang, and H. Su, “THz wave transmission within the metal film coated double-dielectric-slab waveguides and the tunable filter application,” Opt. Communications, 351, 103-108 (2015).

[76] K. Wang, and D. M. Mittleman, “Metal wires for terahertz wave guiding,” Nature, 432, 376-379 (2004).

[77] M. Wächter, M. Nagel, and H. Kurz, “Frequency-dependent characterization of THz Sommerfeld wave propagation on single-wires,” Opt. Express, 13(26), 10815–10822 (2005).

[78] Nick C. J. van der Valka and Paul C. M. Planken, “Effect of a dielectric coating on terahertz surface plasmon polaritons on metal wires,” Appl. Phys. Lett., 87, pp071106

(2005).

[79] M. Awad, M. Nagel, and H. Kurz, “Tapered Sommerfeld wire terahertz near-field imaging,” Appl. Phys. Lett, 94, 051107 (2009).

[80] D. K. Gramotnev, and S. I. Bozhevolnyi, “Plasmonics beyond the diffraction limit,” Nat. Photonics, 4, 83 (2010).

[81] Q. Cao, J. Jahns, “Azimuthally polarized surface plasmons as effective terahertz waveguides,” Opt. Express, 13, 511-518 (2005).

[82] J. Liu, H. Liang, M. Zhang, and H. Su, “Coupling of Sommerfeld waves using odd TM mode of double-dielectric-slab waveguide,” J Opt, 44(1), 53–58 (2014).

[83] C.-H. Lai, Y.-C. Hsueh, H.-W. Chen, Y.-J. Huang, H.-C. Chang, and C.-K. Sun, “Low-index terahertz pipe waveguides,” Opt. Lett., 34, 3457-3459 (2009).

[84] E. Nguema, D. Fèrachou, G. Humbert, J. L. Auguste, and J. M. Blondy, “Broadband terahertz transmission within the air channel of thin-wall pipe,” Opt. Lett., 36, 1782–1784 (2011).

[85] B. You, J.-Y. Lu, J.-H. Liou, C.-P. Yu, H.-Z. Chen, T.-A. Liu, and J.-L. Peng, “Subwavelength film sensing based on terahertz anti-resonant reflecting hollow waveguides,” Opt. Express, 18(18), 19353–19360 (2010).

[86] B. You, J.-Y. Lu, C.-P. Yu, T.-A. Liu, and J.-L. Peng, “Terahertz refractive index sensors using dielectric pipe waveguides,” Opt. Express, 20(6), 5858–5866 (2012).

[87] L. Chen, H. Chen, T. Kao, J. Lu, and C. Sun, “Low-loss subwavelength plastic fiber for terahertz waveguiding”, Opt. Lett., 31(3), 308-310, (2006).

[88] H. Bao, K. Nielsen, H. K. Rasmussen, P. U. Jepsen, and O. Bang, “Design and optimization of mechanically downdoped terahertz fiber directional couplers,” Opt. Express, 22(8), 9486-9497 (2014).

[89]C. Themistos, B. M. A. Rahman, M. Rajarajan, K. T. V. Grattan, B. Bowden, and J. A. Harrington, “Characterization of Silver/Polysterene (PS)-Coated Hollow Glass Waveguides at THz Frequency,” J. Lightwave Technol., 25, 2456-2462 (2007).

[90] M. Gong, T.-I. Jeon, and D. Grischkowsky, “THz surface wave collapse on coated metal surfaces,” Opt. Express, 17(19), 17088-17101 (2009).

[91] J. Saxler, J. G. Rivas, C. Janke, H. P. M. Pellemans, P. H. Bolıvar, and H. Kurz,

“Time-domain measurements of surface plasmon polaritons in the terahertz frequency range,” Phys. Rev. B, 69, 155427 (2004).

[92] T. H. Isaac,W. L. Barnes, and E. Hendry, “Determining the terahertz optical properties of subwavelength films using semiconductor surface plasmons,” Appl. Phy. Lett., 93, 241115 (2008).

[93] J. Liu, H. Liang, M. Zhang, and H. Su, “Metal plate for guiding terahertz surface plasmon-polaritons and its sensing applications,” Opt. Communications, 339, 222–227 (2014).

[94] J.-Y. Lu, H.-Z. Chen, C.-H. Lai, H.-C. Chang, B. You, T.-A. Liu, and J.-L. Peng, “Application of metal-clad anti-resonant reflecting hollow waveguides to tunable terahertz notch filter,” Opt. Express, 19(1), 162–167 (2011).

[95] J. Liu, H. Liang, M. Zhang, and H. Su, “THz wave transmission within the metal-clad anti-resonant reflecting hollow waveguides,” Appl. Opt., 54(14), 4549-4555 (2015).

[96] J. Liu, H. Liang, M. Zhang, and H. Su, “Double-dielectric-slab waveguides for guiding broadband THz wave with low propagation loss and small beam width,” OF4A.5 POEM 2014.

[97] J. Liu, H. Liang, M. Zhang, and H. Su, “THz wave in double-metal-film waveguides and its application of analysis wavelength,” Appl. Opt., 54(28): 8406 – 8411 (2015).

[98] Sarid, D. “Long-range surface-plasma waves on very thin metal films,” Phys. Rev. Lett., 47, 1927–1930 (1981).

[99] R. F. Oulton, V. J. Sorger, D. A. Genov, D. F. P. Pile and X. Zhang, “A hybrid plasmonic waveguide for subwavelength confinement and long-range propagation,” Nat. Photonics, 2, 496-500 (2008).

[100] M. Z. Alam, J. Meier, J. S. Aitchison, and M. Mojahedi, “Propagation characteristics of hybrid modes supported by metal-low-high index waveguides and bends,” Opt. Express, 18(12), 12971-12979 (2010).

[101] H. Liang, S. Ruan, M. Zhang, H. Su, and I. L. Li, “Modified surface plasmon polaritons for the nanoconcentration and long-range propagation of optical energy,” Sci. Reports, 4(5015), 1-3 (2014).

[102] H. Liang, S. Ruan, M. Zhang, H. Su, and I. L. Li, “Characteristics of modified surface plasmon polaritons on double-coated metal nanofilms,” Laser Phys. Lett., 11, 115003, (2014).

[103] H. Liang, S. Ruan, S. Xu, M. Zhang, H. Su, and I. L. Li, “Modified surface plasmon polaritons with ultrahigh figures of merit on metal-gap–dielectric waveguides,” Appl. Phys. Express, 7, 122001 (2014).

[104] A. Phatak, Z. Cheng, C. Qin, and K. Goda, “Design of electro-optic modulators based on graphene-on-silicon slot waveguides,” Opt. Lett., 41(11), 2501-2504 (2016).

[105] M. Mohsin, D. Neumaier, D. Schall, M. Otto, C. Matheisen, A. L. Giesecke, A. A. Sagade, and H. Kurz, “Experimental verification of electro-refractive phase modulation in graphene,” Sci. Reports, 5:10967 (2015).

[106] V. Sorianello, M. Midrio, G. Contestabile, I. Asselberg, J. Van Campenhout, C. Huyghebaerts, I. Goykhman, A. K. Ott, A. C. Ferrari, M. Romagnoli, “Graphene–silicon phase modulators with gigahertz bandwidth,” Nat. Photonics, 12, 40 (2018).

[107] S. Qu, C. Ma, and H. Liu, “Tunable graphene-based hybrid plasmonic modulators for subwavelength confinement,” Sci. Reports, 7: 5190 (2017).

[108] M. Fan, H. Yang, P. Zheng, G. Hu, B. Yun, and Y. Cui, “Multilayer graphene electro-absorption optical modulator based on double-stripe silicon nitride waveguide,” Opt. Express, 25(18), 21619-21629 (2017).

[109] P. Weis, J. L. Garcia-Pomar, M. Hoh, B. Reinhard, A. Brodyanski, and M. Rahm, “Spectrally Wide-Band Terahertz Wave Modulator Based on Optically Tuned Graphene,” ACS Nano., 6(10), 9118–9124 (2012).

[110] Y. Zhou, X. Xu, H. Fan, Z. Ren, J. Bai, and L. Wang, “Tunable magnetoplasmons for efficient terahertz modulator and isolator by gated monolayer graphene,” Phys. Chem. Chem. Phys., 15, 5084 (2013).

[111] E. O. Polat and C. Kocabas, “Broadband Optical Modulators Based on Graphene Supercapacitors,” Nano Lett., 13, 5851−5857 (2013).

[112] J. Gosciniak and D. T. H. Tan, “Theoretical investigation of graphene-based photonic modulators,” Sci. Reports, 3: 1897 (2013).

[113] C. Qiu, W. Gao, R. Vajtai, P. M. Ajayan, J. Kono, and Q. Xu, “Efficient Modulation

of 1.55 µm Radiation with Gated Graphene on a Silicon Microring Resonator," Nano Lett., 14, 6811–6815 (2014).

[114] L. Yang, T. Hu, A. Shen, C. Pei, B. Yang, T. Dai, H. Yu, Y. Li, X. Jiang, and J. Yang, "Ultracompact optical modulator based on graphene-silica metamaterial," Opt. Lett., 39(7), 1909-1912 (2014).

[115] Q.-Y. Wen, W. Tian, Q. Mao, Z. Chen, W.-W. Liu, Q.-H. Yang, M. Sanderson, and H.-W. Zhang, "Graphene based All-Optical Spatial Terahertz Modulator," Sci. Reports, 4: 7409 (2014).

[116] S. Gan, C. Cheng, Y. Zhan, B. Huang, X. Gan, S. Li, S. Lin, X. Li, J. Zhao, H. Chen and Q. Bao, "A highly efficient thermo-optic microring modulator assisted by graphene," Nanoscale, 7, 20249 (2015).

[117] D. Ansell, I.P. Radko, Z. Han, F.J. Rodriguez, S.I. Bozhevolnyi, and A.N. Grigorenko, "Hybrid graphene plasmonic waveguide modulators," Nat. Communications, 6: 8846 (2015).

[118] T. Pan, C. Qiu, J. Wu, X. Jiang, B. Liu, Y. Yang, H. Zhou, R. Soref, and Y. Su, "Analysis of an electro-optic modulator based on a graphene-silicon hybrid 1D photonic crystal nanobeam cavity," Opt. Express, 23(18), 23357-23364 (2015).

[119] N. Kuse, C.-C. Lee, J. Jiang, C. Mohr, T. R. Schibli, and M.E. Fermann, "Ultra-low noise all polarization-maintaining Er fiber-based optical frequency combs facilitated with a graphene modulator," Opt. Express, 23(19), 24342-24350 (2015).

[120] M. Kim, C. Y. Jeong, H. Heo, and S. Kim, "Optical reflection modulation using surface plasmon resonance in a graphene-embedded hybrid plasmonic waveguide at an optical communication wavelength," Opt. Lett., 40(6), 871-874 (2015).

[121] J. Gosciniak, D. T. H. Tan and B. Corbett, "Enhanced performance of graphene-based electro-absorption waveguide modulators by engineered optical modes," J. Phys. D: Appl. Phys., 48, 235101 (2015).

[122] F. Shi, Y. Chen, P. Han, and P. Tassin, "Broadband, Spectrally Flat, Graphene-based Terahertz Modulators," Small, 11(45), 6044–6050 (2015).

[123] J.-S. Shin and J. T. Kim, "Broadband silicon optical modulator using a graphene-integrated hybrid plasmonic waveguide," Nanotechnology, 26, 365201 (2015).

[124] H. Dalir, Y. Xia, Y. Wang, and X. Zhang, "Athermal Broadband Graphene Optical Modulator with 35 GHz Speed," ACS Photonics, 3(9), 1564-1568 (2016).

[125] T. Sun, J. Kim, J. M. Yuk, A. Zettl, F. Wang, and C. Chang-Hasnain, "Surface-normal electro-optic spatial light modulator using graphene integrated on a high-contrast grating resonator," Opt. Express, 24(23), 26035-26043 (2016).

[126] H. Zhang, N. Healy, L. Shen, C. C. Huang, D. W. Hewak, and A. C. Peacock, "Enhanced all-optical modulation in a graphene-coated fibre with low insertion loss," Sci. Reports, 6: 23512 (2016).

[127] L. A. Shiramin and D. V. Thourhout, "Graphene Modulators and Switches Integrated on Silicon and Silicon Nitride Waveguide," IEEE Journal of Selected Topics in Quantum Electronics, 23(1), 3600107 (2017).

[128] I. Chatzakis, Z. Li, A. V. Benderskii and S. B. Cronin, "Broadband terahertz modulation in electrostatically-doped artificial trilayer graphene," Nanoscale, 9, 1721 (2017).

[129] D. E. Aznakayeva, F. J. Rodriguez, O. P. Marshall, and A. N. Grigorenko, "Graphene light modulators working at near-infrared wavelengths," Opt. Express, 25(9) 10255-10260 (2017).

[130] V. Sorianello, G. Contestabile, M. Midrio, M. Pantouvaki, I. Asselbergs, J. V. Campenhout, C. Huyghebaerts, A. Derrico, P. Galli, and M. Romagnoli, "Chirp management in silicon-graphene electro absorption modulators," Opt. Express, 25(16), 19371-19381 (2017).

[131] C. Gao, L. Gao, T. Zhu, and G. Yin, "Incoherent optical modulation of graphene based on an in-line fiber Mach–Zehnder interferometer," Opt. Lett., 42(9), 1708-1711 (2017).

[132] X. Peng, R. Hao, Z. Ye, P. Qin, W. Chen, H. Chen, X. Jin, D. Yang, and E. Li, "Highly efficient graphene-on-gap modulator by employing the hybrid plasmonic effect," Opt. Lett., 42(9), 1736-1739 (2017).

[133] Y. Liao, G. Y. Feng, H. Zhou, J. Mo, H. J. Sun, and S. H. Zhou, "Ultra-Broadband All-Optical Graphene Modulator," IEEE Photonics Tech. Lett., 30(8), 661-664 (2018).

[134] G. Kovacevic, C. Phare, S. Y. Set, M. Lipson, and S. Yamashita, "Ultra-high-speed

graphene optical modulator design based on tight field confinement in a slot waveguide," Appl. Phys. Express, 11, 065102 (2018).

[135] H. Shu, Z. Su, L. Huang, Z. Wu, X. Wang, Z. Zhang and Z. Zhou, "Significantly High Modulation Efficiency of Compact Graphene Modulator Based on Silicon Waveguide," Sci. Reports, 8: 991 (2018).

[136] X. Li, W. Cai, J. An, S. Kim, J. Nah, D. Yang, R. Piner, A. Velamakanni, I. Jung, E. Tutuc, S. K. Banerjee, L. Colombo, and R. S. Ruoff, "Large-area synthesis of high-quality and uniform graphene films on copper foils," Science, 324(5932), 1312-1314 (2009).

[137] N. K. Emani, T. F. Chung, X. J. Ni, A. V. Kildishev, Y. P. Chen, and A. Boltasseva, "Electrically Tunable Damping of Plasmonic Resonances with Graphene," Nano Lett., 12, 5202–5206 (2012).

[138] A. Yariv, Optical Electronics in Modern Communications (Oxford University, 2007).

[139] F. Xia, V. Perebeinos, Y. Lin, Y. Wu, and P. Avouris, "The origins and limits of metal–graphene junction resistance," Nat. Nanotechnol., 6, 179-184 (2011).

[140] G. Kovacevica and S. Yamashita, "Design optimizations for a high-speed two-layer graphene optical modulator on silicon," IEICE Electronics Express, 13(14), 1-11 (2016).

[141] G. W. Hanson, "Dyadic Green's Functions for an Anisotropic, Non-Local Model of Biased Graphene," IEEE Transactions on antennas and propagation, 56(3), 747-757 (2008).

[142] C. Hwang, D. A. Siegel, S.-K. Mo, W. Regan, A. Ismach, Y. Zhang, A. Zettl, and A. Lanzara, "Fermi velocity engineering in graphene by substrate modification," Sci. Reports, 2(590), 1-4 (2012).

[143] J. Liu, Y. Liu, "Ultrafast suspended self-biasing graphene modulator with ultrahigh figure of merit," Opt. Communications, 427: 439-446 (2018).

[144] R. Mendis and D. Grischkowsky, "THz interconnect with low-loss and low-group velocity dispersion," IEEE Microw. Wireless Compon. Lett., 11(11), 444-446 (2001).

[145] J. Liu, Z. U. Khan, and S. Sarjoghian, "Suspended triple-layer graphene modulator with two modulation depths and ultra-high modulation speed," OSA Continuum, 2(3), 827-838 (2019).

[146] J. Liu, Z. U. Khan, and S. Sarjoghian, "Suspended graphene double-layer

modulator with an ultrahigh figure of merit and a sub-wavelength thickness modulator with leaky mode," Appl. Opt., 58(14), 3729-3734 (2019).

[147] M. A. Ordal, R. J. Bell, R. W. Alexander, Jr, L. L. Long, and M. R. Querry, "Optical properties of fourteen metals in the infrared and far infrared: Al, Co, Cu, Au, Fe, Pb, Mo, Ni, Pd,Pt, Ag, Ti, V, and W," Appl. Opt., 24(24), 4493–4499 (1985).

[148] J. Liu, Z. Khan, and S. Sarjoghian, "Layered THz waveguides for SPPs, filter and sensor applications," Journal of Optics, 48(4): 567-581 (2019).

[149] J. Liu, Z. Khan, C. Wang, H. Zhang, and S. Sarjoghian, "Review of graphene modulators from the low to the high figure of merits," Journal of Physics D: Applied Physics, 53: 233002 (2020).

[150] J. Liu, Z. Khan, and S. Sarjoghian, "Metal-clad-suspended self-biasing graphene modulator with tunable figure of merit," Journal of Optics, 49(3): 364-369 (2020).

[151] S. Sarjoghian, A. Rahimian, Y. Alfadhl, T. G. Sunders, J. Liu, and C. G. Parini, "Hybrid Development of a Compact Antenna Based on a Novel Skin-Matched Ceramic Composite for Body Fat Measurement," Electronics, 9: 2139 (2020).

Appendix A

The code of Mathematica calculations of dispersion equations

For all these chapters, the codes of Mathematica dispersion relation calculations are similar, I publish the code for chapter 3 for an example:

```
[Lambda] = 1.55 10^-6; c = 3*10^8; f = c/[Lambda]
c = 3*10^8; k = N[2*[Pi]*f/c]
[Omega] = 2*[Pi]*f; Subscript[[Epsilon], 0] = 8.854 10^-12; T = 300;
Subscript[[Mu], c2] = 0.01*1.6*10^-19;
Subscript[[Mu], c] = (2)^(1/2)*Subscript[[Mu], c2]
[Tau] = 3.3*10^-12; e = 1.6 10^-19; Subscript[k, B] = 1.3806505 10^-23;
[HBar] = (6.63 10^-34)/(2 [Pi]);
Subscript[[Sigma], intra] = (I*e^2 Subscript[k, B]*T)/([Pi]*[HBar]^2
([Omega] + I*[Tau]^-1)) {Subscript[[Mu], c] /(Subscript[k, B] T) +
2*Log[Exp[-(Subscript[[Mu], c] /(Subscript[k, B] T))] + 1]};
Subscript[[Sigma], inter] = (I*e^2)/(4 [Pi]*[HBar])*Log[(2
Abs[Subscript[[Mu], c]] - [HBar]*([Omega] + I*[Tau]^-1))/(2
Abs[Subscript[[Mu], c]] + [HBar]*([Omega] + I*[Tau]^-1))];
Subscript[[Sigma], g1] = Subscript[[Sigma], intra] + Subscript[[Sigma],
inter];
[Delta] = 0.33*10^-9;
Subscript[[Epsilon], 1] = (I*Subscript[[Sigma],
g1])/([Delta]*[Omega]*Subscript[[Epsilon], 0]);
Subscript[[Epsilon], 2] = 22; [Tau] = 3.3*10^-12; e = 1.6 10^-19;
Subscript[k, B] = 1.3806505 10^-23; [HBar] = (6.63 10^-34)/(2 [Pi]);
```

```
Subscript[[Sigma], intra2] = (I*e^2 Subscript[k, B]*T)/([Pi]*[HBar]^2
([Omega] + I*[Tau]^-1)) {Subscript[[Mu], c2] /(Subscript[k, B] T) +
2*Log[Exp[-(Subscript[[Mu], c2] /(Subscript[k, B] T))] + 1]};
Subscript[[Sigma], inter2] = (I*e^2)/(4 [Pi]*[HBar])Log[(2
Abs[Subscript[[Mu], c2]] - [HBar]*([Omega] + I*[Tau]^-1))/(2
Abs[Subscript[[Mu], c2]] + [HBar]*([Omega] + I*[Tau]^-1))];
Subscript[[Sigma], g2] = Subscript[[Sigma], intra2] + Subscript[[Sigma],
inter2]; [Delta] = 0.33*10^-9;
Subscript[[Epsilon], 3] = (I*Subscript[[Sigma],
g2])/([Delta]*[Omega]*Subscript[[Epsilon], 0]);
Subscript[[Epsilon], 4] = 1; a = 0.5*0.33*10^-9; b = a + 17*10^-9; c = b +
0.33*10^-9;
Subscript[k, 1 x] = (Subscript[[Epsilon], 1] k^2 - (Subscript[[Beta], 1] +
I*Subscript[[Beta], 2])^2)^(1/2);
Subscript[k, 2 x] = (Subscript[[Epsilon], 2] k^2 - (Subscript[[Beta], 1] +
I*Subscript[[Beta], 2])^2)^(1/2);
Subscript[k, 3 x] = ((Subscript[[Beta], 1] + I*Subscript[[Beta], 2])^2 -
Subscript[[Epsilon], 3] k^2)^(1/2);
Subscript[k, 4 x] = ((Subscript[[Beta], 1] + I*Subscript[[Beta], 2])^2 -
Subscript[[Epsilon], 4] k^2)^(1/2);
FindRoot[{Re[Subscript[k, 1 x]*a - ArcTan[((1 + Tan[Subscript[k, 2 x] (b -
a)] Subscript[k, 2 x]/Subscript[k, 3 x] - Subscript[k, 3 x]/Subscript[k, 4 x] -
Subscript[k, 2 x]/Subscript[k, 4 x] Tan[Subscript[k, 2 x] (b - a)])
E^(-Subscript[k, 3 x] (c - b)) + (1 - Tan[Subscript[k, 2 x] (b - a)] Subscript[k,
2 x]/Subscript[k, 3 x] + Subscript[k, 3 x]/Subscript[k, 4 x] - Subscript[k, 2
x]/Subscript[k, 4 x] Tan[Subscript[k, 2 x] (b - a)]) E^(Subscript[k, 3 x] (c -
b)))/((-(Subscript[k, 3 x]/Subscript[k, 4 x]) Subscript[k, 1 x]/Subscript[k, 2
x] Tan[Subscript[k, 2 x] (b - a)] + Subscript[k, 1 x]/Subscript[k, 4 x] +
Subscript[k, 1 x]/Subscript[k, 2 x] Tan[Subscript[k, 2 x] (b - a)] -
Subscript[k, 1 x]/Subscript[k, 3 x]) E^(-Subscript[k, 3 x] (c - b)) +
```

```
(Subscript[k, 3 x]/Subscript[k, 4 x] Subscript[k, 1 x]/Subscript[k, 2 x]
Tan[Subscript[k, 2 x] (b - a)] + Subscript[k, 1 x]/Subscript[k, 4 x] +
Subscript[k, 1 x]/Subscript[k, 2 x] Tan[Subscript[k, 2 x] (b - a)] +
Subscript[k, 1 x]/Subscript[k, 3 x]) E^(Subscript[k, 3 x] (c - b)))]] == 0,
Im[Subscript[k, 1 x]*a - ArcTan[((1 + Tan[Subscript[k, 2 x] (b - a)]
Subscript[k, 2 x]/Subscript[k, 3 x] - Subscript[k, 3 x]/Subscript[k, 4 x] -
Subscript[k, 2 x]/Subscript[k, 4 x] Tan[Subscript[k, 2 x] (b - a)])
E^(-Subscript[k, 3 x] (c - b)) + (1 - Tan[Subscript[k, 2 x] (b - a)] Subscript[k,
2 x]/Subscript[k, 3 x] + Subscript[k, 3 x]/Subscript[k, 4 x] - Subscript[k, 2
x]/Subscript[k, 4 x] Tan[Subscript[k, 2 x] (b - a)]) E^(Subscript[k, 3 x] (c -
b)))/((-(Subscript[k, 3 x]/Subscript[k, 4 x]) Subscript[k, 1 x]/Subscript[k, 2
x] Tan[Subscript[k, 2 x] (b - a)] + Subscript[k, 1 x]/Subscript[k, 4 x] +
Subscript[k, 1 x]/Subscript[k, 2 x] Tan[Subscript[k, 2 x] (b - a)] -
Subscript[k, 1 x]/Subscript[k, 3 x]) E^(-Subscript[k, 3 x] (c - b)) +
(Subscript[k, 3 x]/Subscript[k, 4 x]Subscript[k, 1 x]/Subscript[k, 2 x]
Tan[Subscript[k, 2 x] (b - a)] + Subscript[k, 1 x]/Subscript[k, 4 x] +
Subscript[k, 1 x]/Subscript[k, 2 x] Tan[Subscript[k, 2 x] (b - a)] +
Subscript[k, 1 x]/Subscript[k, 3 x]) E^(Subscript[k, 3 x] (c - b)))]] == 0},
{Subscript[\[Beta], 1], 2.5 k}, {Subscript[\[Beta], 2], 10}]
```

Appendix B

The code of Matlab calculations of field equations

For all these chapters, the codes of Matlab calculations of field equations are also similar, I publish the code for chapter 3 for an example:

```
k1=31790.76406426127 -5.6656331215803325*10^6 *i; a=0.5*0.33*10^-9;
f=1.0000004369393385+4.903626303266517*10^-9*i;
g=0.00037480054855311434 +4.958848258626466*10^-6*i;
x1=0:0.01*10^-9:a; f1=abs(cos(k1*x1)); b=a+50*10^-9; x2=a:0.01*10^-9:b;
k2=1.4130433202483756*10^7-28369.144279151726*i;
f2=abs(f*cos(k2*(x2-a))+g*sin(k2*(x2-a))); c=b+0.33*10^-9;
k3=1.4624361095239367*10^7-9.561015841755847*10^6*i;
j=0.6005857802417067 +0.14323822987811993*i; k=0.1602832235759524
-0.14231455950141328 *i; x3=b:0.01*10^-9:c;
f3=abs(j*exp(-k3*(x3-b))+k*exp(k3*(x3-b))); x4=c:0.5*10^-9:100*10^-9;
k4=1.2058584767086009*10^7+33243.39514056001*i;
l=0.7578482095322346+0.0009232314511184447*i;
f4=abs(l*exp(-k4*(x4-c))); x5=-a:0.01*10^-9:0; f5=abs(cos(k1*x5));
x6=-b:0.01*10^-9:-a; f6=abs(f*cos(k2*(x6+a))-g*sin(k2*(x6+a)));
x7=-c:0.01*10^-9:-b; f7=abs(k*exp(-k3*(x7+b))+j*exp(k3*(x7+b)));
x8=-100*10^-9:0.5*10^-9:-c; f8=abs(l*exp(k4*(x8+c)));
x=[x8,x7,x6,x5,x1,x2,x3,x4]; F=[f8,f7,f6,f5,f1,f2,f3,f4];
plot(x,F,'-k','Linewidth',2) hold on
```